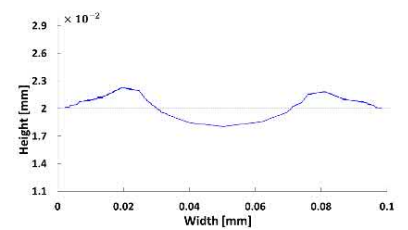
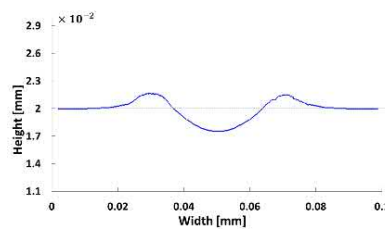
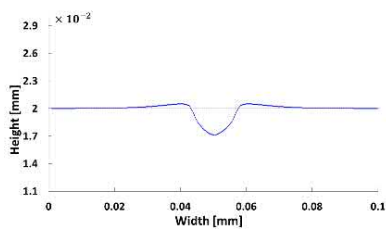
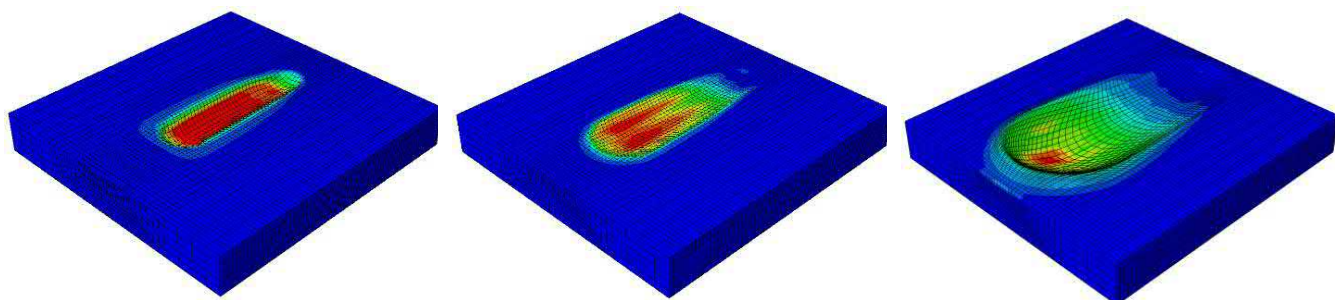




SFB 837
Interaction Modeling in
Mechanized Tunneling

Modeling of Soil-Tool Abrasive Wear Processes in Mechanized Tunneling

Golnaz Hoormazdi



Modeling of Soil-Tool Abrasive Wear Processes in Mechanized Tunneling

Dissertation

Zur

Erlangung des Grades

Doktor-Ingenieur

der

Fakultät für Bau- und Umweltingenieurwissenschaften

der Ruhr-Universität Bochum

von

Golnaz Hoormazdi

aus Shiraz, Iran

Bochum 2021

Herausgeber (Publisher):

Institut für Mechanik

— Schriftenreihe —

Ruhr-Universität Bochum

D-44801 Bochum

ISBN 978-3-935892-65-0

This material is presented to ensure timely dissemination of scholarly and technical work. Copyright and all rights therein are retained by the copyright holders. All persons copying this information are expected to adhere to the terms and constraints invoked by the author's copyright. These works or parts of it may not be used to repost reprint/republish or for creating new collective works for resale or redistribution to servers or lists without the explicit permission of the copyright holder.

Dieses Werk ist urheberrechtlich geschützt. Die dadurch begründeten Rechte, insbesondere die der Übersetzung, des Nachdrucks, des Vortrags, der Entnahme von Abbildungen und Tabellen, der Funksendung, der Mikroverfilmung oder der Vervielfältigung auf anderen Wegen und der Speicherung in Datenverarbeitungsanlagen, bleiben, auch bei nur auszugsweiser Verwertung, vorbehalten. Eine Vervielfältigung dieses Werkes oder von Teilen dieses Werkes ist zulässig. Sie ist grundsätzlich vergütungspflichtig. Zuwiderhandlungen unterliegen den Strafbestimmungen des Urheberrechtsgesetzes.

©2021 Golnaz Hoormazdi, Institut für Mechanik, Ruhr-Universität Bochum

Printed in Germany

Einreichung der Dissertation (thesis submission): 21.04.2021

Tag der mündlichen Prüfung (thesis defense): 18.06.2021

Erster Referent (first referee):

Zweiter Referent (second referee):

Dritte Referentin (third referee):

Vorsitzender (committee chair):

Prof. Dr. rer. nat. Klaus Hackl

Prof. Dr.-Ing. habil. Daniel Balzani

Prof. Dr.-Ing. habil. Stefanie Reese

Jun.-Prof. Dr. Andreas Vogel

Acknowledgments

The work presented in this thesis was carried out within the framework of my research activities at the *Institute of Mechanics of Materials* at Ruhr University of Bochum. The support provided by the Deutsche Forschungsgemeinschaft (DFG) under the grant SFB 837 “Interaction modeling in mechanized tunneling” is gratefully acknowledged.

First of all, I would like to express my deepest appreciation and gratitude to my supervisor and first referee Prof. Dr. rer. nat. Klaus Hackl. Thank you very much for providing me an opportunity to work in your team and trusting in my abilities. Your immense knowledge has enlightened me on the world of material modeling, your excellent continuous scientific support and guidance enabled me to complete this thesis. I have learned a lot from you, not only professionally but also characteristically.

My sincere thanks also go to my second referee, Prof. Dr.-Ing. habil. Daniel Balzani. Thank you for the productive discussions and the friendly interaction. I also wish to express my thanks to Prof. Dr.-Ing. habil. Stefanie Reese for accepting to be my third referee. At this point, I would also like to mention Jun.-Prof. Dr. Andreas Vogel. Thank you for your spontaneous commitment to become chairman of the examination board.

My further thanks also go to all of my colleagues at the *Institute of Mechanics of Materials* for the pleasant working conditions and the excellent social atmosphere. At this point, I should mention Mrs. Ghina Jezdan in particular. Thank you for your helpfulness and support! It was nice to share an office with you, and building a very good private friendship, which I would no longer want to miss! Many thanks also to Dr.-Ing. Ulrich Hoppe. Thank you very much for supporting us through your organization and ensuring a great working atmosphere and that we could always come to you with scientific questions. It has been a pleasure to work with you all!

I especially want to thank my friends and family for motivating and cheering me up even in difficult phases. I thank my parents and my whole family for the constant support in all areas of life and making it possible for me to walk this path. Even though you were far away from me, but I could always feel your deep love. Finally, the biggest thanks go to the most important person in my life, my wonderful husband, Mehrdad. You always believed in me and stand by my side to support me with full strength and never-ending optimism. Thank you for that and for everything else.

Summary

Mechanized tunneling is a construction method that gained high interest in the last decades, due to the high demands on infrastructure development in large cities. A decisive factor for the efficiency of the tunneling projects employing tunnel boring machines (TBMs) is to understand and predict the abrasive wear of the machine components during ground excavation. This constitutes the main topic of the present work.

In this thesis, a novel wear model for the prediction of the abrasive wear rate is developed. It is based on the idea of extending the results of single scratch tests to the total wear rate produced by a mixture of abrasive particles. The introduced wear model leads to closed form relations and avoids complicated and computationally expensive 3D wear simulations. This objective is reached in three steps: in the first step, the Discrete Element Method (DEM) is used to find a relation for the number of contacting particles with the tool specimen. For this purpose, a procedure for parameter identification of the DEM is developed based on an energy minimization approach. It allows to establish a relation between the microscopic contact parameters and macroscopic material parameters as employed in continuum mechanics.

In the second step, a single scratch simulation is performed using the Finite Element Method (FEM) to investigate the cross-sectional geometry of the resulting groove and the dominant wear mechanisms. For simulation of the single scratch test two coupled damage-plasticity material models are developed. Since the modeling of damage involves characteristic softening and localization effects and consequently leads to ill-posed boundary value problems, the material models have to be equipped with regularization strategies. The first model has a gradient-enhanced formulation for regularization of the damage distribution, while the second model uses a variational approach with rate limitation in combination with a so-called emulated representative volume element.

Finally, in the third step, a wear model is introduced to derive relations for the estimation of abrasive wear, which can be applied to homogeneous materials as well as a mixture of particles. Several test cases are performed to investigate the influence of the abrasive particle size and the indentation depth on the wear mechanism. To clarify the computational procedure of the model, two specific examples are discussed in detail.

Contents

Nomenclature	xiii
1 Introduction	1
1.1 Motivation and Objectives	1
1.2 Outline	2
2 Fundamentals	5
2.1 Notation and Conventions	5
2.1.1 Tensor Products	5
2.1.2 Tensor Analysis	6
2.1.3 Voigt Notation	7
2.2 Continuum Mechanics	7
2.2.1 Motion and Configuration	8
2.2.2 Deformation Measures	9
2.2.3 Strain Measures and Linearization	9
2.2.4 Stress Tensor	11
2.3 Lagrange Multiplier Method	12
2.4 Balance Laws	13
2.4.1 Balance of Mass	13
2.4.2 Balance of Linear and Angular Momentum	14
2.4.3 Balance of Energy - First Law of Thermodynamics	14
2.4.4 Entropy Inequality - Second Law of Thermodynamics	15
2.5 Constitutive Equations	16
2.6 Hamilton's Principle and Evolution Equation	18
2.6.1 General Application of Hamilton's Principle	20
2.6.2 Principle of the Minimum of the Dissipation Potential	21
3 Tribology	25
3.1 Mechanized Tunneling	26
3.1.1 Tool Concepts	26
3.2 Wear Mechanisms	28
3.2.1 Abrasion	29
3.2.2 Adhesion	29
3.2.3 Surface Degradation	30
3.2.4 Tribochemical Reaction	30
3.3 Abrasive Wear	30
3.3.1 Nano Scratch Test	31
3.3.2 Dry Sand-Rubber Wheel Test - ASTM G65	31
4 Numerical Methods	33
4.1 Discrete Element Method (DEM)	33
4.1.1 Calculation Cycle	33
4.1.2 Contact Components	35

4.1.3	Contact Models	38
4.2	Finite Element Method (FEM)	39
4.2.1	Variational Formulation	39
4.2.2	Residual and Tangent Matrix	43
4.2.3	Stresses and Material Tangent	44
5	DEM Parameter Identification	47
5.1	Introduction	47
5.1.1	Using Experiments to Calibrate Material	48
5.1.2	Theoretical Approaches	48
5.2	Energy Minimization Approach	49
5.2.1	Microscopic Potential	49
5.2.2	Macroscopic Potential	50
5.2.3	Derive Elastic Constants from Macroscopic Energy	51
5.3	Compression Test	53
5.3.1	Setup of Three-dimensional Test	53
5.3.2	Calibration Procedure	55
5.4	Results	58
5.4.1	Validation of Analytical Relations	59
5.4.2	Influence of Complex Particle Shape	62
5.4.3	Summary of Results	64
6	Material Models and Regularization Schemes	67
6.1	Inelastic Material Response	67
6.1.1	Plastic Material Model	67
6.1.2	Damage Material Model	69
6.2	Localization	72
6.3	Regularization Strategies	74
6.3.1	Viscous Regularization	74
6.3.2	Integral-based Regularization	75
6.3.3	Gradient-enhanced Regularization	76
6.4	Coupled Regularized Damage-Plasticity Model	77
6.4.1	Model I: Gradient-enhanced Regularized Damage-Plasticity with Laplacian	77
6.4.2	Model II: Relaxation-based Regularized Damage-Plasticity with Em- ulated RVE	86
7	Model Comparison with Finite Element Results	93
7.1	Model I: Gradient-enhanced Damage-Plastic Material	93
7.1.1	Plate with a Circular Hole	93
7.1.2	Double-notched Specimen	98
7.2	Model II: Relaxation-based Regularized Damage-Plastic Material	103
7.2.1	Sharp Notch Specimen	103
7.2.2	Double-notched Specimen	107
7.3	Comparative Discussion	110
8	Soil-Tool Interaction	113
8.1	Theoretical Background	113
8.1.1	Kinematics of the Contact Surfaces	114
8.1.2	Treatment of Contact Constraints	115

8.2	Single Scratch Test	116
8.2.1	Numerical Procedure	116
8.2.2	Study of Important Parameters	122
8.3	Abrasive Particle Simulation	125
8.3.1	Homogeneous Material Simulation	125
8.3.2	Mixture of Particles	127
8.4	Estimation of Abrasive Wear Rate	128
9	Conclusions and Outlook	133
9.1	Conclusions	133
9.2	Outlook	134
	References	135
	Curriculum Vitae	143

Nomenclature

Latin notations

a	General tensor of zeroth order
\mathbf{a}	General tensor of first order
A	Area
A_g	Area of the groove
A_s	Area of the shoulders
\mathbf{A}	General tensor of second order
\mathbf{b}	Volume forces
\mathbf{B}	Left Cauchy tensor
$\tilde{\mathbf{B}}$	Strain operator matrix
c	Coordinate number in Section 5.2
\mathbf{C}	Right Cauchy tensor
d	Damage variable
d	Indentation depth in Chapter 8
D	Particle diameter
D_p	Degree of penetration
\mathbf{D}	Coefficient matrix of spatial increments
e	Counter for elements
e_1, e_2, e_3	Cartesian basis
e_i, e_j, e_k, e_l	General Cartesian basis
E	Young's modulus
f	General function in Chapter 2
f	Damage function
$f^{,c}$	Bond strengths in Section 5.3
f_N	Normal contact force
f_{ab}	Degree of wear
F	Force
\mathbf{F}	Deformation gradient
g	Counter for Gauß points
g_N	Normal contact gap
g_T	Tangential contact gap
h	Heat source
\mathbf{H}	Displacement gradient
J	Jacobian
\mathbf{J}	Jacobian matrix
K_H	Rate of hardening
K^n	DEM normal contact stiffness
K^t	DEM tangential contact stiffness
\mathbf{L}	Angular (rotational) momentum

m	Sampling points
n	Counter for nodes
n	Subdomains of Model II
\mathbf{n}	Normal vector
N_e	Number of elements
N_{GP}	Number of Gauß points
N_c	Number of contacting particles
N_n	Number of nodes
\mathbf{N}	Shape function
p	Driving force
\hat{p}	Dissipative force
\mathbf{q}	Heat flux
r_1	Dissipation parameter
r_2	Viscosity parameter
r_{AB}	Ratio of particle diameter
r_d	Damage dissipation parameter
r_p	Plastic yield limit
R	Particle radius
\mathbf{R}	Rotation tensor
\mathbf{R}_u	Residual of displacement field
s	Specific entropy
t	Time
\mathbf{t}	Traction forces
\mathbf{u}	Displacement
\mathbf{U}	Right stretch tensor
V	Volume
v	Velocity
\dot{v}	Wear rate
v_t	Tangential velocity
\mathbf{V}	Left stretch tensor
w	Weight factor in Section 4.2
w	Width of the scratch in Chapter 8
$w(\alpha_p)$	Plastic potential
\mathbf{x}	Space coordinate in the current configuration
\mathbf{X}	Space coordinate in the reference configuration

Greek notations & symbols

α	Regularization parameter
α_p	Plastic hardening variable
β	Regularization parameter
β_i	DEM damping
$\Delta\rho$	Consistency parameter
ε	Strain
$\boldsymbol{\varepsilon}$	Strain tensor
η	Porosity

θ	Temperature
θ	Volume ratio in Chapter 8
λ	Internal variable
Λ	Vector of Laplace operator
μ	Friction coefficient
ν	Poisson's ratio
ξ	Natural coordinates
Π_{ext}	External potential
Π_{int}	Internal potential
ρ	Density
σ_y	Failure stress
σ	Stress tensor
ϕ	Friction angle
φ	Non-local field function
Φ	Yield function
Ψ	Helmholtz free energy
ω	Rotation vector
Ω	Volume of body
Ω_e	Volume of element
Ω_i	Volume of central or neighbor element of Model I
Ω_{rep}	Volume of representative volume element
$\partial\Omega$	Surface of body
\mathbb{A}	General tensor of fourth order
\mathbb{E}	Stiffness tensor
\mathcal{A}	Integration constant
\mathcal{D}	Dissipation function
\mathcal{E}	Internal energy
\mathcal{G}	Gibbs energy
\mathcal{H}	Absolute entropy product
\mathcal{K}	Kinetic energy
\mathcal{L}	Lagrangian
\mathcal{Q}	Thermal power
\mathcal{S}	Entropy production
\mathcal{V}	Dissipative forces
\mathcal{W}	Mechanical power

Abbreviations

cond	Condensed
ERVE	Emulated representative volume element
GP	Gauß point
LAP	Laplace

PMDP	Principle of minimum of dissipation potential
RD	Rate-dependent
REL	Relaxation/relaxed
RI	Rate-independent
RVE	Representative volume element

Mathematical operators

$\arg \min(\cdot)$	Argument of the minimum
$\operatorname{div}(\cdot)$	Divergence
$\det(\cdot)$	Determinant
$\operatorname{grad}(\cdot)$	Gradient
$\inf(\cdot)$	Infimum
$\lim(\cdot)$	Limit of a function
$\min(\cdot)$	Minimum
$\operatorname{sgn}(\cdot)$	Signum function
$\sup(\cdot)$	Supremum
$\operatorname{sym}(\cdot)$	Symmetric part of a matrix
$\operatorname{tr}(\cdot)$	Trace
$\delta(\cdot)$	Variation
$\partial(\cdot)$	Partial derivative
$\Delta(\cdot)$	Increment
$\nabla(\cdot)$	Nabla operator
$d(\cdot)/dt = (\dot{\cdot})$	Time derivative / rate
$d(\cdot)/dx$	Total derivative with respect to x
$\partial(\cdot)/\partial x$	Partial derivative with respect to x
$(\bar{\cdot})$	Reference to the bonded material in Section 5.3
$(\bar{\cdot})$	Effective value in Subsection 6.4.2
$(\tilde{\cdot})$	Voigt notation
$(\hat{\cdot})$	Reference to physical nodal coordinate
$(\cdot)^*$	Legendre-Fenchel transformation
$[\cdot]_+$	Permits only positive values
$(\cdot)^I$	Reference to natural nodal coordinate
$(\cdot)^k$	Reference to last iteration step
$(\cdot)^{k+1}$	Reference to the current iteration step
$(\cdot)^m$	Reference to last time-step
$(\cdot)^{m+1}$	Reference to the current time-step
$(\cdot)'$	First derivative
$(\cdot)''$	Second derivative
$(\cdot)^{-1}$	Inverted
$(\cdot)^T$	Transposed

1 Introduction

1.1 Motivation and Objectives

The rapid world's population growth and quick global urbanization cause an increasing tension on the transportation system of people and goods, and consequently very high demand on infrastructure. Transportation is being addressed as a crucial aspect in economic productivity, accessibility, and the ease of lifestyles in emerging and developing megacities. Since the earth's surface is already being intensively used, the underground space offers an extra dimension to work with and guarantees a sustainable solution for traffic congestion and population growth worldwide. Therefore, tunnel construction has gained more and more attention, with both methods of conventional tunneling and mechanized tunneling.

Mechanized tunneling using tunnel boring machines (TBMs) is a construction process, characterized as an effective and safe method in a wide variety of geological conditions such as subsoil with low bearing capacity and high groundwater level. It offers several advantages, especially in inner-city areas, such as non-affected life above the ground during the construction phase, high quality of the segment elements, and accuracy of the finished tunnel profile. In addition to high investment costs, these advantages are offset by a lack of flexibility due to difficult adaptation to unexpected geological conditions, very intensive planning phase, and long installation stage.

The correct choice of tunnel boring machine and monitoring the parameters influencing the lifetime of cutting tools are important factors that can be considered in the planning phase to avoid unexpected stoppage and consequently to increase the efficiency of the projects. Realistic computer simulations in the planning and research phase can help to understand different processes better and ultimately optimize the profitability of excavations. For example, it can be precisely predicted when tools must be replaced due to wear before failure. Otherwise, significantly longer service time for replacement of completely worn tools leads to very high costs and has a negative effect on logistics. Hence, in the last decades, remarkable attention is paid to the wear, or more precisely abrasive wear, to the excavation tools.

Abrasive wear occurs when the roughness of abrasive particles, penetrates a softer surface under high contact force and slides over it. This behavior is characterized either in the form of plastic deformation or material removal. Many methods have been used to describe the abrasivity of sand and rock, ranging from laboratory tests such as the dry sand-rubber wheel test (ASTM-G65) to numerical simulations. Different numerical methods, such as Finite Element Method (FEM), Smoothed Particle Hydrodynamics (SPH), and Discrete Element Method (DEM), can be used for modeling the contact between abrasive particles and construction tool.

The problem with the application of DEM is that a generally accepted method for the

determination of required material parameters does not exist. Finding a solution for this problem is one goal of this work. A connection should be established between the commonly used material parameters and those required for simulations with DEM. Moreover, the numerical simulation of the contact problems requires a fine resolution of the involved constituents (specimen and abrasive particles). Consequently, a coupled damage-plasticity material model is demanded that allows for time-efficient simulations, which is another goal of this work.

The objective of this work is the development of a novel wear model for the estimation of abrasive wear rate. The idea is to use two numerical methods, i.e., Discrete Element Method (DEM) and Finite Element Method (FEM), to develop closed form relations, and to avoid complicated time-consuming 3D wear simulations. This objective has reached in three steps: The first step is to employ the DEM for finding the number of particles in contact with the construction tool specimen. In the second step, a single scratch test has simulated in Abaqus, using a coupled damage-plasticity material model to investigate the cross-sectional geometry of the resulted groove, the degree of wear, and the dominant wear mechanisms. Finally, in the last step, a wear model has introduced to derive relations for estimation of abrasive wear. The developed model extends the results of the scratch caused by a single abrasive particle into the total abrasive wear rate. This extension has done using relations governed by the DEM particle simulations. A schematic overview of this objective has shown in Figure 1.1.

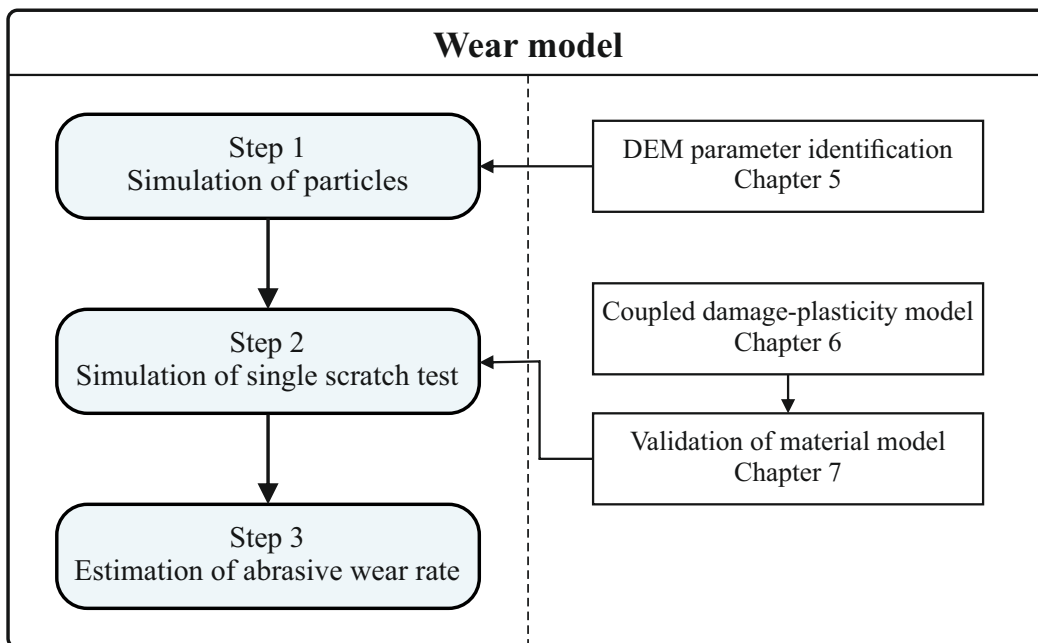


Figure 1.1: Schematic overview of the objective of this thesis

1.2 Outline

This thesis is organized as follows: after this introductory, the mathematical and mechanical fundamentals are presented in Chapter 2. In addition to the presentation of the notations and conventions, relevant areas of continuum mechanics are explained. Furthermore, the thermomechanical balance laws are presented, which establish the basis for constitutive

equations. Finally, Hamilton's principle, as well as the principle of the minimum of the dissipation potential are explained for the derivation of evolution equations.

Chapter 3 is dedicated to the tribological system. The excavation tools, installed on the shield of TBMs regarding the ground to be excavated, are presented. An overview of the different wear mechanisms, that happen to the tools, is given. Furthermore, a detailed insight into abrasive wear, known as the dominant wear mode in mechanized tunneling applications is included.

Chapter 4 demonstrates the fundamental of the two numerical methods utilized in this study, namely: Discrete Element Method (DEM) and Finite Element Method (FEM). It follows by Chapter 5, which contains the preliminary step in DEM simulations, known as parameter identification. An analytical approach based on the minimization of energies at the contact points is introduced and then extended to the entire material. It leads to establish a relation between the microscopic contact parameters and the macroscopic material parameters as employed in continuum mechanics. This parameter identification is verified with a compression test performed by DEM for both bonded and granular materials.

The two newly developed regularized coupled damage-plasticity models are presented in Chapter 6. First, the description of the constitutive equations for plastic material as well as damage behavior together with the issue of localization are discussed. Additionally, the three kinds of regularization techniques are explained briefly in the same chapter. Finally, material models are introduced. The first material model evaluates an efficient Laplace operator for gradient enhancement of damage function and applies suitable operator splits. The second material model uses an emulated representative volume element (ERVE) and states a rate-limitation viscous regularization of damage function. The regularization is performed only on the damage parameter, while in this work, the plastic regime is limited to hardening behavior and is coupled in its local form. Some representative numerical examples for three boundary value problems including a plate with a circular hole, a double-notch specimen, and a sharp-notch specimen are presented in Chapter 7. The specific aspects of the developed material models as well as the influence of regularization on the material behavior are investigated. That follows by a comparative discussion.

The outline of Chapter 8 has depicted in the objective of this thesis. The investigation of soil-tool interaction starts with the theoretical background of contact mechanics and algorithms. The relation between particle size and the number of contacting particles is obtained using DEM simulations. Besides, the scratching movement of a single abrasive particle with a range of predefined radii through a softer surface is simulated. The influence of different parameters on the wear mechanisms and groove shape is investigated. The wear model is introduced to derive a relation for estimation of total abrasive wear rate. Moreover, to clarify the calculation procedure of the model, two specific examples are discussed in detail. Finally, Chapter 9 summarizes results as well as an outlook on further model extensions and investigations.

2 Fundamentals

The aim of this chapter is presenting a rough description of mechanical fundamentals, which is necessary for better understanding of this thesis. First, in Section 2.1, the mathematical notation and conventions are discussed briefly. Section 2.2 reviews some core concepts of continuum mechanics, and Section 2.3 introduces the Lagrange multiplier method for solving the optimization problems. Afterwards, the balance laws of thermodynamics for continuous media are provided in Section 2.4. Based on that, the constitutive equations are applied in Section 2.5. Finally, Hamilton's principle and evolution equations are derived in Section 2.6 to state the behavior of a physical system in a way that is equivalent to the presented balance laws.

2.1 Notation and Conventions

The provided notation and mathematical principles are defined in an exemplary right-handed rectangular Cartesian coordinate system with basis $e_i; i = 1, 2, 3$ and expressed using indicial notation. Thus, a tensor of zeroth order corresponds to a scalar denoted as a, b, c, \dots , whereas the tensor of first order corresponds to a vector denoted as $\mathbf{a}, \mathbf{b}, \mathbf{c}, \dots$, additionally the tensor of second order corresponds to a matrix denoted as $\mathbf{A}, \mathbf{B}, \mathbf{C}, \dots$ with

$$\mathbf{a} = a_i = \begin{pmatrix} a_1 \\ a_2 \\ a_3 \end{pmatrix} \quad \mathbf{A} = A_{ij} = \begin{pmatrix} A_{11} & A_{12} & A_{13} \\ A_{21} & A_{22} & A_{23} \\ A_{31} & A_{32} & A_{33} \end{pmatrix} \quad (2.1)$$

and there are also tensors of higher order, for example fourth order is denoted as $\mathbb{A}, \mathbb{B}, \mathbb{C}, \dots$.

The Einstein summation convention is employed; thus, the repetition of an index in a term denotes a summation with respect to that index over its range. For example, the traction vector t_i , acting in the direction n_i , is given by $t_i = \sigma_{ij}n_j = \sigma_{i1}n_1 + \sigma_{i2}n_2 + \sigma_{i3}n_3$. A dot over a variable indicates a derivative with respect to time (e.g., $\dot{x}_i = \partial x_i / \partial t$). Vertical braces denote the magnitude of a vector or the absolute value of a scalar.

2.1.1 Tensor Products

The dot product (also called scalar product) of two vectors \mathbf{a} and \mathbf{b} is defined as

$$\mathbf{a} \cdot \mathbf{b} = a_i b_j \delta_{ij} = c \quad (2.2)$$

where c is a scalar quantity. Here, δ_{ij} refers to Kronecker delta,

$$\delta_{ij} = \begin{cases} 1 & \text{if } i = j; \\ 0 & \text{otherwise} \end{cases} \quad (2.3)$$

The cross-product of two vectors \mathbf{a} and \mathbf{b} produces a vector \mathbf{c} that is perpendicular to both \mathbf{a} and \mathbf{b} and can be written using the permutation symbol as

$$\mathbf{a} \times \mathbf{b} = c_i = e_{ijk} a_j b_k \quad (2.4)$$

with

$$e_{ijk} = \begin{cases} 0 & \text{if 2 indices coincide;} \\ +1 & \text{if } i, j, k \text{ permute like } 1, 2, 3; \\ -1 & \text{otherwise} \end{cases} \quad (2.5)$$

The dot product of a tensor of second order \mathbf{A} and a vector \mathbf{b} is defined as

$$\mathbf{A} \cdot \mathbf{b} = A_{ij} b_j e_i = \mathbf{c} \quad (2.6)$$

and results in a vectorial quantity \mathbf{c} , and the dot product of two tensors of second order \mathbf{A} and \mathbf{B}

$$\mathbf{A} \cdot \mathbf{B} = A_{ij} B_{jl} e_i \otimes e_l = \mathbf{C} \quad (2.7)$$

provides a tensor of second order \mathbf{C} . Furthermore, from the double dot product of a tensor of fourth order \mathbb{A} and a tensor of second order \mathbf{B} we get a second order tensor \mathbf{C} , described by a double contraction

$$\mathbb{A} : \mathbf{B} = A_{ijkl} B_{kl} e_i \otimes e_j = \mathbf{C} \quad (2.8)$$

Finally, the dyadic product or tensor product of two vectors \mathbf{a} and \mathbf{b} is a second order tensor \mathbf{C} such that

$$\mathbf{a} \otimes \mathbf{b} = a_i b_j e_i \otimes e_j = \mathbf{C} \quad (2.9)$$

2.1.2 Tensor Analysis

The Nabla operator ∇ is formally understood as a vector, where its components are the partial derivative with respect to the basis e_i :

$$\nabla = \left(\frac{\partial}{\partial x_1}, \dots, \frac{\partial}{\partial x_n} \right) \quad (2.10)$$

Since the Nabla operator is not a vector but an operator, special calculation rules also apply here. Its dyadic product with a function f gives the gradient of f

$$\text{grad} f = \nabla f = \frac{\partial f}{\partial x_i} e_i \quad (2.11)$$

while its dot product with a vector \mathbf{a} results in the divergence of \mathbf{a}

$$\text{div} \mathbf{a} = \nabla \cdot \mathbf{a} = \frac{\partial a_i}{\partial x_i} \quad (2.12)$$

The determinant of a 3x3 matrix is calculated as:

$$\begin{aligned} \det \mathbf{A} &= \det \begin{pmatrix} A_{11} & A_{12} & A_{13} \\ A_{21} & A_{22} & A_{23} \\ A_{31} & A_{32} & A_{33} \end{pmatrix} \\ &= A_{11}A_{22}A_{33} + A_{21}A_{32}A_{13} + A_{31}A_{21}A_{32} - A_{13}A_{22}A_{31} - A_{23}A_{32}A_{11} - A_{33}A_{12}A_{21} \end{aligned}$$

(2.13)

And the trace of a 3x3 matrix is calculated as:

$$\begin{aligned} \text{tr} \mathbf{A} &= \text{tr} \begin{pmatrix} A_{11} & A_{12} & A_{13} \\ A_{21} & A_{22} & A_{23} \\ A_{31} & A_{32} & A_{33} \end{pmatrix} \\ &= A_{11} + A_{22} + A_{33} \end{aligned} \quad (2.14)$$

2.1.3 Voigt Notation

The constitutive law in linear elasticity for a homogeneous anisotropic body, the generalized Hooke law, postulates a linear relation between the two second-rank tensor fields, the stress $\boldsymbol{\sigma}$ and the strain $\boldsymbol{\varepsilon}$ as follows

$$\boldsymbol{\sigma} = \mathbb{E} : \boldsymbol{\varepsilon} \quad (2.15)$$

Hereby, the three-dimensional stiffness tensor \mathbb{E} , a tensor of fourth order, is of size $3 \times 3 \times 3 \times 3$ with consequently 81 entries whereas the stress tensor $\boldsymbol{\sigma}$ as well as the strain tensor $\boldsymbol{\varepsilon}$ are of size 3×3 with consequently 9 entries presented as follows

$$\boldsymbol{\sigma} = \begin{pmatrix} \sigma_{11} & \sigma_{12} & \sigma_{13} \\ \sigma_{21} & \sigma_{22} & \sigma_{23} \\ \sigma_{31} & \sigma_{32} & \sigma_{33} \end{pmatrix}, \quad \boldsymbol{\varepsilon} = \begin{pmatrix} \varepsilon_{11} & \varepsilon_{12} & \varepsilon_{13} \\ \varepsilon_{21} & \varepsilon_{22} & \varepsilon_{23} \\ \varepsilon_{31} & \varepsilon_{32} & \varepsilon_{33} \end{pmatrix} \quad (2.16)$$

For ease of calculation and implementation in computer codes that work with matrices, we will express the stress and strain tensors as 6×1 matrices, such that \mathbb{E} will be a 6×6 matrix. This is called Voigt notation and introduced by Voigt (1910). The Voigt notation is used to exploit the symmetry of condensed matter to transform second-order tensors (cf. e.g., stress tensor) to vectors and kinetic fourth-order tensors to square matrices (cf. e.g., elasticity tensor)

$$\begin{pmatrix} \sigma_{11} \\ \sigma_{22} \\ \sigma_{33} \\ \sigma_{23} \\ \sigma_{13} \\ \sigma_{12} \end{pmatrix} = \begin{pmatrix} \mathbb{E}_{1111} & \mathbb{E}_{1122} & \mathbb{E}_{1133} & \mathbb{E}_{1123} & \mathbb{E}_{1113} & \mathbb{E}_{1112} \\ \mathbb{E}_{2211} & \mathbb{E}_{2222} & \mathbb{E}_{2233} & \mathbb{E}_{2223} & \mathbb{E}_{2213} & \mathbb{E}_{2212} \\ \mathbb{E}_{3311} & \mathbb{E}_{3322} & \mathbb{E}_{3333} & \mathbb{E}_{3323} & \mathbb{E}_{3313} & \mathbb{E}_{3312} \\ \mathbb{E}_{2311} & \mathbb{E}_{2322} & \mathbb{E}_{2333} & \mathbb{E}_{2323} & \mathbb{E}_{2313} & \mathbb{E}_{2312} \\ \mathbb{E}_{1311} & \mathbb{E}_{1322} & \mathbb{E}_{1333} & \mathbb{E}_{1323} & \mathbb{E}_{1313} & \mathbb{E}_{1312} \\ \mathbb{E}_{1211} & \mathbb{E}_{1222} & \mathbb{E}_{1233} & \mathbb{E}_{1223} & \mathbb{E}_{1213} & \mathbb{E}_{1212} \end{pmatrix} \cdot \begin{pmatrix} \varepsilon_{11} \\ \varepsilon_{22} \\ \varepsilon_{33} \\ 2\varepsilon_{23} \\ 2\varepsilon_{13} \\ 2\varepsilon_{12} \end{pmatrix} \quad (2.17)$$

2.2 Continuum Mechanics

Continuum mechanics is a branch of mechanics which deals with physical phenomena of materials considered as continuous masses, characterized by position and displacement vectors. Kinematics relations include the geometry of a body, its motion in space as well as its deformation during motion. This section gives a general outline over the core concepts of continuum mechanics such as kinematics, stress measures and mechanical equilibrium which are basis for finite element method. For comprehensive treatment of this topic, the reader is referred to the classical literature, e.g., Ogden and Sternberg (1985), Bonet and Wood (1997), Holzapfel (2000), Simo and Hughes (2006), de Souza Neto et al. (2011), and Belytschko et al. (2013).

2.2.1 Motion and Configuration

A continuum body \mathcal{B} is defined as a set of material points or particles in the three-dimensional Euclidean space at some instant of time t . When the body is in motion, it occupies a continuous sequence of geometrical regions, Ω_0, \dots, Ω called configurations of \mathcal{B} . The configuration Ω associated to the current time t , is called current (or deformed) configuration. The typical material point of the body in the current configuration is described using spatial (Eulerian) coordinate vector \mathbf{x} . For convenience, an initial configuration Ω_0 can be introduced to provide a reference at time $t = 0$ which is referred to as reference (initial, undeformed) configuration and the position of the material point is uniquely described by the reference (Lagrangian) coordinate vector \mathbf{X} . Figure 2.1 illustrates the body \mathcal{B} in the reference and current configuration.

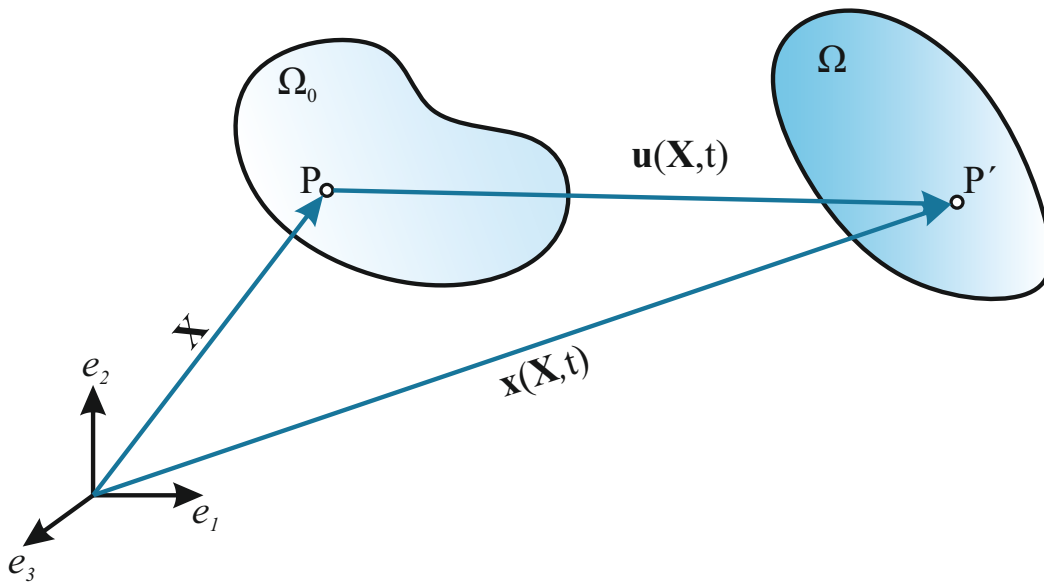


Figure 2.1: Configurations and motion of the body \mathcal{B}

In the following, a clear distinction in writing operators in different configurations is outlined: differential operators containing derivatives with respect to the material coordinates \mathbf{X} are indicated as "Div" and "Grad", whereas the "div" and "grad" which are used to denote the operators with derivatives with respect to the spatial coordinates \mathbf{x} .

The relation between the position vectors of the body \mathcal{B} in the current and the reference configuration results in a vector field called displacement field

$$\mathbf{u}(\mathbf{X}, t) = \mathbf{x}(\mathbf{X}, t) - \mathbf{X} \quad (2.18)$$

The velocity of a material point results from the time derivative of the displacement field and represents the rate of change of its position vector, i.e.,

$$\mathbf{v} = \frac{d\mathbf{x}}{dt} = \frac{\partial \mathbf{x}(\mathbf{X}, t)}{\partial t} \quad (2.19)$$

The acceleration of a material point results from a further time derivative of the displacement field and represents the rate of change of velocity of a material point, i.e.,

$$\mathbf{a} = \frac{d^2\mathbf{x}}{dt^2} = \frac{d\mathbf{v}}{dt} = \frac{\partial \mathbf{v}(\mathbf{X}, t)}{\partial t} \quad (2.20)$$

2.2.2 Deformation Measures

In order to describe the deformation process, the deformation gradient tensor \mathbf{F} which maps an infinitesimal differential line element of the reference configuration $d\mathbf{X}$ to the corresponding one in the current configuration $d\mathbf{x}$ is introduced.

$$d\mathbf{x} = \mathbf{F} \cdot d\mathbf{X} \quad (2.21)$$

where

$$\mathbf{F} = \frac{\partial \mathbf{x}}{\partial \mathbf{X}} = \frac{\partial(\mathbf{u} + \mathbf{X})}{\partial \mathbf{X}} = \mathbf{H} + \mathbf{1} \quad (2.22)$$

with the displacement gradient

$$\mathbf{H} := \frac{\partial \mathbf{u}}{\partial \mathbf{X}} = \text{Grad } \mathbf{u}. \quad (2.23)$$

In general, \mathbf{F} is an unsymmetric second order tensor. Analogously to the transformation relation in Equation (2.21), the deformation of infinitesimal surface elements and volume elements can be also described, which are necessary to define the balance laws and stress measures later. The connection between the volume elements in the reference and current configuration is obtained as

$$dv = \det \mathbf{F} dV = J dV. \quad (2.24)$$

where $J = \det \mathbf{F}$ is named after Jacobian. The deformation gradient \mathbf{F} is invertible. Namely, its determinant has to be strictly positive ($\det \mathbf{F} > 0$) in order to assure the impenetrability of matter (to prevent negative volumes). With the definition of the deformation gradient above, and employing Equation (2.21), the transformation of the surface elements can be written as

$$d\mathbf{a} = J \mathbf{F}^{-T} \cdot d\mathbf{A} \quad (2.25)$$

which shows the relation between deformed- and undeformed surface elements and is known in the literature as Nanson's formula.

The deformation gradient can be uniquely decomposed multiplicatively into an arbitrary proper orthogonal rotation tensor \mathbf{R} and a symmetric positive definite right stretch tensor \mathbf{U} or left stretch tensor \mathbf{V} , so that

$$\mathbf{F} = \mathbf{R} \cdot \mathbf{U} = \mathbf{V} \cdot \mathbf{R} \quad (2.26)$$

The rotation tensor \mathbf{R} is proper orthogonal tensor and therefore, $\mathbf{R} \cdot \mathbf{R}^T = \mathbf{R}^T \cdot \mathbf{R} = \mathbf{I}$ and $\det \mathbf{R} = 1$, where the stretch tensor are symmetric, thus $\mathbf{U} = \mathbf{U}^T$ and $\mathbf{V} = \mathbf{V}^T$.

2.2.3 Strain Measures and Linearization

Strain tensors are defined with respect to the reference configuration or the current configuration. The so-called deformation tensors which describe deformations without being influenced by a pure rotation are introduced as

$$\mathbf{C} := \mathbf{F}^T \cdot \mathbf{F} \quad \text{and} \quad \mathbf{B} := \mathbf{F} \cdot \mathbf{F}^T \quad (2.27)$$

where \mathbf{C} and \mathbf{B} are called the right Cauchy-Green deformation tensor and the left Cauchy-Green deformation tensor, respectively. The first one (\mathbf{C}) is a tensor which refers to the reference configuration, while the second one (\mathbf{B}) belongs to the current configuration. By expressing the deformation gradient in Equation (2.27) with stretch tensors and rotation tensor from Equation (2.26) and utilizing the orthogonality condition of the rotation tensor $\mathbf{R}^T = \mathbf{R}^{-1}$, the Cauchy-Green deformation tensors can be expressed as

$$\begin{aligned}\mathbf{C} &:= \mathbf{F}^T \cdot \mathbf{F} = (\mathbf{R} \cdot \mathbf{U})^T \cdot \mathbf{R} \cdot \mathbf{U} = \mathbf{R}^T \cdot \mathbf{U}^T \cdot \mathbf{R} \cdot \mathbf{U} = \mathbf{F}^T \cdot \mathbf{U} = \mathbf{U}^2 \\ \mathbf{B} &:= \mathbf{F} \cdot \mathbf{F}^T = \mathbf{V} \cdot \mathbf{R} \cdot (\mathbf{V} \cdot \mathbf{R})^T = \mathbf{V} \cdot \mathbf{R} \cdot \mathbf{R}^T \cdot \mathbf{V}^T = \mathbf{V}^T \cdot \mathbf{V} = \mathbf{V}^2\end{aligned}\quad (2.28)$$

In Equation (2.28), the influence of the rigid body rotation on the deformation is efficiently removed. Therefore, the tensors \mathbf{C} and \mathbf{B} represent pure stretching and are positive definite. In addition to the defined quantities, strain measures are necessary to express the deformation at a certain point and later on be able to define constitutive equations. The definition of strain is - unlike the definition of deformation - based on a strain concept. Therefore, different strain measures are mentioned in the literature. A common strain measure is the Green-Lagrange strain tensor

$$\mathbf{E} = \frac{1}{2} (\mathbf{F}^T \cdot \mathbf{F} - \mathbf{I}) = \frac{1}{2} (\text{Grad}^T \mathbf{u} + \text{Grad} \mathbf{u}) + \frac{1}{2} \text{Grad}^T \mathbf{u} \cdot \text{Grad} \mathbf{u} \quad (2.29)$$

in which \mathbf{I} is the second order identity tensor, which operates on line elements in the reference configuration to quantify the actual change in squared length of these line elements, i.e.,

$$dx \cdot dx - d\mathbf{X} \cdot d\mathbf{X} = d\mathbf{X} \cdot 2\mathbf{E} \cdot d\mathbf{X}. \quad (2.30)$$

The equivalent of Green-Lagrange strain tensor in the current configuration is the Euler-Almansi strain tensor

$$\mathbf{e} = \frac{1}{2} (\mathbf{1} - \mathbf{F}^{-T} \cdot \mathbf{F}^{-1}) = \frac{1}{2} (\text{grad}^T \mathbf{u} + \text{grad} \mathbf{u}) + \frac{1}{2} \text{grad}^T \mathbf{u} \cdot \text{grad} \mathbf{u} \quad (2.31)$$

where the displacement gradient in Equation (2.23) is defined with respect to the current configuration

$$\text{grad} \mathbf{u} = \frac{\partial \mathbf{u}}{\partial x}. \quad (2.32)$$

and similarly that expresses the change of squared lengths of these line elements in the current configuration, i.e.,

$$dx \cdot dx - d\mathbf{X} \cdot d\mathbf{X} = dx \cdot 2\mathbf{e} \cdot dx. \quad (2.33)$$

In this thesis, we assume that the displacement remains small in order to ensure satisfactory approximation of the original quantities by the linearized ones. This assumption leads further to the conclusion that $\mathbf{x} \approx \mathbf{X}$. Hence, the initial configuration Ω_0 of the body \mathcal{B} can be considered coincident with the current configuration Ω . In this case we speak of the geometrically linear theory, or the *theory of small strains*.

The above assumption implies that the quadratic terms in definition of Green-Lagrange tensor and Euler-Almansi tensor in Equations (2.29) and (2.31), are small and can be neglected. Thus, we can define the linearized strain tensor

$$\boldsymbol{\varepsilon} = \frac{1}{2} (\text{grad}^T \mathbf{u} + \text{grad} \mathbf{u}). \quad (2.34)$$

From this point on the theory of small strains is applied. The trace of linearized strain tensor is equal to the volume change of an infinitesimal volume element

$$\text{tr}(\boldsymbol{\varepsilon}) = \varepsilon_{kk} = \lim_{dV \rightarrow 0} \frac{dv - dV}{dV}, \quad (2.35)$$

which is also called volume dilatation. For modeling elsto-plasticity in materials, since plastic deformations are considered to be volume conservative, a decomposition of the strain tensor into spherical and deviatoric part is necessary. With the definition of volumetric or spherical strain

$$\varepsilon_{\text{vol}} = \frac{1}{3} \text{tr}(\boldsymbol{\varepsilon}), \quad (2.36)$$

and the deviatoric strain ε_{dev} , the linearized strain tensor can be decomposed as

$$\boldsymbol{\varepsilon} = \frac{1}{3} \text{tr}(\boldsymbol{\varepsilon}) \mathbf{I} + \boldsymbol{\varepsilon}_{\text{dev}}. \quad (2.37)$$

2.2.4 Stress Tensor

To elaborate the concept of stress, we consider a body \mathcal{B} in the current configuration Ω subjected to volume loads \mathbf{b} and traction loads \mathbf{t} on the part $\partial\Omega$ of the boundary as in Figure 2.2.

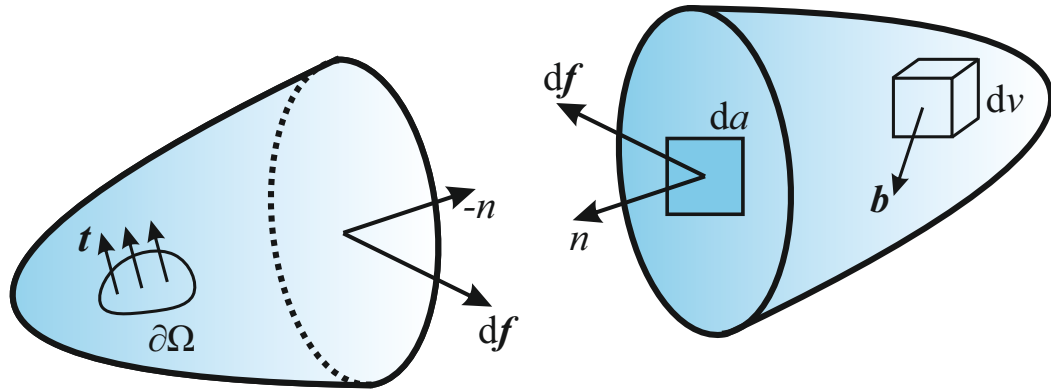


Figure 2.2: Arbitrary control volume and the traction vector

Assume the body is separated into two parts by a surface passing through an arbitrary typical point P with the unit normal vector \mathbf{n} at the interface. Taking an infinitesimally small surface element of size da , the resulting internal force on the element is denoted as df , i.e., the force that is transferred to the other part of the body. The so-called stress vector \mathbf{t}_n can then be defined as

$$\mathbf{t} = \lim_{da \rightarrow 0} \frac{df}{da} \quad (2.38)$$

The stress vector can also be decomposed into a component collinear to the surface normal, called normal stress and denoted $\boldsymbol{\sigma}$, and an orthogonal component, called shear stress and denoted $\boldsymbol{\tau}$. In order to describe the state of stress in a body, three orthogonal cuts with linearly independent associated normal vectors are processed. The resulting stress components at an infinitesimally small volume element are shown in Figure 2.3.

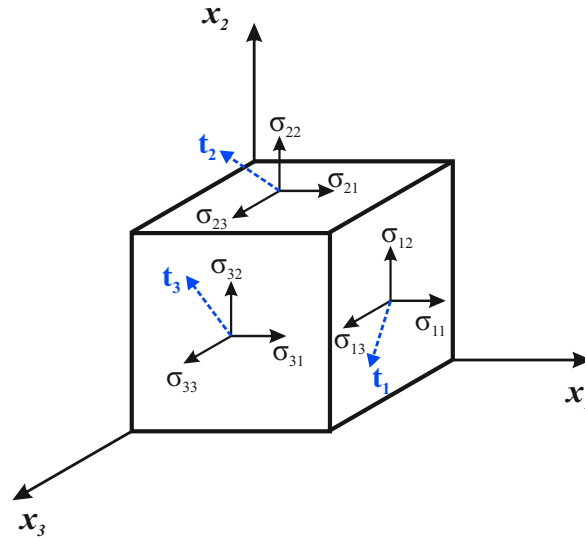


Figure 2.3: Stress components at an infinitesimally small volume element

The stress tensor can be defined by means of Cauchy's theorem

$$\mathbf{t} = \boldsymbol{\sigma} \cdot \mathbf{n} \quad (2.39)$$

which allows to express the stress tensor as

$$\boldsymbol{\sigma} = (\mathbf{t}_1 \quad \mathbf{t}_2 \quad \mathbf{t}_3)^T = \begin{pmatrix} \sigma_{11} & \sigma_{12} & \sigma_{13} \\ \sigma_{21} & \sigma_{22} & \sigma_{23} \\ \sigma_{31} & \sigma_{32} & \sigma_{33} \end{pmatrix} \quad (2.40)$$

Further, $\boldsymbol{\sigma}$ is symmetric;

$$\boldsymbol{\sigma} = \boldsymbol{\sigma}^T \quad (2.41)$$

which can be proved by balance of angular momentum for the infinitesimal volume element in Figure 2.3.

2.3 Lagrange Multiplier Method

In optimization problems the idea is to optimize (i.e., find the local maximum or minimum of a function) subjected to one or more constraints. In simple cases, the secondary condition can be inserted directly into the function to be optimized. Moreover, the Lagrange multiplier method offers a solution for more complex constraints. Let $f(x_1, x_2, \dots, x_n)$ be the function of optimization, which is subjected to k constraints from $g_1(x_1, x_2, \dots, x_n)$ to $g_k(x_1, x_2, \dots, x_n)$. According to the Lagrange method, first the constraints are rearranged so that they are equal to 0. Then they are each multiplied by a Lagrange multiplier λ_i and added to the function. This is how the so-called Lagrange function results:

$$\mathcal{L}(x_1, \dots, x_n, \lambda_1, \dots, \lambda_k) = f(x_1, \dots, x_n) + \lambda_1 g_1(x_1, \dots, x_n) + \dots + \lambda_k g_k(x_1, \dots, x_n) \quad (2.42)$$

Taking the partial derivative of this function with respect to all variables of x_1, \dots, x_n and $\lambda_1, \dots, \lambda_k$, and set the derivatives equal to zero:

$$\begin{aligned}
 \frac{\partial \mathcal{L}(x_1, \dots, x_n, \lambda_1, \dots, \lambda_k)}{\partial x_1} &:= 0 \\
 &\vdots \\
 \frac{\partial \mathcal{L}(x_1, \dots, x_n, \lambda_1, \dots, \lambda_k)}{\partial x_n} &:= 0 \\
 \frac{\partial \mathcal{L}(x_1, \dots, x_n, \lambda_1, \dots, \lambda_k)}{\partial \lambda_1} &:= 0 \\
 &\vdots \\
 \frac{\partial \mathcal{L}(x_1, \dots, x_n, \lambda_1, \dots, \lambda_k)}{\partial \lambda_k} &:= 0
 \end{aligned} \tag{2.43}$$

The solution of this system of equations results in stationary points of the initial problem. Moreover, the Lagrange method is also generalized by the Kuhn-Tucker conditions, which can also be considered for inequality constraints of the form $h(x_1, \dots, x_n) \leq c$.

2.4 Balance Laws

This section concerns the most important balance relations of continuum thermodynamics. The balance of mass, the balance of linear and angular momentum, the balance of energy, and the entropy inequality will be presented. The first and second laws of thermodynamics are the foundation for Hamilton's principle allowing for a thermodynamically consistent derivation of the presented material models. A detailed review on this subject can be found in Silhavy (1997), Holzapfel (2000), Truesdell and Noll (2004) and Gurtin et al. (2010).

2.4.1 Balance of Mass

In a closed system, the mass of a body is generally conserved during the motion. In other words, the total mass can be expressed as

$$m = \int_{\Omega} \rho \, dV \tag{2.44}$$

where ρ is the mass density related to the current configuration. Hence, the conservation of mass can be expressed in the local form as

$$\dot{\rho} + \rho \nabla \cdot \mathbf{v} = 0 \tag{2.45}$$

Within the framework of the small strain theory, which is assumed to accurately describe problems throughout this thesis, one can apply the condition $\dot{\rho} = 0$.

2.4.2 Balance of Linear and Angular Momentum

For a given body in a spatial domain Ω with boundary surface $\partial\Omega$ subjected to volume forces \mathbf{b} in the body and the surface traction vector \mathbf{t} acting upon the boundary surface, the balance of linear momentum states that the change of the linear momentum in time is balanced by the sum of these external forces and can be mathematically expressed by

$$\frac{d}{dt} \int_{\Omega} \rho \mathbf{v} dV = \int_{\Omega} \rho \mathbf{b} dV + \int_{\partial\Omega} \mathbf{t} dA \quad (2.46)$$

With Cauchy theorem, the surface traction vector \mathbf{t} is calculated from Cauchy stress tensor $\boldsymbol{\sigma}$ and the unit normal vector \mathbf{n} as

$$\mathbf{t} = \boldsymbol{\sigma} \cdot \mathbf{n} \quad (2.47)$$

Using the divergence theorem and integrating over the whole surface of the body, one obtains

$$\int_{\partial\Omega} \mathbf{t} dA = \int_{\partial\Omega} \boldsymbol{\sigma} \cdot \mathbf{n} dA = \int_{\Omega} \nabla \cdot \boldsymbol{\sigma} dV \quad (2.48)$$

Utilizing the conservation of mass (Equation (2.45)), the balance of linear (translational) momentum can be expressed in the local form as

$$\nabla \cdot \boldsymbol{\sigma} + \rho \mathbf{b} = 0 \quad (2.49)$$

The total angular (rotational) momentum of a body with reference to a point \mathbf{x}_0 is defined by

$$\mathbf{L} = \int_{\Omega} \mathbf{r} \times \rho \mathbf{v} dV, \quad \mathbf{r} = \mathbf{x} - \mathbf{x}_0 \quad (2.50)$$

The change of the total angular momentum \mathbf{L} is balanced by the sum of the moments exerted by the body force and the surface traction with reference to the same point

$$\frac{d}{dt} \int_{\Omega} \mathbf{r} \times \rho \mathbf{v} dV = \int_{\Omega} \mathbf{r} \times (\rho \mathbf{b}) dV + \int_{\partial\Omega} \mathbf{r} \times \mathbf{t} dA \quad (2.51)$$

By means of the balance of linear momentum (Equation (2.49)), the conservation of mass (Equation (2.45)), Cauchy's theorem (Equation (2.47)) and the divergence theorem, it follows the symmetry of Cauchy stress tensor

$$\boldsymbol{\sigma} = \boldsymbol{\sigma}^T \quad (2.52)$$

2.4.3 Balance of Energy - First Law of Thermodynamics

In the context of thermodynamics, the total energy of a closed system (no exchange of mass with the surroundings), is preserved during the process of motion. It means that, no energy can be naturally created or destroyed, but it can be transformed from one form to another one. This leads to the first law of thermodynamics that reads: the change of the total energy of a body, consist of the internal energy \mathcal{E} and the kinetic energy \mathcal{K} , is balanced by the

mechanical power of external forces \mathcal{W} and the heat supply (heat power) \mathcal{Q} . The global form is given by

$$\dot{\mathcal{E}} + \dot{\mathcal{K}} = \mathcal{W} + \mathcal{Q} \quad (2.53)$$

Hereby, the kinetic energy \mathcal{K} is given by

$$\mathcal{K} = \int_{\Omega} \frac{1}{2} \rho \mathbf{v} \cdot \mathbf{v} \, dV \quad (2.54)$$

and the internal energy \mathcal{E} is defined by

$$\mathcal{E} = \int_{\Omega} \Psi \, dV + \int_{\Omega} \theta s \, dV \quad (2.55)$$

including the Helmholtz free energy Ψ , the absolute temperature θ and the specific entropy s . Moreover, the mechanical power results from the volume and surface forces

$$\mathcal{W} = \int_{\Omega} \mathbf{b} \cdot \mathbf{v} \, dV + \int_{\Omega} \mathbf{t} \cdot \mathbf{v} \, dA \quad (2.56)$$

Finally, the thermal power \mathcal{Q} due to the internal heat source h and heat flux q_n is presented by

$$\mathcal{Q} = \int_{\Omega} h \, dV + \int_{\Omega} q_n \, dA \quad (2.57)$$

The heat flux q_n represents the rate at which heat enters the body (inward normal flux) across the boundary surface $\partial\Omega$ and can be transformed using the dot product between the Cauchy heat flux and the outward unit normal vector, known as the Stock's heat flux theorem, as

$$q_n = -\mathbf{q} \cdot \mathbf{n} \quad (2.58)$$

Substituting Equations (2.54), (2.55), (2.56) and (2.57) into Equation (2.53) and with the help of the Cauchy's theorem (Equation (2.47)) and the balance of linear momentum (Equation (2.49)), the balance of energy can be assembled as follows

$$\int_{\Omega} \left(\dot{\Psi} + (\dot{\theta}s) + \frac{d}{dt} \frac{1}{2} \rho \mathbf{v} \cdot \mathbf{v} \right) dV = \int_{\Omega} \left(\frac{d}{dt} \frac{1}{2} \rho \mathbf{v} \cdot \mathbf{v} + \boldsymbol{\sigma} : \dot{\boldsymbol{\varepsilon}} + h - \nabla \cdot \mathbf{q} \right) dV \quad (2.59)$$

After some manipulations and eliminating the identical integrals transfers the balance of energy into its local form and provides

$$\dot{\Psi} + \dot{\theta}s + \theta\dot{s} = \boldsymbol{\sigma} : \dot{\boldsymbol{\varepsilon}} - \nabla \cdot \mathbf{q} + h. \quad (2.60)$$

2.4.4 Entropy Inequality - Second Law of Thermodynamics

The balance of energy declares the energy transfer in a thermodynamics process, but does not account for the direction of the energy transfer. However, natural processes show certain asymmetry, so that the transfer always goes in one direction. This can be dealt by the second law of thermodynamics. The entropy of a body is denoted as the absolute entropy production \mathcal{H} and corresponds to

$$\mathcal{H} = \int_{\Omega} \left(\dot{s} + \nabla \cdot \frac{\mathbf{q}}{\theta} - \frac{h}{\theta} \right) dV, \quad (2.61)$$

to represent the total disorder of the system. The second law of thermodynamics states the non-negativity regarding closed systems and leads to the inequality relation

$$\mathcal{H} \geq 0. \quad (2.62)$$

which is known as the entropy inequality. The volume-weighted quantity of the absolute entropy production \mathcal{H} is the entropy production \mathcal{S} defined as

$$\mathcal{H} = \int_{\Omega} \mathcal{S} dV \quad (2.63)$$

The local form of the second law of thermodynamics, after some calculations and elimination of identical integrals, can be expressed by

$$\begin{aligned} \mathcal{S} &= \dot{s} + \nabla \cdot \frac{\mathbf{q}}{\theta} - \frac{h}{\theta} \\ &= \dot{s} + \frac{1}{\theta} \nabla \cdot \mathbf{q} - \frac{1}{\theta^2} \mathbf{q} \cdot \nabla \theta - \frac{h}{\theta} \end{aligned} \quad (2.64)$$

The non-negativity also applies for the entropy production \mathcal{S} , thus

$$\mathcal{S} \geq 0 \quad (2.65)$$

The local form of the first law of thermodynamic can be solved for internal heat source h as follows

$$h = \dot{\Psi} + \dot{\theta} s + \theta \dot{s} - \boldsymbol{\sigma} : \dot{\boldsymbol{\varepsilon}} + \nabla \cdot \mathbf{q} \quad (2.66)$$

Multiplying the local form of the second law of thermodynamics in Equation (2.64) with the absolute temperature θ provides the first subsequent equation. Taking into account h from Equation (2.66) leads to the second one

$$\begin{aligned} \theta \mathcal{S} &= \theta \dot{s} + \nabla \cdot \mathbf{q} - \frac{1}{\theta} \mathbf{q} \cdot \nabla \theta - h \\ &= \theta \dot{s} + \nabla \cdot \mathbf{q} - \frac{1}{\theta} \mathbf{q} \cdot \nabla \theta - \dot{\Psi} - \dot{\theta} s - \theta \dot{s} + \boldsymbol{\sigma} : \dot{\boldsymbol{\varepsilon}} - \nabla \cdot \mathbf{q} \end{aligned} \quad (2.67)$$

and after some simplification the second law of thermodynamics can be written as

$$\theta \mathcal{S} = -\dot{\Psi} - \frac{1}{\theta} \mathbf{q} \cdot \nabla \theta - \dot{\theta} s + \boldsymbol{\sigma} : \dot{\boldsymbol{\varepsilon}} \geq 0 \quad (2.68)$$

which contains the internal dissipation $\theta \mathcal{S}$ on the left-hand side and the Clausius-Duhem inequality on the right-hand side.

2.5 Constitutive Equations

The kinematics and the balance laws, presented in the previous section, are material-independent in its formulation and therefore universally valid for any continuum body. However, an initial and/or boundary value problem cannot be solved using these equations alone. Thus, to characterize the material response and close the system, additional relations called constitutive equations are needed. A large number of constitutive laws for different materials; i.e. pure elasticity, plasticity, visco-plasticity, damage and etc, have been developed so far.

For more details on this topic, readers are referred to Truesdell and Noll (2004), Chadwick (2012) and Haupt (2013).

The general formulation of the constitutive equations connects the so-called response functions which include the Helmholtz free-energy Ψ , stress tensor $\boldsymbol{\sigma}$, heat flux \mathbf{q} , and entropy s , to the set of process variables which include the strain tensor $\boldsymbol{\varepsilon}$, the temperature θ , the gradient of temperature $\nabla\theta$, and the internal variable λ , which are assumed to be scalar for most of the material models used in this thesis. Therefore, it follows

$$\begin{aligned}\Psi &= \Psi(\boldsymbol{\varepsilon}, \theta, \nabla\theta, \lambda) \\ \boldsymbol{\sigma} &= \boldsymbol{\sigma}(\boldsymbol{\varepsilon}, \theta, \nabla\theta, \lambda) \\ \mathbf{q} &= \mathbf{q}(\boldsymbol{\varepsilon}, \theta, \nabla\theta, \lambda) \\ s &= s(\boldsymbol{\varepsilon}, \theta, \nabla\theta, \lambda)\end{aligned}\tag{2.69}$$

Hence, the general Helmholtz free energy Ψ can be customized to describe a desired material behavior. Application of the material time rate to the Helmholtz free-energy gives

$$\dot{\Psi} = \frac{\partial\Psi}{\partial\boldsymbol{\varepsilon}} : \dot{\boldsymbol{\varepsilon}} + \frac{\partial\Psi}{\partial\theta} \dot{\theta} + \frac{\partial\Psi}{\partial(\nabla\theta)} \cdot (\nabla\dot{\theta}) + \frac{\partial\Psi}{\partial\lambda} \dot{\lambda}\tag{2.70}$$

Substituting $\dot{\Psi}$ into in Equation (2.68), and after some rearrangement the local form of the Clausius-Duhem inequality becomes

$$\left(\boldsymbol{\sigma} - \frac{\partial\Psi}{\partial\boldsymbol{\varepsilon}}\right) : \dot{\boldsymbol{\varepsilon}} - \left(s + \frac{\partial\Psi}{\partial\theta}\right)\dot{\theta} - \frac{\partial\Psi}{\partial(\nabla\theta)} \cdot (\nabla\dot{\theta}) - \frac{\partial\Psi}{\partial\lambda} \dot{\lambda} - \frac{1}{\theta} \mathbf{q} \cdot \nabla\theta \geq 0\tag{2.71}$$

Equation (2.71) has to be valid for all materials or processes. Let us now consider two special cases. The first case is a process of pure elastic deformation with constant temperature in time and space and without evolving any internal variables, which consequently results only in a change of strain tensor. Therefore, the stress tensor can be calculated in accordance with

$$\begin{aligned}\boldsymbol{\sigma} - \frac{\partial\Psi}{\partial\boldsymbol{\varepsilon}} &= 0 \\ \Leftrightarrow \boldsymbol{\sigma} &= \frac{\partial\Psi}{\partial\boldsymbol{\varepsilon}}\end{aligned}\tag{2.72}$$

The second one is pure heating or cooling under constant strain and again without internal variables, where only the temperature varies in time but remains constant in space. Hereby, the entropy s is delivered by

$$\begin{aligned}s + \frac{\partial\Psi}{\partial\theta} &= 0 \\ \Leftrightarrow s &= -\frac{\partial\Psi}{\partial\theta}\end{aligned}\tag{2.73}$$

According to Bargmann and Steinmann (2005), the Helmholtz free energy Ψ in the classical theory has to be independent of the temperature gradient, therefore

$$\begin{aligned}\frac{\partial\Psi}{\partial(\nabla\theta)} &= 0 \\ \Leftrightarrow \Psi &= \Psi(\boldsymbol{\varepsilon}, \theta, \lambda)\end{aligned}\tag{2.74}$$

Now, in view of stresses (Equation (2.72)) and entropy (Equation (2.73)), the Clausius-Duhem inequality (Equation (2.71)) takes the form

$$p \dot{\lambda} - \frac{1}{\theta} \mathbf{q} \cdot \nabla \theta \geq 0 \quad (2.75)$$

The first term in the above inequality represents the mechanical dissipation, where an additional quantity p is defined as the thermodynamic driving force and provides information about the evolution direction of the internal variable. The following applies

$$\begin{aligned} -\frac{\partial \Psi}{\partial \lambda} \dot{\lambda} &\geq 0 \\ \Leftrightarrow -\frac{\partial \Psi}{\partial \lambda} &=: p \end{aligned} \quad (2.76)$$

The second term of inequality (2.75) represents the thermal dissipation and has to fulfill the heat conduction inequality. According to the work of Holzapfel (2000), Gurtin et al. (2010) and Demtröder (2017), a suitable constitutive law which relates the heat flux q to the temperature gradient $\nabla \theta$ is

$$\begin{aligned} -\frac{1}{\theta} \mathbf{q} \cdot \nabla \theta &\geq 0 \\ \Leftrightarrow \mathbf{q} &\sim -\nabla \theta \end{aligned} \quad (2.77)$$

What remains to be specified is the response function governing the evolution of the internal variables, which will be achieved in Section 2.6 with Hamilton's principle.

2.6 Hamilton's Principle and Evolution Equation

The objective of Hamilton's principle is to derive the equations governing the mechanical behavior of continuous media in a way that is equivalent to the balance laws presented in Section 2.4. In this section, after the introduction of dissipation potentials for rate-independent and rate-dependent materials, first the general application of Hamilton's principle addressed to materials including a gradient of the internal variable is presented in Subsection 2.6.1, and then the special case known as the principle of the minimum of the dissipation potential (PMDP) is illustrated in Subsection 2.6.2. The numerical implementation of evolution equations obtained from the Hamilton's principle and the PMDP is discussed as well.

The variational principle known today as the Hamilton's principle for dynamic systems of particles is based on the work of Hamilton (1835). Since then, the principle is widely used in continuum mechanics, as in the works of Bedford (1985) and Bailey (2002). More works, especially in the field of microstructure, can be found in Hackl (1997), Ortiz and Repetto (1999) and Carstensen et al. (2002b).

In the case of non-conservative materials, the dissipative processes should also be taken into account. Therefore, here the dissipation function \mathcal{D} is introduced to describe the amount of energy used for irreversible transformation of elastic or kinetic energy to dissipative energy. Based on the concept of the so-called generalized standard material, introduced

in Halphen and Nguyen (1975), which covers a number of inelastic material behaviors, several approaches for the dissipation function are generally possible, the most common ones are presented subsequently.

The first one is for classical rate-independent elastoplastic-type material models

$$\mathcal{D} := r_1 |\dot{\lambda}| \quad (2.78)$$

where r_1 is the dissipation parameter. The second example is for rate-dependent viscoelastic-type material models

$$\mathcal{D} := \frac{r_2}{2} \dot{\lambda}^2 \quad (2.79)$$

with the parameter r_2 describing the viscosity of the material. Combining these two approaches, gives the dissipation function for elasto-viscoplastic-type materials as follows

$$\mathcal{D} := r_1 |\dot{\lambda}| + \frac{r_2}{2} \dot{\lambda}^2 \quad (2.80)$$

The next required component to formulate the Hamilton's principle, is Gibbs energy, which for continuous materials is given by

$$\mathcal{G} := \Pi_{\text{int}} + \Pi_{\text{ext}} \quad (2.81)$$

where Π_{int} is the internal potential derived from Helmholtz free energy Ψ based on the strains $\boldsymbol{\varepsilon}$ and internal variables λ , thus

$$\Pi_{\text{int}} := \int_{\Omega} \Psi(\boldsymbol{\varepsilon}, \lambda) dV \quad (2.82)$$

and Π_{ext} is the external potential derived from the volume forces \mathbf{b} and the surface tractions \mathbf{t} as follows

$$\Pi_{\text{ext}} := - \int_{\Omega} \mathbf{b} \cdot \mathbf{u} dV - \int_{\partial\Omega} \mathbf{t} \cdot \mathbf{u} dA \quad (2.83)$$

Using this expression, Equation (2.81) assumes the form

$$\mathcal{G} := \int_{\Omega} \Psi(\boldsymbol{\varepsilon}, \lambda) dV - \int_{\Omega} \mathbf{b} \cdot \mathbf{u} dV - \int_{\partial\Omega} \mathbf{t} \cdot \mathbf{u} dA \quad (2.84)$$

Using the kinetic energy from Equation (2.54), finally, the Hamilton's principle for continuous and non-conservative materials reads

$$\int_{t_0}^{t_1} (\delta\mathcal{K} - \delta\mathcal{G} + \delta\mathcal{V}) dt = 0 \quad (2.85)$$

Restricting our attention to the static case by neglecting the kinetic energy, hence the simplified Hamilton's principle results as

$$\delta\mathcal{G} + \delta\mathcal{V} = 0 \quad (2.86)$$

where $\delta\mathcal{V}$ is refer to the virtual work of dissipative forces and is defined by

$$\delta\mathcal{V} = \int_{\Omega} \hat{p} \delta\lambda dV \quad (2.87)$$

Thereby, \hat{p} is the so-called dissipative force, which shows the dissipative character of microstructural evolution and is derived from the dissipation potential \mathcal{D} as

$$\hat{p} := -\frac{\partial \mathcal{D}}{\partial \dot{\lambda}} \quad (2.88)$$

In this point, substituting Equations (2.87) and (2.88) into (2.86) Hamilton's principle for continuous and non-conservative material under static conditions is provided by

$$\delta \mathcal{G} + \int_{\Omega} \frac{\partial \mathcal{D}}{\partial \dot{\lambda}} \delta \lambda dV = 0, \quad (2.89)$$

and will be used in further calculations. It is worth to mention that, in the case of conservative materials, naturally no dissipative process is taken into account. Hence, the simplified Hamilton's principle for continuous and conservative materials in static case reads

$$\delta \mathcal{G} = 0. \quad (2.90)$$

2.6.1 General Application of Hamilton's Principle

In the general case of Hamilton's principle, as mentioned before, in addition to the displacement field \mathbf{u} (or strains $\boldsymbol{\varepsilon}$) and the internal variable λ , the gradient of internal variable $\nabla \lambda$ also enters into Gibbs energy, thus

$$\mathcal{G} = \mathcal{G}(\boldsymbol{\varepsilon}, \lambda, \nabla \lambda) \quad (2.91)$$

Application of Hamilton's principle yields the necessary condition for stationarity

$$\delta \mathcal{G} + \int_{\Omega} \frac{\partial \mathcal{D}}{\partial \dot{\lambda}} \delta \lambda dV = \delta_{\mathbf{u}} \mathcal{G} + \delta_{\lambda} \mathcal{G} + \int_{\Omega} \frac{\partial \mathcal{D}}{\partial \dot{\lambda}} \delta \lambda dV = 0 \quad \forall \delta \mathbf{u}, \delta \lambda \quad (2.92)$$

where the variations $\delta \mathbf{u}$ and $\delta \lambda$ may be chosen individually, and therefore, the two stationarity conditions

$$\int_{\Omega} \frac{\partial \Psi}{\partial \boldsymbol{\varepsilon}} : \delta \boldsymbol{\varepsilon} dV - \int_{\Omega} \mathbf{b} \cdot \delta \mathbf{u} dV - \int_{\partial \Omega} \mathbf{t} \cdot \delta \mathbf{u} dA = 0 \quad \forall \delta \mathbf{u} \quad (2.93)$$

$$\int_{\Omega} \frac{\partial \Psi}{\partial \lambda} \delta \lambda dV + \int_{\Omega} \frac{\partial \Psi}{\partial \nabla \lambda} \cdot \delta \nabla \lambda dV + \int_{\Omega} \frac{\partial \mathcal{D}}{\partial \dot{\lambda}} \delta \lambda dV = 0 \quad \forall \delta \lambda \quad (2.94)$$

have to hold individually. Introduction of the mechanical stress by $\boldsymbol{\sigma} = \partial \Psi / \partial \boldsymbol{\varepsilon}$, Equation (2.93) constitutes as the strong form of the balance of linear momentum, viz.

$$\nabla \cdot \boldsymbol{\sigma} + \mathbf{f} = 0 \quad \forall \mathbf{x} \in \Omega \quad (2.95)$$

and Neumann boundary condition, as

$$\boldsymbol{\sigma} \cdot \mathbf{n} = \mathbf{t} \quad \forall \mathbf{x} \in \partial \Omega \quad (2.96)$$

which can be solved by employing the finite element method. Moreover, for the second stationarity condition in terms of the variation of λ , Equation (2.94), an integration by parts provides

$$\frac{\partial \Psi}{\partial \lambda} - \nabla \cdot \left(\frac{\partial \Psi}{\partial \nabla \lambda} \right) + \frac{\mathcal{D}}{\dot{\lambda}} = 0 \quad \forall \mathbf{x} \in \Omega \quad (2.97)$$

$$\left(\frac{\partial \Psi}{\partial \nabla \lambda} \right) \cdot \mathbf{n} = 0 \quad \forall \mathbf{x} \in \partial \Omega \quad (2.98)$$

where Equation (2.97) is refer to as the Helmholtz equation and Equation (2.98) is again the Neumann boundary condition. This general application of Hamilton's principle is presented for topology optimization by Junker and Hackl (2016) and for damage modeling by Junker et al. (2019).

2.6.2 Principle of the Minimum of the Dissipation Potential

The principle of the minimum of the dissipation potential (PMDP) is the special case of Hamilton's principle. Various versions of this principle already appear in the works done by Martin and Ponter (1966), Maier (1969), and Maugin (1992), and are widely used in the literature. Here, it is assumed that the Gibbs energy is no longer a function of the gradient of the internal variable $\nabla \lambda$, thus

$$\mathcal{G} = \mathcal{G}(\boldsymbol{\varepsilon}, \lambda) \quad (2.99)$$

Analogously to the general form of Hamilton's principle, the first stationarity condition is the same as Equation (2.93), where applying the integration by parts provides the strong form of the balance of linear momentum (see Equations (2.95) and (2.96)). In the case of PMDP, the second stationarity condition simplifies to

$$\int_{\Omega} \frac{\partial \Psi}{\partial \lambda} \delta \lambda dV + \int_{\Omega} \frac{\partial \mathcal{D}}{\partial \dot{\lambda}} \delta \dot{\lambda} dV = 0 \quad \forall \delta \lambda \quad (2.100)$$

Elimination of the identical integrals results in the simple expression

$$\frac{\partial \Psi}{\partial \lambda} + \frac{\partial \mathcal{D}}{\partial \dot{\lambda}} = 0 \quad (2.101)$$

known as Biot's equation, for more details refer to Biot (1962). Performing the integration with respect to $\dot{\lambda}$ provides

$$\frac{\partial \Psi}{\partial \lambda} \dot{\lambda} + \mathcal{D} + \mathcal{A} \rightarrow \min_{\dot{\lambda}} \quad (2.102)$$

where \mathcal{A} is an arbitrary integration constant and can be defined by

$$\mathcal{A} := \frac{\partial \Psi}{\partial \boldsymbol{\varepsilon}} : \dot{\boldsymbol{\varepsilon}} \quad (2.103)$$

Introducing a Lagrangian \mathcal{L} gives

$$\mathcal{L} := \dot{\Psi} + \mathcal{D} \rightarrow \min_{\dot{\lambda}} \quad (2.104)$$

with $\dot{\Psi}$ being the rate of the Helmholtz free energy Ψ . According to Hackl and Fischer (2008), the PMDP can be formulated as follows:

From all admissible fluxes (possibly constrained by conservation and boundary conditions), those fluxes are taken which minimize the Lagrangian in Equation (2.104).

Since the Lagrangian \mathcal{L} is assumed to be minimized with respect to the rate of internal variables $\dot{\lambda}$, the time derivative of Helmholtz free energy in Equation (2.104) is always the product of thermodynamical driving forces and the associated internal variables, where the derivative of Ψ with respect to strains can be neglected. Application of Hamilton's principle in either general form or as PMDP provides the evolution equation for the internal variable λ .

For the first case of a rate-independent material, $\mathcal{D}_{\text{RI}} = r_1 |\dot{\lambda}|$ (see Equation (2.78)), the evolution equation is formulated in the form of

$$\dot{\lambda}_{\text{RI}} = \frac{|\dot{\lambda}|}{r_1} p = \Delta\rho p \quad (2.105)$$

where $\Delta\rho = |\dot{\lambda}|/r_1$ is identified as consistency parameter for $\dot{\lambda} \neq 0$. In order to determine the consistency parameter, Legendre transformation is applied as follows

$$\mathcal{D}_{\text{RI}}^* = \sup_{\dot{\lambda}} \{p \dot{\lambda} - \mathcal{D}_{\text{RI}}\} = \sup_{\dot{\lambda}} \{|\dot{\lambda}|(p \operatorname{sgn} \dot{\lambda} - r_1)\} = \sup_{\dot{\lambda}} \left\{ \frac{|\dot{\lambda}|}{r_1} (p^2 - r_1^2) \right\} \quad (2.106)$$

The corresponding yield function is obtained as

$$\Phi := p^2 - r_1^2 \leq 0 \quad (2.107)$$

which is equal to

$$\Phi := |p| - r_1 \leq 0 \quad (2.108)$$

The internal variable will be updated from previous time-step $(\cdot)^m$ to the current time-step $(\cdot)^{m+1}$ according to

$$\lambda_{\text{RI}}^{m+1} = \lambda^m + \begin{cases} \Delta\rho p(\varepsilon, \lambda) & \text{for } |p| > r_1 \\ 0 & \text{else} \end{cases} \quad (2.109)$$

The consistency parameter $\delta\rho$ has to be estimated such that the condition $\Phi \leq 0$ holds true. Therefore Kuhn-Tucker conditions read

$$\Delta\rho \geq 0, \quad \Phi \leq 0, \quad \Delta\rho \Phi = 0 \quad (2.110)$$

Choosing the driving force from current or previous time-step will determine the numerical scheme for solving the evolution equation; i.e., $p(\varepsilon^m, \lambda^m)$ leads to explicit time discretization which is also referred to forward Euler method, whereas $p(\varepsilon^{m+1}, \lambda^{m+1})$ leads to implicit time discretization and referred to backward Euler method. There are also combined time discretization, where different methods are applied to the strain and internal variables and results in an operator split; i.e., $p(\varepsilon^m, \lambda^{m+1})$ using strain from previous time-step and internal variables from current one, or vice versa $p(\varepsilon^{m+1}, \lambda^m)$ the internal variable from the previous time-step combined with the strains of the current time-step.

For the second case, where the dissipation function of rate-dependent material consists of two parts, $\mathcal{D}_{\text{RD}} = r_1 |\dot{\lambda}| + \frac{r_2}{2} \dot{\lambda}^2$ (see Equation (2.80)), the evolution equation can be calculated as

$$\dot{\lambda}_{\text{RD}} = \frac{1}{r_2} [|p| - r_1]_+ \quad (2.111)$$

where $[x]_+ := (x + |x|)/2$ only returns the positive values. In this case a yield function is not necessarily introduced and the evolution of λ is limited by the viscosity parameter r_2 and by the assuming a specific value for the time increment Δt , which allows to update the internal variable with

$$\lambda_{\text{RD}}^{m+1} = \lambda^m + \begin{cases} \frac{\Delta t}{r_2} (|p(\varepsilon, \lambda)| - r_1) & \text{for } |p| > r_2 \\ 0 & \text{else} \end{cases} \quad (2.112)$$

Similar to the first case, different choices of driving force with respect to the current or previous time-step leads to different scheme for solving the evolution equation numerically.

3 Tribology

Tribology is an interdisciplinary science to study the mechanisms that take place between interacting surfaces in relative motion and is fundamentally about the principles of friction, lubrication, and wear. The term tribology was derived from the Greek term *tribos*, translated as rubbing. Tribology research is considerably versatile, but some industries place higher demands on tribological systems due to their continuous operation requirements or extreme conditions, such as transport and manufacturing. The main focus of this work is on computational tribology, which aims to model the behavior of tribological systems, through combining the theories of continuum mechanics, contact mechanics, and fracture mechanics.

A tribological system consists of four elements: the main body, the counter body, interface media, and the surrounding medium. This system considering all relevant influencing factors is represented in Figure 3.1 schematically. The intermediate medium can be a lubricant, wear particles, or a layer formed by mechanical interactions between the main and counter body. Furthermore, the load system, composed of normal force, relative motion, and temperature, acts on the wear pairing and determines the mechanical interactions between the involving bodies. From these considerations, it is clear that wear is not a material property but a system property.

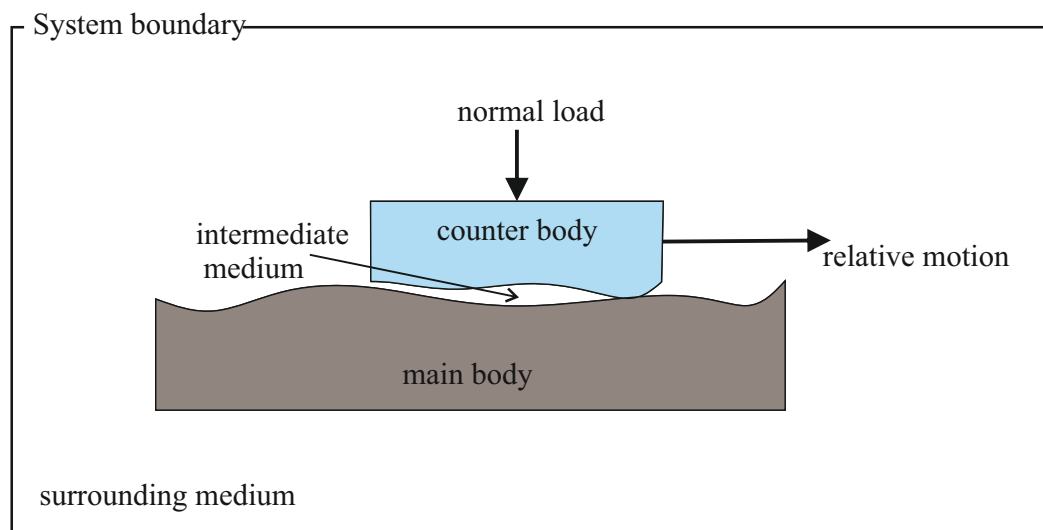


Figure 3.1: Schematic representation of a tribological system, inspired by Röttger (2019)

In this chapter, first, an overview of the mechanized tunneling and different tools that could be installed on the cutter head of the tunnel boring machines (TBMs) are given in Section 3.1. Following by the definition of the wear in Section 3.2, as well as the introduction of the wear mechanisms. Finally, Section 3.3 deals with the detailed explanation of the abrasive wear, as it is known as the dominant wear mechanism that happens at the cutting tools in mechanized tunneling.

3.1 Mechanized Tunneling

Mechanized tunneling, as compared to conventional tunneling, is dedicated to all excavation techniques performed mechanically using different machines, from the simplest like diggers to the most complicated like TBMs. These machines can build up tunnels in difficult geological environments, as well as not very stable soil with high groundwater. Furthermore, they can prevent large disturbances and subsidence on the surface, and guarantee the stability of the tunnel during the construction phase, i.e., peripheral support in the case of shield TBMs, or both peripheral and frontal support by earth pressure TBMs or slurry shields.

Additionally, mechanized tunneling provides a high excavation speed, as well as good quality and profile accuracy of the finished work. It enhances the health and safety condition of the workforce and has a little interference with the environment (little noise, hardly any vibrations, and unchanged groundwater level). However, the main drawback of this technique is that a significantly long time and effort is needed for the planning phase and installation of the shield machine and the lack of flexibility due to the certain restrictions in the tunnel geometry, which make the method not economically optimized for short tunnels.

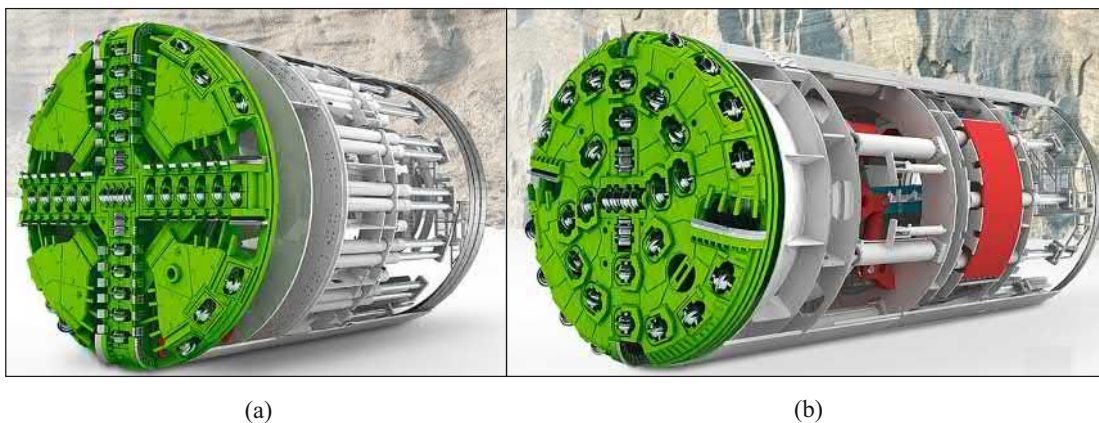


Figure 3.2: Tunnel boring machines (TBM) a) earth pressure shield (EPB) for use in soft soil, b) double shield TBM for excavation in hard rock Herrenknecht (2021)

For excavation in the hard rock, when there is a risk due to falling rocks during operation, or for tunneling in the soft ground below the groundwater level, TBMs can be equipped with a shielding system. According to Röttger et al. (2015), the shield machines used in this case can present a supporting system using compressed air, earth pressure, or liquid substances (bentonite). Figure 3.2 shows two examples of equipped TBMs for quarry in soft soil and excavation in hard rock.

3.1.1 Tool Concepts

Different tool concepts have been developed to place on the shield of TBMs concerning the ground to be excavated. They should be adopted to the geology and the corresponding excavation mechanism for the type of ground. They are described in detail in the work of Küpferle et al. (2017a). For example, as illustrated in Figure 3.3, the cutting discs are introduced for excavation in hard rocks, while chisel, reamer, and ripper are used for

quarrying soil. However, since they do not influence the further investigations in this work, they are only discussed briefly in the following.

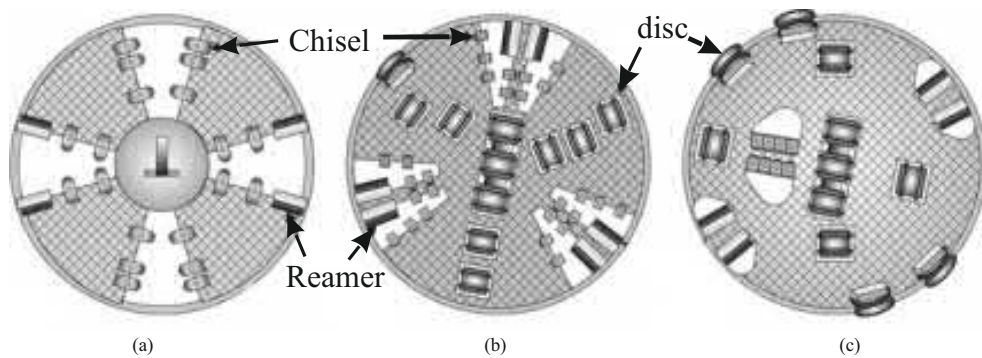


Figure 3.3: Front view of the shield for tunneling machines a) standard configuration, b) configuration for soil ground and c) configuration for hard rock (Röttger et al. (2015))

Cutting Disc

Cutting discs or wheels are originally used for excavation in hard rock since chisel and other burin tools quickly become blunted in contact with the abrasive rock. They apply a great point load on the rock, causing fragmentation and crack propagation, thus leading to the formation of crack networks and finally breakage of larger pieces instead of grinding up. As shown in Figure 3.4, in addition to single cutting wheels (mono-disc), there are also multiple edge cutter rings arranged in parallel. They can be equipped with scrapers to carry out the fragments, bearings, and cemented carbide studs.

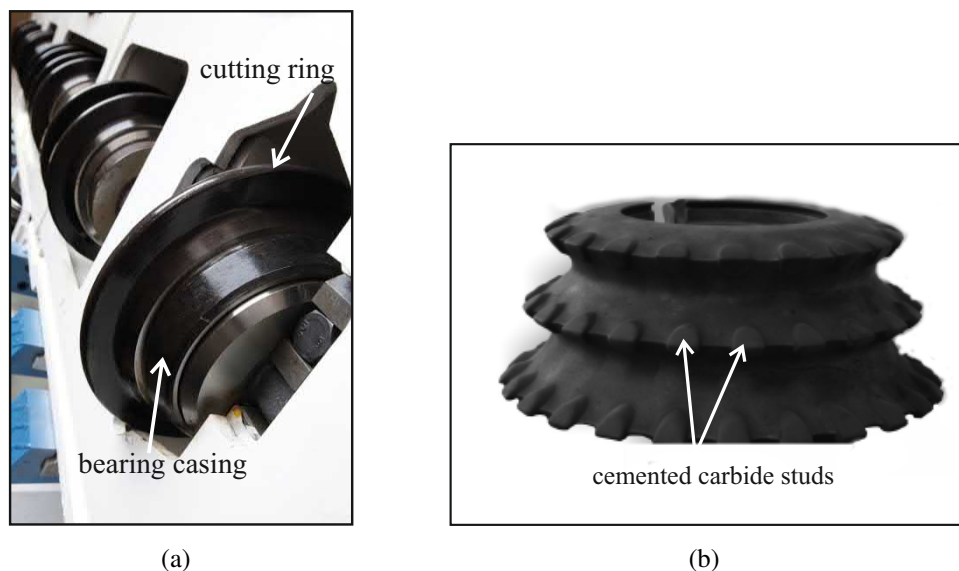


Figure 3.4: Cutting discs of a TBM (a) Mono-disc consists of bearing casing and cutting ring (Tunnel-Online (2013)) (b) multi-edge cutting ring with cemented carbide studs (Küpfelerle et al. (2017a))

The cutting wheels are made of wear-resistant, high-alloyed work steel with high carbon content. Frenzel et al. (2008) concluded that the material should achieve the greatest

possible hardness, as well as a certain fracture toughness to withstand the high mechanical stresses during operation in hard rock.

One failure mechanism of cutting discs can be flank wear due to abrasion, which happens when they penetrate too deep into the rock, and is the function of the penetration depth, the rotational speed of the cutting wheels and the properties of the ground to be excavated. Rad (1975) quoted that the dominant wear mechanism, in this case, is the two-body abrasion, i.e., scratching of the material surface. Additionally, due to the low density of the ground or adhesive-acting suspensions or mechanical failure, disc cutters can experience frequent blockage and stop rotating, so that the non-rotating cutting discs will be worn locally from one side and develop a flat surface.

Another mechanism causes wear due to surface spalling. Czichos et al. (1995) shows that the three-body abrasion, i.e., indentation of abrasive particles into tool material, leads to continuous wear of the material surfaces if they move relative to the material surface. Additionally, cycling indentation of abrasive particles into the tool material can lead to disruption and ultimately brittle material break-out.

Chisel, Ripper, and Reamer

Another group of tools used for excavation in the soil is chisel, ripper, and reamer. Chisel and ripper are installed perpendicular to the cutter head and used for scratching the tunnel face. The main difference between chisel and ripper is that rippers are direction-independent, i.e., they can be used in both rotational directions of the cutter head and therefore have a cutting edge for both directions of rotation. While chisel due to its geometry can only move in one advanced direction. Reamers are usually arranged at regular intervals in the outer radius of the cutter head. They serve to transfer the quarried soil behind the cutter head through the excavation chamber.

The material used for these tools is similar. They are made of the main steel substrate, responsible for transferring forces from the tunneling device into the ground to be excavated. Due to the different requirements, such as wear resistance, material strength, and toughness, the tool is locally protected by coating or deposition welding of materials such as cemented carbide pins or ceramic edges. The tool can lose its functionality either due to high-impact loads caused by hitting boulders or geological inhomogeneities or from cycling loads promoting fatigue failure. According to Theisen (1997), the service life can be improved by utilizing a material that possesses sufficient hardness (resistance against plastic deformation and crack formation) alongside high fracture toughness (resistance against crack propagation).

3.2 Wear Mechanisms

The term wear is defined as damage to the surface of a solid body, involving progressive material removal, due to relative motion and frictional contact with another surface. This process is usually slow but is considered as one of the major factors causing damage and

consequently failure of components during the lifetime of tools or machines. Therefore, wear is an important topic from the economical point of view and efficiency of the project.

In general, wear is a complex procedure that depends on different mechanical, physical, chemical, and electrical phenomena which take place at the same time or change irregularly. Thus, different wear classifications can be considered from many points of view, depends on the methods of mechanics, physics, and chemistry. According to Zum Gahr (1987), wear mechanisms can be divided into four main categories: abrasion, adhesion, surface degradation, and tribochemical reaction. Which mechanism dominates an application depends on the tribological system. In mechanized tunneling, an analysis of excavation tools represents that abrasion and surface degradation are the dominant wear mechanisms [Gharahbagh et al. (2011), Düllmann et al. (2013)]. These individual wear mechanisms are briefly presented here.

3.2.1 Abrasion

Abrasion occurs when the roughness of hard solids, i.e., abrasive particles, penetrates into softer surfaces under high contact force and slides over them. What happens at the microscopic level depends on the hardness, strength, and volume fraction of hard particles in the tool material (Theisen (1997)). Ductile materials experience deformation and machining processes that lead to failure due to fatigue. In the case of brittle materials, on the other hand, these roughnesses primarily lead to micro-breaking. Depending on the type of material, the focus is on entirely different processes at the microscopic level.

Zum Gahr (1987) concluded that abrasion can be categorized into four micromechanisms: micro-chipping, micro-plowing, micro-fatigue, and micro-fracture. Micro-chipping and micro-plowing results in homogeneous wear rates by abrasive degradation, whereby an abrasive particle is penetrating into the material and sliding relative to the surface, thus leads to material removal. As the wear process continues, both mechanisms can transform into micro-fatigue, leading to crack formation and propagation under active cyclic loading. Finally, the resulting crack networks can lead to a break out of material, which is known as micro-fracture.

3.2.2 Adhesion

Adhesion at the microscopic level happens when two solid bodies slide on each other under high normal stress, and they do not separate at the original interface, but at the new interface, which runs through one of them. The solid, through which the new separating surface runs, loses mass on the surface, which remains attached to the second solid. The basic requirement for this type of wear is that the connection established at the original separating surface has a higher shear strength than the shear strength of one of the two solid bodies.

Depending on the material of the two solid bodies, the connection could be based on mechanical interlocking, diffusion of atoms or molecules, electron transfer, or chemical bonds on the surface. Therefore, adhesion can be reduced by building up a separating lubricating film or by forming reaction layers from the lubricant additives that are matched to both

solids, as explained by (Köppl 2014).

3.2.3 Surface Degradation

The surface degradation is due to cyclic loading of a base and a counter body between which high contact forces are present, and leads to micro-cracks on or below the surface of the base body, detachment of flat fragments on the surface, and thus material removal. Micro-cracks can arise from local stress peaks, even if the macroscopic load is within the elastic limits of the material, see the work done by K pferle et al. (2017b).

3.2.4 Tribochemical Reaction

Tribochemical reaction refers to wear mechanism that results from a chemical process on the surface of a solid and consequently material loss which is activated by the mechanical and thermal stress. For example, the oxidation of metals counts under atmospheric conditions.

The insight of the above-mentioned wear mechanisms is beyond the scope of this work. For more details, readers are referred to Rabinowicz and Tanner (1966), Popov (2010) and K ppl (2014). In real applications, the wear process is more complicated and is normally a combination of different wear mechanisms mentioned above. The focus of our work is on mechanized tunneling, and therefore the prediction of wear of the cutting tools, where the abrasive wear is the dominated specific type. Accordingly, the volume loss depends on the material properties of contacting bodies, as well as contact behavior such as pressure, sliding velocity, and temperature. This is explained in more detail in the following section.

3.3 Abrasive Wear

Abrasive wear is the most dominant wear process in tunneling tools, which is caused due to hard particles that are forced against, penetrate and move along a solid surface (ASTM 2013). The abrasive wear process is classified according to the tribological system into two groups: two-body and three-body abrasive wear. In two-body abrasion, wear is caused by fixed hard protuberances of one surface sliding over the other, while in three-body abrasion particles are trapped between two contacting surfaces and slide or roll freely. According to Harsha and Tewari (2003), since in three-body abrasion the loose abrasive particles rather roll than slide, the rate of material removal is less than two-body abrasion.

Wear is not a simple material property, but rather a system-dependent quantity (Arbeitsblatt 2002). According to Friedrich et al. (1991), the abrasive wear process can not only be characterized by material properties but also by the surface properties of the involving partners., see Figure 3.5.

Different test methods are developed for estimation of abrasive wear such as Cerchar test, LCPC test, pin-on-disc machine and, dry sand-rubber wheel test, for example in the work of K sling and Thuro (2010). The abrasive wear that happens to the cutting tools of TBM

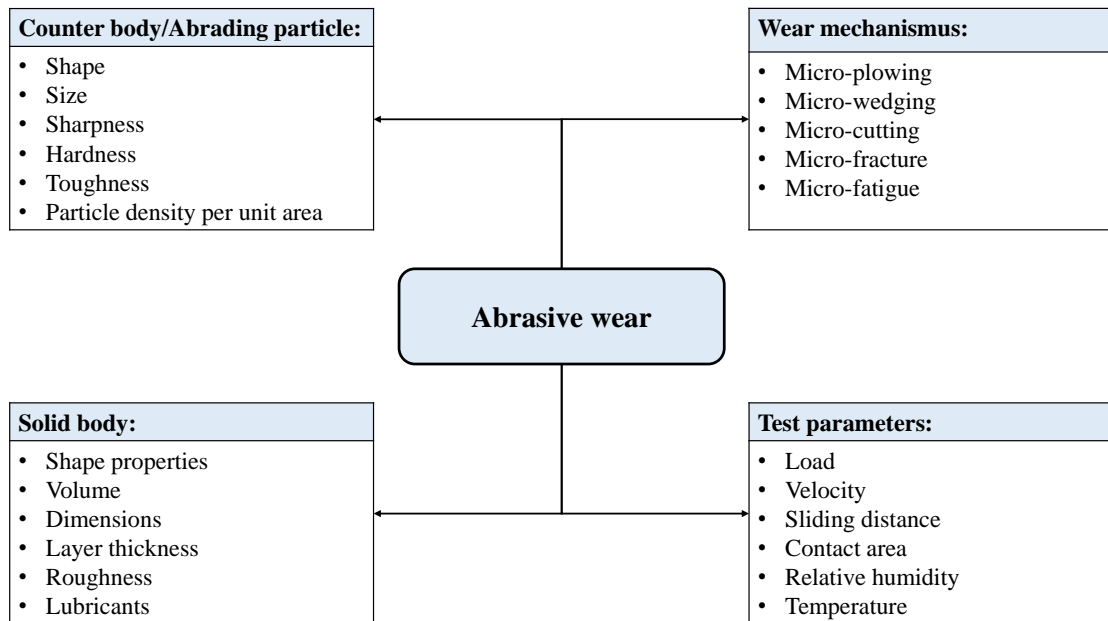


Figure 3.5: parameters influencing the abrasive wear performance

is categorized as the two-body abrasion (grooving), as the abrasive particles penetrate and scratch the surface of the tool during excavation. An investigation of the damage process at the microstructural level will help to estimate the wear behavior of different materials in advance. In the present work, the single scratch events with predefined indenter size and shapes are performed to analyze the grooving process at the microstructural level, which is based on the nano-scratch laboratory test. Then the wear behavior is modeled based on the dry sand-rubber wheel test. These two laboratory experiments are explained in the following.

3.3.1 Nano Scratch Test

Abrasion can be experimentally reproduced using a single scratch test, in which a moving indenter penetrates the surface of the specimen. Tests were conducted with scratch software from CSM instruments, equipped with a sphero-conical diamond (tip radius $10\ \mu\text{m}$). A gradually increasing load (3 mN to 603 mN) is applied to the specimen by a cantilever arm, where the indenter is placed. The applied normal force (f_N), as well as the resulting scratch geometry (A_g), are continuously measured during the scratch test. This testing procedure is a reference for our numerical simulations of single scratch asperity, which will be presented in Section 8.2.

3.3.2 Dry Sand-Rubber Wheel Test - ASTM G65

The standard test procedure for the dry sand-rubber wheel (ASTM-G65) is broadly used to investigate the abrasive wear resistance of metallic materials. The abrasive particles are guided by a nozzle in between a rubber-coated wheel and the specimen. The rotating rubber wheel, which is pressed against the specimen with a defined load through a lever arm, drags

the abrasive particles with controlled size and composition across the polished specimen surface. The rotation of the wheel is such that its contact face moves in the direction of grit flow. The pivot axis of the lever arm lies within a plane, which is approximately tangential to the rubber wheel surface and normal to the horizontal diameter along which the load is applied. The test setup is shown schematically in Figure 3.6 and is considered as a reference for our wear model, which will be introduced later in Section 8.4.

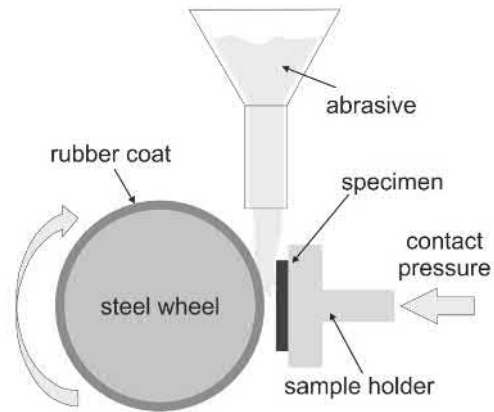


Figure 3.6: Schematic overview of the dry sand-rubber wheel test

4 Numerical Methods

In this chapter, we discuss the fundamentals of the two numerical methods used in this thesis. Section 4.1 is dedicated to the Discrete Element Method (DEM), while in Section 4.2 the essential motivation and principles of the Finite Element Method (FEM) are discussed.

4.1 Discrete Element Method (DEM)

The Discrete Element Method (DEM), originally proposed by Cundall and Strack (1979), is a popular numerical technique in which the material behavior is represented by interactions between a collection of arbitrarily shaped particles. Note that the term "particle", in the present context, denotes a body that occupies a finite amount of space. Each particle moves independently of one another and interacts only at contacts or interfaces between the particles. In recent years, it has found its applications in both fundamental research and engineering fields. It is suitable for simulating granules, such as soil, whether static or dynamic. However, it could also be considered for solids if there is a breakout of individual parts, large deformations or if different bodies come into contact with each other.

The DEM has a time-stepping algorithm and is based on the idea that the chosen time-step is so small that during a single time-step, disturbances cannot propagate further from any particle than its immediate neighbors. It is the most precious advantage of DEM that the nonlinear interaction of a large number of particles can be solved without requiring an excessive amount of memory or an iterative procedure; since it assumes constant velocity and acceleration over each time-step.

4.1.1 Calculation Cycle

A thorough description of the method is given in a two-part paper by Cundall and Hart (1992). The general DEM can handle deformable polygonal-shaped particles. In this study, we use the PFC^{3D} code for our simulations, which is known as a simplified implementation of the DEM because of the following restrictions:

1. The particles are considered as rigid bodies.
2. The contacts occur over an infinitesimally small area (i.e., point contact).
3. Behavior at the contacts uses a soft-contact approach where the rigid particles are allowed to overlap one another at contact points. The overlaps are very small in comparison to particle size and are related to contact forces via the force-displacement law.

4. Bonds can exist at contacts between particles.
5. All particles are spherical. However, the clump logic supports the creation of a more complex arbitrary shape.

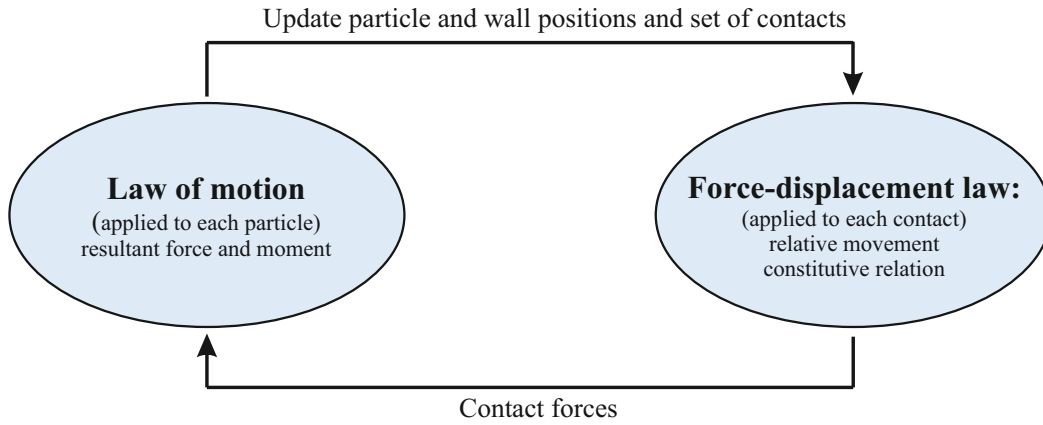


Figure 4.1: Calculation cycle in PFC^{3D}. Image inspired by (Itasca 1999)

Calculations in DEM are performed by alternating between Newton's second law applied to the particles and the force-displacement law applied to the contacts between particles. At the beginning of each time-step, a set of contacts is updated from particle and wall positions. The force-displacement law is used to update the contact forces arising from the relative motion between the two entities at the contact based on the chosen contact constitutive model. Next, Newton's second law is applied to determine the motion of each particle arising from the contact and body forces acting upon it. The calculation cycle is represented in Figure 4.1. The calculations performed in each of the two boxes of Figure 4.1 can be done effectively in parallel.

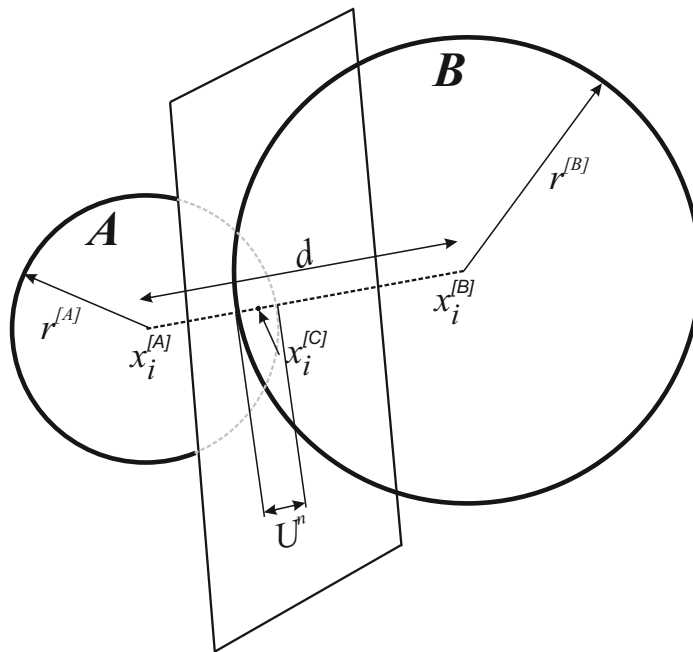


Figure 4.2: Illustration of ball-ball contact. Image inspired by (Itasca 1999)

Assume there is a contact between two particles A and B, with radii $r^{[A]}$ and $r^{[B]}$, as it is illustrated in Figure 4.2. For ball-ball contact, the unit normal, \mathbf{n}_i , which describes the contact plane, is given by

$$\mathbf{n}_i = \frac{\mathbf{x}_i^{[B]} - \mathbf{x}_i^{[A]}}{d} \quad (4.1)$$

where d is the distance between the ball centers

$$d = \left| \mathbf{x}_i^{[B]} - \mathbf{x}_i^{[A]} \right| \quad (4.2)$$

The overlap U^n , is defined to be a relative contact displacement in the normal direction, and is given by

$$U^n = r^{[A]} + r^{[B]} - d \quad (4.3)$$

The location of the contact point is given by

$$\mathbf{x}_i^{[C]} = \mathbf{x}_i^{[A]} + (r^{[A]} - \frac{1}{2}U^n) \mathbf{n}_i \quad (4.4)$$

Almost the same relationship describes the contact between a particle and a wall element, this is explained in more detail in PFC manual (Itasca 1999).

The contact force \mathbf{F}_i can be decomposed into normal and tangential components with respect to the contact plane as

$$\mathbf{F}_i = \mathbf{F}_i^n + \mathbf{F}_i^t \quad (4.5)$$

The normal contact force is calculated by

$$\mathbf{F}_i^n = K^n U^n \mathbf{n}_i \quad (4.6)$$

where K^n is the normal contact stiffness and depends on the chosen contact model. The most common contact models will be briefly explained later. The following applies to the tangential direction analogous to the relationship:

$$\Delta \mathbf{F}_i^t = -K^t \Delta \mathbf{U}_i^t \quad (4.7)$$

where K^t is the tangential stiffness at the contact and $\Delta \mathbf{U}_i^t = \mathbf{V}_i^t \Delta t$ is the incremental displacement in the tangential direction, depends on the shear component of the contact velocity \mathbf{V}_i^t and the time-step Δt . In contrast to the normal direction, incremental values for force and displacement are used in the tangential direction.

4.1.2 Contact Components

The mechanical behavior of the material is described via the contact between particles. At each point, at least one of these possibilities could be applied: contact, slip, or bonding. In PFC there are two standard contact models (linear and Hertz) and several alternative ones. In the following, the components of contact, as well as the contact models, will be briefly explained.

Stiffness

The contact stiffnesses in the normal and tangential direction, K^n and K^t , are essential components for every contact model. These are determined from the stiffness, which is assigned to the particles and the wall elements, depending on the selected contact law. They relate the contact forces and relative displacements in the normal and shear directions via Equations (4.6) and (4.7).

If no other components, such as bonds, damping, or friction, are added to the contact, it is only active under pressure. It means that, the stiffness is only defined for the compressive connection of two particles via the contact stiffness. If a connection is created using bonds, these bonds also define the stiffness for the tensile forces. The contact stiffnesses differ for the linear and Hertz contact models, as will be described in Section 4.1.3.

Slip

The inelastic behavior of contact is defined by slip behavior for compressive normal forces and breaking of bonds for tensile forces. The slip behavior is described by the dimensionless friction coefficient μ . Here, μ is equal to $\tan(\phi)$, where ϕ is the particle friction angle. Sufficient tangential forces will cause particles to slip relative to each other or other surfaces. The extent of slippage under tangential force is determined by:

$$|\mathbf{F}^t| \leq \mu |\mathbf{F}^n| \quad (4.8)$$

Usually, $0 < \mu < 1$ should be applied, but in some cases $\mu > 1$ can also occur. Then the tangential force can become larger than the normal force acting in contact.

Bonds

More complex behavior can be modeled by allowing the particles to be bonded together at their contact point. Consequently, the bond is broken, when the inter-particle forces acting at any bond exceed the bond strength. This allows tensile forces to develop between particles. The two standard bonding behaviors are embodied in contact bonds and parallel bonds. A contact bond can be envisioned as a pair of elastic springs (or a point of glue) with constant normal and shear stiffnesses acting at the contact point. These two springs have specific shear and tensile normal strengths. Here, the bond strength is defined as $f^{n,c}$ in the normal and $f^{t,c}$ in the tangential direction. A parallel bond provides the force-displacement behavior of a finite-sized piece of cementitious material deposited between two balls. It can be envisioned as a set of elastic springs with constant normal and shear stiffnesses, uniformly distributed over a circular cross-section lying on the contact plane and centered at the contact point. The different behavior of the bonds in the normal and the tangential direction is illustrated in Figure 4.3.

If the representative tangential force is reached, then the bonds break, and the contact forces are set to zero. Note that, in addition to tensile forces, parallel bonds can also be used to transmit moments.

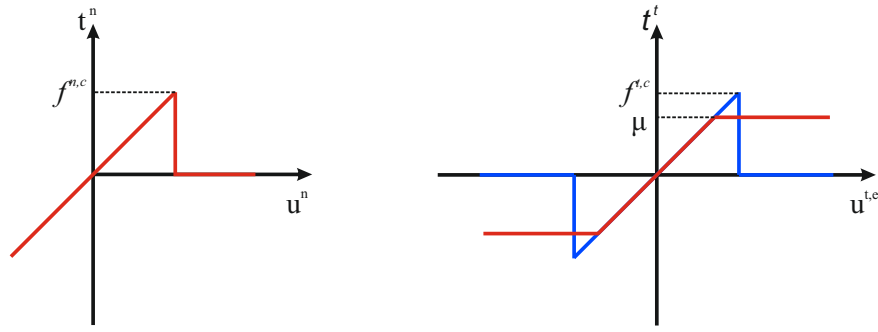


Figure 4.3: Contact laws in normal (left) and shear (right) direction, slip behavior versus breaking of contact bonds

Clumps

The clump logic is used to create and modify groups of particles, to have complex shaped grains. A clump behaves as a rigid body with a deformable boundary (i.e., the particles comprising the clump remain at a fixed distance from each other) and will not break apart, regardless of the forces acting upon it. In this sense, a clump differs from a group of particles that are bonded to one another.

The internal contacts of a clump are skipped during the calculation cycle, which results in savings of computational time compared to a similar calculation where all contacts are active. Particles within a clump may overlap to any extent; contact forces are not generated between these particles, but any contact forces that exist when the clump is created or when a particle is added to the clump will be preserved unchanged during cycling.

Damping

To consider the damping effect, a damping force term is added to the equations of motion. On the other hand, dampers can be added to the contact in both normal and tangential directions. These then act in parallel with the active contact model and available bonds. In this case, a damping force is added to the contact force:

$$\mathbf{D}_i = \beta_i |\mathbf{V}_i| \quad (4.9)$$

where, β_i is the damping constant and \mathbf{V}_i is the relative velocity at the contact. However, the damping constant β_i will not be specified directly in DEM, but via a ratio d_i , which describes the influence of the damping constant in the critical damping constant β_i^{crit} is:

$$\beta_i = d_i \beta_i^{\text{crit}} \quad (4.10)$$

for $d_i = 1$ critical damping is achieved, so the system finds its equilibrium as quickly as possible. If nothing is defined, then $d_i = 0$ will be applied.

4.1.3 Contact Models

Linear Model

The linear contact model is the most common contact law, which is also used in our work. In this model, contact stiffnesses are constant and calculated from the stiffnesses of two contacting entities $[A]$ and $[B]$. In the normal direction, it is given by

$$K^n = \frac{k_n^{[A]} k_n^{[B]}}{k_n^{[A]} + k_n^{[B]}} \quad (4.11)$$

and in tangential direction by

$$K^t = \frac{k_t^{[A]} k_t^{[B]}}{k_t^{[A]} + k_t^{[B]}} \quad (4.12)$$

Bonds and dampers described in Section 4.1.2 can be inserted into this model as well.

Hertz Model

The Hertz model provides sliding and stiffness that varies as a function of the elastic constants of the two contacting entities, overlap and normal force. It is not defined for tensile forces, and is therefore incompatible with bonding. The contact normal stiffness is given by

$$K^n = \left(\frac{2\langle G \rangle \sqrt{2\tilde{r}}}{3(1 - \langle \nu \rangle)} \right) \sqrt{U^n} \quad (4.13)$$

and the contact shear stiffness is given by

$$K^t = \left(\frac{2(\langle G \rangle^2 3(1 - \langle \nu \rangle) \tilde{r})^{1/3}}{2 - \langle \nu \rangle} \right) |F_i^n|^{1/3} \quad (4.14)$$

U^n is the sphere overlap, $|F_i^n|$ is the magnitude of the normal contact force. The multipliers to both of these equations are a function of the geometric and material properties of the two entities in contact, with G being the shear modulus, ν the Poisson's ratio, and \tilde{r} the mean particle radius.

Other contact models

The literature contains a large number of other contact models that have been developed for a wide variety of applications. A comprehensive introduction of all types of contacts between particles can be found in the work of Schütte (2001). There are also individual contact models designed for special applications; for example, smooth joint models are used by Obermüller (1989) to model the boundary surfaces, or by Straßberger (1997) in the prediction of instabilities of rock formations.

In addition to the application-specific contact models, there are also attempts to develop a contact model whose parameters can be determined from simple standardized tests (see Westerhoff (1995)). The mentioned models are only examples, the list can be expanded as required.

4.2 Finite Element Method (FEM)

The purpose of this section is to introduce the Finite Element Method (FEM). Generally, FEM is a numerical technique for solving problems that are described by Partial Differential Equations (PDEs) or can be formulated as functional minimization. A more precise finite element solution can be obtained by increasing the number of simple elements or using elements with more complicated shape functions.

4.2.1 Variational Formulation

In mathematical modeling of problems in engineering fields, it is often not easy to solve the system of partial differential equations analytically, due to the complexity of the geometry of the domain or the high non-linearity of the material behavior. In order to find an approximate solution for such a problem, it is more common and suitable to use the so-called weak (or integral) formulation of the investigated problem. The starting point of variational approach in finite element method is Gibbs energy \mathcal{G} , as

$$\mathcal{G} = \int_{\Omega} \Psi \, dV - \int_{\Omega} \mathbf{b} \cdot \mathbf{u} \, dV - \int_{\partial\Omega} \mathbf{t} \cdot \mathbf{u} \, dA \quad (4.15)$$

The stationarity condition for the Gibbs energy with respect to the displacement field \mathbf{u} is derived as

$$\delta\mathcal{G} = \int_{\Omega} \frac{\partial\Psi}{\partial\boldsymbol{\varepsilon}} : \delta\boldsymbol{\varepsilon} \, dV - \int_{\Omega} \mathbf{b} \cdot \delta\mathbf{u} \, dV - \int_{\partial\Omega} \mathbf{t} \cdot \delta\mathbf{u} \, dA \stackrel{!}{=} 0 \quad \forall \delta\mathbf{u} \quad (4.16)$$

where the partial derivative of energy with respect to the strain $\partial\Psi/\partial\boldsymbol{\varepsilon}$ corresponds to the stress $\boldsymbol{\sigma}$. Due to the fact that the equilibrium condition is fulfilled for the state of minimal energy, the energy expression can be minimized with respect to the primary variable \mathbf{u} . Hence, it holds that the variation of the Gibbs energy must vanish for any change in the displacement field \mathbf{u} , i.e., $\delta\mathcal{G} = 0$. Therefore, variation of Gibbs energy can be written as

$$\int_{\Omega} \boldsymbol{\sigma} : \delta\boldsymbol{\varepsilon} \, dV \stackrel{!}{=} \int_{\Omega} \mathbf{b} \cdot \delta\mathbf{u} \, dV + \int_{\partial\Omega} \mathbf{t} \cdot \delta\mathbf{u} \, dA \quad \forall \delta\mathbf{u} \quad (4.17)$$

It is also known as the principle of virtual work.

The core idea of finite element method is to simplify a problem with significant computational effort by discretizing the continuum body into N_e number of finite elements. Consequently, both the total volume Ω and the boundary $\partial\Omega$ are composed of the element volumes Ω_e and element boundaries $\partial\Omega_e$ as follows:

$$\Omega = \sum_{e=1}^{N_e} \Omega_e, \quad \partial\Omega = \sum_{e=1}^{N_e} \partial\Omega_e \quad (4.18)$$

The discretization can then be entered into the integrals of the variational formulations in accordance with

$$\sum_{e=1}^{N_e} \int_{\Omega_e} \boldsymbol{\sigma} : \delta \boldsymbol{\varepsilon} dV \stackrel{!}{=} \sum_{e=1}^{N_e} \int_{\Omega_e} \mathbf{b} \cdot \delta \mathbf{u} dV + \sum_{e=1}^{N_e} \int_{\partial \Omega_e} \mathbf{t} \cdot \delta \mathbf{u} dA \quad \forall \delta \mathbf{u} \quad (4.19)$$

when adding up the evaluated terms *element by element*, the global node numbering must be taken into account. This procedure is called assembly and is described in Fish and Belytschko (2007) in detail.

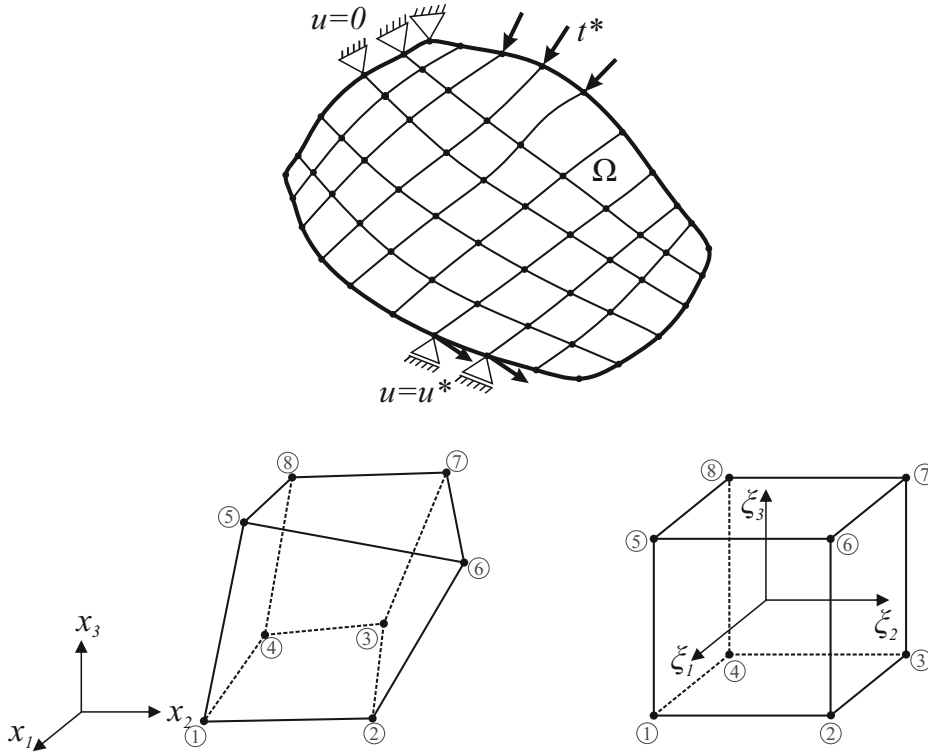


Figure 4.4: Discretized body (Top) arbitrary and reference element in physical and natural coordinate system (Bottom)

The elements are built up through their surfaces by a specific number of nodes N_n (eight for cubic-like or hexahedral element), where they are described by their physical coordinates \mathbf{x} as

$$\mathbf{x} = (x_1 \quad x_2 \quad x_3)^T \quad (4.20)$$

Hexahedral (or brick-type) linear 8-node three-dimensional isoparametric element is depicted in Figure 4.4, in both an arbitrary shape related to the physical coordinate as well as reference shape related to the natural coordinate. The nodal coordinates of the reference element are described by the natural coordinate vector

$$\boldsymbol{\xi} = (\xi_1 \quad \xi_2 \quad \xi_3)^T \quad (4.21)$$

where they make up the master or unit cube of three-dimensional elements on which the shape functions of arbitrary shaped hexahedral elements can be formed. The term “isoparametric” means that nodal coordinates $\hat{\mathbf{x}}$ and nodal displacement field $\hat{\mathbf{u}}$ are specified in parametric form and are interpolated with the same shape functions. Furthermore, the same

functions are also applied to the variation of the nodal displacements $\delta \hat{\mathbf{u}}$ according to the Galerkin (or Bubnov-Galerkin) method. This allows to formulate

$$\mathbf{x} = \mathbf{N} \cdot \hat{\mathbf{x}}, \quad \mathbf{u} = \mathbf{N} \cdot \hat{\mathbf{u}}, \quad \delta \mathbf{u} = \mathbf{N} \cdot \delta \hat{\mathbf{u}} \quad (4.22)$$

with so-called *shape functions* \mathbf{N} . As it is already shown in Figure 4.4, considering the origin of the natural coordinate system in the origin of a cube with an edge length of two, then the trilinear shape functions (eight nodes) can be found as

$$\begin{aligned} N^1(\xi) &= \frac{1}{8}(1 + \xi_1)(1 - \xi_2)(1 - \xi_3) & N^5(\xi) &= \frac{1}{8}(1 + \xi_1)(1 - \xi_2)(1 + \xi_3) \\ N^2(\xi) &= \frac{1}{8}(1 + \xi_1)(1 + \xi_2)(1 - \xi_3) & N^6(\xi) &= \frac{1}{8}(1 + \xi_1)(1 + \xi_2)(1 + \xi_3) \\ N^3(\xi) &= \frac{1}{8}(1 - \xi_1)(1 + \xi_2)(1 - \xi_3) & N^7(\xi) &= \frac{1}{8}(1 - \xi_1)(1 + \xi_2)(1 + \xi_3) \\ N^4(\xi) &= \frac{1}{8}(1 - \xi_1)(1 - \xi_2)(1 - \xi_3) & N^8(\xi) &= \frac{1}{8}(1 - \xi_1)(1 - \xi_2)(1 + \xi_3) \end{aligned} \quad (4.23)$$

The eight shape functions are assembled to a matrix, accordingly

$$\mathbf{N} = \mathbf{N}(\boldsymbol{\xi}) = \begin{pmatrix} N^1(\boldsymbol{\xi}) & 0 & 0 & N^2(\boldsymbol{\xi}) & 0 & 0 & \dots & N^8(\boldsymbol{\xi}) & 0 & 0 \\ 0 & N^1(\boldsymbol{\xi}) & 0 & 0 & N^2(\boldsymbol{\xi}) & 0 & \dots & 0 & N^8(\boldsymbol{\xi}) & 0 \\ 0 & 0 & N^1(\boldsymbol{\xi}) & 0 & 0 & N^2(\boldsymbol{\xi}) & \dots & 0 & 0 & N^8(\boldsymbol{\xi}) \end{pmatrix} \quad (4.24)$$

The nodal coordinates $\hat{\mathbf{x}}_e$ and nodal displacement $\hat{\mathbf{u}}_e$ of a specific element are assembled to the vectors

$$\begin{aligned} \hat{\mathbf{x}}_e &= (\hat{x}_1^1 \quad \hat{x}_2^1 \quad \hat{x}_3^1 \quad \hat{x}_1^2 \quad \hat{x}_2^2 \quad \hat{x}_3^2 \quad \dots \quad \hat{x}_1^8 \quad \hat{x}_2^8 \quad \hat{x}_3^8)^T \\ \hat{\mathbf{u}}_e &= (\hat{u}_1^1 \quad \hat{u}_2^1 \quad \hat{u}_3^1 \quad \hat{u}_1^2 \quad \hat{u}_2^2 \quad \hat{u}_3^2 \quad \dots \quad \hat{u}_1^8 \quad \hat{u}_2^8 \quad \hat{u}_3^8)^T \end{aligned} \quad (4.25)$$

so that the coordinates \mathbf{x} and displacements \mathbf{u} depend on the natural coordinates according to $\mathbf{x} = \mathbf{x}(\boldsymbol{\xi})$ and $\mathbf{u} = \mathbf{u}(\boldsymbol{\xi})$, respectively.

As next, the correlation between the strain tensor and the element displacement vector has to be defined. Utilizing the definition of linearized strain tensor by

$$\boldsymbol{\varepsilon} = \frac{1}{2}(\nabla \mathbf{u} + \mathbf{u} \nabla) \quad (4.26)$$

and under consideration of the Voigt notation, one can evaluate the approximated strain components as

$$\tilde{\boldsymbol{\varepsilon}} = \tilde{\mathbf{B}} \cdot \mathbf{u} \quad (4.27)$$

where the strain operator matrix $\tilde{\mathbf{B}}$ contains the corresponding derivatives and allows a linear mapping between strains and displacements. It is defined in three-dimensional space

according to

$$\tilde{\mathbf{B}} := \begin{pmatrix} \frac{\partial}{\partial x_1} & 0 & 0 \\ 0 & \frac{\partial}{\partial x_2} & 0 \\ 0 & 0 & \frac{\partial}{\partial x_3} \\ 0 & \frac{\partial}{\partial x_3} & \frac{\partial}{\partial x_2} \\ \frac{\partial}{\partial x_3} & 0 & \frac{\partial}{\partial x_1} \\ \frac{\partial}{\partial x_2} & \frac{\partial}{\partial x_1} & 0 \end{pmatrix} \quad (4.28)$$

Now, inserting the approximation of displacement from Equation (4.22) into Equation (4.27) results in

$$\tilde{\varepsilon} = \tilde{\mathbf{B}} \cdot \mathbf{N} \cdot \hat{\mathbf{u}} = \mathbf{B} \cdot \hat{\mathbf{u}} \quad (4.29)$$

where the multiplication of $\tilde{\mathbf{B}} \cdot \mathbf{N}$ corresponds to the derivative of shape functions dependent of natural coordinates $\boldsymbol{\xi}$ with respect to the physical coordinates \mathbf{x} and denotes the operator matrix $\mathbf{B} = \tilde{\mathbf{B}} \cdot \mathbf{N}$. Each component k of \mathbf{B} can be calculated using the chain rule as

$$\frac{\partial \mathbf{N}_k(\boldsymbol{\xi})}{\partial \mathbf{x}} = \frac{\partial \mathbf{N}_k(\boldsymbol{\xi})}{\partial \boldsymbol{\xi}} \frac{\partial \boldsymbol{\xi}}{\partial \mathbf{x}} \quad (4.30)$$

and these components can be formulated into a matrix as follows

$$\begin{pmatrix} \frac{\partial \mathbf{N}(\boldsymbol{\xi})}{\partial \xi_1} \\ \frac{\partial \mathbf{N}(\boldsymbol{\xi})}{\partial \xi_2} \\ \frac{\partial \mathbf{N}(\boldsymbol{\xi})}{\partial \xi_3} \end{pmatrix} = \begin{pmatrix} \frac{\partial x_1}{\partial \xi_1} & \frac{\partial x_2}{\partial \xi_1} & \frac{\partial x_3}{\partial \xi_1} \\ \frac{\partial x_1}{\partial \xi_2} & \frac{\partial x_2}{\partial \xi_2} & \frac{\partial x_3}{\partial \xi_2} \\ \frac{\partial x_1}{\partial \xi_3} & \frac{\partial x_2}{\partial \xi_3} & \frac{\partial x_3}{\partial \xi_3} \end{pmatrix} \begin{pmatrix} \frac{\partial \mathbf{N}(\boldsymbol{\xi})}{\partial x_1} \\ \frac{\partial \mathbf{N}(\boldsymbol{\xi})}{\partial x_2} \\ \frac{\partial \mathbf{N}(\boldsymbol{\xi})}{\partial x_3} \end{pmatrix} \quad (4.31)$$

or alternatively written in shorter form as

$$\frac{\partial \mathbf{N}(\boldsymbol{\xi})}{\partial \boldsymbol{\xi}} = \mathbf{J} \cdot \frac{\partial \mathbf{N}(\boldsymbol{\xi})}{\partial \mathbf{x}} \quad (4.32)$$

which introduces the well-known Jacobian matrix \mathbf{J} . Then, the derivatives with respect to the coordinates \mathbf{x} can be found according to

$$\frac{\partial \mathbf{N}(\boldsymbol{\xi})}{\partial \mathbf{x}} = \mathbf{J}^{-1} \cdot \frac{\partial \mathbf{N}(\boldsymbol{\xi})}{\partial \boldsymbol{\xi}} \quad (4.33)$$

Finally, it only remains to calculate the integrals in Equation (4.19) numerically, as the analytical integration is hardly possible due to time expenses. Within the framework of this thesis, the common numerical method of Gauß quadrature is taken into account. The Gauß quadrature of a function $f(x)$ over the parameter space $x \in [-1, 1]$ is given by the sum

$$\int_{-1}^1 f(x) dx \approx \sum_{j=1}^m w(x_j) f(x_j) \quad (4.34)$$

where $w(x_j)$ are the weight coefficients to the function $f(x_j)$, evaluated at certain integration or so-called Gauß points x_j . For polynomials of polynomial degree $p \leq 2m - 1$ Gauß quadrature method delivered exact results, while higher-order polynomials and other functions can be integrated approximately. For specific application, the integral is extended into three-dimensional consideration, thus

$$\int_{-1}^1 \int_{-1}^1 \int_{-1}^1 f(\boldsymbol{\xi}) \det \mathbf{J}(\boldsymbol{\xi}) d\xi_1 d\xi_2 d\xi_3 = \sum_{g=1}^{N_{GP}} w_{GP} f(\boldsymbol{\xi}_{GP}^g) \det \mathbf{J}(\boldsymbol{\xi}_{GP}^g) \quad (4.35)$$

The transformation of integrals from the physical coordinates into the natural coordinates is performed using the determinant of the Jacobian matrix. In this case, quadratic function are used; i.e., $m = 2$, and therefore the $N_{GP} = m^3 = 8$ are given by

$$\boldsymbol{\xi}_{GP}^i \in \left\{ \left(\begin{array}{c} \pm \frac{1}{\sqrt{3}} \\ \pm \frac{1}{\sqrt{3}} \\ \pm \frac{1}{\sqrt{3}} \end{array} \right) \right\} \quad i \in \{1, \dots, 8\} \quad (4.36)$$

4.2.2 Residual and Tangent Matrix

The principle of virtual work in Equation (4.19) for an arbitrary (constant) variation of displacement $\delta \mathbf{u}$ can be written as

$$\mathbf{R}_u = \sum_{e=1}^{N_e} \int_{\Omega_e} \mathbf{B}^T \cdot \tilde{\boldsymbol{\sigma}} dV - \sum_{e=1}^{N_e} \int_{\Omega_e} \mathbf{N}^T \cdot \mathbf{b} dV - \sum_{e=1}^{N_e} \int_{\partial\Omega_e} \mathbf{N}^T \cdot \mathbf{t} dA \stackrel{!}{=} \mathbf{0} \quad (4.37)$$

where \mathbf{R}_u provides the residual of the displacement field. In order to seek for the zero point of \mathbf{R}_u , the well-known Newton-Raphson solution scheme is applied in an iterative way. For more details regarding this method see works of Zienkiewicz et al. (2005) and Fish and Belytschko (2007). By formulating the residual at the iteration step $k + 1$

$$\mathbf{R}_u^{k+1} = \mathbf{R}_u^k + \frac{d\mathbf{R}_u^k}{d\mathbf{u}^k} \cdot \Delta \mathbf{u}^{k+1} \stackrel{!}{=} \mathbf{0} \quad (4.38)$$

the displacement increment $\Delta \mathbf{u}^{k+1}$ can be found according to

$$\Delta \mathbf{u}^{k+1} = - \left[\frac{d\mathbf{R}_u^k}{d\mathbf{u}^k} \right]^{-1} \cdot \mathbf{R}_u^k \quad (4.39)$$

Here, \mathbf{R}_u^k corresponds to the residual from Equation (4.37) evaluated for the previous iteration step k , and the derivative of the residuum with respect to the displacements $d\mathbf{R}_u^k/d\mathbf{u}^k$ is denoted as the tangent matrix and can be determined as

$$\frac{d\mathbf{R}_u^k}{d\mathbf{u}^k} = \sum_{e=1}^{N_e} \int_{\Omega_e} \mathbf{B}^T \cdot \frac{d\tilde{\boldsymbol{\sigma}}}{d\hat{\mathbf{u}}} dV = \sum_{e=1}^{N_e} \int_{\Omega_e} \mathbf{B}^T \cdot \frac{d\tilde{\boldsymbol{\sigma}}}{d\tilde{\boldsymbol{\varepsilon}}} \cdot \mathbf{B} dV \quad (4.40)$$

Then, the displacements are updated as

$$\mathbf{u}^{k+1} = \mathbf{u}^k + \Delta \mathbf{u}^{k+1} \quad (4.41)$$

If the residual for this updated displacement is zero or at least reaches a specified tolerance, the iteration steps can be ended. Otherwise, the next iteration is continued until the state is reached.

4.2.3 Stresses and Material Tangent

As discussed in Subsection 4.2.2, for determining residual and tangent matrix and subsequently updating the displacements, stresses and material tangent should be calculated in advance. In the case of linear constitutive relationship given by Hook's law

$$\tilde{\boldsymbol{\sigma}} = \tilde{\boldsymbol{\sigma}}(\tilde{\boldsymbol{\varepsilon}}) = \mathbb{E} \cdot \tilde{\boldsymbol{\varepsilon}} \quad (4.42)$$

the material tangent matrix $d\tilde{\boldsymbol{\sigma}}/d\tilde{\boldsymbol{\varepsilon}}$ in Equation (4.40) can be trivially determined by

$$\frac{d\tilde{\boldsymbol{\sigma}}}{d\tilde{\boldsymbol{\varepsilon}}} = \mathbb{E}, \quad (4.43)$$

that corresponds exactly to the stiffness matrix \mathbb{E} . Since this tangent matrix is obviously constant for a linear elastic material model, the displacements can be updated either analytically or using the Newton-Raphson method which converges in one iteration.

To implement the non-linear material behavior in the finite element method, the material tangent matrix is the total derivative of the stress with respect to the strain. We should emphasize that the non-linearity in this context only refers to the non-linear relationship between stress and strain, i.e., non-linear constitutive equations. Therefore, geometrical non-linearity, i.e., non-linear relation between displacement and strain, is not considered in this work. In the case of non-linear constitutive relationship, stresses are a function of strains and internal variables, and generally formulated as

$$\tilde{\boldsymbol{\sigma}} = \tilde{\boldsymbol{\sigma}}(\tilde{\boldsymbol{\varepsilon}}, \lambda) \quad (4.44)$$

Here, in agreement with the procedure presented in Junker and Hempel (2017), we perform a consistent linearization from Taylor expansion for stresses, meaning

$$\tilde{\boldsymbol{\sigma}}^{m+1} = \tilde{\boldsymbol{\sigma}}^m + \left. \frac{\partial \tilde{\boldsymbol{\sigma}}}{\partial \tilde{\boldsymbol{\varepsilon}}} \right|^m \cdot \Delta \tilde{\boldsymbol{\varepsilon}} + \left. \frac{\partial \tilde{\boldsymbol{\sigma}}}{\partial \lambda} \right|^m \Delta \lambda \quad (4.45)$$

with $\Delta \tilde{\boldsymbol{\varepsilon}} = \tilde{\boldsymbol{\varepsilon}}^{m+1} - \tilde{\boldsymbol{\varepsilon}}^m$ and $\Delta \lambda = \lambda^{m+1} - \lambda^m$ being the increment of strains and internal variables, respectively, and $\tilde{\boldsymbol{\sigma}}^m$ the stress from previous time-step. It is important to mention that in this thesis, λ refers to the vector of internal variables and consists of internal variables regarding the plasticity as well as internal variables regarding the damage. Thus, this will be explained in detail for each material model used in this work in Chapter 6. Then, the material tangent matrix is derived as

$$\left. \frac{d\tilde{\boldsymbol{\sigma}}}{d\tilde{\boldsymbol{\varepsilon}}} \right|^{m+1} = \left. \frac{\partial \tilde{\boldsymbol{\sigma}}}{\partial \tilde{\boldsymbol{\varepsilon}}} \right|^m + \left. \frac{\partial \tilde{\boldsymbol{\sigma}}}{\partial \lambda} \right|^m \otimes \left. \frac{\partial \lambda}{\partial \tilde{\boldsymbol{\varepsilon}}} \right|^{m+1} \quad (4.46)$$

The individual derivatives of the stress, i.e., the first two terms on the right-hand side, will be calculated uncomplicated. The implementation of plasticity follows an explicit Euler procedure. Therefore, the derivatives of the plastic internal variables with respect to the strain at the previous time-step are not interned in the calculations. For the implementation of damage, we consider an implicit update scheme, with both rate-dependent and rate-independent behavior of the evolution equations.

For *rate-independent* material behavior, the evolution equation according to Equation (2.109) is

$$\lambda^{m+1} = \lambda^m + \Delta \rho(\tilde{\boldsymbol{\varepsilon}}^{m+1}) p(\tilde{\boldsymbol{\varepsilon}}^{m+1}, \lambda^m) \quad (4.47)$$

and consequently third term of Equation (4.46) can be derived as

$$\left. \frac{\partial \lambda}{\partial \tilde{\epsilon}} \right|^{m+1} = \Delta \rho \frac{\partial p(\tilde{\epsilon}^{m+1}, \lambda^m)}{\partial \tilde{\epsilon}^{m+1}} + \frac{\partial \Delta \rho(\tilde{\epsilon}^{m+1})}{\partial \tilde{\epsilon}^{m+1}} p(\tilde{\epsilon}^{m+1}, \lambda^m) \quad (4.48)$$

The derivative of driving force can be calculated directly, while for calculation of the derivative of the consistency parameter $\Delta \rho$, we need also the yield function Φ , and based on Equation (2.108), it reads

$$\begin{aligned} \Phi &= |p(\tilde{\epsilon}^{m+1}, \lambda^{m+1})| - r_1 \stackrel{!}{=} 0 \\ &= |p(\tilde{\epsilon}^{m+1}, \lambda^m + \Delta \rho(\tilde{\epsilon}^{m+1}) p(\tilde{\epsilon}^{m+1}, \lambda^{m+1})| - r_1 \stackrel{!}{=} 0 \end{aligned} \quad (4.49)$$

Setting the derivative of yield function equal to zero, i.e.,

$$\frac{d\Phi}{d\tilde{\epsilon}^{m+1}} = \frac{\partial \Phi}{\partial \tilde{\epsilon}^{m+1}} + \frac{\partial \Phi}{\partial \Delta \rho} \frac{\partial \Delta \rho}{\partial \tilde{\epsilon}^{m+1}} \stackrel{!}{=} 0 \quad (4.50)$$

Rearranging the above equation

$$\frac{\partial \Delta \rho}{\partial \tilde{\epsilon}^{m+1}} = - \left[\frac{\partial \Phi}{\partial \Delta \rho} \right]^{-1} \frac{\partial \Phi}{\partial \tilde{\epsilon}^{m+1}} \quad (4.51)$$

Finally, substituting Equation (4.51) into Equation (4.48) leads to the calculation of the derivative of the internal variable as

$$\left. \frac{\partial \lambda}{\partial \tilde{\epsilon}} \right|^{m+1} = \Delta \rho \frac{\partial p(\tilde{\epsilon}^{m+1}, \lambda^m)}{\partial \tilde{\epsilon}^{m+1}} - \left[\frac{\partial \Phi}{\partial \Delta \rho} \right]^{-1} \frac{\partial \Phi}{\partial \tilde{\epsilon}^{m+1}} p(\tilde{\epsilon}^{m+1}, \lambda^m) \quad (4.52)$$

For *rate-dependent* material behavior, the evolution equation according to Equation (2.112) is

$$\lambda^{m+1} = \lambda^m + \frac{\Delta t}{r_2} p(\tilde{\epsilon}^{m+1}, \lambda^m) - r_1 \quad (4.53)$$

which unlike to the previous case, leads to the easy calculation of the desired derivative of the internal variable as

$$\left. \frac{\partial \lambda}{\partial \tilde{\epsilon}} \right|^{m+1} = \frac{\Delta t}{r_2} \frac{\partial p(\tilde{\epsilon}^{m+1}, \lambda^m)}{\partial \tilde{\epsilon}^{m+1}} \quad (4.54)$$

5 DEM Parameter Identification

The Discrete Element Method (DEM) has many advantages compared to continuum methods, especially regarding processes that include loosening, fracturing, defragmentation as well as filling and flow processes. This leads to a wide range of applications in various fields of engineering. The main problem that remains within this method is connecting the contact parameters that govern the material behavior to the basic physical properties of the investigated material.

The main focus of this chapter is to develop a parameter identification approach for discrete element simulations including granular materials as well as rocks. In Section 5.1, after introducing different concepts for parameter identification of DEM, the advantages and disadvantages of each procedure are explained. An analytical prediction based on an energy minimization approach is introduced in Section 5.2. It leads to a relation between the macroscopic elastic constants and the microscopic contact parameters. Ideally, this relation should be applicable a priori, before the actual simulation is started. Section 5.3 deals with the setup and calibration of compression tests, performed in PFC^{3D} software for solid and granular materials. Section 5.4 uses the results of the compression test for validation of the developed analytical parameter identification relations. Furthermore, the influence of complex particle ensembles on material properties is investigated.

5.1 Introduction

The discrete element method is a promising approach for modeling soil-tool interaction and can be used to overcome some difficulties encountered by analytical methods and finite element simulations, as discussed by Coetzee and Els (2009). The major obstacle concerning the use of DEM is the required input parameters. Often, the parameters defining the constitutive model have no direct physical meaning and are therefore hard to determine. This is especially valid for very complex materials such as soil; for more detail, please refer to Donzé et al. (2009).

Current studies on parameter identification that figure out the required inter-particle parameters can be divided into two main categories: one group that uses calculations to replicate specified experimental results and the other that uses the theoretical approach. Both procedures are designed to find a connection between the parameters on the microscopic and macroscopic scale, such as contact stiffnesses and particle radius on the one hand and Young's modulus and Poisson's ratio on the other. An overview of these two groups is given in the following.

5.1.1 Using Experiments to Calibrate Material

There are many publications regarding different applications of the discrete element method, in which the required DEM parameters are derived from a calibration process using experiments. Belheine et al. (2009) proposed a calibration for material behavior by simulating a drained triaxial test for a soil sample. Since the calculation time for a limited specimen is within reason and the numerical results are quite close to the experimental ones, this could be a promising approach. There remains the known problem that the soil characteristics can deviate drastically between laboratory experiments and in-situ conditions. Therefore, other groups, such as Asaf et al. (2007), use a field test for the calibration process. Here also, a good agreement can be achieved, but the results are limited to the two-dimensional case. These are just two examples of several publications with a similar approach to finding DEM parameters for some specified applications, some other examples can be found in the work of Cleary et al. (1998), and Tanaka et al. (2007). The main drawback is that new test simulations and experiments are required for every new material because the results cannot be transferred to another material, application, or packing density.

5.1.2 Theoretical Approaches

Due to the obvious drawback mentioned in Section 5.1.1, some groups aim to find a theoretical base to connect the macroscopic to the microscopic material parameters. Although due to the work of Donzé et al. (2009), none of the analytical approaches are generally accepted yet, a short overview of the different methods will be given in this section. The theoretical studies focus on defining the microstructural strain, which results from the behavior of granular material and relating it to the macroscopic strain. An overview is given by Bagi (2006), who subdivides the methods into two classes:

- An equivalent continuum is defined for all or part of the assembly. The translation field of this equivalent continuum is then designed to fit the characteristic translations of the single-particle centers. Usually, the equivalent continuum is set up through the nodes of each particle center, while the particles do not necessarily need to be in contact. The exact choice of the equivalent continuum differs in the different approaches; see for example works of Bagi (1996), Cambou et al. (2000), Kuhn (1997), Kruyt and Rothenburg (1996).
- On the other hand, there is the “best-fit” method, in which a translation gradient tensor is defined and the smallest deviation from the characteristic displacement of the specimen is determined. This method was developed by Cundall and Strack (1979) and adapted in the works of Liao et al. (1997), Cambou et al. (2000) and others.

In the first group, the assembly needs to be thoroughly investigated to identify the equivalent continua. Then, the resulting deformations need to be matched to the expected continuum results. Depending on the chosen approach, this leads to good results; however, a considerable (computational) effort is also required. The same is true for the best-fit method. Here, the computational time comes into play because the displacements of all particle centers or, in some cases, even all contact points need to be identified.

5.2 Energy Minimization Approach

A variational approach is provided to relate the local contact parameters to the macroscopic material properties, such as elastic stiffness and yield state of the soil. This method was briefly introduced in Hoormazdi and Hackl (2018) and is presented in more detail in this section.

5.2.1 Microscopic Potential

The relative displacement of two particles at the contact point is denoted by \mathbf{u} , and has one elastic part, one inelastic part, and one part due to relative rotation, as given by

$$\mathbf{u} = \mathbf{u}^e + \mathbf{u}^i + \mathbf{u}^r. \quad (5.1)$$

The component of relative displacement in normal direction \mathbf{u}^n is assumed to be purely elastic, whereas the tangential component \mathbf{u}^t contains an inelastic part and a rotational part as well. Therefore, it holds that

$$\mathbf{u}^n = \mathbf{u}^{n,e}, \quad \mathbf{u}^t = \mathbf{u}^{t,e} + \mathbf{u}^{t,i} + \mathbf{u}^r. \quad (5.2)$$

In tangential direction, displacements have to be measured as small deviations from the current configuration, and therefore this decomposition is only valid for infinitesimally small displacements. Let an infinitesimal rotation of the particle be expressed by the rotation vector $\boldsymbol{\omega}_i$, then the rotational part of the relative displacement is given by

$$\mathbf{u}^r = -r^{[A]} \boldsymbol{\omega}_1 \times \mathbf{n} - r^{[B]} \boldsymbol{\omega}_2 \times \mathbf{n}. \quad (5.3)$$

where $r^{[A]}$ and $r^{[B]}$ are particle radii and \mathbf{n} is the unit normal vector, see Figure 5.1. Obviously it holds $\mathbf{u}^n \times \mathbf{u}^r = \mathbf{0}$.

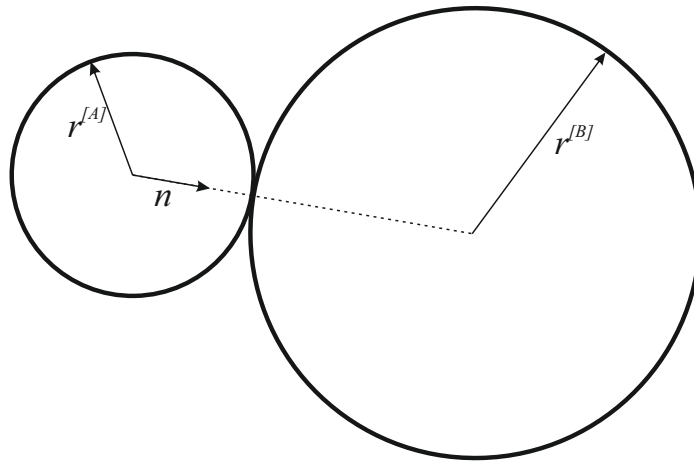


Figure 5.1: Two contacting particles

Based on this consideration and Helmholtz free energy defined in Section 2.5, the potentials at the contact level in the normal and tangential directions are given as

$$\Psi^n(\mathbf{u}^n) = \frac{K^n}{2} (u^n)^2, \quad \Psi^t(\mathbf{u}^{t,e}) = \frac{K^t}{2} (u^{t,e})^2 \quad (5.4)$$

where K^n , K^t are contact stiffnesses in the normal and tangential directions and will be calculated from particle stiffnesses later. The contact forces in the normal and tangential direction can be derived from these potentials as follows:

$$\mathbf{t}^n = \frac{\partial \Psi^n}{\partial \mathbf{u}^n}, \quad \mathbf{t}^t = \frac{\partial \Psi^t}{\partial \mathbf{u}^{t,e}} \quad (5.5)$$

Forces are generated using the force-displacement law by considering an appropriate contact model that defines the interaction between particles as well as the interaction between particles and walls. As it is mentioned in Section 4.1.3, in the present work, a linear contact model is applied. The contact forces in normal and tangential direction can then be derived from the potentials defined in Equation (5.4), which also correspond to the linear contact law:

$$\mathbf{t}^n = K^n \mathbf{u}^n, \quad \mathbf{t}^t = K^t \mathbf{u}^{t,e} \quad (5.6)$$

5.2.2 Macroscopic Potential

Now, that the contact point has been examined in more detail and potentials have been established at the contact level, they should be converted into a macroscopic potential. Let us for this purpose assume a (nearly) monodisperse medium consisting of spheres of (average) radius r . We further assume that all relative displacements and contact forces may be described as a function of the normal direction \mathbf{n} , independent of the corresponding individual particle. Specifically, the total relative displacement is then given as $\mathbf{u} = \mathbf{u}(\mathbf{n})$, and the elastic one as $\mathbf{u}^e = \mathbf{u}^e(\mathbf{n})$. We define the average over all directions of a quantity \mathbf{f} for the 3D case as

$$\langle \mathbf{f} \rangle = \frac{1}{4\pi} \int_{\mathbb{S}^2} \mathbf{f}(\mathbf{n}) \, dS, \quad (5.7)$$

where the integration is performed over the unit sphere \mathbb{S}^2 . The macroscopic specific free energy Ψ^m of a corresponding continuum is then given as

$$\Psi^m = \rho_c \langle \Psi(\mathbf{u}^e(\mathbf{n})) \rangle. \quad (5.8)$$

Here, ρ_c denotes the number of contacts between particles per unit volume and will be discussed more in detail in Section 5.3. It is approximately given by

$$\rho_c = \frac{c}{2} \frac{1 - \eta}{\frac{4}{3}\pi r^3}, \quad (5.9)$$

where η is the porosity and c is the coordination number, i.e., the average number of contacts a particle has with its neighbors.

The macroscopic deformation gradient can be calculated as the directional average of the relative displacements

$$\nabla \mathbf{u}^m = \frac{1}{r} \langle \mathbf{u} \otimes \mathbf{n} \rangle. \quad (5.10)$$

Let us now assume that the directional distribution of relative displacement $\mathbf{u}(\mathbf{n})$ as well as the particle rotations $\boldsymbol{\omega}$ will be arranged by the medium in such a way as to minimize the free energy for a given macroscopic deformation gradient. Furthermore we will take $\boldsymbol{\omega}$ to be an average rotation constant for all particles. The macroscopic free energy can then be calculated as

$$\Psi^m(\nabla \mathbf{u}^m, \mathbf{u}^{t,i}) = \rho_c \min\{\langle \Psi(\mathbf{u}^e) \rangle \mid \mathbf{u}, \boldsymbol{\omega}; \nabla \mathbf{u}^m = \frac{1}{r} \langle \mathbf{u} \otimes \mathbf{n} \rangle\} \quad (5.11)$$

5.2.3 Derive Elastic Constants from Macroscopic Energy

This section shows the derivation of the elastic material constants, i.e., the elasticity modulus E and the Poisson' ratio from contact parameters. The next part dedicated to the considerations applied to the granular materials, followed by the part representing relations valid for bonded material.

Granular Material

Making use of elastic and inelastic contact deformations defined in Equations (5.2) and (5.3), and substituting the formulas of Equation (5.4) into Equation (5.11) results in the following macroscopic free energy

$$\Psi^m(\nabla \mathbf{u}^m, \mathbf{u}^{t,i}) = \rho_c \min \left\{ \left\langle \frac{K^n}{2} (\mathbf{u} \cdot \mathbf{n})^2 + \frac{K^t}{2} |\mathbf{u} - (\mathbf{u} \cdot \mathbf{n})\mathbf{n} - \mathbf{u}^{t,i} + 2r \boldsymbol{\omega} \times \mathbf{n}|^2 \right\rangle \mid \mathbf{u}, \boldsymbol{\omega}; \nabla \mathbf{u}^m = \frac{1}{r} \langle \mathbf{u} \otimes \mathbf{n} \rangle \right\}. \quad (5.12)$$

In order to minimize the macroscopic free energy, we introduce the Lagrange multiplier $\bar{\boldsymbol{\sigma}}$, and formulate the Lagrangian as

$$\mathcal{L}^m = \rho_c \left\langle \frac{K^n}{2} (\mathbf{u} \cdot \mathbf{n})^2 + \frac{K^t}{2} |\mathbf{u} - (\mathbf{u} \cdot \mathbf{n})\mathbf{n} - \mathbf{u}^{t,i} + 2r \boldsymbol{\omega} \times \mathbf{n}|^2 \right\rangle + \bar{\boldsymbol{\sigma}} : \left(\nabla \mathbf{u}^m - \frac{1}{r} \langle \mathbf{u} \otimes \mathbf{n} \rangle \right). \quad (5.13)$$

Stationarity conditions of \mathcal{L}^m with respect to \mathbf{u} and $\boldsymbol{\omega}$ give

$$\rho_c \left(K^n (\mathbf{u} \cdot \mathbf{n})\mathbf{n} + K^t (\mathbf{u} - (\mathbf{u} \cdot \mathbf{n})\mathbf{n} - \mathbf{u}^{t,i}) + 2r K^t \boldsymbol{\omega} \times \mathbf{n} \right) - \frac{1}{r} \bar{\boldsymbol{\sigma}} \cdot \mathbf{n} = \mathbf{0} \quad \forall \delta \mathbf{u} \quad (5.14)$$

$$\langle (\mathbf{u} - \mathbf{u}^{t,i}) \times \mathbf{n} \rangle - 2r \boldsymbol{\omega} = \mathbf{0} \quad \forall \delta \boldsymbol{\omega} \quad (5.15)$$

where we make use of $\mathbf{u}^{t,i} \cdot \mathbf{n} = 0$, $(\boldsymbol{\omega} \times \mathbf{n}) \cdot \mathbf{n} = 0$, and $(\boldsymbol{\omega} \times \mathbf{n}) \times \mathbf{n} = -\boldsymbol{\omega}$. Equation (5.14) may be solved for the relative displacement as

$$\mathbf{u} = \mathbf{u}^{t,i} + \left[\left(\frac{1}{K^n} - \frac{1}{K^t} \right) \mathbf{n} \otimes \mathbf{n} + \frac{1}{K^t} \mathbf{I} \right] \cdot \left(\frac{1}{\rho_c r} \bar{\boldsymbol{\sigma}} \cdot \mathbf{n} - 2r K^t \boldsymbol{\omega} \times \mathbf{n} \right). \quad (5.16)$$

Substitution of Equation (5.16) into Equation (5.10) for macroscopic deformation gradient gives

$$\nabla \mathbf{u}^m = \nabla \mathbf{u}^{m,i} + \frac{1}{\rho_c r^2} \left[\left(\frac{1}{K^n} - \frac{1}{K^t} \right) \langle \mathbf{n} \otimes \mathbf{n} \otimes \mathbf{n} \otimes \mathbf{n} \rangle : \bar{\boldsymbol{\sigma}} + \frac{1}{K^t} \langle \mathbf{n} \otimes \mathbf{n} \rangle \cdot \bar{\boldsymbol{\sigma}} \right] + 2r \langle \mathbf{n} \otimes \mathbf{n} \rangle \times \boldsymbol{\omega}. \quad (5.17)$$

A straightforward calculation gives

$$\langle \mathbf{n} \otimes \mathbf{n} \rangle = \frac{1}{3} \mathbf{I}, \quad \langle \mathbf{n} \otimes \mathbf{n} \otimes \mathbf{n} \otimes \mathbf{n} \rangle : \bar{\boldsymbol{\sigma}} = \frac{1}{15} \text{tr} \boldsymbol{\sigma} \mathbf{I} + \frac{2}{15} \boldsymbol{\sigma}, \quad (5.18)$$

where $\boldsymbol{\sigma} = \text{sym } \bar{\boldsymbol{\sigma}}$. Now, we introduce the total and inelastic macroscopic strain $\boldsymbol{\varepsilon} = \text{sym } \nabla \mathbf{u}^m$, $\boldsymbol{\varepsilon}^i = \text{sym } \nabla \mathbf{u}^{m,i}$. Then we can rewrite Equation (5.16) after systematization using Equation (5.18) as

$$\boldsymbol{\varepsilon} = \boldsymbol{\varepsilon}^i + \frac{1}{\rho_c r^2} \left[\frac{1}{15} \left(\frac{1}{K^n} - \frac{1}{K^t} \right) \text{tr } \boldsymbol{\sigma} \mathbf{I} + \left(\frac{2}{15} \frac{1}{K^n} + \frac{1}{5} \frac{1}{K^t} \right) \boldsymbol{\sigma} \right]. \quad (5.19)$$

Equation (5.19) constitutes an isotropic linear-elastic material law in which we can identify $\boldsymbol{\sigma}$ as a stress tensor and $\boldsymbol{\varepsilon}$ as strain tensor. The macroscopic Young's modulus and Poisson's ratio are given as

$$E = 15 \rho_c r^2 \left(\frac{3}{K^n} + \frac{2}{K^t} \right)^{-1}, \quad \nu = \frac{K^n - K^t}{2K^n + 3K^t}. \quad (5.20)$$

This direct relation between the microscopic contact stiffnesses on one hand and the macroscopic elastic constants on the other, makes it possible to predict elastic constants, prior and without time-consuming calibration procedure, directly from the chosen microscopic ones for particle assemblies in a DEM calculation. Rewrite Equation (5.20) for contact stiffnesses results in

$$K^n = \frac{E}{3 \rho_c r^2 \cdot (1 - 2\nu)}, \quad K^t = \frac{E}{3 \rho_c r^2 \cdot (1 + 3\nu)} \quad (5.21)$$

Now, it is possible to assign an appropriate contact stiffness based on Equation (5.21) to a material, modeled with DEM, with which the material obtains the required macroscopic stiffness. Here, as already mentioned, the contact stiffness does not correspond to the particle stiffness but is calculated from the particle stiffness according to the selected contact law.

Bonded Material

The relations between the contact parameters and material properties already derived for granular material in the previous part are also valid for cohesive materials and solids. Furthermore, it is also important to determine the strength of the bonds. To achieve this, the parameter identification procedure presented in Section 5.2 is expanded here for the calculation of the bond strengths.

To derive the bond strengths in the normal and tangential directions, the relative displacement of contact obtained from Equation (5.16) is considered. From this, the component of displacement in the normal direction is defined as

$$u^n = \frac{1}{\rho_c r} \frac{1}{K^n} \mathbf{n} \cdot \boldsymbol{\sigma} \cdot \mathbf{n}, \quad (5.22)$$

and after a straightforward calculation using $\mathbf{u}^{t,e} \times \mathbf{n} = \mathbf{0}$, the elastic part of displacement is

$$\mathbf{u}^{t,e} = \frac{1}{\rho_c r} \frac{1}{K^t} (\boldsymbol{\sigma} \cdot \mathbf{n} - (\mathbf{n} \cdot \boldsymbol{\sigma} \cdot \mathbf{n}) \mathbf{n}). \quad (5.23)$$

Employing Equation (5.6), this yields expressions for the contact forces in the form

$$\mathbf{t}^n = \frac{1}{\rho_c r} (\mathbf{n} \cdot \boldsymbol{\sigma} \cdot \mathbf{n}) \mathbf{n}, \quad \mathbf{t}^t = \frac{1}{\rho_c r} (\boldsymbol{\sigma} \cdot \mathbf{n} - (\mathbf{n} \cdot \boldsymbol{\sigma} \cdot \mathbf{n}) \mathbf{n}). \quad (5.24)$$

Here, $\sigma^n = (\mathbf{n} \cdot \boldsymbol{\sigma} \cdot \mathbf{n})$ is interpreted as the normal component of the stress vector regarding the cutting plane with a normal basis of \mathbf{n} , and $\sigma^t = \boldsymbol{\sigma} \cdot \mathbf{n} - (\mathbf{n} \cdot \boldsymbol{\sigma} \cdot \mathbf{n})\mathbf{n}$ as its tangential component. Therefore, Equation (5.24) can be simplified as

$$\mathbf{t}^n = \frac{1}{\rho_c r} \boldsymbol{\sigma}^n \quad \mathbf{t}^t = \frac{1}{\rho_c r} \boldsymbol{\sigma}^t \quad (5.25)$$

If the tensile force \mathbf{t}^n acting at the contact is interpreted as the strength of the contact bond in the normal direction, it can be replaced by $f^{n,c}$. The same applies to the tangential direction. Finally, Equation (5.25) gives a failure criterion in which the bond's break occurs either in the normal direction or in the tangential direction.

The failure stress of contact connections in the normal direction can be obtained as Rankine stress $\sigma_y^{\text{Rankine}}$, and in the tangential direction as Tresca stress σ_y^{Tresca} . These relations are reformed after the bond strengths

$$\sigma_y^{\text{Rankine}} = \rho_c r f^{n,c} \quad \text{and} \quad \sigma_y^{\text{Tresca}} = \rho_c r f^{t,c} \quad (5.26)$$

where with the known failure stresses, the above equation results in the bond strengths in the normal and tangential direction.

5.3 Compression Test

In order to verify the macroscopic material constants obtained from the microscopic contact parameters through analytical relations derived in Section 5.2, a series of confined and unconfined compression tests are conducted. Thus, the elastic constants E and ν determined analytically according to Equation (5.20) can be compared with those resulting from the evaluation of the numerical compression test. The tests are performed using the discrete element method via the PFC^{3D} code.

5.3.1 Setup of Three-dimensional Test

A cylindrical material vessel with a height of $h_v = 63.4$ mm and a radius of $r_v = 15.85$ mm is created with wall elements. The wall elements are made frictionless and their normal stiffnesses are set to be a bit larger than the normal stiffness of an average particle to ensure that the ball-wall overlaps remain small. The top and bottom walls are used as loading platens, and the velocity of sidewalls is controlled by a servomechanism to produce a constant confining stress. For fully unconfined tests, the side walls are removed. Spherical particles are created at half their final size and are placed randomly into the vessel. The particle radii are then increased in three steps until the porosity of the specimen reaches 35% and the system is allowed to settle down under zero friction. The final radius of the particles is between R_{\min} and R_{\max} and satisfies the normal particle size distribution.

To reduce the magnitude of locked-in stresses and to create a dense, isotropic, and well-connected system, the specified isotropic stress is obtained as the average of the direct stresses. In our models for granular and rock material, σ_0 is set equal to approximately 1%

of the uniaxial compressive stress. The microscopic material parameters are then assigned to the particles.

In the next step, for the bonded material model, parallel bonds are installed between the particles in the assembly that are in the near neighborhood and the corresponding properties are assigned.

To perform an unconfined compression test, the specimen is removed from the material vessel by deleting the confining walls, and the assembly is allowed to relax and achieve static equilibrium.

The actual test starts by applying the confining and axial stresses. Loading is performed by moving the platens towards each other at a final velocity of v_p , calculated by a given strain rate $\dot{\varepsilon}_p$, and setting $v_p = \frac{1}{2} \dot{\varepsilon}_p L_0$, where L_0 is the initial length of the specimen. Note that for quasi-static loading, the chosen value of $\dot{\varepsilon}_p$ is strongly dependent on L_0 .

The test continues until a specific test termination criterion is reached. For a bonded material, the deviatoric stress $\sigma_d = \sigma_1 - \sigma_c$ is increased continuously to a maximum value. When the material fails, the deviatoric stress is decreased and the test is terminated once the σ_d meets the condition $|\sigma_d| < \alpha |\sigma_d|_{\max}$. For an unbonded material, a strain-controlled test is performed. Therefore, tests are terminated when the applied axial strain reaches a specific value, i.e., $\varepsilon_a < \alpha$.

From the compression test, the following macroscopic elastic material constants are extracted:

1. Young's modulus (E) and Poisson's ratio (ν) can be derived as

$$E = \frac{\sigma_a}{\varepsilon_a} \quad (5.27)$$

and

$$\nu = -\frac{\Delta\varepsilon_x}{\Delta\varepsilon_a} = 1 - \frac{\Delta\varepsilon_v}{\Delta\varepsilon_a} \quad (5.28)$$

where σ_a and ε_a are the axial stress and strain, respectively, ε_x is the strain in the perpendicular direction, and $\Delta\varepsilon_v = \Delta\varepsilon_x + \Delta\varepsilon_a$ is the volumetric strain.

2. The peak strength (σ_f) is the maximum value of the axial stress existing at peak load.
3. For the bonded particle model, the crack initiation stress (σ_{ci}) corresponds to the point during the test at which a specified fraction (0.01) of the total number of cracks at peak load have been formed.

These values are taken from the numerical calculation by applying three different procedures:

- (i) Wall-based:

Forces and displacements of the wall elements are monitored and lead to the required stress and strain calculations.

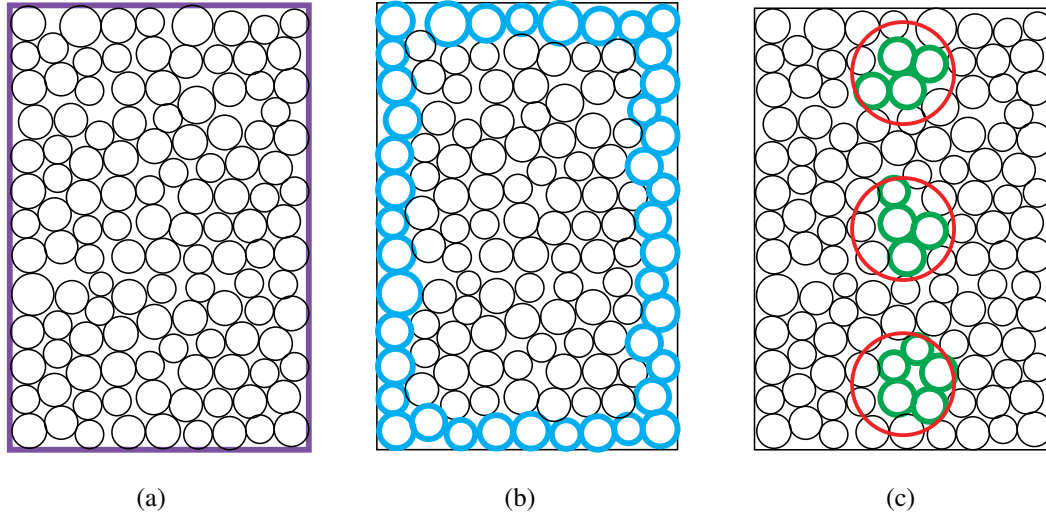


Figure 5.2: Three measurement schemes: (a) wall-based (b) specimen-based (c) measurement-sphere-based

(ii) Specimen-based:

The outer dimension (ball elements) of the specimen are monitored and used to calculate stresses and strains.

(iii) Measurement-sphere-based:

Three measurement spheres are installed in the specimen. They are located in the upper, middle, and lower part of the specimen. Forces and displacements from these spheres are averaged.

Figure 5.2 illustrate the three different ways for measuring forces and displacements in compression test.

Here, K^n , K^t , and r are averaged values, taken directly from the simulation, and ρ_c is calculated according to

$$\rho_c = \frac{n_c}{V}, \quad (5.29)$$

where n_c is the number of contact points and V is the volume of the specimen.

5.3.2 Calibration Procedure

Macroscopic Properties of Material

Sand and gravel are two types of typical granular materials and are classified as cohesionless soil. Here, *Chende sand* is used as an example for the calibration procedure of granular material. The laboratory-scale properties that typically characterize sand are Young's modulus (E), Poisson's ratio (ν), unconfined compressive strength (σ_f), and strength envelope (consist of peak strength and corresponding confining pressure P_c). When real granular material is simulated, the microscopic parameters have to be adjusted to match the realistic macroscopic behavior.

Table 5.1: Mechanical macro-properties of materials

Lac du Bonnet granite		Chende sand	
E (GPa)	69	E (MPa)	87
ν	0.26	ν	0.32
σ_f (MPa)	200	σ_f (kPa)	1150
σ_{ci} (MPa)	90		
ϕ (deg)	59	ϕ (deg)	32
c (MPa)	30		
ρ (kg/m ³)	2630	ρ (kg/m ³)	2630

Rock behaves like a cemented granular material and is modeled by a bonded particle assembly in PFC. In this study, *Lac du Bonnet granite* is assumed to be the intended physical material. In addition to the above-mentioned macro-properties, the crack initiation stress (σ_{ci}) should also be considered for characterizing solid materials. The observed laboratory properties are obtained from a 63 mm diameter specimen with a length-to-diameter ratio of 2.5. The macromechanical properties of Chende sand and Lac du Bonnet granite are given in Table 5.1. The micro-properties should be chosen so that they match the macro-properties given in this table.

Microscopic Properties

For programs that simulate continuum media, the input parameters such as modulus and strength are calculated directly from the results of laboratory tests. However, for codes such as PFC, which simulates the macro scale material behavior from the interaction of microscale material components, it is difficult to find the input properties directly. In this case, the appropriate micro-parameters can be chosen using a calibration procedure, by first determining the behavior of the intended physical material and then comparing the response of the synthetic material with the relevant measured response of the physical material. In the following, first the calibration procedure for solid material and then the procedure for granular material are discussed.

a. Solid material

Rock is modeled as a synthetic material consisting of non-uniformly sized grains (spherical particles and/or clumps) and cement (parallel bonds). The eight micro-properties with a short-term response required to characterize a parallel-bonded material, are as follows:

$$\left\{ E_c, \frac{k_n}{k_s}, \mu \right\}$$

$$\left\{ \bar{\lambda}, \bar{E}_c, \frac{\bar{k}_n}{\bar{k}_s}, \bar{\sigma}_c, \bar{\tau}_c \right\} \quad (5.30)$$

where E_c and \bar{E}_c are the Young's modulus of particles and bonds, respectively; k_n/k_s and \bar{k}_n/\bar{k}_s are the normal to shear stiffness ratios of particles and bonds, respectively; μ is the particle friction coefficient; $\bar{\lambda}$ is a radius multiplier used to set parallel bond radii; $\bar{\sigma}_c$ and

$\bar{\tau}_c$ are the normal and shear strength, respectively, of cement-like material represented by parallel bonds.

The R_{\max}/R_{\min} ratio should be set to be greater than 1, in order to avoid uniform packing, which tends to produce anisotropic macro-properties. The following calibration sequence should be used to match elastic properties, peak strength, and crack initiation with minimum iterations. The elastic parameters are controlled by five micro-properties, E_c , \bar{E}_c , $\bar{\lambda}$, k_n/k_s , and \bar{k}_n/\bar{k}_s . Here, $\bar{\lambda}$ is set equal to 1 to produce cemented-based materials with complete filling of the throat between bonded particles. As $\bar{\lambda} \rightarrow 0$, the bonded material approaches granular material.

First, to reproduce a given Young's modulus, the model should be forced to behave elastically with no bond failure by setting the material strength to a large value and then varying E_c and \bar{E}_c . In this study, the difference between E_c , \bar{E}_c is kept constant to reduce the number of unknowns, i.e., Young's modulus of the bond is always set to be 100 GPa larger than the Young's modulus of the particle. Poisson's ratio of the investigated material is affected by k_n/k_s and \bar{k}_n/\bar{k}_s for bonded materials. Again, to reduce the number of free parameters, both ratios of normal to shear stiffness for particles and bonds are set equal. Young's modulus of the material has a linear relation with the micro elastic modulus. In addition, as the ratio of normal to shear stiffness increases, Poisson's ratio increases. Both values will be calibrated by performing a few iterations.

Next, the unconfined compressive strength is matched by varying the mean material strengths for a fixed ratio of standard deviation to mean strength at zero confining pressure condition. The normal and shear strengths of the bond are set equal to one another, otherwise, it will affect the failure mode by controlling the relative number of shear and tensile failure events. For a fixed ratio of standard deviation to mean material strength and a fixed ratio of normal to shear material strength, the peak strength is linearly related to the mean material normal strength. The intended compressive strength of the specimen will be reached after a small number of tests.

The last investigated parameter is the crack initiation stress, which will be matched by varying the ratio of standard deviation to mean material strength. Increasing this ratio lowers the stress at which the first crack initiates. Since this may also change the peak strength, a few iterations may be needed to match both values.

The particle friction coefficient can be used to reproduce post-peak behavior. After calibrating the macro-properties, the Mohr circle can be obtained by performing a set of triaxial tests with different confining pressures. The test results for Lac du Bonnet granite are shown in Figure 5.3, which includes Mohr circles at confining pressures of 0.1, 1, 10, and 20 MPa and the failure envelope. The cohesion of 55 MPa and a peak friction angle of 33° are obtained from the Mohr circles for this specimen.

b. Granular material

A granular material is an assembly of particles that move independently of one another and interact only at contact points. The Young's modulus, Poisson's ratio, peak friction angle, and peak compressive strength are mechanical properties that characterize granular materials. The four micro-properties with a short-term response required to

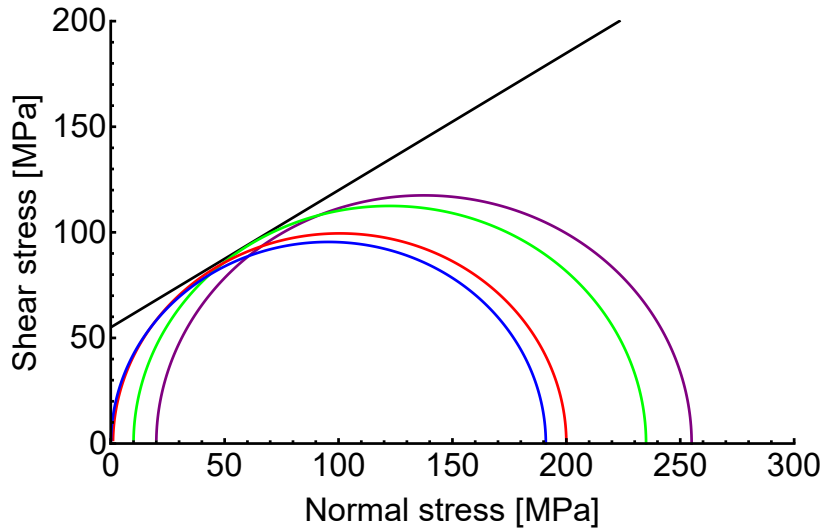


Figure 5.3: Mohr circle for Lac du Bonnet granite

characterize a granular material, are as follows:

$$\{n, E_c, k_n/k_s, \mu\} \quad (5.31)$$

where n is the material porosity, E_c is Young's modulus of the particle, k_n/k_s is the ratio of normal to shear stiffness, and μ is the overall particle friction coefficient. The calibration procedure for an unbonded material is mainly a subset of that for a bonded material and is performed step-by-step at a confining pressure of 300 kPa to minimize the number of iterations. The elastic modulus is controlled by two micro-parameters E_c and k_n/k_s , and the strength is controlled by μ . The response of the granular material is affected by the initial material porosity n . First, for fixed values of porosity, stiffness ratio, and particle friction coefficient, Young's modulus will be calibrated by varying E_c . The relation between peak secant modulus and E_c is typically nonlinear. Poisson's ratio depends on the stiffness ratio and very little on other parameters. As the stiffness ratio increases, Poisson's ratio also increases.

The peak strength is controlled by a single micro-parameter μ . Once the elastic responses have been calibrated, the peak strength at given confinement can be reproduced. It will vary as a function of confinement and will increase with the increasing value of μ until it reaches an upper limit, which is a function of grain shape and particle distribution size. Then, based on the calibrated DEM model, the triaxial tests will be performed under lateral confining stresses of 100, 300, 500, and 700 kPa. Figure 5.4 shows the Mohr circle at the stage of peak stress for Chende sand and the mean friction angle stands by 39° .

5.4 Results

In this section, first, a series of triaxial compression tests are performed in Subsection 5.4.1 with calibrated parameters and variable particle radii to validate the predicted macroscopic elastic parameters derived from the analytical relations in Section 5.2. Then, the influence of complex particle shape on the material strength and behavior are presented in Subsection 5.4.2.

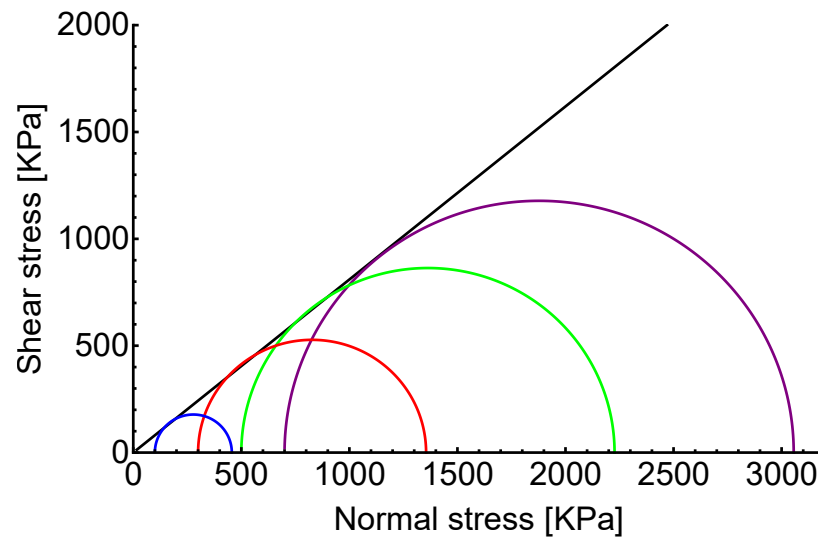


Figure 5.4: Mohr circle for Chende sand

5.4.1 Validation of Analytical Relations

Elastic properties

The tests are carried out with five different discretizations, whose average particle radius is in the range of 0.76 mm to 2.86 mm. The test properties are listed in Table 5.2. To have more accurate results for each case, five different specimens are created by varying the random number generator during the material genesis procedure. The final results are an average of all the specimen results.

Table 5.2: Particle discretization for investigation of elastic properties

Test number	1	2	3	4	5
Mean radius [mm]	0.76	1.0	1.49	2.18	2.86
Number of particles	16115	6860	2089	644	277

Figures 5.6 and 5.7 show the results of Young's modulus and Poisson's ratio for solid and granular materials, respectively. These results are always related to the legend in Figure 5.5. As the test number increases, the particle radius increases, and thus the number of particles in the assembly decreases. PI marks the predicted values of Young's modulus and Poisson's ratio according to Equation (5.20). Figure 5.6(a) shows the results of Young's modulus for the solid material. The predicted Young's modulus decreases with an increase in test number, which is due to the use of higher contact stiffness values. In all cases, the specimen-based and wall-based outputs are almost the same and very close to predicted values, whereas the measurement-based results overestimate it. For a larger number of particles, the scatter between results becomes smaller, i.e., wall-based, specimen-based, and predicted results become almost identical, and measurement-based goes closer.

These tests are also used to verify Poisson's ratio. The corresponding results are presented in Figure 5.6(b). For all different numbers of particles, the ratio of normal to tangential contact stiffnesses is kept constant, which leads to a constant value for the predicted Poisson's ratio, according to Equation (5.20).

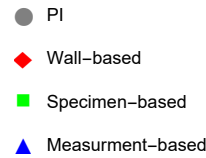


Figure 5.5: Legend representing the different measurement schemes corresponding to Figures 5.6 and 5.7

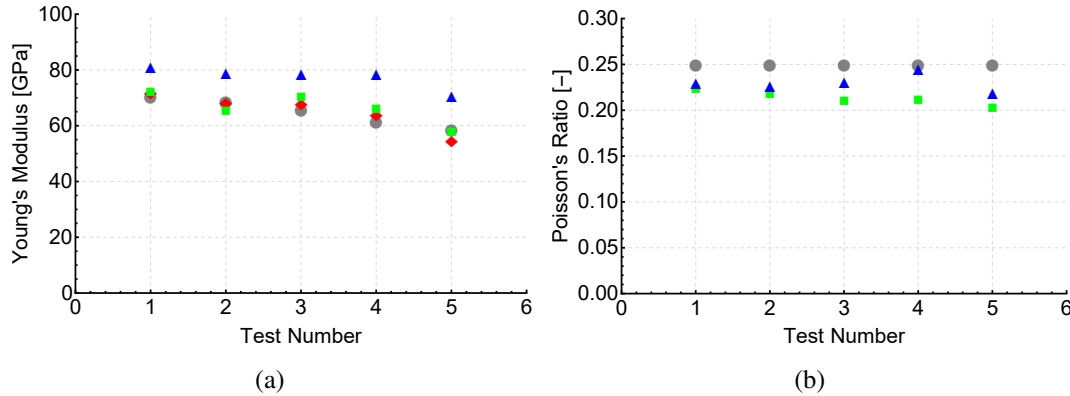


Figure 5.6: Comparison between three-dimensional compression test results and predicted analytical values (a) Young's modulus and (b) Poisson's ratio for solid material

The same investigations have been performed for granular material and the results are presented in Figure 5.7. Similar to the solid material, the wall-based and specimen-based Young's modulus are almost identical, whereas in this case, the measurement-sphere-based outputs correspond better to the analytically predicted values. This can be explained by the location of measurement spheres - one each located in the upper, lower, and the middle of the specimen - so that the boundary areas are overrepresented. Therefore, for estimation of the Young's modulus of the granular materials the measurement-sphere-based results are in a very good agreement with analytical results compared to the results of two other schemes, namely wall-based and specimen-based. Furthermore, for this compression test, it is obvious that we must observe a minimum number of particles to obtain reliable results. If the number of particles is not sufficient, the contact forces will not be distributed very well and may be higher in the middle of the specimen, far from the boundaries. Therefore, if the average is taken from the three measurement spheres, the forces are overestimated, which results in overestimation of the Young's modulus. The results in Figures 5.6 and 5.7 show that a minimum number of 2089 particles (Test 3) produces convincing results. From these calculations, it can be concluded that the accuracy of the predictions for both Young's modulus and Poisson's ratio according to Equation (5.20) are very good and acceptable.

Bond strength

Here, the failure stress, which is required to calculate the bond strength in normal and tangential directions, according to Equation (5.26), is investigated. For this reason, three different tests are carried out with fixed particle radius, in which only the strengths of the bonds are varied. In test 1, the bond strengths in normal and tangential directions are set to be equal, so the following applies: $f^{n,c} = f^{t,c}$. In Test 2, the focus is on the bonds in the normal

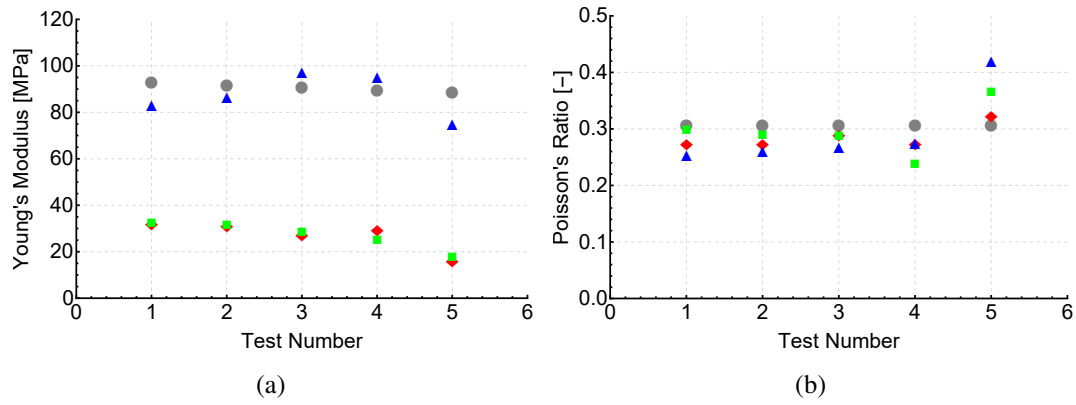


Figure 5.7: Comparison between three-dimensional compression test results and predicted analytical values: (a) Young's modulus and (b) Poisson's ratio for granular material

direction so that the failure hypothesis according to Rankine can be verified, see Equation (5.26). Here $f^{n,c} = 100f^{t,c}$. Test 3 is used to compare the failure hypothesis according to Tresca, so here the tangential bonds are significantly strengthened, $100f^{n,c} = f^{t,c}$ applies. For clarity, these test cases are summarized in Table 5.3.

Table 5.3: Test properties for investigation of bond strength

Test 1	$f^{n,c} = f^{t,c}$
Test 2	$f^{n,c} = 100 \cdot f^{t,c}$
Test 3	$100 \cdot f^{n,c} = f^{t,c}$

The results for the failure stress are summarized in Figure 5.8, which are based on the different measurement methods for stresses and strains, i.e., wall-based, specimen-based and measurement-sphere-based, as well as the Tresca and Rankine failure limits. In Test 1 with equal normal and tangential bond strengths, the two failure stresses determined according to Equation (5.26) are identical. They easily overestimate the values obtained from the simulation.

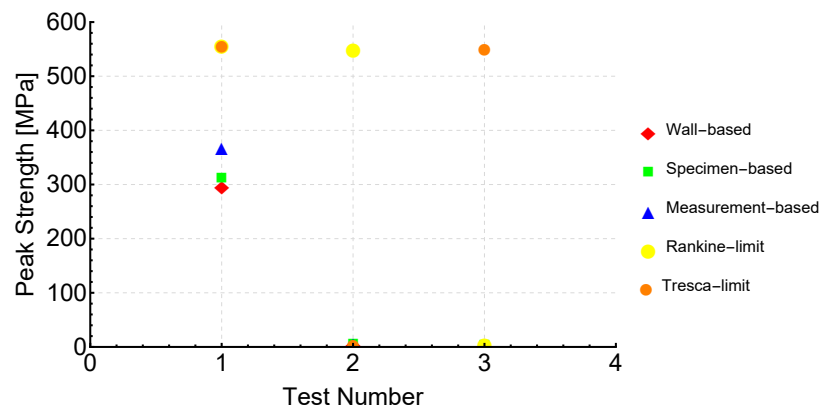


Figure 5.8: Yield strengths resulting from the triaxial tests compared with the values according to the parameter identification for three test cases according to Table 5.3

The simulation results for Test 2 correspond very well with the failure stress according to Tresca σ_y^{Tresca} . Since the normal bonds in Test 2 are selected to be significantly stronger

than the tangential bonds, here the tangential bonds are the ones that trigger the failure. The failure after Tresca is therefore expected here and confirmed by the results. With the same logic, in Test 3 there is a correspondence between the simulation results and the failure stress according to Rankine.

In general, there is a very good agreement between the predicted values of the parameter identification and the values resulting from the DEM simulation. The deviations occurring by a maximum factor of 2 may appear large at first glance. However, if one considers how strongly the three differently determined simulation results already vary, it becomes clear that such a deviation is hardly significant. Equation (5.26) is therefore suitable for predicting failure stresses or for deriving the corresponding bond strengths from known failure stresses.

5.4.2 Influence of Complex Particle Shape

To study the effects of bonding and grain shape, a set of tests using complex shaped materials is also provided. Therefore, first, a homogeneous assembly with all spherical grains, and second a mixture of spherical and clumped grains, are created. The base material has a minimum radius of 0.8 mm and a ball-size ratio (R_{\max}/R_{\min}) of 1.66. The micro-properties assigned to the grains and bonds are listed in Table 5.4. The clumped-grain material consists of 50% peanuts (3-particle clumps), 25% dyads (2-particle clumps), and 25% spheres. The clump logic is presented in Section 4.1.2 in detail. Solid (bonded) and granular (non-bonded) materials are produced for each grain system giving a total of four models. All materials are tested under two confined compression conditions, i.e., at 1 and 10 MPa confinement. The grain shapes are illustrated in Figure 5.9.

Table 5.4: PFC short-term micro-properties for grains and bonds

Grains	Bonds
$R_{\min} = 0.8 \text{ mm}$	$\bar{\lambda} = 1$
$R_{\max}/R_{\min} = 1.66$	
$E_c = 70 \text{ GPa}$	$\bar{E}_c = 70 \text{ GPa}$
$k_n/k_s = 2.5$	$\bar{k}_n/\bar{k}_s = 2.5$
$\mu = 0.5$	$\bar{\sigma}_c = \bar{\sigma}_t = (\text{mean} \pm \text{std.dev.})$ $170 \pm 35 \text{ MPa}$
$\rho = 2630 \text{ Kg/m}^3$	

For granular material, the confined compression tests are performed by loading the specimen until the axial strain of 1%. According to Figure 5.10, the stress-strain curves increase rapidly and then continue with a nearly steady-state plateau, which here is denoted as the strength of the material. By comparing the curves in this figure for the spherical and mixed-shape materials at 1 and 10 MPa confinements, two important facts could be concluded:

1. The mixed-shape material is stronger than the homogeneous spherical material (e.g.,

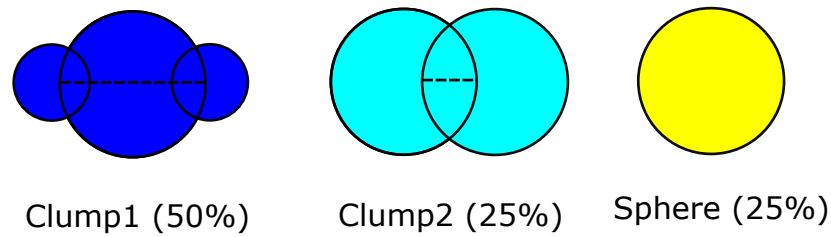


Figure 5.9: Cluster grain shapes

at 1 MPa confinement, the strength of the mixed-shape material is ~ 4.1 MPa, while that of the spherical material is ~ 2.5 MPa);

2. The peak strength increases with confinement (e.g., for the mixed-shape grains, the strength at 1 MPa confinement is ~ 4.1 MPa, while at 10 MPa confinement it is ~ 41 MPa).

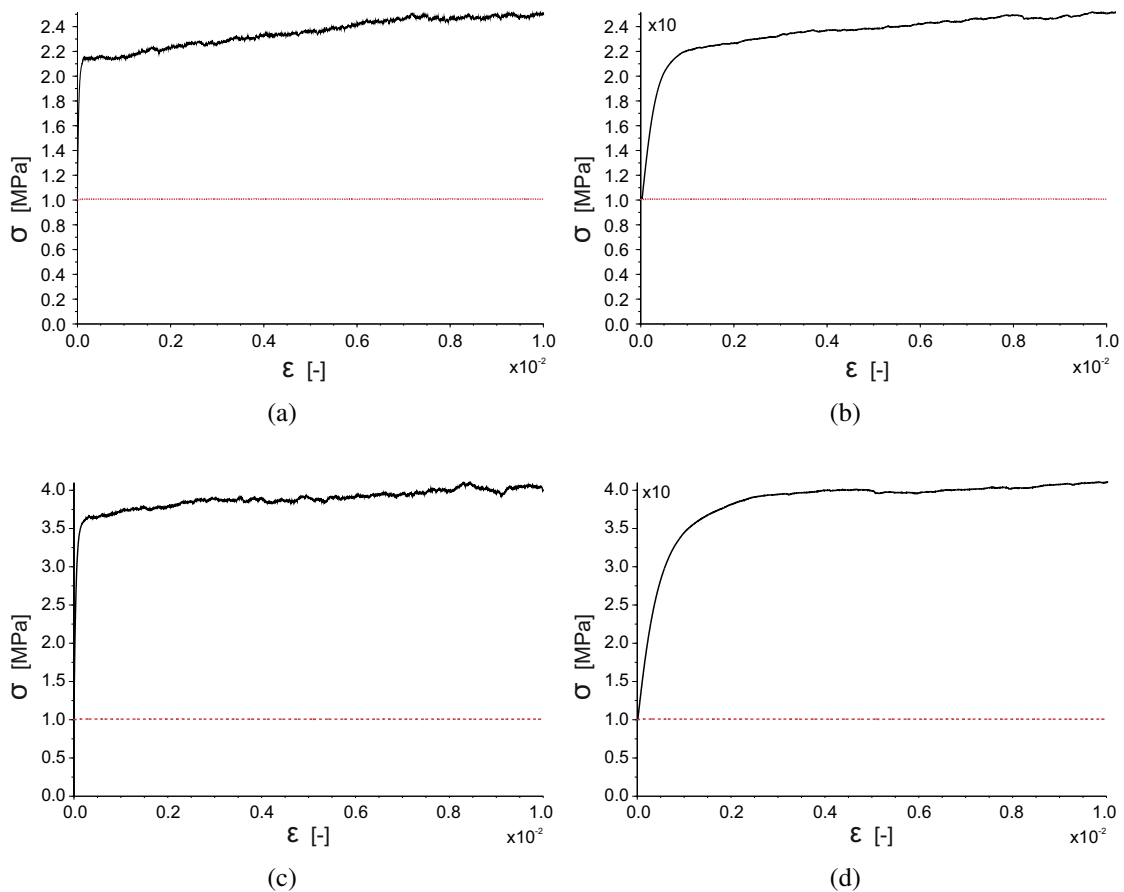


Figure 5.10: Axial and confining stresses versus axial strain for granular material with homogeneous spherical grains (top) at (a) 1 MPa confinement and (b) 10 MPa confinement and with mixed-shape grains (bottom) at (c) 1 MPa confinement and (d) 10 MPa confinement

The same tests are also performed on the bonded material. In this case, the resulted stress-strain curves are nearly linear until peak (denoted here as the strength), and then experience a stress drop (as shown in curves of Figure 5.11). By comparing the curves for the spherical and mixed-shape grains at 1 and 10 MPa confinement, again we conclude two important results:

1. The mixed-shape material is stronger (e.g., at 1 MPa confinement, compare Figure 5.11(c) where the strength of the mixed-shape material is ~ 205 MPa, with Figure 5.11(a) for spherical material where the strength is ~ 194 MPa);
2. The peak strength increases with confinement (e.g., for the mixed-shape grains, the strength at 1 MPa confinement is ~ 205 MPa, while at 10 MPa confinement it is ~ 230 MPa).

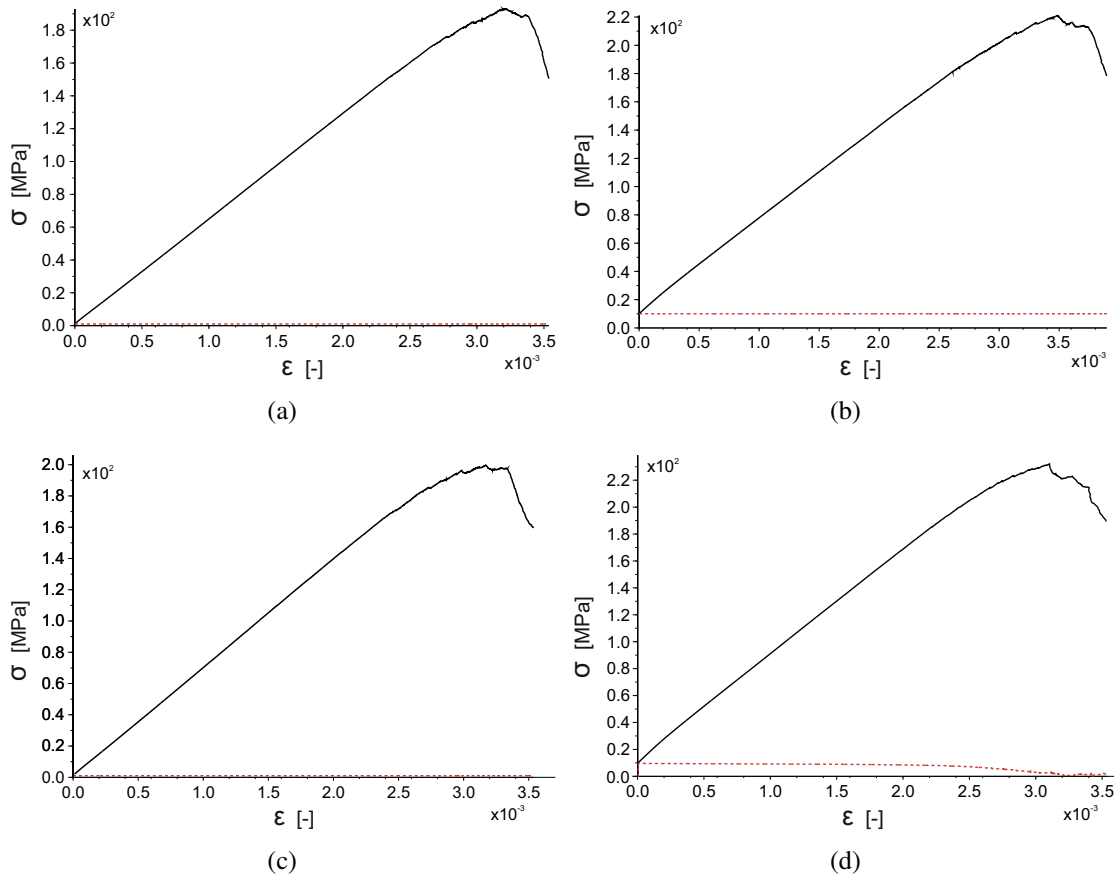


Figure 5.11: Axial and confining stresses versus axial strain for bonded material with homogeneous spherical grains (top) at (a) 1 MPa confinement and (b) 10 MPa confinement and with mixed-shape grains (bottom) at (c) 1 MPa confinement and (d) 10 MPa confinement

Both of these behaviors are expected for granular materials as well as bonded materials. The presence of non-spherical grains has increased the material strength.

5.4.3 Summary of Results

In this chapter, an approach to DEM parameter identification based on energy minimization has been presented in Section 5.2. By defining contact energy and relating that to the energy of the entire assembly, equations are derived for the elastic parameters. The relations depend on the contact parameters, the mean particle radius, and the number of contacts per unit sector, which includes information regarding the packing density. They relate the macroscopic

material properties to the microscopic contact parameters and are introduced in Equation (5.20) for granular materials and Equation (5.26) for bonded materials.

A numerical compression test has been simulated in PFC^{3D} software in Section 5.3 to verify the analytical relations developed for predicting elastic parameters. A calibration procedure for rock and cohesionless soil is recommended in Subsection 5.3.2 and first applied to the simulation of Lac du Bonnet granite and Chende sand using a series of compression tests. For both these materials, a set of compression tests with different confining pressures are performed to obtain the Mohr circles, which could model the failure envelope and friction angle with a good agreement.

Comparisons of the results of the numerical compression apparatus and analytical predictions in Subsection 5.4.1 further prove that the parameter identification procedure we proposed can serve as a reliable method to obtain the macroscopic behavior of materials based on the mechanical micro-properties. To be able to estimate the influence of the discretization, all tests are carried out with five different particle sizes. From the simulations, three different values are recorded for each property, depending on how the forces and deformations are measured: Wall-based, specimen-based and measurement-sphere-based. For granular materials, the validity of the parameter identification can be shown both for Young's modulus and Poisson's ratio. For bonded materials, in addition to the two mentioned parameters, the relationship between the failure stress on the macroscopic level and the bond strengths on the contact level, i.e., Equation (5.26) is also verified with a very good agreement.

Finally, a set of compression tests are performed with complex particle ensembles. The results are compared to the homogeneous spherical particle simulations in Subsection 5.4.2, to investigate the influence of particle shapes on the strength of materials. As expected, the mixed shape materials are stronger than the homogeneous materials in both granular and solid cases.

6 Material Models and Regularization Schemes

This chapter corresponds to the constitutive relations for describing the behavior of certain materials subjected to external loads and boundary conditions. Based on the discussion in previous chapters, this work intends to investigate the abrasive behavior and wear resistance of metallic specimens. Therefore, the developed material models must contain the inelastic behavior, i.e., the plastic deformations as well as damage. Thus, Section 6.1 is devoted to inelastic materials. The issue of localization, which is a characteristic of the material models involving softening effects is given in Section 6.2, follows by an overview of different regularization techniques in Section 6.3. Since the focus of our work is on metallic material, the plastic regime is restricted to the hardening behavior and therefore the regularization is performed only on the damage parameter. Finally, two coupled regularized damage-plasticity material models are introduced in Section 6.4, including the principles governing the evolution of internal variables.

6.1 Inelastic Material Response

6.1.1 Plastic Material Model

A schematic plot of the stress-strain behavior for a plastically loaded metallic bar under uniaxial tension is presented in Figure 6.1, where the axial stress σ is plotted against the axial strain ϵ . The linear elasticity is one of the most commonly used theories for designing engineering structures, where the material is loaded within a typically small range of stresses, such that after removal of the external loads the material will partially return to its original state without the evolution of permanent (plastic) strains. Although the elasticity is satisfactory for most engineering materials early on, many materials loaded to sufficiently high stress, and beyond the so-called yield stress σ_y exhibit permanent deformation, i.e., evolution of plastic strains take place. This process is described by the plasticity theory. Accordingly, exceeding the critical threshold will cause deformation, which will not return to its original state when the external loading conditions are removed. Accompanying the evolution of the plastic strain, an evolution of the yield stress itself can also be observed. This phenomenon is known as hardening.

Plastic strains come from microscale level, e.g, for ductile materials such as metals, they can be explained in terms of the theory of dislocations and nucleation resulting slip on specific crystallographic planes as independently introduced by Orowan (1934) and Taylor (1934). Although the movement of dislocations occurs with all loading, this movement is insignificant until the yield point occurs. At this point, loading causes dislocations to be generated, moved, and stored. The ease with which dislocations can move determines the hardness of the material. The above-mentioned properties can be observed not only in metals but also in a wide variety of materials. For instance, in materials such as concrete and

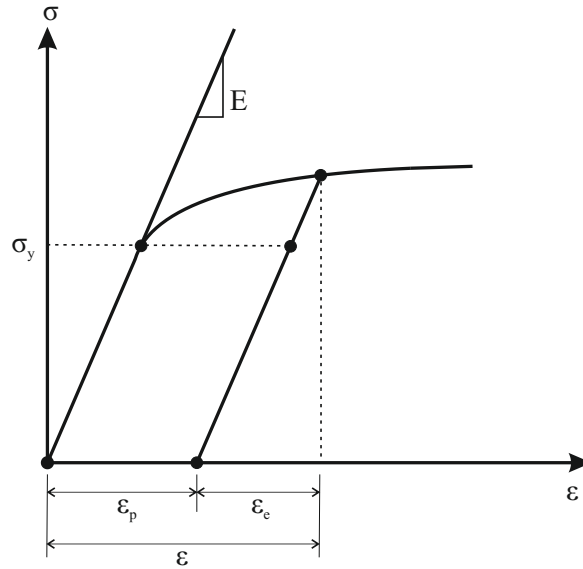


Figure 6.1: Stress-strain curve for a plastically loaded material. Image inspired by de Souza Neto et al. (2011)

rocks or soils, permanent strains are occurred due to opening and closing of cracks, sliding of grains over one another, and pore collapse at high confinement.

The different mentioned micromechanisms result in varying macroscopic behavior for materials under plastic loading. The plastic deformations in metals run almost with conservation of volume and finish in an increase in the strength (hardening behavior) of the material. On the other hand, due to the reorientation of the particle structures in the soil-like materials and concrete, the plastic deformation is connected to the volume change and results in a decrease in the strength (softening behavior). For a more comprehensive treatment of the theory of plasticity, the reader is referred to Hill (1998), Jirásek and Bazant (2001), Lubliner (2008), and de Souza Neto et al. (2011).

By considering small strain case, $\boldsymbol{\varepsilon}$ stands for linearized strain tensor, derived from the displacements \boldsymbol{u} by $\boldsymbol{\varepsilon} = \frac{1}{2}(\nabla\boldsymbol{u} + \boldsymbol{u}\nabla)$ and is decomposed into a recoverable elastic strain ($\boldsymbol{\varepsilon}_e$), and an irreversible plastic strain ($\boldsymbol{\varepsilon}_p$)

$$\boldsymbol{\varepsilon} = \boldsymbol{\varepsilon}_e + \boldsymbol{\varepsilon}_p \quad (6.1)$$

The Helmholtz free energy function accounting for elastic and plastic deformations, which develops both reversible and irreversible deformations, is defined in the form

$$\Psi(\boldsymbol{\varepsilon}, \boldsymbol{\varepsilon}_p, \alpha_p) = \frac{1}{2}(\boldsymbol{\varepsilon} - \boldsymbol{\varepsilon}_p) : \mathbb{E} : (\boldsymbol{\varepsilon} - \boldsymbol{\varepsilon}_p) + w(\alpha_p) \quad (6.2)$$

The internal variables are the plastic strains ($\boldsymbol{\varepsilon}_p$), which are assumed to be a deviatoric quantity, e.g., $\boldsymbol{\varepsilon}_p : \boldsymbol{I} = 0$, and the plastic hardening variable α_p . The plastic potential $w(\alpha_p)$ defines the hardening behavior and it is considered as a function of history dependent variable α_p .

Various plasticity models have been used throughout the literature to define the yield surface, like the models of Tresca (1869), Rankine (1872), Mohr (1900), Mises (1913), and Drucker and Prager (1952). Besides, several plasticity theories are defined to consider the change in size, shape, and position of the yield surface, such as the isotropic hardening (Hill

(1998)), which corresponds to the changes in the size of the yield surface and the kinematic hardening (Prager (1956)), which corresponds to the changes in the location of the yield surface. In this thesis, the consideration is restricted to the linear isotropic hardening with the relation $w(\alpha_p) = \frac{1}{2}K_H\alpha_p^2$, where the parameter K_H defines the rate of hardening.

In the view of Equation (6.2), the constitutive relation for the stress tensor $\boldsymbol{\sigma}$ is introduced by

$$\boldsymbol{\sigma} = \frac{\partial \Psi}{\partial \boldsymbol{\varepsilon}} = \mathbb{E} : (\boldsymbol{\varepsilon} - \boldsymbol{\varepsilon}_p). \quad (6.3)$$

and based on the introduced internal variables, the corresponding thermodynamic conjugates involved in the formulation become

$$\boldsymbol{\sigma}_p = \frac{\partial \Psi}{\partial \boldsymbol{\varepsilon}_p} = \text{dev} \mathbb{E} : (\boldsymbol{\varepsilon} - \boldsymbol{\varepsilon}_p). \quad (6.4)$$

and

$$p_p = -\frac{\partial \Psi}{\partial \alpha_p} = -w'(\alpha_p) \quad (6.5)$$

In the present study for classical rate-independent plasticity, the dissipation function is a homogeneous function of order one and reads

$$\mathcal{D}_p = r_p |\dot{\boldsymbol{\varepsilon}}_p| \quad (6.6)$$

with r_p being the dissipation parameter related to plasticity. In addition to the energies, the usual constraints for plasticity have to be specified. Thus,

$$\boldsymbol{\varepsilon}_p : \mathbf{I} = 0 \quad \text{and} \quad \dot{\alpha}_p = |\dot{\boldsymbol{\varepsilon}}_p| \quad (6.7)$$

which motivate to define

$$c_1 := \dot{\boldsymbol{\varepsilon}}_p : \mathbf{I} = 0 \quad \text{and} \quad c_2 := \dot{\alpha}_p - |\dot{\boldsymbol{\varepsilon}}_p| = 0. \quad (6.8)$$

The plasticity model in this thesis uses the von Mises yield criteria (as in Mises (1913)) with isotropic linear hardening, where the model quantities are summarized in Table 6.1. The material parameter r_p represents the plastic yield limit and K_H defines the rate of hardening.

6.1.2 Damage Material Model

Damage can be characterized as the presence and evolution of microscopic defects (micro-cracks, voids, cavities, etc) which lead to macroscopic damage and failure (complete loss of load-carrying capacity) of the material at the end. The characteristic behavior of damage and the scale at which it occurs depend upon the specific type of material considered. The damage evolution results from the nucleation process of microscopic cracks and voids, growth, and coalescence leading to macroscopic damage at the end. This mechanism is schematically presented in Figure 6.2.

Plasticity material model
<ul style="list-style-type: none"> Yield function Φ_p and plastic potential $w(\alpha_p)$: $\Phi_p := \text{dev}\boldsymbol{\sigma} - (r_p - K_H\alpha_p) \leq 0, \quad w(\alpha_p) = \frac{1}{2}K_H\alpha_p^2$ Stress tensor $\boldsymbol{\sigma}$ and the thermodynamic conjugates $\boldsymbol{\sigma}_p$ and p_p: $\boldsymbol{\sigma} = \mathbb{E} : (\boldsymbol{\varepsilon} - \boldsymbol{\varepsilon}_p)$ $\boldsymbol{\sigma}_p = \text{dev}\mathbb{E} : (\boldsymbol{\varepsilon} - \boldsymbol{\varepsilon}_p), \quad p_p = -K_H\alpha_p$

Table 6.1: Summary of the plastic material model

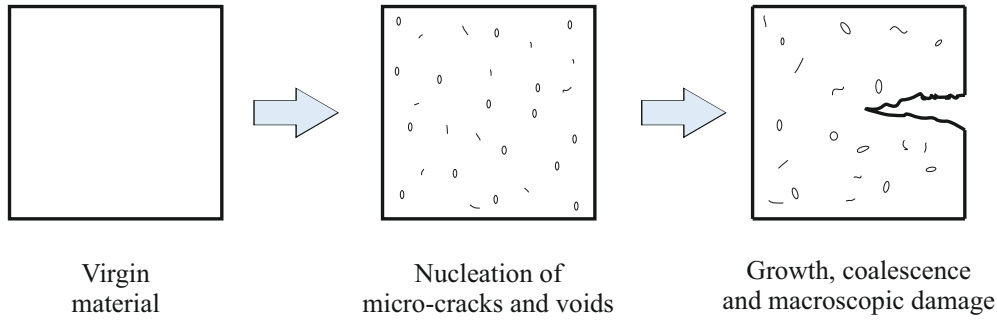


Figure 6.2: Schematic illustration of damage evolution in materials. Image inspired by de Souza Neto et al. (2011)

The mechanisms that characterize the mechanical degradation of materials can be divided by their global response during damage into two distinct classes: brittle and ductile damage. Brittle damage occurs mainly in the form of breaking of atomic bonds along specific crystallographic planes in the presence of relatively slight plastic deformations. This behavior arises as a consequence of unstable cracks, which propagate rapidly without an increase in applied stress and usually have a preferred direction nearly perpendicular to the direction of the applied load. Brittle damage can be observed typically in ceramics such as glass and concrete or in metals at low temperatures.

On the other hand, ductile damage is normally associated with extensive plastic deformation ahead of crack. The formation of stable cracks, which resist further extension unless applied force is increased, usually develops slowly in comparison to the brittle case. The global response of ductile material results in the further evolution of local plastic deformation. It causes coalescence of cavities and finally is followed by a smooth drop. This behavior is basically what material models in the present thesis describes, as the focus here is on metallic materials and specifically steel. The ductile and brittle damage and their corresponding stress-strain diagrams are schematically illustrated in Figure 6.3.

Besides, damage can be considered from different scales, starting from rarely studied atomic scale, following by introduced microscopic scale considering the micro-cracks and their propagation, and finally ending up with a macroscopic scale which will be described by continuum damage mechanics and can be related to the previous microscopic scale by techniques of transition, averaging or homogenization. Continuum damage mechanics (CDM) represents and models the effects of distributed micro-cracks and micro-voids and their

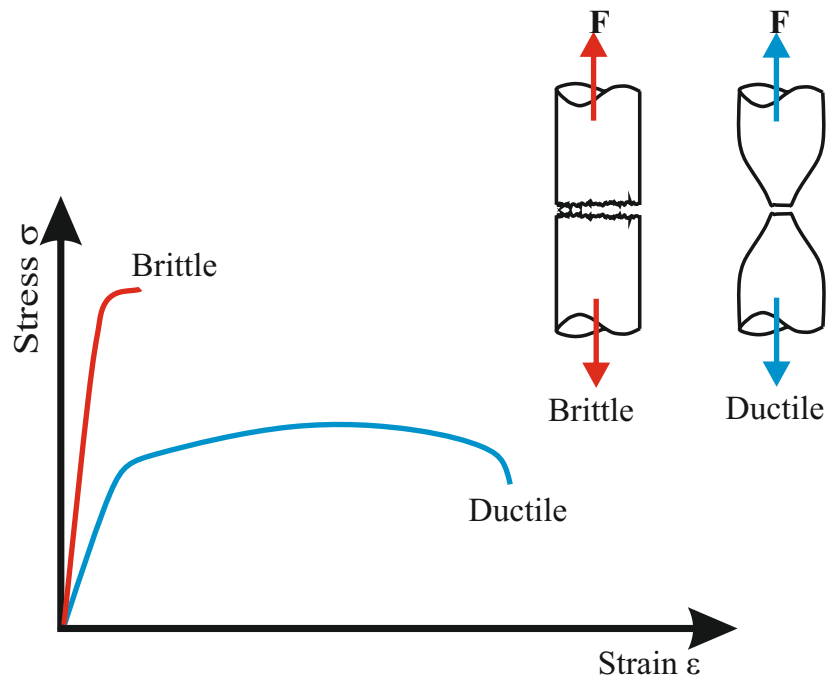


Figure 6.3: Schematic illustration of brittle and ductile damage and their corresponding stress-strain diagrams. Image inspired by Schwarz (2019)

growth on the material behavior at the macro scale by a continuous damage variable. This concept was proposed by Kachanov (1958) without a clear physical meaning for damage, thus CDM is rather a phenomenological approach for damage.

According to the literature, there is a wide range of damage variables, varying from scalars to first-, second- or higher-order tensors. Tensorial damage variables are used for considering anisotropic effects of damage evolution in different directions, as in the works of Chaboche (1981), and Menzel et al. (2005). Meanwhile, in many problems, it is sufficient to consider damage as an isotropic evolution process, wherein these cases, a scalar damage variable will adequately describe the state of damaged material, for instance in the work of Lemaitre (1971). Many theories are developed to show the classical interpretation of scalar damage variables. Among them, the first one was given by Rabotnov (1969), who proposed the reduction of the cross-sectional area due to micro-cracking as a suitable measure for the state of internal damage, i.e., $d = A_d/A$, denoting respectively by A and A_d the areas of the virgin and damaged materials. The second one was proposed by Gurson (1977), known as Gurson's void growth theory, considered the current volume fraction of the voids in the representative volume element as the damage internal variable, i.e., $d = V_p/V$. In both definitions, $d = 0$ corresponds to the virgin material, and $d = 1$ represents a total loss of load-bearing capacity.

The Helmholtz free energy function Ψ of a material accounting for isotropic damage process is modified in the form

$$\Psi(\boldsymbol{\varepsilon}, d) = \frac{1}{2} f(d) \boldsymbol{\varepsilon} : \mathbb{E} : \boldsymbol{\varepsilon} = f(d) \Psi_0 \quad (6.9)$$

with the energy Ψ_0 related to the purely elastic or undamaged material and the scalar variable d determines the deterioration of material stiffness. The damage function $f(d)$ has to be at least twice differentiable in order to ensure damage depending driving forces and also has

to fulfill the condition

$$f(d) : (0, d_\infty) \rightarrow [0, 1) \mid \{f(0) = 1, f(d_\infty) = 0\} \quad (6.10)$$

where $f(d) = 1$ is related to completely undamaged state and $f(d) = 0$ stands for complete material stiffness loss (damaged) state. A typical choice for damage function, satisfying the above mentioned conditions, is

$$f(d) = e^{-d}, \quad (6.11)$$

with an unbounded domain interval for d , i.e., $d \in [0, \infty)$ and its obvious property $f'(d) = -f(d)$. It is used in the work of Dimitrijevic and Hackl (2008) and will be applied in Model I in this work. In addition, a more common damage function is

$$f(d) = (1 - d)^2 \quad (6.12)$$

where in this case, the domain interval is bounded from above, i.e., $d \in [0, 1]$. This damage function is often applied in the literature, for example in the works of Miehe et al. (2010) and Brepols et al. (2017) and will be used for Model II in the present work.

With regard to Equation (6.9), the constitutive equation for stress tensor σ becomes

$$\sigma = \frac{\partial \Psi}{\partial \varepsilon} = f(d) \mathbb{E} : \varepsilon, \quad (6.13)$$

and the thermodynamic conjugate corresponds to internal variable d is

$$p_d = -\frac{\partial \Psi}{\partial d} = -\frac{1}{2} f'(d) \varepsilon : \mathbb{E} : \varepsilon = -f'(d) \Psi_0 \quad (6.14)$$

Similar to the plasticity, the dissipation function for brittle damage is also a homogeneous function of order one and is chosen as

$$\mathcal{D}_d = r_d |\dot{d}| \quad (6.15)$$

with r_d being the dissipation parameter related to damage. The model quantities according to the considerations of this section are summarized in Table 6.2.

6.2 Localization

Degradation of stiffness, strength, and/or other material properties in one way or the other (e.g., due to plasticity or damage), leads to softening behavior which typically occurs in conjunction with strain hardening of the material. The application of such material models is closely related to the localization process, which is characterized by the fact that the predicted deformation shrinks into a narrow zone with a high concentration of strains (Bazant et al. (1984)). The width of the localization zone is small but finite and depends on the material microstructure. Therefore, the width can be considered as a material-specific quantity called ‘‘material length scale’’, determined explicitly using the size of the averaging zone (Jirásek (2002)).

The implementation of conventional local material models involving softening phase in the finite element simulations tends toward an ill-posed boundary value problem after the

Damage material model
<ul style="list-style-type: none"> • Yield function Φ_d: $\Phi_d := p_d - r_d \leq 0,$ • Damage functions $f(d)$: <ul style="list-style-type: none"> – Model I: $f(d) = e^{-d}$ – Model II: $f(d) = (1 - d)^2$ • Stress tensor σ and the thermodynamic conjugate p_d: $\sigma = f(d) \mathbb{E} : \varepsilon,$ $p_d = -f'(d) \Psi_0,$

Table 6.2: Summary of the damage material model

onset of softening due to non-convex and non-coercive energy functions and suffers from strongly mesh-dependent results. If the mesh size is selected to be infinitely fine, then the energy dissipated in the localization zone will vanish, leading to the occurrence of a crack whose formation requires no energy. Such behavior is non-physical and undesirable. Therefore, if coercivity and convexity of an energy function are not satisfied, the minimization problem leads to microstructure and prevents finding a global stationarity point for numerical calculations as investigated in the works of Ball (1977), Dacorogna (1982) and Francfort and Mielke (2006).

An energy function is coercive if it has a superlinear growth, as it is illustrated in Figure 6.4(a). Thus,

$$\lim_{|x| \rightarrow \infty} \frac{\Psi(A)}{|A|} = \infty. \quad (6.16)$$

Finding a stationarity point for non-coercive energy function that becomes constant after some strain limit is problematic, as it is no longer growing. Furthermore, an energy function is convex, if any point described by $0 \leq \lambda \leq 1$, on the arbitrary secant of two points A_1 and A_2 is always above the function, thus

$$\Psi(\lambda A_1 + (1 - \lambda)A_2) \leq \lambda \Psi(A_1) + (1 - \lambda)\Psi(A_2) \quad \forall \quad A_1, A_2, \quad 0 \leq \lambda \leq 1 \quad (6.17)$$

The illustration of convexity is provided in Figure 6.4(b). Similarly, non-convex energy functions have also a problem for finding a stationarity point, as the local extremum may not necessarily coincide with the global one. This is why convexity can also be interpreted as the stability of the function regarding superimposed fluctuations of the argument of the function.

The strain localization problem is not related to the finite element method, but to the material formulation itself. Therefore, continuum material models experiencing softening behavior should be equipped with a regularization (localization limiter) strategy to reduce (if not completely avoid) mesh dependency in the finite element analysis. This complex phenomenon can be modeled successfully by combining theoretical and numerical methods

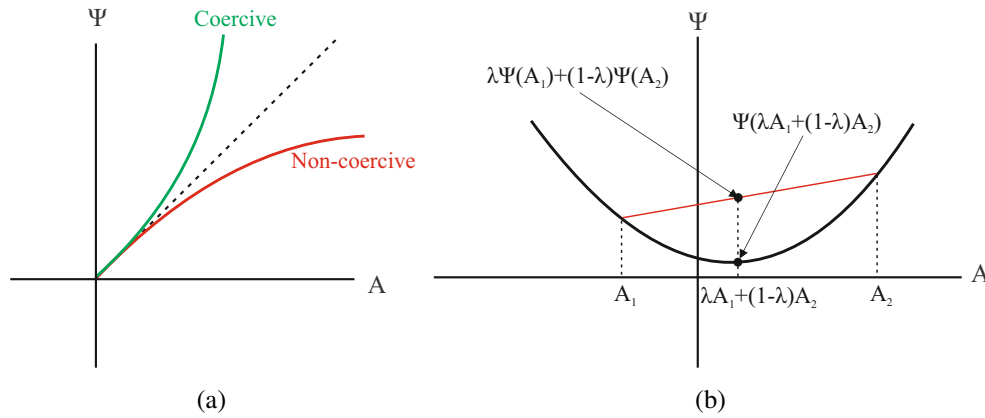


Figure 6.4: Schematic illustration of (a) coercivity (b) convexity with respect to an energy function Ψ

to allow the prediction of their behavior. Each method is related to its particular restrictions and range of applicability.

6.3 Regularization Strategies

The local continuum material models do not consider the microstructural processes and thus do not enter characteristic internal material length scales into the formulation. This property has almost no influence on the utilization of material models involving hardening. In contrast, the reliability of the results achieved from material models including softening behavior is extremely affected by this phenomenon.

To overcome the above-mentioned problem, some regularization techniques are proposed that introduce a material length scale into the formulation and are based on a general idea that the displacement field remains continuous in the whole domain. The most common regularization schemes are gradient-enhanced regularization, integral-type regularization, and viscous regularization, discussed in more detail subsequently.

6.3.1 Viscous Regularization

The main idea of viscous regularization is to add rate effects into the constitutive model, so that concurrently with an increase in deformation rate in softer elements, the strain rate also increases to make the element stiffer again. This method prevents the accumulation of deformation in one element and forces the neighbored elements to engage in damage. Thus, the dissipated energy has the same amount as in the case of no regularization. Although this solution for localization adds an artificial feature, “the viscosity”, to the material behavior, it does not need any additional global discretization, since it only operates at the local level. Furthermore, mesh-independent and stable results are achieved with a simple implementation in common non-linear finite element packages. It has a lower computation effort in comparison to other regularization schemes. However, we should mention that in this method the simulations are strongly dependent on the loading velocity.

Needleman (1988) first introduced the idea of viscous regularization with a simple one-dimensional case study, where he removed the pathological mesh dependency in strain-softening boundary value problems by presenting a rate-dependent formulation and rendered the governing equations well-posed for both static and dynamic problems.

Viscoplastic regularization was also used by Sluys and De Borst (1992) specifically for dynamic problems of cracked medium related to wave propagation and reflections on the cracked zone. Soyarslan (2009) devised Perzyna-type viscosity for regularization of post-peak response with softening due to local isotropic damage coupled with hyperelastic-plastic material behavior. Moreover, the concept of Perzyna viscoplasticity was used in the work of Faria et al. (1998) to introduce a new constitutive model for massive concrete considering two scalar damage variables and plastic strain tensor as internal variables. Chaboche et al. (2001) limited the rate-dependence of viscous damage models by applying some interface debonding models. This was sufficient to eliminate any solution jumps, i.e., localization of strain, but with a much lower rate effect. An almost similar idea to the one applied in Model II in this thesis was also used in the work of Allix (2013) by bounding the rate of internal variables to limit the rate-dependencies in the damage model. Since there was not much literature available for viscoplastic regularization of static problems, Niazi et al. (2012) applied a detailed numerical study of viscous regularization for a local anisotropic damage model by introducing two length scales; a primary and a secondary length scale. His work was dedicated to static problems and compared the reason for the existence and limitations of different regularization strategies.

6.3.2 Integral-based Regularization

In the integral-type strategy, the non-local variables are introduced as certain weighted averages of the corresponding local quantities over a neighborhood at a point. This idea is illustrated by the following formulation based on the work of Bažant and Jirásek (2002), where the non-local counterpart of a local field $\xi(x)$ in the domain Ω is defined as

$$\bar{\xi}(x) = \int_{\Omega} \alpha(\|x - y\|) \xi(y) dy, \quad (6.18)$$

where $\alpha(\|x - y\|)$ represents the non-local weight function. The non-local variables obtained this way replace the corresponding local one in the constitutive equations. Based on the selected weight function, either as the Gauß function or as the Green function, an internal length scale of the non-local continuum will be introduced, see the work of Peerlings et al. (2001).

Kröner (1967) and Eringen and Edelen (1972) incorporated non-local terms through integral equations, leading to non-local elasticity theories. More popular in the latter approach, the non-local treatment and weighted functions were limited to control the strain-softening and the elastic part was considered in the local form. Extension into continuum damage mechanics is presented by Pijaudier-Cabot and Bažant (1987) and Bazant and Pijaudier-Cabot (1988). An integral-based strategy was also proposed by Comi (2001), who modeled the tension-compression asymmetry character of rock-like materials using two isotropic damage variables and two internal length scales. Moreover, the application of this strategy in non-local plasticity can also be found in the work of Eringen (1981), Svedberg and Runesson (1998), and Jirásek and Rolshoven (2003). A coupled damage-plasticity model based on

the non-local integral-based regularization for ductile failure is proposed by Nguyen et al. (2015). They focused on the determination of model parameters with a novel calibration procedure, based on the experimental technique, as well as facilitating the implementation of the model into existing finite element codes.

Although this method offers a high degree of flexibility based on its averaging procedure, the difficulties regarding the numerical implementation into nonlinear finite element code are its obvious drawback. Therefore, it loses its prevalence over time for regularization of the strain localization phenomena, however, it is still quite popular in the field of topology optimization.

6.3.3 Gradient-enhanced Regularization

The gradient enhancement is the most versatile regularization approach, that introduces higher-order gradient terms (normally Laplacian) of the non-local variables into the constitutive relations and belongs to the group of non-local strategies. The gradient-enhancement can be considered as the differential counterpart of integral formulations. Several formulations are available for applying the gradient to the model. First models applied the gradient to the strains, known as micromorphic models, as in the work of Pijaudier-Cabot et al. (1988). The most common approach is to introduce a list of additional variables, which is coupled to the list of internal variables via an interaction term. By penalizing the gradients of the additional variables, one attains the regularization as a pure minimization of the potential functional with respect to displacements and additional variables. This approach is illustrated with a specific energetic formulation based on the work of Dimitrijevic and Hackl (2011), where the enhanced Helmholtz-free-energy function is obtained by

$$\begin{aligned} \Psi = & \frac{1}{2} f(d)(\boldsymbol{\varepsilon} - \boldsymbol{\varepsilon}_p) : \mathbb{E} : (\boldsymbol{\varepsilon} - \boldsymbol{\varepsilon}_p) + w(\alpha_p) \\ & + \frac{\beta_d}{2} (\varphi_d - d)^2 + \frac{c_d}{2} |\nabla \varphi_d|^2 + \frac{\beta_p}{2} (\varphi_p - \alpha_p)^2 + \frac{c_p}{2} |\nabla \varphi_p|^2 \end{aligned} \quad (6.19)$$

where the numerical parameters β_d and β_p represent the energy penalizing the difference between the corresponding non-local and local fields, whereas c_d and c_p stand for the gradient parameters that implicitly introduce a damage and a plastic internal material length, respectively. Calculation of the introduced field functions φ_d and φ_p requires two additional stationarity conditions

$$\int_{\Omega} \left[\beta_d (\varphi_d - d) + c_d (\nabla \delta \varphi_d \cdot \nabla \varphi_d) \right] \delta \varphi_d \, dV = 0 \quad \forall \delta \varphi_d \quad (6.20)$$

$$\int_{\Omega} \left[\beta_p (\varphi_p - \alpha_p) + c_p (\nabla \delta \varphi_p \cdot \nabla \varphi_p) \right] \delta \varphi_p \, dV = 0 \quad \forall \delta \varphi_p \quad (6.21)$$

that are coupled to the standard principle of virtual work defined for the determination of displacements. Generally, this regularization leads to a guaranteed ellipticity of the boundary value problem and the mesh-independent results, which is an obvious advantage, especially for quasi-static loading conditions. However, the main drawback of this scheme is the introduction of additional variables, i.e., both the displacement and the non-local variables become the global unknown and must be discretized at the global level. In the context of the finite element method, this leads to additional nodal unknowns and consequently larger computational effort.

The first gradient models were derived from integral-type formulations, by expanding the local variables in the Taylor series around the material points, see e.g., Mühlhaus and Alfantis (1991) and Peerlings et al. (2001). This approach could be pursued with a phase-field framework as well. For example, Miehe et al. (2010) proposed a thermodynamically consistent framework for phase-field models of crack propagation in elastic solids, developed incremental variational principles for rate-independent diffusive fracture, and considered their numerical implementations by multi-field finite element methods. Brepols et al. (2017) outlined a regularized gradient-extended damage-plasticity model based on the micromorphic approach using a “two-surface” formulation.

In the literature, many works deal with coupled plastic-damage material models, which combine either gradient damage with local hardening plasticity, for instance in the works of Makowski et al. (2006) and Nedjar (2001), or the gradient isotropic softening plasticity with the local damage behavior, as in the works of de Borst et al. (1999) and Svedberg and Runesson (2000), or the gradient damage coupled with gradient enhanced softening plasticity, for example in the work of Dimitrijevic and Hackl (2011). Within a continuum framework, plasticity and damage couplings have been studied either in a large strain format, e.g., Voyiadjis and Kattan (1992), Lubarda (1994), and Zhu and Cescotto (1995), or in a small strain format, e.g., Silmo (1987), Ju (1989), Hansen and Schreyer (1994), and Doghri (1995).

6.4 Coupled Regularized Damage-Plasticity Model

In this section, two coupled regularized damage-plasticity material models are presented. Model I is presented in Subsection 6.4.1, which evaluates an efficient Laplacian for gradient-enhancement of damage function and is based on a combination of the finite element method with strategies from meshless methods. In Subsection 6.4.2, Model II is introduced using an emulated representative volume element (ERVE) for viscous regularization of damage function. From a theoretical point of view, this coupling between damage and plasticity is treated naturally with a simple adequate choice of dissipation function. The regularization is performed only on the damage parameter, while here, the plastic regime is limited to the hardening behavior.

6.4.1 Model I: Gradient-enhanced Regularized Damage-Plasticity with Laplacian

Model I is dedicated to a regularization strategy based on gradient enhancement of the Helmholtz free energy function for a coupled damage-plasticity model, which renders the model well-posed. The enhancement is provided, following a new approach recently introduced by Junker et al. (2019) and Schwarz et al. (2019).

Variational Material Modeling

The total Helmholtz free energy function for this coupled material model reads

$$\Psi = \Psi_m + \Psi_r \quad (6.22)$$

consists of the mechanical energy Ψ_m and the regularization energy Ψ_r . In view of Equations (6.2) and (6.9), the mechanical part of Helmholtz free energy function accounting for damage and plastic deformation, which develops both irreversible deformations as well as deterioration of stiffness, is given by

$$\Psi_m = \Psi_m(\boldsymbol{\varepsilon}, \boldsymbol{\varepsilon}_p, d, \alpha_p) = \frac{1}{2} f(d) (\boldsymbol{\varepsilon} - \boldsymbol{\varepsilon}_p) : \mathbb{E} : (\boldsymbol{\varepsilon} - \boldsymbol{\varepsilon}_p) + w(\alpha_p) = f(d) \Psi_0 + w(\alpha_p). \quad (6.23)$$

The definition of the involved quantities in the above equation is already given in Subsections 6.1.1 and 6.1.2. For the present model, the damage function $f(d) = e^{-d}$ with the internal damage variable $d \in [0; 1)$ and its obvious property $f'(d) = -f(d)$ is chosen.

The regularization of the model is achieved by the gradient enhancement of the damage function f , specifically by adding a potential that is convex in the highest gradients to the mechanical contribution of the Helmholtz free energy Ψ_m in Equation (6.23). The most simple approach is given by

$$\Psi_r = \frac{1}{2} \beta |\nabla f|^2, \quad (6.24)$$

where β stands for the gradient parameter and used as a switch between local and enhanced model: setting $\beta = 0$ obtains a local coupled damage-plasticity model, see Junker et al. (2019) for more details.

The last ingredient for applying the Hamilton's principle is the dissipation function, which determines the type of differential equation, i.e., rate-dependent or rate-independent. In the current model, dissipation function is a combination of two homogeneous functions of order one, and thus reads

$$\mathcal{D} = \mathcal{D}_d + \mathcal{D}_p = r_d |\dot{d}| + r_p |\dot{\boldsymbol{\varepsilon}}_p| \quad (6.25)$$

with r_d and r_p being the dissipation parameters related to damage and plasticity, respectively. For more information, regarding the choice of dissipation function for the damage behavior refer to, e.g., Dimitrijevic and Hackl (2011), Junker et al. (2019) and for plasticity refer to Carstensen et al. (2002a), and Mielke (2003).

Now, by taking into account the above-mentioned terms, Hamilton's principle for non-conservative continua reads

$$\delta \mathcal{G} + \int_{\Omega} \frac{\partial \mathcal{D}}{\partial \dot{\boldsymbol{v}}} \cdot \delta \boldsymbol{v} \, dV = 0 \quad \forall \delta \boldsymbol{u}, \delta \boldsymbol{v}, \quad (6.26)$$

where δ denotes the (total) variation, \boldsymbol{u} is the displacement and \boldsymbol{v} refers to a set of internal variables, for further details see Hamilton (1834) and Hamilton (1835). Referring to the enhanced free energy function, the Gibbs energy can be obtained as

$$\mathcal{G} := \int_{\Omega} \Psi(\boldsymbol{\varepsilon}, \boldsymbol{v}) \, dV - \int_{\Omega} \boldsymbol{b} \cdot \boldsymbol{u} \, dV - \int_{\partial\Omega} \boldsymbol{t} \cdot \boldsymbol{u} \, dA \quad (6.27)$$

where \boldsymbol{v} is the already introduced vector of internal variables describing the microstructure of the material. The quantity \boldsymbol{b} refers to the external body force of the body Ω , and \boldsymbol{t} is the surface traction at the surface of the body $\partial\Omega$.

Considering the constraints for plasticity, defined in Equation (6.8), the corresponding virtual potential is given by

$$\delta\mathcal{C} = \int_{\Omega} \lambda \frac{\partial c_1}{\partial \dot{\boldsymbol{\varepsilon}}_p} : \delta \boldsymbol{\varepsilon}_p \, dV + \int_{\Omega} \gamma \left(\frac{\partial c_2}{\partial \dot{\alpha}_p} \delta \alpha_p - \frac{\partial c_2}{\partial \dot{\boldsymbol{\varepsilon}}_p} : \delta \boldsymbol{\varepsilon}_p \right) \, dV. \quad (6.28)$$

where the two Lagrange parameters λ and γ ensure $c_{1,2} = 0$. Mention that formulation in terms of rates in the constraints $c_{1,2}$ demands a similar definition of the virtual potential as also necessary for the non-conservative forces given by $\partial\mathcal{D}/\partial\dot{v}$. The virtual potential for the constraints allows to write the final form of the Hamilton principle as

$$\delta\mathcal{G} + \int_{\Omega} \frac{\partial\mathcal{D}}{\partial\dot{d}} \delta d \, dV + \int_{\Omega} \frac{\partial\mathcal{D}}{\partial\dot{\boldsymbol{\varepsilon}}_p} : \delta \boldsymbol{\varepsilon}_p \, dV + \delta\mathcal{C} = 0 \quad \forall \delta \mathbf{u}, \delta d, \delta \boldsymbol{\varepsilon}_p, \delta \alpha_p \quad (6.29)$$

The variations $\delta \mathbf{u}$, δd , $\delta \boldsymbol{\varepsilon}_p$ and $\delta \alpha_p$ are independent of each other. Consequently, the stationarity condition postulated by the Hamilton's principle yields the following system of variational integral equations:

$$\delta_{\mathbf{u}}\mathcal{G} = 0 \quad \forall \delta \mathbf{u} \quad (6.30)$$

$$\delta_d\mathcal{G} + \int_{\Omega} \frac{\partial\mathcal{D}}{\partial\dot{d}} \delta d \, dV = 0 \quad \forall \delta d \quad (6.31)$$

$$\delta_{\boldsymbol{\varepsilon}_p}\mathcal{G} + \int_{\Omega} \frac{\partial\mathcal{D}}{\partial\dot{\boldsymbol{\varepsilon}}_p} : \delta \boldsymbol{\varepsilon}_p \, dV + \delta_{\boldsymbol{\varepsilon}_p}\mathcal{C} = 0 \quad \forall \delta \boldsymbol{\varepsilon}_p \quad (6.32)$$

$$\delta_{\alpha_p}\mathcal{G} + \delta_{\alpha_p}\mathcal{C} = 0 \quad \forall \delta \alpha_p \quad (6.33)$$

yielding

$$\int_{\Omega} \frac{\partial\Psi_m}{\partial\boldsymbol{\varepsilon}} : \delta \boldsymbol{\varepsilon} \, dV - \int_{\Omega} \mathbf{b} \cdot \delta \mathbf{u} \, dV - \int_{\partial\Omega} \mathbf{t} \cdot \delta \mathbf{u} \, dA = 0 \quad \forall \delta \mathbf{u} \quad (6.34)$$

$$\int_{\Omega} \Psi_0 f' \delta d \, dV + \int_{\Omega} \beta \nabla f \cdot \nabla (f' \delta d) \, dV + \int_{\Omega} \partial\mathcal{D}_d \delta d \, dV = 0 \quad \forall \delta d \quad (6.35)$$

$$\int_{\Omega} \left(\frac{\partial\Psi_m}{\partial\boldsymbol{\varepsilon}_p} + \partial\mathcal{D}_p + \lambda \mathbf{I} - \gamma \frac{\dot{\boldsymbol{\varepsilon}}_p}{|\dot{\boldsymbol{\varepsilon}}_p|} \right) : \delta \boldsymbol{\varepsilon}_p \, dV = 0 \quad \forall \delta \boldsymbol{\varepsilon}_p \quad (6.36)$$

$$\int_{\Omega} \left(\frac{\partial\Psi_m}{\partial\alpha_p} + \gamma \right) \delta \alpha_p \, dV = 0 \quad \forall \delta \alpha_p. \quad (6.37)$$

Due to the non-differentiability of \mathcal{D} at $\dot{d} = 0 \wedge |\dot{\boldsymbol{\varepsilon}}_p| = 0$, the set-valued subdifferentials $\partial\mathcal{D}_d$ and $\partial\mathcal{D}_p$ are defined as

$$\partial\mathcal{D}_d := \begin{cases} r_d & \text{for } \dot{d} \neq 0 \\ [-r_d, r_d] & \text{else} \end{cases} \quad (6.38)$$

and

$$\partial\mathcal{D}_p := \begin{cases} r_p \frac{\dot{\boldsymbol{\varepsilon}}_p}{|\dot{\boldsymbol{\varepsilon}}_p|} & \text{for } |\dot{\boldsymbol{\varepsilon}}_p| \neq 0 \\ [-r_p, r_p] & \text{else} \end{cases} \quad (6.39)$$

and entered into the stationarity conditions (Equations (6.35) and (6.36)).

The first equation in the system (Equation (6.34)) is the standard principle of virtual work and can be solved by employing the finite element method. It introduces the mechanical stress by

$$\boldsymbol{\sigma} = \frac{\partial\Psi_m}{\partial\boldsymbol{\varepsilon}} = f \mathbb{E} : (\boldsymbol{\varepsilon} - \boldsymbol{\varepsilon}_p). \quad (6.40)$$

The equation in terms of the variation of d (Equation (6.35)) is quite inconvenient to solve, therefore, by applying an integration by part to the second term, it transformed into an integral over the boundary of the body and a volume integral involving second-order differential term:

$$\int_{\Omega} \beta \nabla f \cdot \nabla (f' \delta d) \, dV = \int_{\partial\Omega} \beta \mathbf{n} \cdot \nabla f f' \delta d \, dA - \int_{\Omega} \beta \nabla^2 f f' \delta d \, dV \quad (6.41)$$

with the normal vector \mathbf{n} . We immediately used a spatially constant penalty parameter for the gradient. The Laplace operator ∇^2 is introduced as

$$\nabla^2 f := \nabla \cdot \nabla f = \sum_{i=1}^3 \frac{\partial^2 f}{\partial x_i^2}. \quad (6.42)$$

Inserting Equation (6.41) into the stationarity condition in Equation (6.35) transforms it to its strong form

$$f' \Psi_0 - \beta f' \nabla^2 f + \partial \mathcal{D}_d \ni 0 \quad \mathbf{x} \in \Omega \quad (6.43)$$

$$\nabla f \cdot \mathbf{n} = 0 \quad \mathbf{x} \in \partial\Omega \quad (6.44)$$

of which Equation (6.44) constitutes as the Neumann boundary condition for Equation (6.43). The set-valued character of $\partial \mathcal{D}_d$ turns the formula into a differential inclusion. The Legendre-Fenchel transformation of the dissipation function \mathcal{D}_d

$$\begin{aligned} \mathcal{D}_d^* &= \sup_{\dot{d}} \{ p_d \dot{d} - \mathcal{D}_d \} \\ &= \sup_{\dot{d}} \{ |\dot{d}| (p_d \operatorname{sgn} \dot{d} - r_d) \} \quad \forall \mathbf{x} \end{aligned} \quad (6.45)$$

allows for a simplified representation (with the driving force for the damage function $p_d := -f' \Psi_0 + \beta f' \nabla^2 f$). Since material healing is not observed during damage processes, it holds $\operatorname{sgn} \dot{d} = \{0, 1\}$, such that we find the yield function $\Phi_d := p_d - r_d \leq 0$. Consequently, Equation (6.43) rearranges to (see also Junker et al. (2019))

$$\begin{aligned} &p_d \in \partial \mathcal{D}_d \\ \Leftrightarrow &\begin{cases} \dot{d} > 0 : & p_d = r_d \\ \dot{d} = 0 : & p_d \leq r_d \end{cases} \end{aligned} \quad (6.46)$$

It remains to evaluate the last two stationarity conditions, i.e., Equations (6.36) and (6.37). The condition Equation (6.36) can only be fulfilled if the integrator is zero, viz.

$$\frac{\partial \Psi_m}{\partial \boldsymbol{\varepsilon}_p} + \partial \mathcal{D}_p + \lambda \mathbf{I} - \gamma \frac{\dot{\boldsymbol{\varepsilon}}_p}{|\dot{\boldsymbol{\varepsilon}}_p|} \ni \mathbf{0}. \quad (6.47)$$

Again, the set-valued character of the subdifferential, now $\partial \mathcal{D}_p$, request the differential inclusion. It remains to compute the Lagrange parameter λ . To this end, Equation (6.47) is double-contracted with the unity matrix \mathbf{I} and the constraint c_1 is inserted. This yields

$$\lambda = -\frac{1}{3} \frac{\partial \Psi_m}{\partial \boldsymbol{\varepsilon}_p} : \mathbf{I} = \frac{1}{3} \boldsymbol{\sigma} : \mathbf{I} \quad (6.48)$$

since $\mathbf{I} : \mathbf{I} = 3$ and $\partial\Psi_m/\partial\varepsilon_p = -\boldsymbol{\sigma}$. Consequently, it holds

$$\dot{\varepsilon}_p = \frac{|\dot{\varepsilon}_p|}{r_p - \gamma} \left[\boldsymbol{\sigma} - \left(\frac{1}{3} \boldsymbol{\sigma} : \mathbf{I} \right) \mathbf{I} \right] = \frac{|\dot{\varepsilon}_p|}{r_p - \gamma} \text{dev} \boldsymbol{\sigma}, \quad (6.49)$$

where the well known stress deviator can be identified. An indicator whether or not plastic strains evolve can be found in form of a yield function when a Legendre transformation for the dissipation function for the plastic strains is employed:

$$\begin{aligned} \mathcal{D}_p^* &= \sup_{\dot{\varepsilon}} \{ \dot{\varepsilon}_p : \text{dev} \boldsymbol{\sigma} - \mathcal{D}_p - \gamma(\dot{\alpha}_p - |\dot{\varepsilon}_p|) \} \\ &= \sup_{\dot{\varepsilon}} \left\{ \frac{|\dot{\varepsilon}_p|}{r_p - \gamma} \text{dev} \boldsymbol{\sigma} : \text{dev} \boldsymbol{\sigma} - r_p |\dot{\varepsilon}_p| + \gamma |\dot{\varepsilon}_p| \right\} - \gamma \dot{\alpha}_p \\ &= \sup_{\dot{\varepsilon}} \left\{ \frac{|\dot{\varepsilon}_p|}{r_p - \gamma} \left(\underbrace{|\text{dev} \boldsymbol{\sigma}|^2 - (r_p - \gamma)^2}_{=: \tilde{\Phi}_p} \right) \right\} - \gamma \dot{\alpha}_p. \end{aligned} \quad (6.50)$$

Due to the supremum, the constraints enter with a negative sign in contrast to the minimum in the Hamilton principle (due to the convexity of all functions). We can read off the yield function Φ_p

$$\Phi_p := |\text{dev} \boldsymbol{\sigma}| - (r_p - \gamma) \leq 0 \quad (6.51)$$

from the Legendre transform, which has the same roots as $\tilde{\Phi}$ but a more convenient form in plasticity. Finally, the Lagrange parameter γ can be determined from Equation (6.37) to be

$$\gamma = -\frac{\partial\Psi_m}{\partial\alpha_p} = -K_H \alpha_p. \quad (6.52)$$

The hardening variable may only increase (see Equation (6.7)). Thus, $\gamma \leq 0$ since $K_H > 0$, from which follows that the prefactor $|\dot{\varepsilon}_p|/(r_p - \gamma) =: \Delta\rho$ is positive and may be identified as consistency parameter. We thus end up with the evolution equations for plasticity as

$$\dot{\varepsilon}_p = \Delta\rho \text{dev} \boldsymbol{\sigma}, \quad \Delta\rho \geq 0, \quad \Phi_p \leq 0, \quad \Delta\rho \Phi_p = 0$$

$$\dot{\alpha}_p = |\dot{\varepsilon}_p| = \Delta\rho(r_p - \gamma) = \Delta\rho(r_p + K_H \alpha_p) \quad (6.53)$$

which complement the field equations for the displacements and the damage function, viz.

$$\int_{\Omega} \boldsymbol{\sigma} : \delta\varepsilon \, dV - \int_{\Omega} \mathbf{b} \cdot \delta\mathbf{u} \, dV - \int_{\partial\Omega} \mathbf{t} \cdot \delta\mathbf{u} \, dA = 0 \quad \forall \delta\mathbf{u} \quad (6.54)$$

and

$$\dot{d} \geq 0, \quad \Phi_d = f' \Psi_0^+ - \beta \nabla^2 f - r_d \leq 0, \quad \dot{d} \Phi_d = 0 \quad (6.55)$$

Note that we replaced in Equation (6.55) the total contribution of the mechanical part of the Helmholtz free energy related to damage Ψ_0 by Ψ_0^+ which represents only the energetic contribution due to tension loading. This is a significant improvement in the modeling of

materials instead of taking Ψ_0 , which exhibit great sensitivity of their mechanical behavior to pressure, resulting in a lower strength in tension than compression. To resolve the problem, we formulate the free energy function in a way that evolution of the damage function will be triggered only by the positive part of the elastic strain tensor. Corresponding to the model of Mazars and Pijaudier-Cabot (1989), the always positive local part of the Helmholtz free energy related to damage is

$$f\Psi_0^+ = \frac{1}{2}f(d)\boldsymbol{\varepsilon}_e^+ : \mathbb{E} : \boldsymbol{\varepsilon}_e^+, \quad (6.56)$$

where $\boldsymbol{\varepsilon}_e^+$ represents the contribution of the positive part of the elastic strain tensor $\boldsymbol{\varepsilon}_e = \boldsymbol{\varepsilon} - \boldsymbol{\varepsilon}_p$, which is calculated as:

$$\boldsymbol{\varepsilon}_e^+ = \sum_{i=1}^3 \varepsilon_{e,i} \mathbf{e}_i \otimes \mathbf{e}_i \quad \text{for } \varepsilon_{e,i} > 0 \quad (6.57)$$

where $\varepsilon_{e,i}$ stands for the eigenvalues of the elastic strain tensor and \mathbf{e}_i are the corresponding eigenvectors.

Numerical Treatment

The discussion of the numerical treatment starts with the weak form of the balance of the linear momentum (Equation (6.54)), and the evolution equations for the plastic strain and damage, Equations (6.53) and (6.55), respectively. Due to use of the strong form of damage evolution equation and implementation of Laplace function, the principle structure of the algorithm remains the same as a typical finite element routine with displacements being the only degrees of freedom at the nodes. According to Subsection 4.2.1, and by introducing $\boldsymbol{\sigma}$ and $\boldsymbol{\varepsilon}$ as the vector of Voigt notation, the stationarity condition for displacement \mathbf{u} (Equation 6.54) can be written in terms of the residual \mathbf{R}_u

$$\mathbf{R}_u = \sum_{e=1}^{N_e} \int_{\Omega_e} \mathbf{B}^T \cdot \boldsymbol{\sigma} \, dV - \sum_{e=1}^{N_e} \int_{\Omega_e} \mathbf{N}^T \cdot \mathbf{b} \, dV - \sum_{e=1}^{N_e} \int_{\partial\Omega_e} \mathbf{N}^T \cdot \mathbf{t} \, dA \stackrel{!}{=} 0. \quad (6.58)$$

that constitutes in general as a non-linear algebraic equation for the displacement field at the current time-step $m + 1$.

For simplicity, we perform an explicit Euler integration scheme to Equation (6.53) for plastic strain field at the material point level which yields for the rate-independent case

$$\begin{aligned} \boldsymbol{\varepsilon}_p^{m+1} &= \boldsymbol{\varepsilon}_p^m + \Delta\rho \operatorname{dev}\boldsymbol{\sigma}^m = \boldsymbol{\varepsilon}_p^m + \Delta\rho f^m \operatorname{dev}\mathbb{E} : (\boldsymbol{\varepsilon}^{m+1} - \boldsymbol{\varepsilon}_p^m) \\ \alpha_p^{m+1} &= \alpha_p^m + \Delta\rho(r_p + K_H\alpha_p^m) \end{aligned} \quad (6.59)$$

where the superposition m refers to the previous time-step, and $m + 1$ is the current time-step. The set of evolution equations for plasticity field is closed by Kuhn-Tucker conditions gives as

$$\Delta\rho \geq 0, \quad \Phi_p := |\operatorname{dev}\boldsymbol{\sigma}(f^m, \boldsymbol{\varepsilon}^{m+1}, \boldsymbol{\varepsilon}_p^m)| - (r_p - \gamma) \leq 0, \quad \Delta\rho\Phi_p = 0 \quad (6.60)$$

During the iteration process at the integration point level, the plastic internal variables are not treated as additional unknowns, but are updated in terms of the consistency parameter $\Delta\rho$, as in Equation (6.59), which is determined explicitly from the definition of the yield function and the consistency condition by inserting Equation (6.59) into the yield function

$$\begin{aligned}\Phi_p^{m+1} &= |\text{dev}\boldsymbol{\sigma}(f^m, \boldsymbol{\varepsilon}^{m+1}, \boldsymbol{\varepsilon}_p^{m+1})| - (r_p - \gamma) \\ &= |f^m \text{dev}\mathbb{E} : (\boldsymbol{\varepsilon}^{m+1} - \boldsymbol{\varepsilon}_p^{m+1})| - (r_p + K_H \alpha_p^{m+1}).\end{aligned}\quad (6.61)$$

and solving the algebraic equation for the parameter $\Delta\rho$ iteratively e.g., by means of Newton's method. The internal variables which needs to be updated during the iteration in the integration point level are $\boldsymbol{\varepsilon}_p$ and α_p .

For evolution of the damage function, first, we have to discretize the differential inequality for damage (Equation (6.55)). As long as, damage function directly depends on the elasto-plastic energy, it is therefore coupled to the local strains and will increase the computational effort for calculation of displacement field of the current time-step, $\boldsymbol{\varepsilon}^{m+1}$. In order to avoid an increase in the number of unknowns at the nodes, the first operator split is introduced, which leads to an algorithm that not only requires a minimum of computational effort, but also is stable. Thus, with the consideration of explicit Euler scheme for plastic strains and damage function from the last time-step f^m , the stresses are calculated by

$$\boldsymbol{\sigma}^{m+1} = \boldsymbol{\sigma}^{m+1}(\boldsymbol{\varepsilon}^{m+1}, \boldsymbol{\varepsilon}_p^m, f^m) = \boldsymbol{\sigma}^m + f^m \mathbb{E} : (\boldsymbol{\varepsilon}^{m+1} - \boldsymbol{\varepsilon}_p^m) \quad (6.62)$$

Consequently, this split converts the stationarity condition (Equation (6.58)) into a *linear* algebraic equation with a constant tangent matrix for each time-step including the following material tangent

$$\left. \frac{d\boldsymbol{\sigma}}{d\boldsymbol{\varepsilon}} \right|^{m+1} = f^m \mathbb{E} \quad (6.63)$$

The solution for the displacement field is thus completely standard and can be performed with any finite element routine. Due to the explicit character of the operator split, relatively small load increments are required. However, it is already presented in original model by Junker et al. (2019) that this drawback is of minor importance since exactly this split, together with the numerical solution for the damage function, renders the global algorithmic treatment being quite fast.

In contrast to the evolution of the plastic parameters at each integration point, the damage function is defined at the *center of mass* of each finite element. Consequently, all Gauß points in the same element make use of the same damage function f_i . Therefore, the indicator function is defined element-wise, such as

$$\Phi_{d,i} = f_i \bar{\Psi}_{0,i} - \beta f_i \nabla^2 f_i - r_d \leq 0 \quad (6.64)$$

where $\nabla^2 f_i$ is the second derivative of damage function or rather Laplace operator for each element i .

The calculation procedure for Laplace operator in the present study restricted to the generalized three-dimensional unstructured finite element mesh. We skip the detailed procedure, therefore, for more information regarding the description of Laplace in one dimensional, as

well as the two- (2D) or three-dimensional (3D) cases for structured meshes, we refer to the original publication by Jantos et al. (2019).

Initially, the Taylor series expansion for the damage function around the central element mid point \mathbf{x}_i is formed as

$$\Delta f_{i,j} = f_j - f_i = \sum_{k=1}^3 \left(\frac{\partial f_i}{\partial x_k} \Delta x_{j,k} + \frac{1}{2} \sum_{p=1}^3 \frac{\partial^2 f_i}{\partial x_k \partial x_p} \Delta x_{j,k} \Delta x_{j,p} \right) \quad (6.65)$$

The index j runs over all elements that form the neighborhood around element i , where in three-dimensional case besides to the six next-neighbors, three additional neighbored elements are also necessary to close the system of equations, i.e., $j \in \{n, s, e, w, f, b, o, p, q\}$. We use a more general procedure well-known in meshless methods for computing the Laplace operator, where a central element is considered for evaluation of the Laplacian of the damage function, and is associated to six next-neighbors: *north*, *east*, *south*, *west*, *front* and *back* in the three-dimensional case (Jantos et al. (2019)). The three additional elements have to be selected once for each spatial plane and preferably close to the central element. Usually, these additional elements are the closest ones located in diagonal direction as illustrated in Figure 6.5 for 2D case for simplicity. A search through the mesh prior to each computation finds all neighbor relations and boundary elements, on which the Neumann boundary conditions are applied according to Equation (6.44).

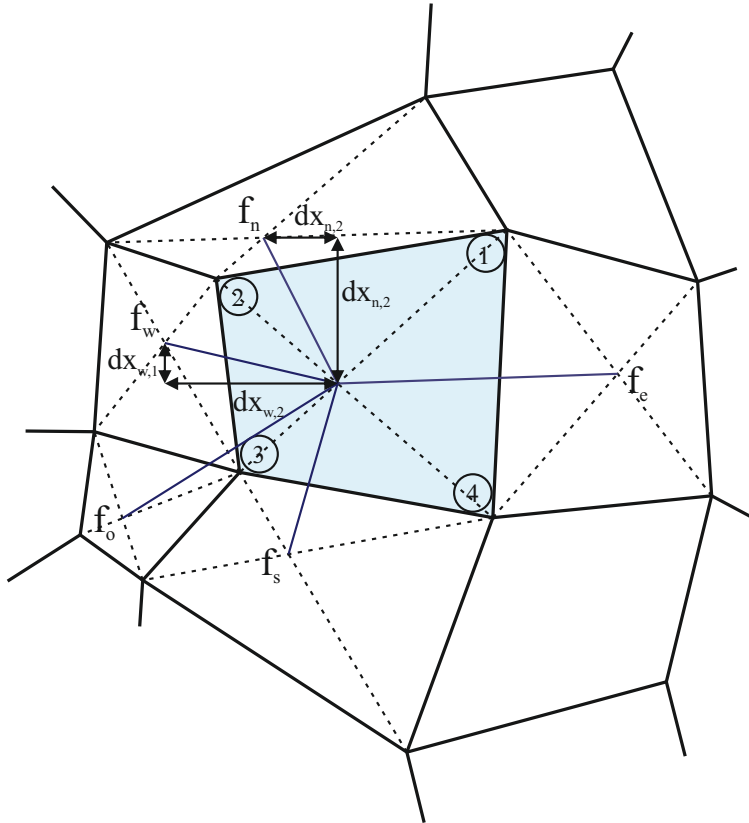


Figure 6.5: Neighbor relations for an unstructured quadrilateral mesh in two-dimensional case

The increments denote the distance between the central and the neighboring elements

given as

$$\Delta \mathbf{x}_j := \mathbf{x}_i - \mathbf{x}_j = \begin{pmatrix} x_{i,1} - x_{j,1} \\ x_{i,2} - x_{j,2} \\ x_{i,3} - x_{j,3} \end{pmatrix}. \quad (6.66)$$

We evaluate the Taylor expansion for nine elements j and obtain a linear equation system with the first and second derivatives as unknowns. The boundary conditions can be applied correctly, e.g., by introducing pseudo/ghost elements outside of Ω defined as mirror points of the boundary elements on $\partial\Omega$ (see work of Stacey (1994) for more detail). The allocation of neighbors to the respective elements and the determination of the spatial increments is here again done once before the main calculation starts. The linear system of equations is formed by collecting the Taylor series expansion in Equation (6.65) for all elements in the neighborhood

$$\Delta \mathbf{f}_i = \mathbf{D} \cdot \partial \mathbf{f}_i \quad (6.67)$$

with the known increments of the damage function $\Delta \mathbf{f}_i$

$$\Delta \mathbf{f}_i = (\Delta f_{i,j}) \mathbf{e}_j, \quad j \in \{n, s, e, w, f, b, o, p, q\} \quad (6.68)$$

and the vector of the unknown partial derivatives $\partial \mathbf{f}_i$

$$\partial \mathbf{f}_i := \left(\frac{\partial f_i}{\partial x_1} \quad \frac{\partial f_i}{\partial x_2} \quad \frac{\partial f_i}{\partial x_3} \quad \frac{\partial^2 f_i}{\partial x_1 \partial x_2} \quad \frac{\partial^2 f_i}{\partial x_1 \partial x_3} \quad \frac{\partial^2 f_i}{\partial x_2 \partial x_3} \quad \frac{\partial^2 f_i}{\partial x_1^2} \quad \frac{\partial^2 f_i}{\partial x_2^2} \quad \frac{\partial^2 f_i}{\partial x_3^2} \right)^T. \quad (6.69)$$

The coefficient matrix contains the entries \mathbf{D}

$$\begin{aligned} D_{j,1} &= \Delta x_{j,1}, & D_{j,4} &= \Delta x_{j,1} \Delta x_{j,2}, & D_{j,7} &= \frac{(\Delta x_{j,1})^2}{2}, \\ D_{j,2} &= \Delta x_{j,2}, & D_{j,5} &= \Delta x_{j,1} \Delta x_{j,3}, & D_{j,8} &= \frac{(\Delta x_{j,2})^2}{2}, \\ D_{j,3} &= \Delta x_{j,3}, & D_{j,6} &= \Delta x_{j,2} \Delta x_{j,3}, & D_{j,9} &= \frac{(\Delta x_{j,3})^2}{2} \end{aligned} \quad (6.70)$$

for each neighbor j and is thus a 9×9 matrix. It is determined by the finite element discretization and does not change during the computation of a specific boundary value problem. The partial derivatives $\partial \mathbf{f}_i$ can be computed by inversion of Equation (6.67) and read

$$\partial \mathbf{f}_i = \mathbf{D}^{-1} \cdot \Delta \mathbf{f}_i. \quad (6.71)$$

We are only interested in the unmixed second derivatives for the computation of the Laplace operator. Thus, we define the operator-matrix \mathbf{B}^{∇^2} , which only contains the last three lines of the inverse of the coefficient matrix. Consequently,

$$B_{l,j}^{\nabla^2} := D_{l+6,j}^{-1}, \quad l \in \{1, 2, 3\}, \quad j \in \{1, \dots, 9\}, \quad (6.72)$$

such that

$$\mathbf{B}^{\nabla^2} \cdot \Delta \mathbf{f}_i = \frac{\partial^2 f_i}{\partial x_l^2} \mathbf{e}_l, \quad l \in \{1, 2, 3\}. \quad (6.73)$$

The coefficient matrix D depends only on the mesh topology and so does the operator matrix B^{∇^2} . Thus, the operator matrix can be computed for each element prior to the computations and stored in arrays with size 3×9 for each element of the mesh. The Laplace operator for each element i can be simply computed by

$$(\Lambda_f)_i = \sum_{l=1}^3 \left(B^{\nabla^2} \cdot \Delta \mathbf{f}_i \right)_l \quad (6.74)$$

and its derivative with respect to the damage function at each element i is given by

$$(\mathbf{D}\Lambda_f)_i := \frac{\partial (\Lambda_f)_i}{\partial f_i} = \sum_{l=1}^3 \left(B^{\nabla^2} \cdot \frac{\partial \Delta \mathbf{f}_i}{\partial f_i} \right)_l = - \sum_{l=1}^3 \left(B^{\nabla^2} \cdot \mathbf{1} \right)_l \quad (6.75)$$

with the identity vector $\mathbf{1}$, which has a length of 9. These notations will be used to write the yield function and update the damage function as

$$\Phi_{d,i}^k = f_i^k \bar{\Psi}_{0,i}^{m+1} - \beta f_i^k (\Lambda_f)_i - r_d \leq 0 \quad (6.76)$$

and

$$f_i^{k+1} = \begin{cases} f_i^k - \frac{\Phi_i^k}{\bar{\Psi}_{0,i}^{m+1} - \beta (\Lambda_f)_i - \beta f_i^k (\mathbf{D}\Lambda_f)_i} & \text{if } \Phi_{d,i}^k > 0 \\ f_i^k & \text{else .} \end{cases} \quad (6.77)$$

The above equations are subjected to the time discretization which together with the dissipation parameters r_d and r_p controls the behavior of material, i.e., purely elastic, elastoplastic and elastoplastic-damage cases. For purely elastic case, no plastic flow and damage occurs in the interval $[t^m, t^{m+1}]$, and the condition

$$\Phi_p(f, \varepsilon, \varepsilon_p, \alpha_p) \leq 0 \quad \Phi_d(f, \varepsilon, \varepsilon_p) \leq 0 \quad (6.78)$$

are satisfied, thus with $\Delta\rho = 0$ no evolution of internal variables take place. In the plastic loading, the consistency parameter is strictly positive and the constraints are given as

$$\Delta\rho > 0 \quad \Phi_p(f, \varepsilon, \varepsilon_p, \alpha_p) = 0 \quad \Phi_d(f, \varepsilon, \varepsilon_p) \leq 0 \quad (6.79)$$

and in the third case, for elastoplastic-damage loading, both the plastic and damage evolution occur and the solutions are defined by the Equations (6.59) and (6.77) according to the constraints of

$$\Phi_p(f, \varepsilon, \varepsilon_p, \alpha_p) = 0 \quad \Phi_d(f, \varepsilon, \varepsilon_p) = 0 \quad (6.80)$$

The numerical treatment for the general three-dimensional unstructured finite element mesh is presented in Algorithm 1.

6.4.2 Model II: Relaxation-based Regularized Damage-Plasticity with Emulated RVE

Model II presents a regularized damage model coupled with local plasticity based on a variational approach with rate limitation in combination with a so-called Emulated Representative Volume Element (ERVE). Its formulation is provided at first in the model introduced by Junker et al. (2019) and Schwarz et al. (2019).

Algorithm 1: Model I: Finite element algorithm

for $i \leq n_e$ **do**

Elastic predictor step

input: $t^{m+1}, \boldsymbol{\varepsilon}^{m+1}$

Set: $f_i^k = f^m, \boldsymbol{\varepsilon}_{p,i}^k = \boldsymbol{\varepsilon}_{p,i}^m, \alpha_{p,i}^k = \alpha_{p,i}^m$

compute: $\Phi_{p,i}^k = |\text{dev} \boldsymbol{\sigma}(f_i^k, \boldsymbol{\varepsilon}_i^{m+1}, \boldsymbol{\varepsilon}_{p,i}^k)| - (r_p + K_H \alpha_{p,i}^k)$

Check for plastic processes in material level

if $\Phi_{p,i}^k < \text{tol}$ **then**

no plastic increment $\Delta\rho = 0$

$\boldsymbol{\varepsilon}_{p,i}^{k+1} = \boldsymbol{\varepsilon}_{p,i}^k$

$\alpha_{p,i}^{k+1} = \alpha_{p,i}^k$

else

Solve Eq. (6.61) for $\Delta\rho$

$\boldsymbol{\varepsilon}_{p,i}^{k+1} = \boldsymbol{\varepsilon}_{p,i}^k + \Delta\rho f_i^m \text{dev} \mathbb{E} : (\boldsymbol{\varepsilon}_i^{m+1} - \boldsymbol{\varepsilon}_{p,i}^k)$

$\alpha_{p,i}^{k+1} = \alpha_{p,i}^k + \Delta\rho (r_p + K_H \alpha_{p,i}^k)$

update: $\boldsymbol{\varepsilon}_{p,i}^{m+1} = \boldsymbol{\varepsilon}_{p,i}^{k+1}$

$\alpha_{p,i}^{m+1} = \alpha_{p,i}^{k+1}$

after convergence of the finite element routine for $\hat{\mathbf{u}}^{m+1}$:

compute: Laplace operator Λ_f and derivative $D\Lambda_f$

for $i \leq n_e$ **do**

input: $\bar{\Psi}_{0,i}^{m+1}$

Check for damage processes in element level

compute: $\Phi_{d,i}^k = f_i^k \bar{\Psi}_{0,i}^{m+1} - \beta f_i^k (\Lambda_f)_i - r_d$

if $\Phi_{d,i}^k < \text{tol}$ **then**

$\Phi_{d,i}^k = 0$

$f_i^{k+1} = f_i^k$

else

$f_i^{k+1} = f_i^k - \frac{\Phi_{d,i}^k}{\bar{\Psi}_{0,i}^{m+1} - \beta (\Lambda_f)_i - \beta f_i^k (D\Lambda_f)_i}$

update: $f_i^{m+1} = f_i^{k+1}$

Variational Material Modeling

The model is specifically based on the mechanical part of Helmholtz free energy function for isotropic damage and plasticity, thus

$$\Psi_m = \frac{1}{2} f(d) (\boldsymbol{\varepsilon} - \boldsymbol{\varepsilon}_p) : \mathbb{E} : (\boldsymbol{\varepsilon} - \boldsymbol{\varepsilon}_p) + w(\alpha_p) = f(d) \Psi_0 + w(\alpha_p). \quad (6.81)$$

For the current model, the damage function $f(d) = (1 - d)^2$ with the internal damage variable $d \in [0; 1]$ is used. The constraints are similar to the one presented in Equation (6.8). Moreover, the rate-independent formulation for dissipation function can be defined as

$$\mathcal{D}_p(\dot{\boldsymbol{\varepsilon}}_p) = r_p |\dot{\boldsymbol{\varepsilon}}_p|, \quad (6.82)$$

and

$$\mathcal{D}_d(\dot{d}) = \begin{cases} r_d \dot{d} & \text{for } \dot{d} \geq 0 \\ \infty & \text{for } \dot{d} < 0 \end{cases}, \quad (6.83)$$

for plasticity and damage, respectively. Applying the principle of the minimum of the dissipation potential (PMDP), the evolution equations are obtained for plastic internal variables as

$$\dot{\boldsymbol{\varepsilon}}_p = \frac{|\dot{\boldsymbol{\varepsilon}}_p|}{r_p + K_H \alpha_p} \text{dev} \boldsymbol{\sigma}, \quad \dot{\alpha}_p = |\dot{\boldsymbol{\varepsilon}}_p| = \Delta \rho (r_p + K_H \alpha_p) \quad (6.84)$$

and for damage variable d as

$$\dot{d} = \arg \min \left\{ \dot{\Psi}_m(\boldsymbol{\varepsilon}, \boldsymbol{\varepsilon}_p, \alpha_p, d) + \mathcal{D}_d(\dot{d}) \mid \dot{d} \right\} \quad (6.85)$$

where r_p and r_d are interpreted as the yield-limits for initiation of plasticity and damage, respectively.

Implementation of this procedure within a material point level is almost easy without any mathematical problem. However, the lack of coercivity and convexity of the corresponding energy function results in an ill-posed boundary value problem in the context of the finite element method. This ill-posedness reveals as mesh dependency both in the global behavior of the system, i.e., force-displacement diagram and in the distribution of internal variables such as damage parameter. It is worth to mention, that this effect comes from the damage behavior, as the plasticity is limited again to the hardening behavior and therefore does not enter a new source of instability.

As explained in Section 6.2, for existence of a solution, two conditions should be fulfilled: *coercivity*, i.e., superlinear growth of energy as a function of strain, and *quasiconvexity* or in stronger form *convexity*, i.e., the stability of the solution regarding superimposed fluctuations of the displacement field. Initially, the ill-posedness of the continuum problem can be removed in a time-incremental procedure. Introducing a dissipation distance within a time increment Δt results in a point-wise minimization problem including condensed energy. A straightforward way to achieve coercivity of the condensed energy is by rate-limitation of the damage evolution.

Although the convexity of the energy is now ensured, the stability of the results will be achieved by calculation of the quasiconvex envelope of the potential. Therefore, the problem will be limited to find the optimal fluctuation by minimization defined on a representative volume element Ω_{rep} of unit volume. Considering the strain field and the damage variable as the two unknown in each time increment leads to a high-dimensional global optimization problem with a numerically expensive solving procedure. Therefore, a specific damage distribution is assumed inside the Ω_{rep} , i.e., what's happening inside Ω_{rep} is not calculated directly, rather it is modeled. This procedure is called *Emulated Representative Volume Element (ERVE)*. More details regarding this approach can be found in Schwarz et al. (2020).

Emulated Representative Volume Element

To describe the damage distribution inside Ω_{rep} , the RVE is divided into a specific number of subdomains of equal volume, which results in the mentioned Emulated Representative Volume Element (ERVE). Each subdomain possesses a constant strain ε_i as well as constant damage d_i . Instead of minimizing with respect to \mathbf{u} , we will do the minimization with respect to all ε_i yielding a given overall strain, resulting in

$$\Psi^{\text{rel}}(\varepsilon, \varepsilon_p, \alpha_p, \{d_i\}) = \inf \left\{ \frac{1}{n} \sum_{i=1}^n f(d_i) \Psi_0(\varepsilon_i, \varepsilon_p, \alpha_p) \mid \varepsilon_i; \varepsilon = \frac{1}{n} \sum_{i=1}^n \varepsilon_i \right\}. \quad (6.86)$$

considering the effective damage function as

$$\bar{f} = n \left[\sum_{i=1}^n \frac{1}{f(d_i)} \right]^{-1}. \quad (6.87)$$

The minimization problem in Equation (6.86) gives

$$\varepsilon_i = \frac{\bar{f}}{f(d_i)} \varepsilon, \quad (6.88)$$

and

$$\Psi^{\text{rel}}(\varepsilon, \varepsilon_p, \alpha_p, \{d_i\}) = \bar{f} \Psi_0, \quad (6.89)$$

The corresponding damage dissipation function is defined as

$$\mathcal{D}_d^{\text{rel}}(\{\dot{d}_i\}) = \frac{1}{n} \sum_{i=1}^n \mathcal{D}_d(\dot{d}_i), \quad (6.90)$$

and evolution of \dot{d}_i is given as

$$\{\dot{d}_i\} = \arg \min \left\{ \dot{\Psi}^{\text{rel}}(\varepsilon, \varepsilon_p, \alpha_p, \{d_i\}) + \mathcal{D}_d^{\text{rel}}(\{\dot{d}_i\}) \mid \{\dot{d}_i\} \right\}. \quad (6.91)$$

We apply the time-incremental setting, which provides the dissipation distance by

$$\Delta \mathcal{D}_d^{\text{rel}}(\{d_{0i}\}, \{d_{1i}\}, \Delta t) = \frac{1}{n} \sum_{i=1}^n \Delta \mathcal{D}_d(d_{0i}, d_{1i}, \Delta t), \quad (6.92)$$

and the corresponding variational formulation by

$$\{d_i\} = \arg \min \left\{ \Psi^{\text{rel}}(\boldsymbol{\varepsilon}, \boldsymbol{\varepsilon}_p, \alpha_p, \{d_i\}) + \Delta \mathcal{D}_d^{\text{rel}}(\{d_{0i}, \{d_{1i}\}, \Delta t) \mid \{d_i\} \right\}. \quad (6.93)$$

The damage driving forces for each subdomains are introduced as

$$p_{d,i} = -\frac{\partial \Psi^{\text{rel}}}{\partial d_i} = -\frac{\bar{f}^2 f'(d_i)}{n f(d_i)^2} \Psi_0. \quad (6.94)$$

Finally, the minimization in Equation (6.91) allows to determine

$$\begin{aligned} p_{d,i} < \frac{r_d}{n} &\Rightarrow d_i = d_{0i} \\ p_{d,i} = \frac{r_d}{n} &\Rightarrow d_{0i} < d_i < d_{0i} + k\Delta t \\ p_{d,i} > \frac{r_d}{n} &\Rightarrow d_i = d_{0i} + k\Delta t \end{aligned} \quad (6.95)$$

Based on our experience, the second case of Equation (6.95) is never realized in numerical simulations. In order to eliminate the rate-dependent results, instead of the positive parameter k , the amount of evolving damage is limited by the power of external forces as

$$\ell_{\text{ext}}(\dot{\mathbf{u}}) = \int_{\Omega} \mathbf{f} \cdot \dot{\mathbf{u}} \, dV + \int_{\partial\Omega} \mathbf{t} \cdot \dot{\mathbf{u}} \, dA \quad (6.96)$$

where for finite element implementation can be calculated as

$$\ell_{\text{ext}}(\dot{\mathbf{u}}) = \frac{\Delta \mathbf{u} \cdot \sum \mathbf{f}^*}{\Delta t} \quad (6.97)$$

with the applied displacement increment $\Delta \mathbf{u} = \mathbf{u}^{m+1} - \mathbf{u}^m$, the rate of damage evolution is then limited to

$$0 \leq \dot{d} \leq \alpha \ell_{\text{ext}} \quad (6.98)$$

where α is a factor to adjust the power of regularization.

Algorithmic Implementation

For the determination of stresses and material tangent, a linearized Taylor expansion is used. Thus, starting with the definition of stress as

$$\tilde{\boldsymbol{\sigma}} = \tilde{\boldsymbol{\sigma}}(\tilde{\boldsymbol{\varepsilon}}, \tilde{\boldsymbol{\varepsilon}}_p, \mathbf{d}) = \bar{f}(\mathbf{d}) \mathbb{E} \cdot (\tilde{\boldsymbol{\varepsilon}} - \tilde{\boldsymbol{\varepsilon}}_p) \quad (6.99)$$

and referring to Equation (4.45), the linearized stresses are given by

$$\tilde{\boldsymbol{\sigma}}^{m+1} = \tilde{\boldsymbol{\sigma}}^m + \left. \frac{\partial \tilde{\boldsymbol{\sigma}}}{\partial \tilde{\boldsymbol{\varepsilon}}} \right|^m \cdot \Delta \tilde{\boldsymbol{\varepsilon}} + \left. \frac{\partial \tilde{\boldsymbol{\sigma}}}{\partial \tilde{\boldsymbol{\varepsilon}}_p} \right|^m \cdot \Delta \tilde{\boldsymbol{\varepsilon}}_p + \left. \frac{\partial \tilde{\boldsymbol{\sigma}}}{\partial \mathbf{d}} \right|^m \cdot \Delta \mathbf{d} \quad (6.100)$$

with $\Delta \tilde{\boldsymbol{\varepsilon}} = \tilde{\boldsymbol{\varepsilon}}^{m+1} - \tilde{\boldsymbol{\varepsilon}}^m$, $\Delta \tilde{\boldsymbol{\varepsilon}}_p = \tilde{\boldsymbol{\varepsilon}}_p^{m+1} - \tilde{\boldsymbol{\varepsilon}}_p^m$, and $\Delta \mathbf{d} = \mathbf{d}^{m+1} - \mathbf{d}^m$ being the increment of strains, plastic strains, and damage variable, respectively, and $\tilde{\boldsymbol{\sigma}}^m$ the stresses from previous time-step. It is important to mention that, here \mathbf{d} is a vector of damage variables with the

length of n corresponds to the number of subdomains in each ERVE. The material tangent can be derived as

$$\left. \frac{d\tilde{\boldsymbol{\sigma}}}{d\tilde{\boldsymbol{\varepsilon}}} \right|^{m+1} = \left. \frac{\partial \tilde{\boldsymbol{\sigma}}}{\partial \tilde{\boldsymbol{\varepsilon}}} \right|^m + \left. \frac{\partial \tilde{\boldsymbol{\sigma}}}{\partial \tilde{\boldsymbol{\varepsilon}}_p} \right|^m \cdot \left. \frac{\partial \tilde{\boldsymbol{\varepsilon}}_p}{\partial \tilde{\boldsymbol{\varepsilon}}} \right|^{m+1} + \left. \frac{\partial \tilde{\boldsymbol{\sigma}}}{\partial \mathbf{d}} \right|^m \cdot \left. \frac{\partial \mathbf{d}}{\partial \tilde{\boldsymbol{\varepsilon}}} \right|^{m+1} \quad (6.101)$$

First, for the plasticity part, similar to Model I, an explicit Euler integration scheme is applied for simplicity, that results in the elimination of the parts regarding the increment of plastic strain, $\Delta \tilde{\boldsymbol{\varepsilon}}_p$, and derivative of plastic strain with respect to the strain, $\partial \tilde{\boldsymbol{\varepsilon}}_p / \partial \tilde{\boldsymbol{\varepsilon}}$, in the current time-step. Consequently, the stresses are resulting in

$$\begin{aligned} \tilde{\boldsymbol{\sigma}}^{m+1} = & \bar{f}(\mathbf{d}^m) \mathbb{E} \cdot (\tilde{\boldsymbol{\varepsilon}}^{m+1} - \tilde{\boldsymbol{\varepsilon}}_p^m) + \\ & \left(\mathbb{E} \cdot (\tilde{\boldsymbol{\varepsilon}}^m - \tilde{\boldsymbol{\varepsilon}}_p^m) \right) \otimes \sum_{j=1}^n \left(\frac{f'(d_j^m)}{n f^2(d_j^m)} \bar{f}(\mathbf{d}^m) e_j \right) \cdot \Delta \mathbf{d} \end{aligned} \quad (6.102)$$

Based on Subsection 4.2.3, and since the damage evolution given by

$$d_i^{m+1} = d_i^m + \alpha \ell_{\text{ext}} \Delta t \quad (6.103)$$

contains a loop of continually changing driving force, it is quite difficult to determine the derivative of vectorial damage with respect to the strain, as needed in Equation (6.101). Therefore, we perform a numerical derivation of the damage derivative by applying the tolerance of $tol = 10^{-8}$ to the Ψ_0 , i.e.,

$$\begin{aligned} \left. \frac{\partial \mathbf{d}}{\partial \tilde{\boldsymbol{\varepsilon}}} \right|^{m+1} &= \left. \frac{\partial \mathbf{d}}{\partial \Psi_0} \right|^{m+1} \otimes \left. \frac{\partial \Psi_0}{\partial \tilde{\boldsymbol{\varepsilon}}} \right|^{m+1} \\ &= \frac{\mathbf{d}_{tol}^{m+1}(\Psi_0^{m+1} + tol) - \mathbf{d}^{m+1}(\Psi_0^{m+1})}{tol} \otimes \left(\mathbb{E} \cdot (\tilde{\boldsymbol{\varepsilon}}^{m+1} - \tilde{\boldsymbol{\varepsilon}}_p^m) \right) \end{aligned} \quad (6.104)$$

Finally, inserting Equation (6.104) into Equation (6.101), the material tangent provides as

$$\begin{aligned} \left. \frac{d\tilde{\boldsymbol{\sigma}}}{d\tilde{\boldsymbol{\varepsilon}}} \right|^{m+1} &= \bar{f}(\mathbf{d}^m) \mathbb{E} + \left(\mathbb{E} \cdot (\tilde{\boldsymbol{\varepsilon}}^m - \tilde{\boldsymbol{\varepsilon}}_p^m) \right) \otimes \sum_{j=1}^n \left(\frac{f'(d_j^m)}{n f^2(d_j^m)} \bar{f}(\mathbf{d}^m) e_j \right) \cdot \\ & \frac{\mathbf{d}_{tol}^{m+1}(\Psi_0^{m+1} + tol) - \mathbf{d}^{m+1}(\Psi_0^{m+1})}{tol} \otimes \left(\mathbb{E} \cdot (\tilde{\boldsymbol{\varepsilon}}^{m+1} - \tilde{\boldsymbol{\varepsilon}}_p^m) \right) \end{aligned} \quad (6.105)$$

The numerical implementation of this procedure on the material point level results in the following simple Algorithm 2.

Algorithm 2: Model II: Rate-independent finite element algorithm

input: $\boldsymbol{\varepsilon}^{m+1}, \boldsymbol{\varepsilon}_p^m, \alpha_p^m, \mathbf{d}^m, \ell_{\text{ext}}$

Set: $\mathbf{d}^{m+1} = \mathbf{d}^m, \boldsymbol{\varepsilon}_p^{m+1} = \boldsymbol{\varepsilon}_p^m, \alpha_p^{m+1} = \alpha_p^m$

Check for plastic process

calc: $\Phi_p(\boldsymbol{\varepsilon}^{m+1}, \boldsymbol{\varepsilon}_p^{m+1}, \alpha_p^{m+1}, \mathbf{d}^{m+1})$

if $\Phi_p > 0$ **then**

$$\left[\begin{array}{l} \boldsymbol{\varepsilon}_p^{m+1} = \boldsymbol{\varepsilon}_p^{m+1} + \Delta\rho \bar{f}(d^{m+1}) \text{dev}\mathbb{E} : (\boldsymbol{\varepsilon}^{m+1} - \boldsymbol{\varepsilon}_p^{m+1}) \\ \alpha_p^{m+1} = \alpha_p^{m+1} + \Delta\rho(r_p + K_H \alpha_p^{m+1}) \end{array} \right.$$

Check for damage process

for $i = 1, \dots, n$ **do**

calc: $p_{d,i}(\boldsymbol{\varepsilon}^{m+1}, \boldsymbol{\varepsilon}_p^{m+1}, \alpha_p^{m+1}, \mathbf{d}^{m+1})$

if $p_{d,i} > \frac{r_d}{n}$ **then**

$$\left[d_i^{m+1} = d_i^{m+1} + \alpha \ell_{\text{ext}} \Delta t \right.$$

if $d_i^{m+1} > 0.999$ **then**

$$\left[\text{set: } d_i^{m+1} = 0.999 \right.$$

set: $\mathbf{d}^{m+1}(d_i^{m+1})$

calc: $\tilde{\boldsymbol{\sigma}}^{m+1} = \tilde{\boldsymbol{\sigma}}(\boldsymbol{\varepsilon}^{m+1}, \boldsymbol{\varepsilon}_p^m, \alpha_p^m, \mathbf{d}^{m+1})$

calc: $\frac{d\tilde{\boldsymbol{\sigma}}^{m+1}}{d\tilde{\boldsymbol{\varepsilon}}^{m+1}} = \frac{d\tilde{\boldsymbol{\sigma}}}{d\tilde{\boldsymbol{\varepsilon}}}(\boldsymbol{\varepsilon}^{m+1}, \boldsymbol{\varepsilon}_p^m, \alpha_p^m, \mathbf{d}^{m+1})$

7 Model Comparison with Finite Element Results

This chapter aims to present the numerical results obtained in the simulations utilizing the two coupled damage-plasticity material models introduced in Chapter 6. In the following, the behavior of material models is distinguished utilizing several problems. The numerical examples involving gradient-enhanced damage-plastic material model are presented in Section 7.1, while the examples employing the relaxation-based regularized damage-plastic material model are given in Section 7.2. The influence of regularization on the material behavior is investigated using two regularization states for each material model; i.e., almost localized state and strongly regularized one. For each case, two different boundary value problems including three mesh discretization levels are considered. Furthermore, the solution of each boundary value problem provides the global response in terms of force-displacement diagrams and distribution of internal parameters, such as damage function and accumulative plastic strain. Finally, in Section 7.3 a comparative discussion of material models is presented.

7.1 Model I: Gradient-enhanced Damage-Plastic Material

In this chapter, the calculation results presented utilizing the Laplacian damage model coupled with plasticity, Model I. Two appropriate examples are selected that illustrate the influence of the regularization procedure and mesh-independent behavior. The first one introduces the results of a square specimen with a circular hole in its middle, while the second one represents an asymmetrically notched specimen. The material parameters presented in Table 7.1 are applied in the calculations. The selected results of the tests have presented in the following.

Table 7.1: Material parameters used in the numerical examples in conjunction with the gradient enhanced damage model coupled with plasticity

E [MPa]	ν [-]	r_d [MPa]	r_p [MPa]	K_H [MPa]
200000	0.33	0.05	60	8000

7.1.1 Plate with a Circular Hole

The first example is a plate with a circular hole in the center subjected to tension applied as a uniform displacement at the top and bottom ends of the specimen in opposite directions. The actual boundary value problem and the specimen dimension have illustrated in Figure 7.1. Due to symmetry, only one-fourth of the model has simulated. The simulation has repeated using different mesh sizes. The chosen coarse mesh has 900 elements, the middle-size one

has 4038, and the fine mesh consists of 8014, see Figure 7.2. For reducing the computation time, the refinement accomplishes only in the area where the damage expects to occur.

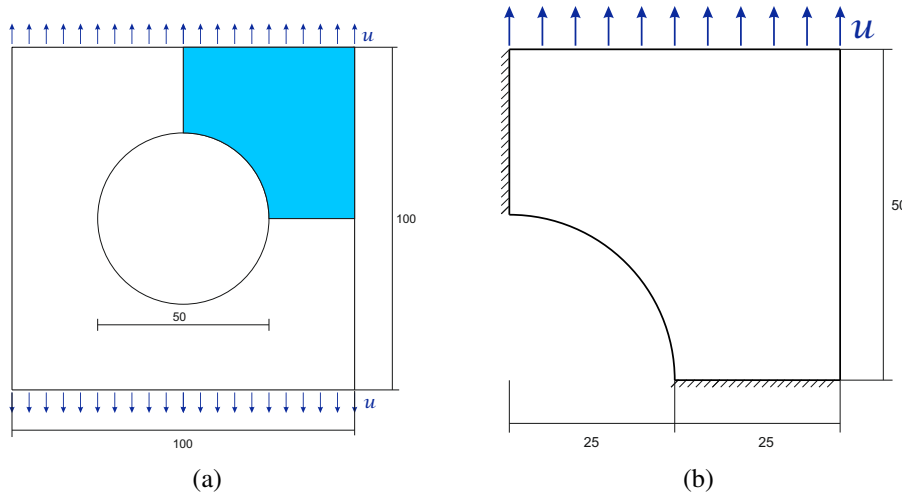


Figure 7.1: Plate specimen with circular hole (a) Geometry and dimensions [mm], (b) Considered boundary value problem. Thickness is 3 mm.

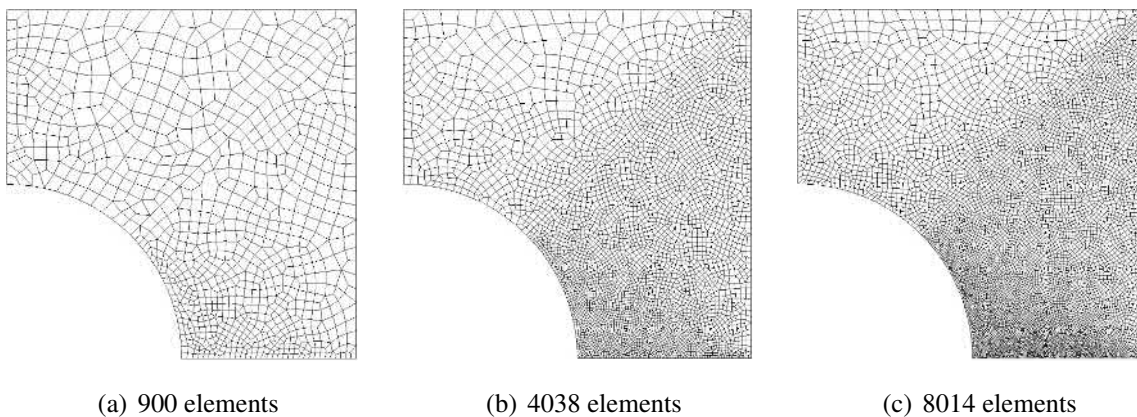


Figure 7.2: Finite element meshes with (a) 900 elements, (b) 4038 elements, and (c) 8014 elements for plate specimen with circular hole

The damage initiates at the cavity on the left-hand side and progresses horizontally towards the outer edge of the specimen until it reaches the right edge that has considered as fully-damaged. The procedure has illustrated in Figure 7.3, consists of the damage distribution in three states labeled as damage initiation, intermediate stage, and fully-damaged state.

As explained in Chapter 6, characteristic localization conducts to instabilities and mesh-dependent results. Two different values of the regularization parameter considered for analyzing its influence on the local and global material behavior. An almost-local damage distribution with $\beta = 0.1$ [MPa mm²] and a parameter related to a regularized damage distribution with $\beta = 1$ [MPa mm²] have been chosen. Hereto, the structural response in terms of force-displacement diagram has been presented in Figures 7.4 and 7.5, respectively. In the almost-local version of the model, $\beta = 0.1$, as damage propagates through the specimen, a slight difference between the curves becomes visible, which originates from the effect of weak regularization. For the case with larger value of β , which is a strongly regularized

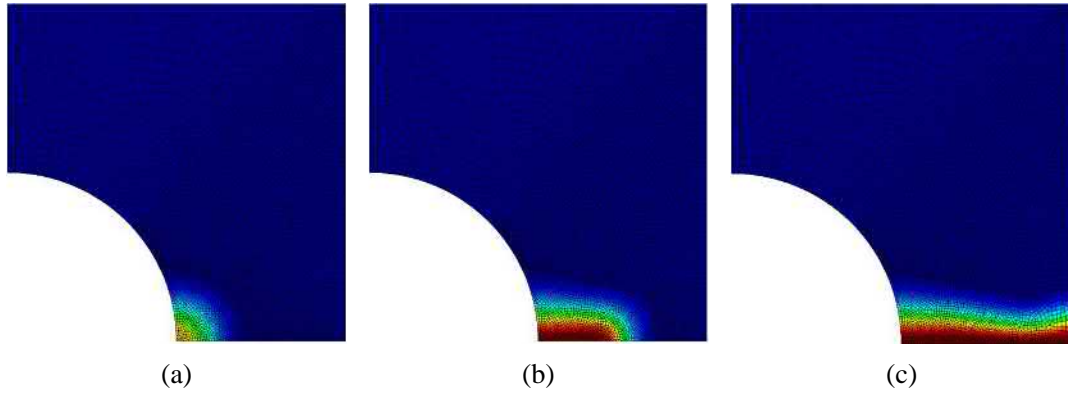


Figure 7.3: Damage distribution with $\beta = 1$ [MPa mm²] for the plate specimen for various states (a) Damage initiation (b) Intermediate stage and (c) Fully-damaged state. The results correspond to the mesh with 4038 elements.

version of the model, the mesh convergence is noticeable. Besides, increasing the regularization parameter results in a bigger plastic zone and thus a larger maximum load, where the damage begins. The points at which the damage snapshots of Figure 7.3 have been taken are marked with blue dots in the diagram of Figure 7.5.

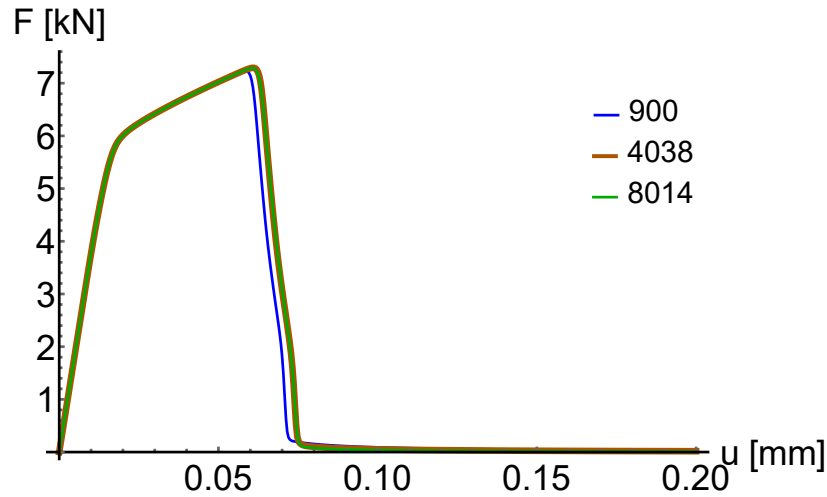


Figure 7.4: Force-displacement diagram for plate specimen with $\beta = 0.1$ [MPa mm²]. Comparisons are presented for different mesh sizes: 900, 4038 and 8014 elements

The corresponding plastic hardening parameter (α_p) increases in the direction of the induced crack. The width of the shear bands are finite and independent of the used spatial discretization. It begins from the minimum value of almost zero (e.g., -3.0×10^{-5}) and ends up with the maximum value of 0.006 at the end of the simulation, see Figure 7.6. Note that the scale bar for the contour levels for both simulations is the same. Figure 7.7 depicts the damage contours of three different discretizations. The damaged zone has been limited to a thin area (colored in red) at the bottom edge of the specimen, as the β decreases. It identifies a crack in a continuous sense. It is important to point out that the damaged zone remains almost unchanged for the different mesh sizes at both values of β . It proves that the material model is mesh-independent. We have also to mention that β is an input parameter, which has to be chosen based on the behavior of a real physical material.

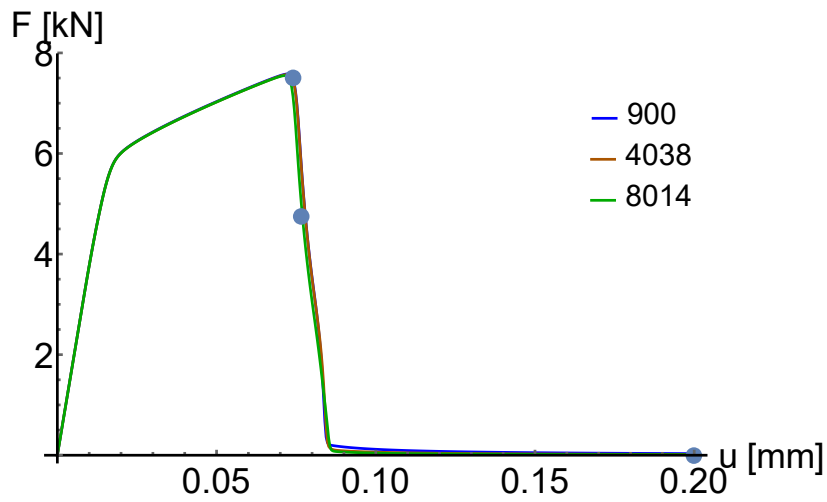


Figure 7.5: Force-displacement diagram for regularized version of the model, i.e $\beta = 1$ [MPa mm²]. Comparisons are presented for different mesh sizes: 900, 4038 and 8014 elements

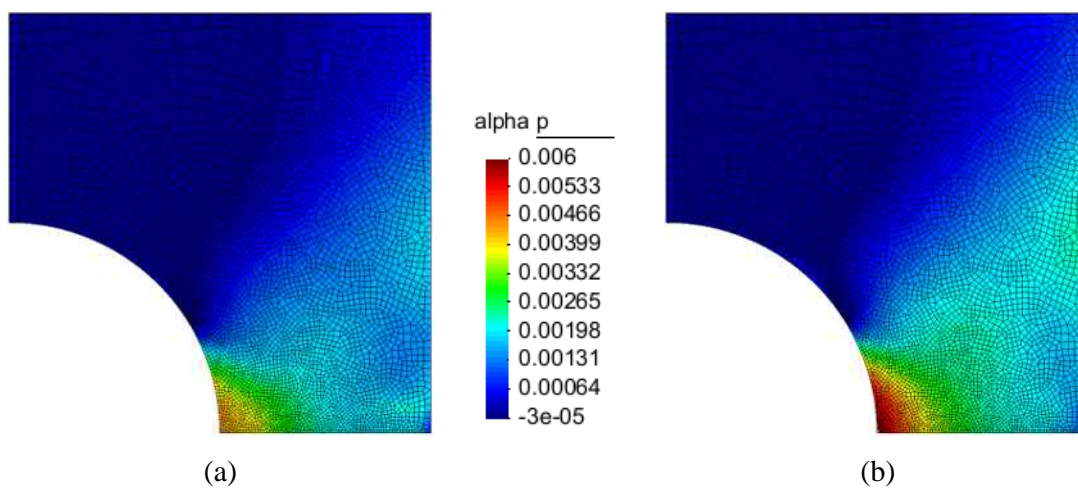


Figure 7.6: Distribution of the plastic hardening parameter with (a) $\beta = 0.1$ [MPa mm²] and (b) $\beta = 1$ [MPa mm²] for the plate specimen with 4038 elements.

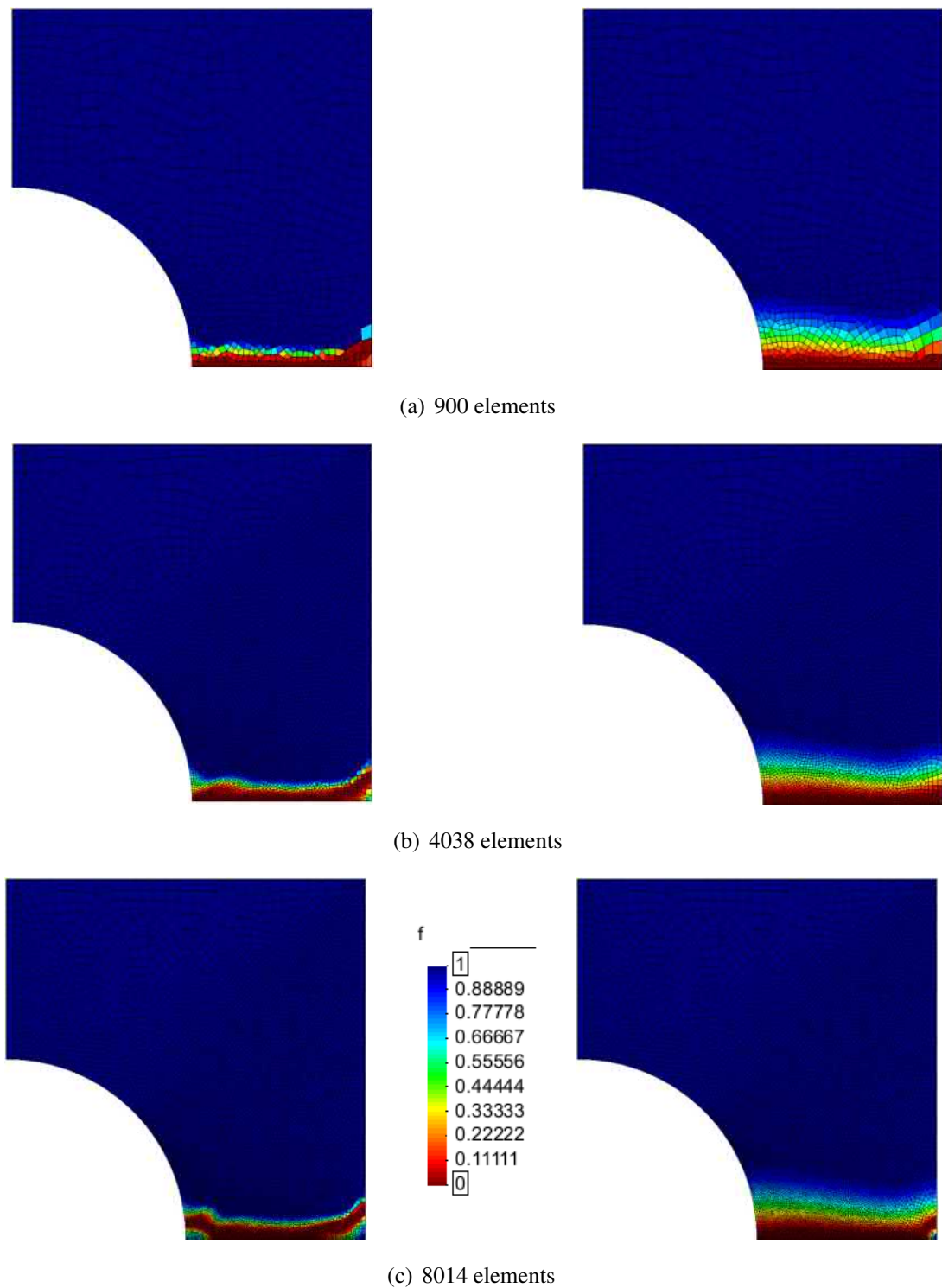


Figure 7.7: Damage distribution with $\beta = 0.1$ [MPa mm²] (left-hand side) and $\beta = 1$ [MPa mm²] (right-hand side) for the plate specimen with (a) 900 elements, (b) 4038 elements and (c) 8014 elements

7.1.2 Double-notched Specimen

The next boundary value problem deals with a double-notched specimen subjected to a vertically time-dependent displacement u at the top edge and fixed at the bottom edge. The boundary value problem and its corresponding finite element discretizations have illustrated in Figure 7.8. In all the simulations, a coarse mesh with 1010 elements, a middle-size mesh with 4033 elements, and a fine mesh with 8477 elements have considered. The focus of refinement is on the center part of the specimen, where the damage process expects to occur.

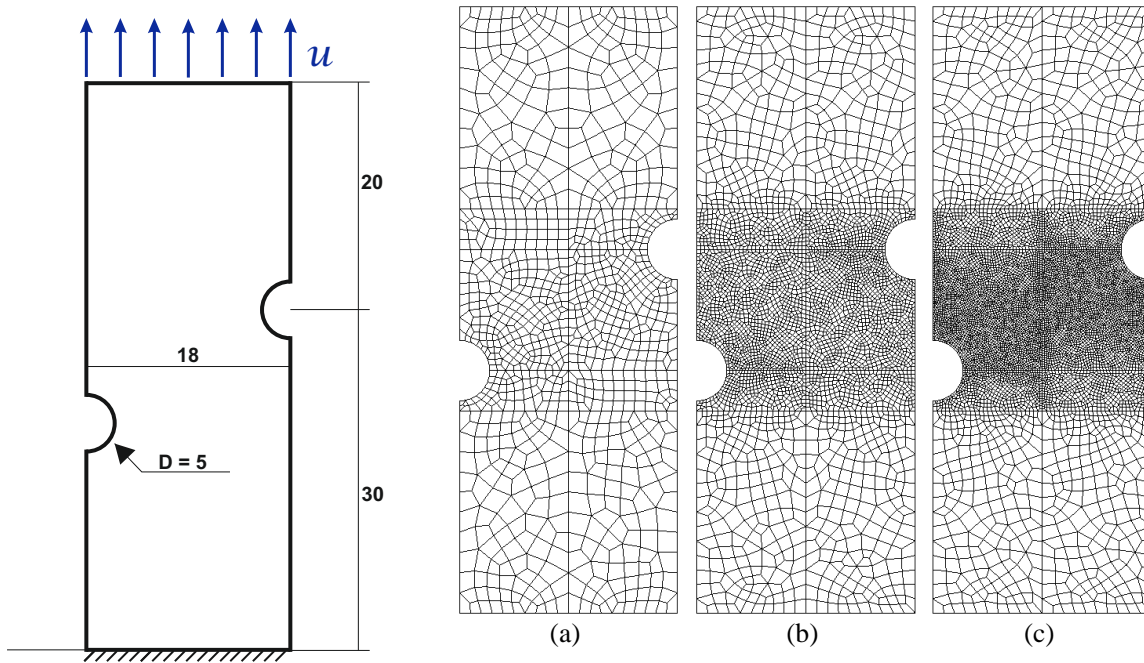


Figure 7.8: (left) Double-notched specimen with its dimensions [mm] and loading. Thickness is 3 mm, which is discretized with one finite element, (right) Finite element meshes with (a) 1010 elements, (b) 4033 elements, and (c) 8477 elements for the double-notched specimen

Similar to the first example, two values are considered for β to compare the regularization effect: $\beta = 0.1$ [MPa mm²] for almost-local case and $\beta = 1$ [MPa mm²] for regularized case. Figure 7.9 illustrates the damage contours in three different stages, marked with blue dots on the force-displacement curve, for mesh discretization with 4033 elements at both values of $\beta = 0.1$ at the top row and $\beta = 1$ at the bottom row. At the first stage, the damage begins independently at the root of each notch and then spreads rapidly toward each other. In almost-local case ($\beta = 0.1$), the final damage zone looks like nearly two independent cracks. Possible differences in the shape of the damaged area of the last time-step at the top row coincide with the fluctuation of the force-displacement diagram, where the large reduction of stress happens in a small time interval. It will not have a significant influence on practical applications. These time-steps present the states in which the global stiffness reduces remarkably.

In the regularized case ($\beta = 1$), the two initiated cracks meet at the middle to form a thick damage zone placed diagonally within the specimen. This behavior leads to a fully damaged area that has an almost “S-shape”. When the gradient parameter reduces to smaller

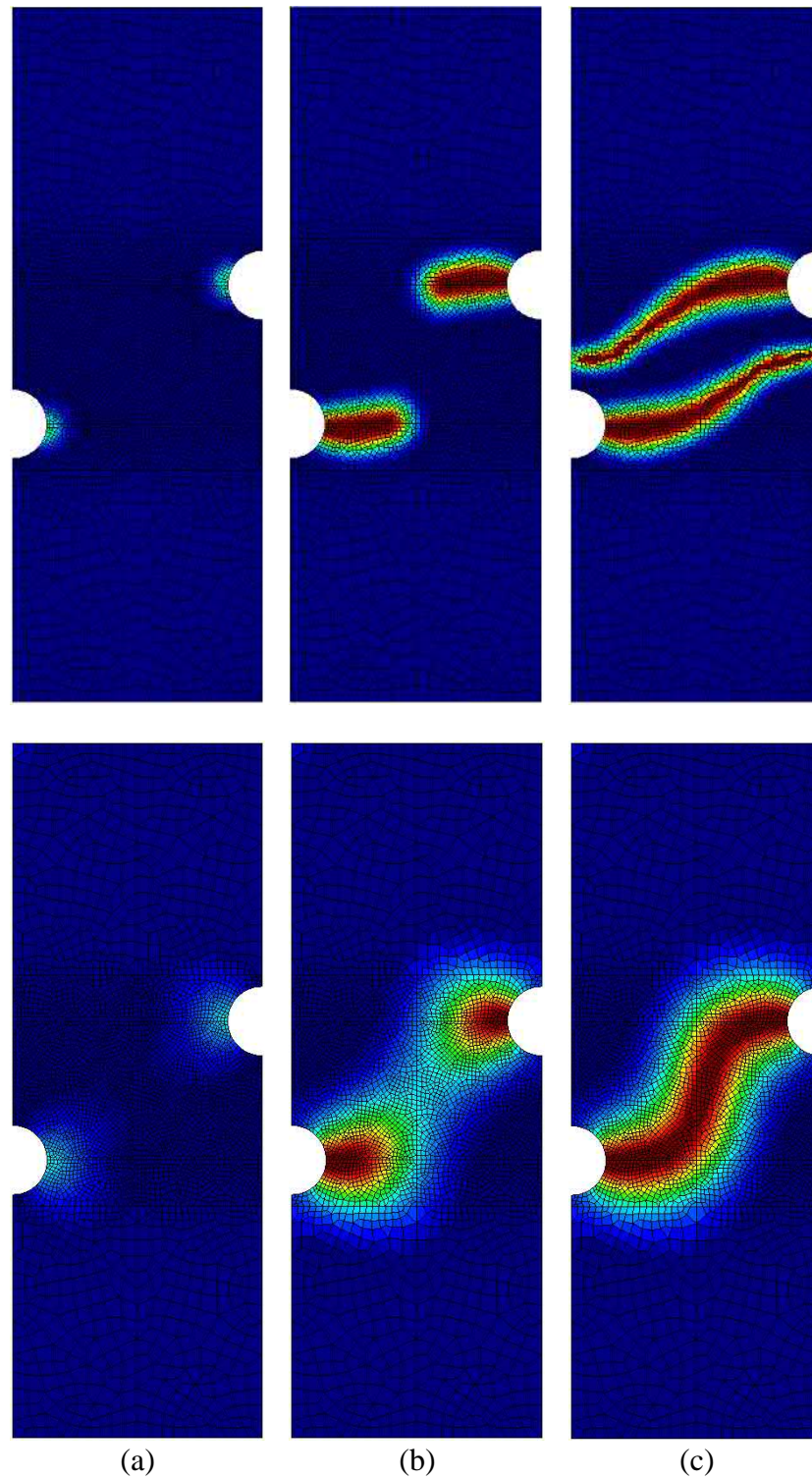


Figure 7.9: Damage distribution with $\beta = 0.1$ [MPa mm²] (top row) and $\beta = 1$ [MPa mm²] (bottom row) for the double-notched specimen for various states (a) Damage initiation (b) Intermediate stage and (c) Fully-damaged state. The results correspond to the mesh with 4033 elements.

values, then the width of the damage zone shrinks more. Therefore localization occurs in a relatively narrower area. Furthermore, in the global response of structure for smaller values of β (Figure 7.10), in contrast to the force-displacement diagram for regularized case (Figure 7.11), the point of maximum load decreases and shifts to the left. It is reasonable due to the

thin totally damaged zone that may interpret as a crack in the continuous sense. It could be assumed as a transition from damage modeling to fracture mechanics. In continuum damage mechanics, cracks are smeared out over a failure zone where the displacement is still continuous. In fracture mechanics, displacement is discontinuous through the crack face that can propagate only between elements.

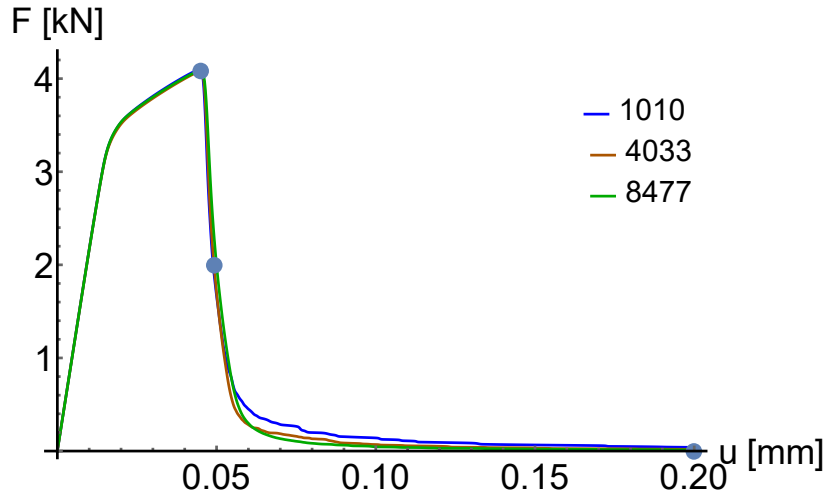


Figure 7.10: Force-displacement diagrams for almost-local version of the model, i.e $\beta = 0.1$ [MPa mm²] for double-notched specimen. Comparisons are presented for different mesh sizes: 1010, 4033 and 8477 elements

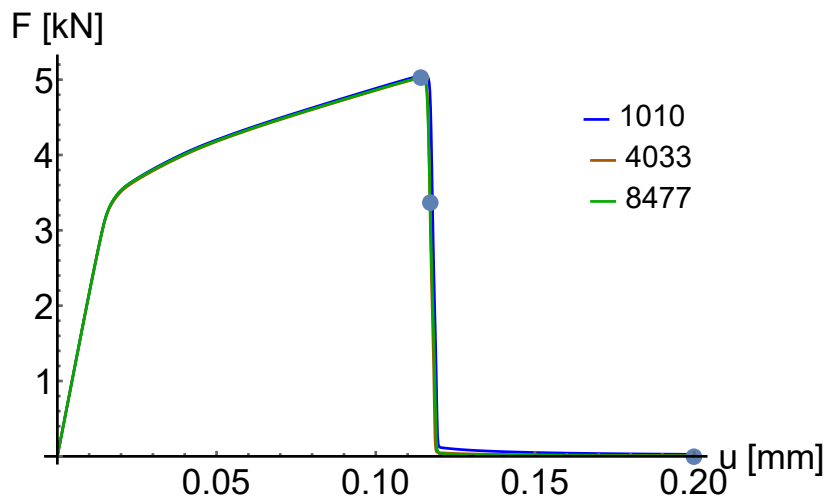


Figure 7.11: Force-displacement diagrams for regularized version of the model, i.e $\beta = 1$ [MPa mm²] for double-notched specimen. Comparisons are presented for different mesh sizes: 1010, 4033 and 8477 elements

The corresponding contours for accumulative plastic strain are illustrated in Figure 7.12 for mesh with 4033 elements in both values of $\beta = 0.1$ on the left-hand side and $\beta = 1$ on the right-hand side. The influence of gradient parameter on the shear bands is more obvious in this example, where for a larger value of β , a wider shear band with a larger maximum value for α_p occurs. Figure 7.13 is also used to illustrate the damage contours for different meshes to prove the obtained mesh-independent results for both values of β .

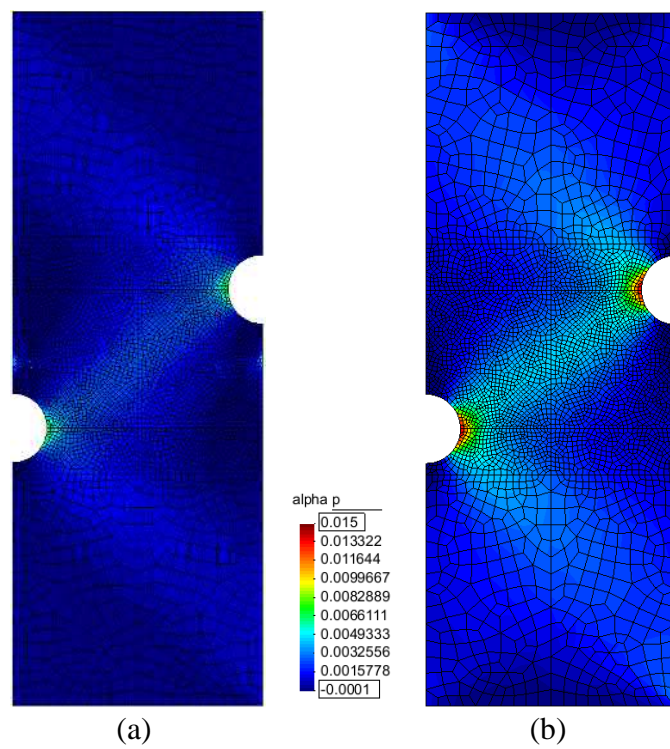


Figure 7.12: Distribution of the plastic hardening parameter with (a) $\beta = 0.1$ [MPa mm²] and (b) $\beta = 1$ [MPa mm²] for double-notched specimen with 4033 elements.

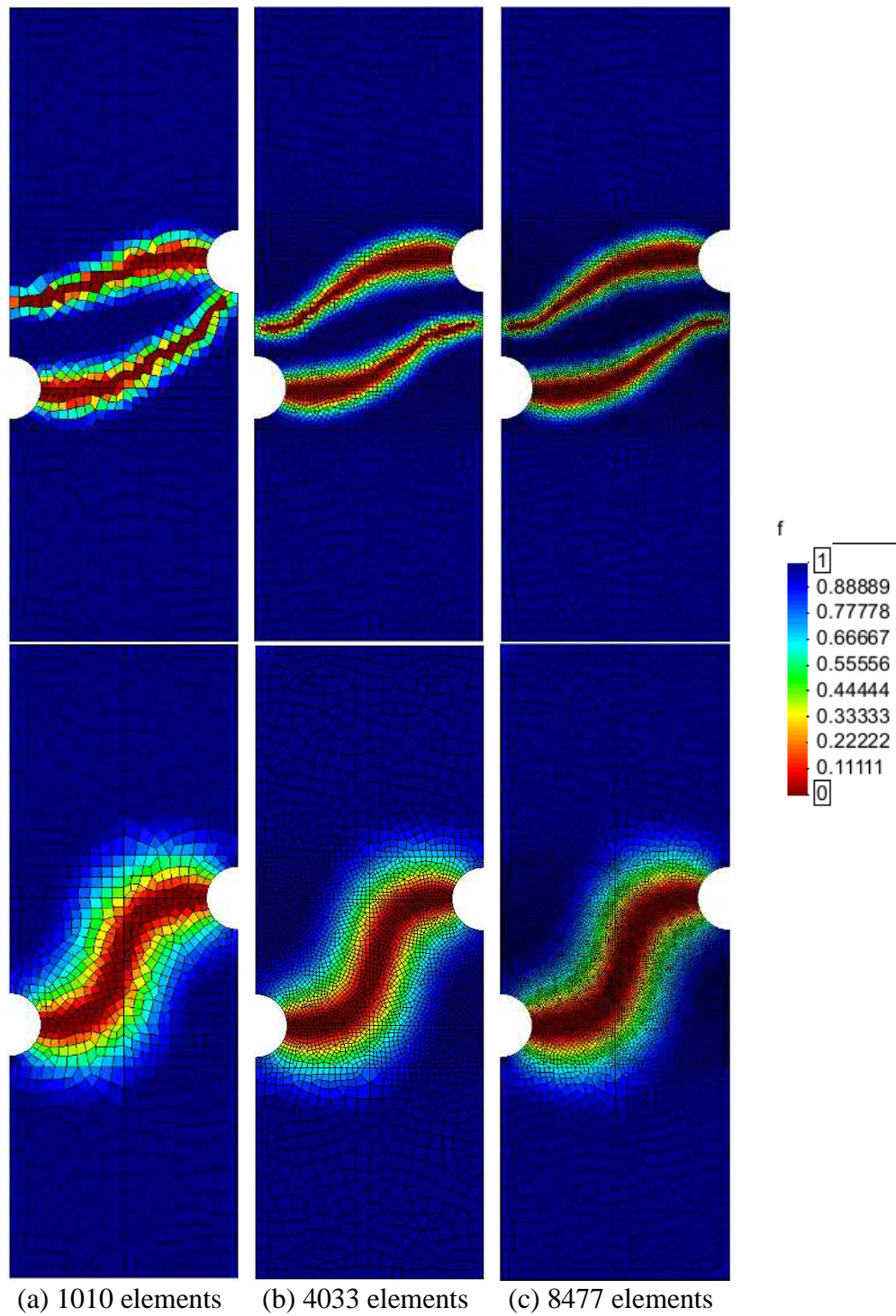


Figure 7.13: Damage distribution with $\beta = 0.1$ [MPa mm²] (top row) and $\beta = 1$ [MPa mm²] (bottom row) for double-notched specimen with (a) 1010 elements, (b) 4033 elements and (c) 8477 elements

7.2 Model II: Relaxation-based Regularized Damage-Plastic Material

The focus of this section is investigating the behavior of the ERVE material, i.e., Model II. For this purpose, two representative examples have considered. The first simulation is a rectangular brick with a preexisting crack known as a sharp notch specimen. The second one is the same problem treated in Subsection 7.1.2. The material model parameters used in these calculations have specified in Table 7.2. The selected results of the tests have presented in the rest of this section.

Table 7.2: Material parameters used in the numerical examples in conjunction with the ERVE damage model coupled with plasticity

E [MPa]	ν [-]	r_d [MPa]	n [-]	Δt [s]	r_p [MPa]	K_H [MPa]
200000	0.33	0.1	20	1	60	8000

7.2.1 Sharp Notch Specimen

The first boundary value problem for representing the results of Model II is a rectangular specimen with the dimension of 50×40 mm and a 25 mm sharp horizontal notch on the left-hand side, subjected to a time proportional displacement u applied on the top and bottom edges. Due to symmetry, only one-half of the specimen has simulated (highlighted in blue). The geometry and the actual boundary value problem with its dimensions have illustrated in Figure 7.14. The Finite element results are presented for three mesh sizes, coarse mesh with 996 elements, middle-size one with 4080 elements, and fine one with 8046 elements. The sharp notch results in a stress singularity at the bottom edge right in the center. Consequently, the refinement is mainly limited to this area, Figure 7.15.

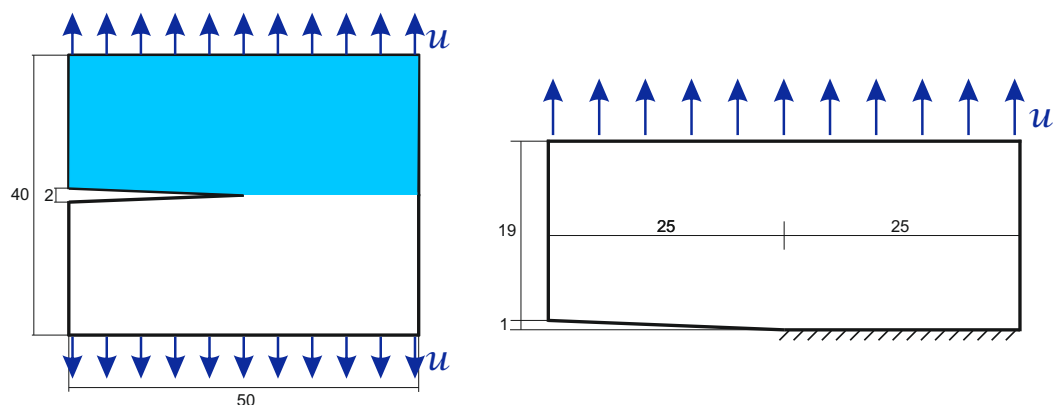
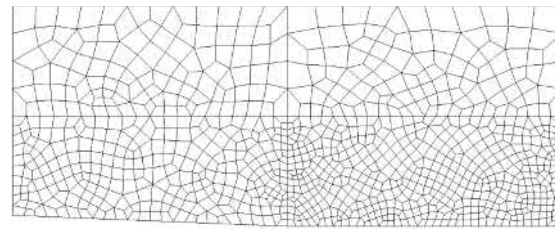
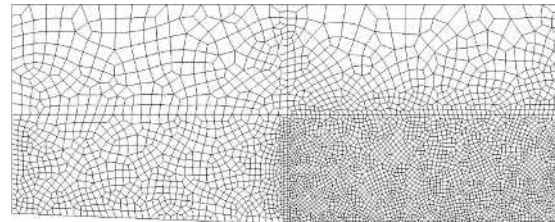


Figure 7.14: Sharp notch specimen with its dimensions [mm] and loading. Thickness is 3 mm, which is discretized with one finite element.

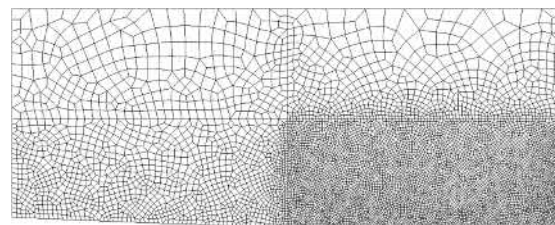
For Model II, two stages of regularization using different values of regularization parameter have considered; i.e., $\alpha = 0.05$ [1/(N mm)] applies only a slight regularization to keep the damage distribution almost-local and $\alpha = 0.005$ [1/(N mm)] provides stronger regularized damage distribution. The force-displacement curves for the three finite element meshes are shown in Figures 7.16 and 7.17 for $\alpha = 0.05$ and $\alpha = 0.005$ [1/(N mm)], respectively.



(a) 996 elements



(b) 4080 elements



(c) 8046 elements

Figure 7.15: Finite element meshes with (a) 996 elements, (b) 4080 elements, and (c) 8046 elements for the sharp notch specimen.

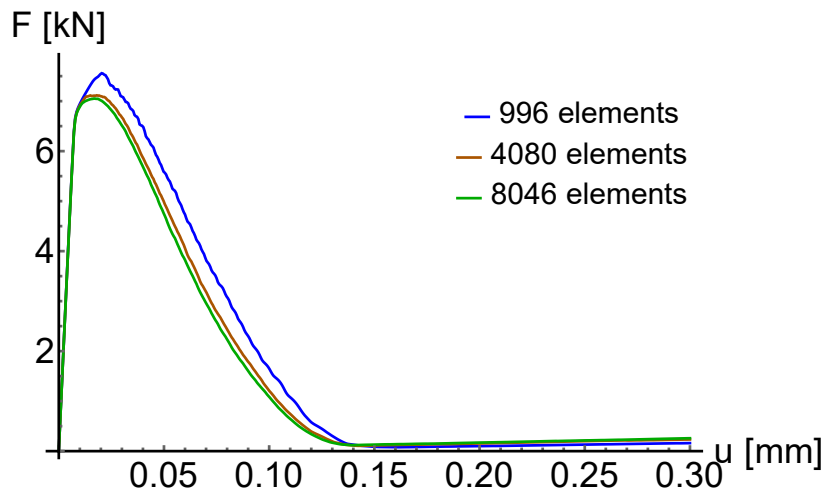


Figure 7.16: Force-displacement diagrams for almost-local version of the model, i.e. $\alpha = 0.05$ [1/(N mm)] for sharp notch specimen. Comparisons are presented for different mesh sizes: 996, 4080, and 8046 elements.

It depicts that for the lower values of α , the damage occurs earlier and results in lower maximum reaction force F . Consequently, a smaller plastic zone is also observable. Comparing the diagrams of different values of α shows that for almost-local damage ($\alpha = 0.05$), there is a slight mesh-dependency as expected. However, by improving the regularization effect,

the mesh-independency proved. As an alternative interpretation, the coarse mesh cannot capture the sharp cracks accurately.

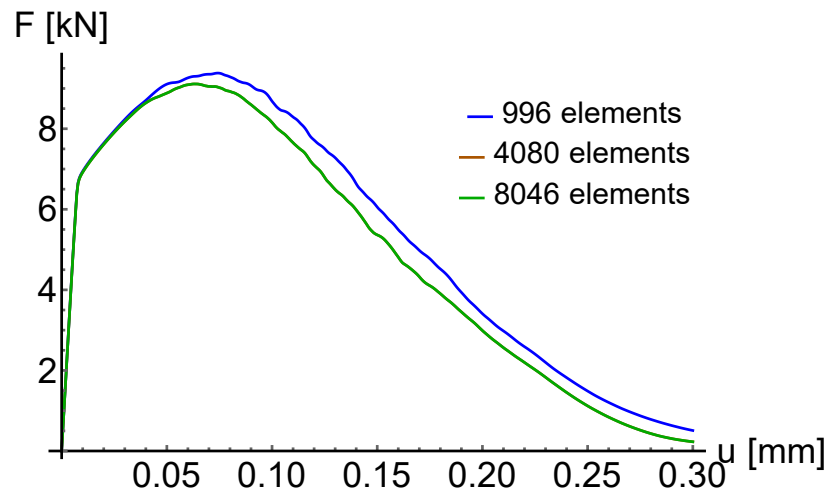


Figure 7.17: Force-displacement diagrams for regularized version of the model, i.e $\alpha = 0.005$ [1/(N mm)] for sharp notch specimen. Comparisons are presented for different mesh sizes: 996, 4080, and 8046 elements.

As illustrated in Figure 7.18 for three mesh discretization, the damage starts to develop at the notch tip and progresses towards the outer right edge until the specimen has considered fully damaged. It proves that our algorithm can consider the transitions from undamaged to the damaged zones. The results for $\alpha = 0.05$ [1/(N mm)] are given on the left-hand side, whereas those for $\alpha = 0.005$ [1/(N mm)] are drawn on the right-hand side. In case of localized damage, the totally damaged zone (area in red color) forms a thin and sharp area, which recognizes as a crack. However, using a stronger regularization effect results in a wider damage zone. The plastic hardening parameter or accumulative plastic strain develops in this region in the range of $[-5 \times 10^{-6}, 0.022]$. It has presented in Figure 7.19 for the middle-size mesh with 4080 elements. When the value of α decreases, then the width of the shear band increases. It has the same effect on the maximum value of α_p within the bands. Comparing the meshes related to the damage distribution shows a good agreement and proves that the mesh is strongly independent.

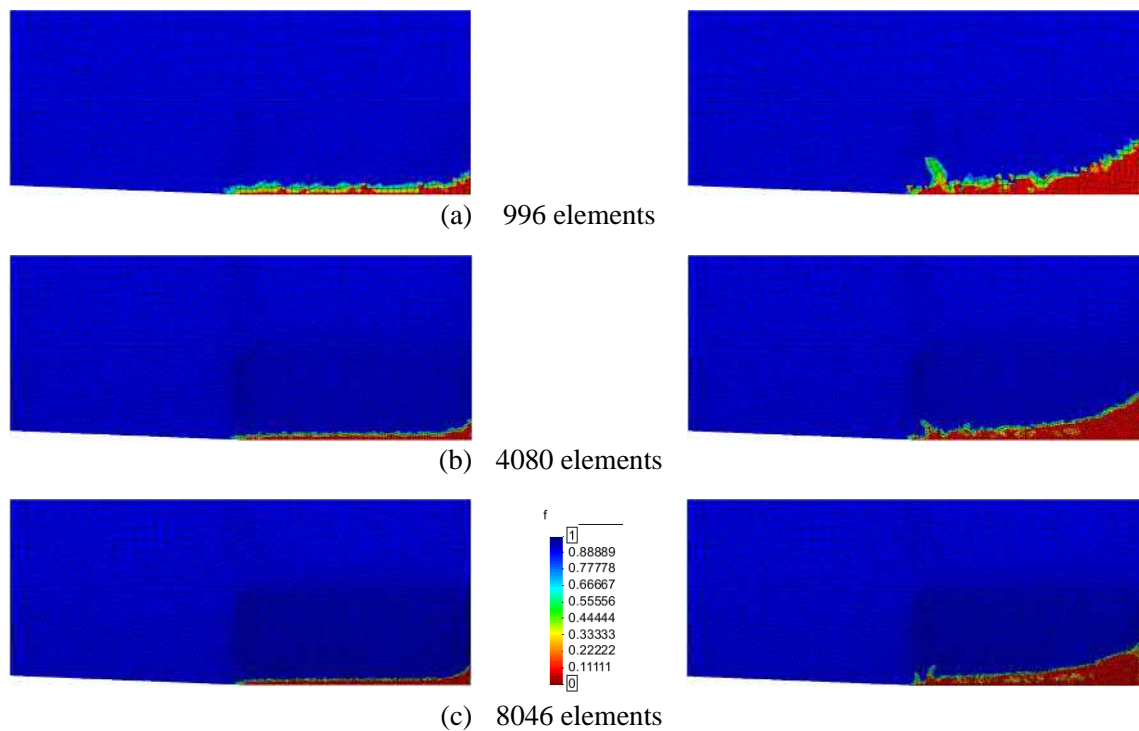


Figure 7.18: Damage distribution with $\alpha = 0.05$ [1/(N mm)] (left) and $\alpha = 0.005$ [1/(N mm)] (right) for sharp notch specimen with (a) 996 elements, (b) 4080 elements and (c) 8046 elements

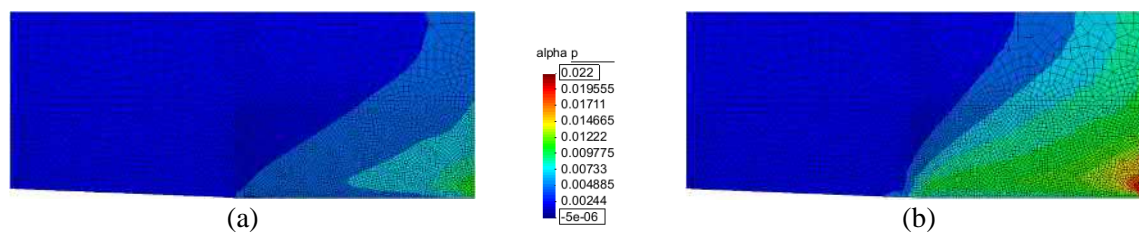


Figure 7.19: Distribution of the plastic hardening parameter with $\alpha = 0.05$ [1/(N mm)] (left) and $\alpha = 0.005$ [1/(N mm)] (right) for sharp notch specimen with 4080 elements.

7.2.2 Double-notched Specimen

The geometry of the problem with the finite element discretization has explained in Figure 7.8. For this example, selected results are again presented for two different values of regularization parameter; i.e $\alpha = 0.05$ [1/(N mm)] for almost localized damage and $\alpha = 0.005$ [1/(N mm)] for stronger regularized damage.

Taking into account the global structural response, a perfect agreement in terms of force-displacement curves are underlined in Figures 7.20 and 7.21 for $\alpha = 0.05$ [1/(N mm)] and $\alpha = 0.005$ [1/(N mm)], respectively. Generally, weaker regularized damage comes with a steep decrease in global structural responses due to sudden crack initiation and propagation, which will verify in the following force-displacement curves.

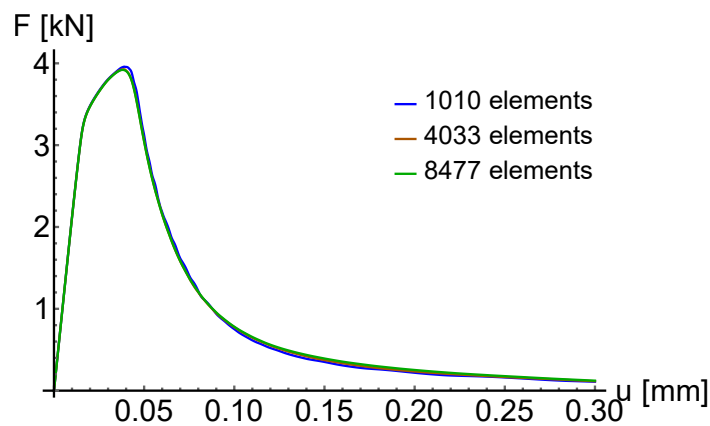


Figure 7.20: Force-displacement diagrams for almost-local version of the model, i.e $\alpha = 0.05$ [1 / (N mm)] for double-notched specimen. Comparisons are presented for different mesh sizes: 1010, 4033, and 8477 elements.

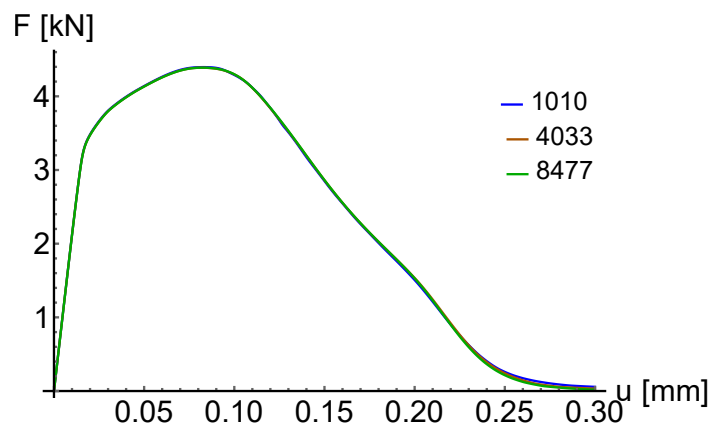


Figure 7.21: Force-displacement diagrams for regularized version of the model, i.e $\alpha = 0.005$ [1 / (N mm)] for double-notched specimen. Comparisons are presented for different mesh sizes: 1010, 4033, and 8477 elements.

The corresponding contours of equivalent plastic strain α_p , shown in Figure 7.22 for $\alpha = 0.05$ [1 / (N mm)] on the left-hand side and $\alpha = 0.005$ [1 / (N mm)] on the right-hand side, illustrate that accumulative plastic strain propagate almost in the same region as the damage function. Figure 7.23 shows the damage distribution for three mesh discretization in the slight (left-hand side) and strong (right-hand side) regularization state. The main

characteristic of Model II is similar to the one of Model I: two cracks initiate independently at the root of notches and propagate rapidly to the opposite edges. Due to the respective damage model, some dissimilarities can be observed in the damage distribution, especially at the end of the simulation. For $\alpha = 0.05$ [1 / (N mm)], the cracks tend completely horizontally toward the opposite side and not to the opposite notch, as previously observed in Figure 7.13 for the material model I. Moreover, in the strongly regularized case, the initiated cracks merged at the middle of the specimen to form an “I-shape” thick damage zone.

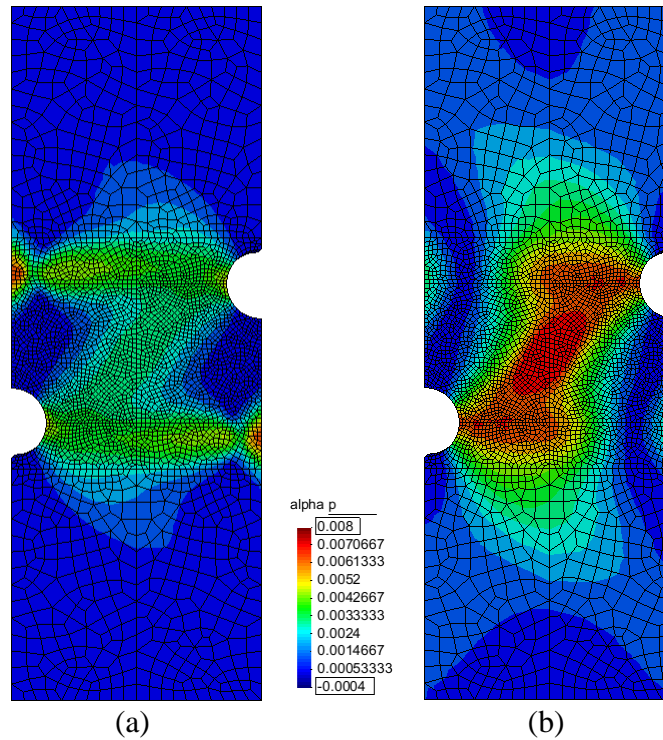


Figure 7.22: Distribution of the accumulated plastic strain with (a) $\alpha = 0.05$ [1 / (N mm)] and (b) $\alpha = 0.005$ [1 / (N mm)] for double-notched specimen with 4033 elements.

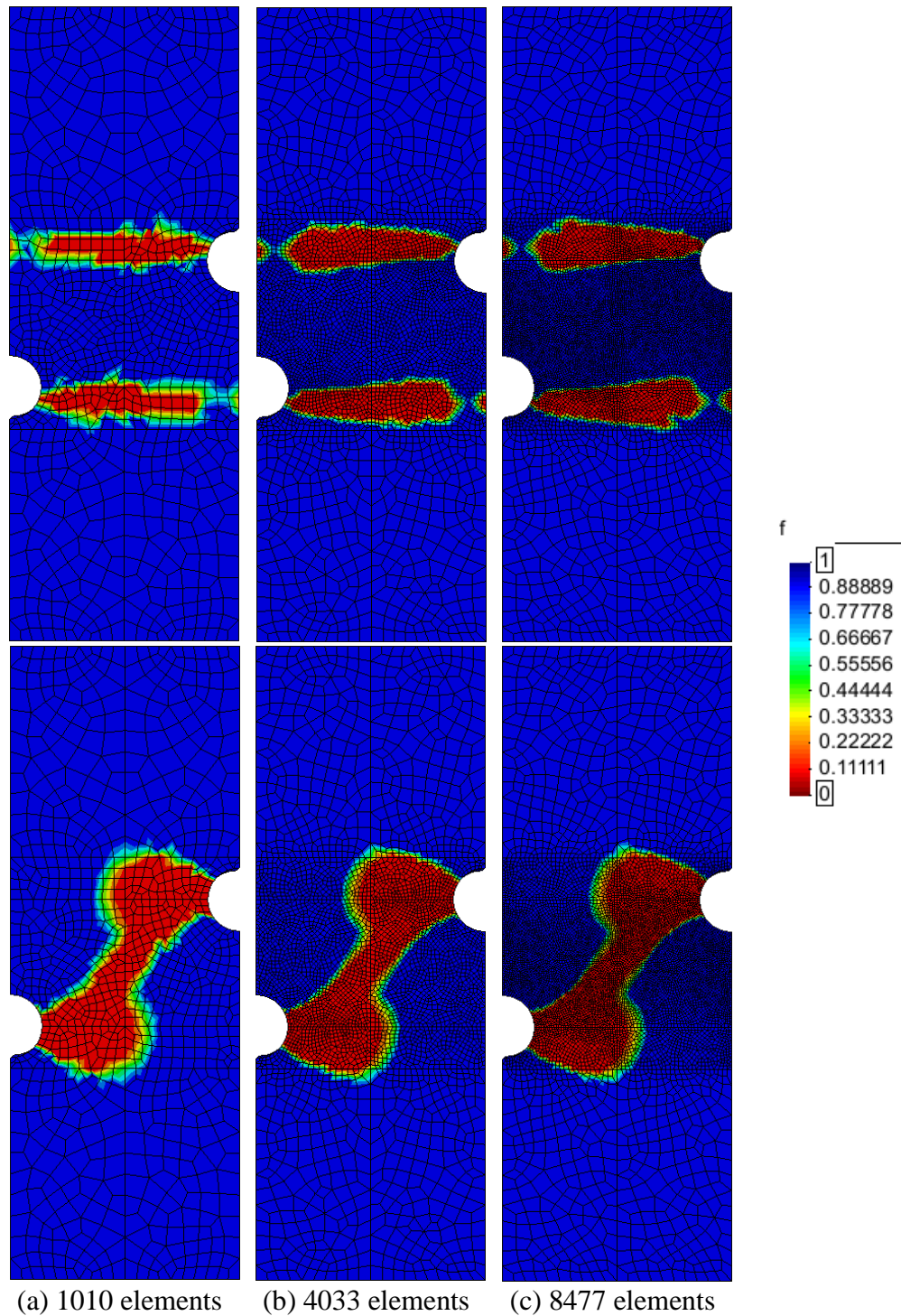


Figure 7.23: Damage distribution with $\alpha = 0.05$ [1 / (N mm)] (Top) and $\alpha = 0.005$ [1 / (N mm)] (Bottom) for double-notched specimen with (a) 1010 elements, (b) 4033 elements, and (c) 8477 elements.

7.3 Comparative Discussion

In this chapter, the finite element results of several examples are carried out and discussed to prove the applicability of the two developed damage-plastic material models, Model I and Model II. Simulations performed for localized damage corresponding to a brittle-like behavior and regularized damage corresponding to ductile behavior.

Both material models provide mesh-independent damage and accumulative plastic distribution. In localized damage, the numerical fluctuation leads to some tiny dissimilarity, especially for coarse meshes. For example, for double notch specimens with material Model I, the cracks are thicker for coarse mesh and can be handled with some optimization effort for mesh discretization. Besides, due to different formulations for models, the damage zone characters can be deviant. Model I shows a smooth distribution of the damage with a mellow transition zone between the damaged and undamaged parts. Contrary to that, Model II represents a sharp transition zone that results in thicker cracks or a wide damaged zone in localized or regularized cases, respectively.

The global response of force-displacement curves verifies the mesh-independent results for both material models. Some differences occur in the localized damage case, but they will remove by increasing the regularization effects. By the way, the agreement is still acceptable. Due to different formulation, the character of the force drops for models varies consequently. The curves of Model I experience a very steep drop and approach zero forces with increasing displacement. However, in Model II, the curves exhibit a very smooth drop, especially for regularized damage cases.

The first boundary value problem is the plate with circular hole discussed in Subsection 7.1.1, in which the material Model I, gradient-enhanced regularization, is implemented. In this example, the cracks initiate at the hole and propagate toward the outer edge of the damage distribution points for both regularization cases. The only exception is the force-displacement curve for localized damage, where a slight difference in the peak value of force is noticeable. However, a more strong regularization overlooks the problem with coarse mesh.

Taking into account the double-notched specimen, presented in Subsections 7.1.2 and 7.2.2, the characteristic behavior of both models has compared more accurately. The main characteristic of both models is similar. They provide mesh-independent damage distributions, starting from each notch and propagating towards each other. For almost-localized case, final damage zones are two separate cracks, while in the regularized case, they meet in the middle to form a thicker damaged zone. However, this single crack is interpreted as S-shape for Model I and has an I-shape for Model II. The force-displacement curves of Model I display a very sharp force drop compared to the slightly decreasing force of Model II. The contours of accumulative plastic strain are formed better with Model II, as the plastic strains should propagate almost in the same region as the damage. Moreover, the influence of regularization on plastic strain distribution is more distinct for Model II.

The last boundary value problem is a sharp notch specimen in Subsection 7.2.1, illustrate the results of Model II. For this example, the influence of the boundary conditions is strong, especially regarding the global responses. The force drops show a slight division for coarse mesh, but a better agreement occurs by damage distributions. Due to this perspective, the

boundary conditions do not harm the mesh independence.

After this comparative discussion, the most compatible choice depends on the application. Due to the simulation of abrasive wear and the difficulties entered through contact modeling, material Model II (ERVE) is more efficient to use in this study. For this material model, the implementation is done only at the material point level and leads to direct modeling in commercial finite element software, Abaqus. Despite this most significant advantage, the transition between damaged and undamaged zone is sharper for Model II. However, this disadvantage can be disappeared by optimizing the regularization.

8 Soil-Tool Interaction

The abrasivity of soil and rock is a significant factor with remarkable influence on the wear of mechanical tools in different processes such as tunneling, underground mining, or quarrying. In such subsurface engineering projects, the construction time in the planning phase is decisive. It is estimated based on different factors such as tool wear. Therefore, realistic prediction of the tool wear during tunneling is prominent for the excavation progress. Abrasive wear happens in any situation where two materials with different hardness are in contact during relative motion and depends on two parameters. The first one is the machinery, such as the devices and tools used for excavation. The other parameter is the geological condition of the soil and rock in contact with the tools.

Many different methods have described the abrasive behavior of sand and rock, such as laboratory tests, field tests, and computer simulations. Each method has its strengths and weaknesses. The aim is to introduce a more efficient wear model that estimates the abrasive wear rate caused by a mixture of particles. For achieving this goal, the behavior of a scratch caused by a single abrasive particle has extended to the abrasive wear of the particle mixture employing relations produced with 3D particle simulations. Numerical methods used for this procedure are FEM for simulation of single scratch test and DEM for modeling particle mixture. First, in Section 8.1 the theoretical background of contact mechanics, constraints, and algorithms is explained briefly. It is followed by Section 8.2, presenting the steps for numerical simulation of a single scratch test and its results for different test cases. Besides, the influence of various parameters on the scratch and wear mechanisms is studied. The equations for calculating contacting particles derived from DEM particle simulations are introduced in Section 8.3. Finally, in Section 8.4, the relations for estimation of abrasive wear are introduced.

8.1 Theoretical Background

Contact mechanics, built upon the mechanics of materials and continuum mechanics, focus on computations evolving pressure and stresses acting perpendicular to the contacting surfaces (adhesion) and stresses acting tangentially between surfaces (friction). Classical contact mechanics is associated with Hertz (1882), as he dealt with contact problems between elastic bodies with curved surfaces. These classical results still form the base of many industrial situations, but they are not a proper approach to deal with contact in many engineering applications. About one hundred years later, Johnson, Kendall, and Roberts (1971) found a similar solution for adhesive contact (known as JKR-Theory). It may come from the general observation that solid bodies do not adhere to one another. JKR-Theory was rejected by Derjaguin, Muller, and Toporov (1975) as they developed another adhesive theory in the 1970s (known as DTM-Theory). Further advancements in contact mechanics are followed by studying the importance of surface roughness for bodies in contact by Bowden et al. (2001). Their theory found out that the contact area between friction partners is

less than the apparent contact area, which drastically influenced the tribology commitments.

In general, contacting bodies very often experience non-linear plastic and permanent deformations, and therefore mostly should be solved numerically. Computational modeling of contact is a very challenging procedure. The choice of contact algorithm, discretization, and constraints have a considerable impact on analysis and can lead to the lack of convergence of numerical algorithms. Abaqus finite element software is applied to model the contact in a single scratch test. Here, some of the computational algorithms and the required constraints for dealing with contact problems are clarified.

8.1.1 Kinematics of the Contact Surfaces

According to the kinematics of contacting surfaces, contact occurs between a slave body and a master body. Indeed, some parts of their surfaces occupy the same position. The contact relations decompose into normal and tangential components. It is due to the identification of an active contact zone by contact constraints.

Normal Contact and Impermeability

It is significant to find out that a point on the slave surface is in contact with an arbitrary point on the master surface or not. Thus, a search for the closest point is applied. It leads to the calculation of the normal gap g_N . In a continuum model, two points are not allowed to occupy the same position in space. The constraint in the normal direction, known as impermeability, is executed from the normal gap and the contact pressure. Thus, assuming that no penetration is allowed, the whole contact problem reduces to a boundary-based problem, by demanding that $g_N \geq 0$ keeps for all material points during the deformation. Contact happens when the gap $g_N = 0$ and the normal contact traction in the case of non-adhesion is compressive, $t_N \leq 0$. Due to the complementarity condition, if there is no contact, then no compressive traction occurs. Alternatively, if there are no compressive stresses, then the distance must be positive. These relations are as follows

$$g_N \geq 0, \quad t_N \leq 0, \quad g_N t_N = 0 \quad (8.1)$$

which are known as Karush-Kuhn-Tucker conditions for optimality.

Tangential Contact and Friction

Stating the relative movement between the contact surfaces, the concept of the tangential gap g_T is given. Two surfaces are so-called stick to each other if they have no relative movement in the tangential direction, i.e., $g_T = 0$. In contrast to the stick state, there is a tangential displacement in the slip state between a given point on the slave surface and its projection on the master surface.

In contact, the tangential behavior is described based on the constitutive equations of a friction model. When surfaces are in contact, they usually transmit both shear and normal

forces across their interface. Utilizing a friction model, the general relationship between these two force components is defined. It usually expresses in terms of the stresses at the interface of the contacting bodies. The most commonly used friction model developed in the last decades is the standard Coulomb law, which is based on the framework of elasto-plasticity and is described by

$$\mathbf{t}_T = -\mu|\mathbf{t}_N| \quad (8.2)$$

where μ is known as the coefficient of friction and is gained by experiments. In the case of isotropic friction, it assumes that the friction coefficient μ is the same in all directions. For a 3D simulation, there are two orthogonal components of shear stress, t_T^1 and t_T^2 , along with the interface between the two bodies. These components act in the local tangent directions for the contact surfaces and are combined into an "equivalent shear stress" t_T , for the slip/stick calculations, where $t_T = \sqrt{t_T^1{}^2 + t_T^2{}^2}$.

8.1.2 Treatment of Contact Constraints

Several methods have been implemented to treat the contact constraints, which are employed frequently from optimization theory. Among them, the penalty method and the augmented Lagrange method are discussed briefly in the following. Hence, the penalty method is a stiff approximation of hard contact and is applied in this work. The augmented Lagrange method uses the same kind of stiff approximation as the penalty method. It also uses augmentation iterations to improve the accuracy of the approximation. For a detailed description of these methods readers are referred to, Laursen (2013) and Wriggers and Zavarise (2004).

Penalty Method

Among many solution methods available for contact constraints, the penalty method seems to be the most popular in the practical finite element implementations of contact problems. It is frequently applied because its implementation procedure is straightforward and results in a pure displacement formulation. In this scheme, the contact force is proportional to the penetration distance, so some degree of penetration between the contacting bodies is allowed, possibly $g_N \leq 0$. The penalty method can be implemented such that there are no Lagrange multipliers. Because numerical softening associated with the penalty method can relieve over constraint issues, they allow for improved solver efficiency and consequently less computational time and cost.

Within the penalty method, the contact stresses are directly linked to the deformations by the so-called penalty stiffness parameters (c_N and c_T in the normal and tangential direction, respectively). Here, the normal contact stress is indeed followed by

$$t_N = c_N g_N \quad (8.3)$$

The tangential stress for slip/stick criteria corresponding to the Coulomb constitutive law is given by

$$\mathbf{t}_T = \begin{cases} -c_T g_T, & \text{for stick} \\ -\mu|\mathbf{t}_N| & \text{for slip} \end{cases} \quad (8.4)$$

It is common to have convergence difficulties in the first increment of an analysis, which can be removed by an appropriate choice of penalty stiffness parameters. Small penalty stiffness parameters typically result in better convergence of the Newton iterations and better robustness but can lead to stress inaccuracy due to large penetration. Increasing the stiffness parameters improves the accuracy of the results, where the perfect case is achieved when the values go to infinity. However, we need to note that, very high contact stiffness will lead to numerical errors related to ill-conditioning.

Augmented Lagrange Method

The augmented Lagrange method is based on an extended penalty method while keeping penetrations small. It may require additional iterations in some cases. However, this approach can make the resolution of contact conditions easier and avoid problems with over constraints. There are many articles written on the application of the augmented Lagrangian method in the finite element method, among them are Simo and Laursen (1992); Laursen and Simo (1993); Zavarise et al. (1995); Refaat and Meguid (1997).

8.2 Single Scratch Test

Abrasion can be numerically reproduced in a controlled way by simulating a single asperity scratch test where a pin or a conical indenter penetrates into the surface of the specimen and slides over it. Scratch damage can range from plastic grooving in ductile material to cracking and chipping in brittle material. The scratched surface is characterized by the active micromechanisms of abrasion, which are influenced by the deformation behavior of the specimen.

8.2.1 Numerical Procedure

A three-dimensional scratch process was modeled and simulated using the developed coupled damage-plasticity material model, implemented as a user subroutine (UMAT) in Abaqus. A schematic illustration of the scratch system has shown in Figure 8.1. A Cartesian system assigns. The y -axis is pointing to the indentation direction, the z -axis is parallel to the surface and shows the sliding direction and the x -axis is pointing out of this figure. The model consists of a rigid tip with a predefined radius and a flat deformable specimen. The specimen is fixed and the tip slides over the surface such that a groove forms. The width and length of the specimen are not relevant parameters in this simulation. But they should be large enough to eliminate the boundary effects.

In the simulations, a displacement-control loading has been applied in two steps:

- first, in the indentation step, a vertical displacement along the thickness (y -axis in Figure 8.1) is applied to press the indenter down till it reaches the specified indentation depth;

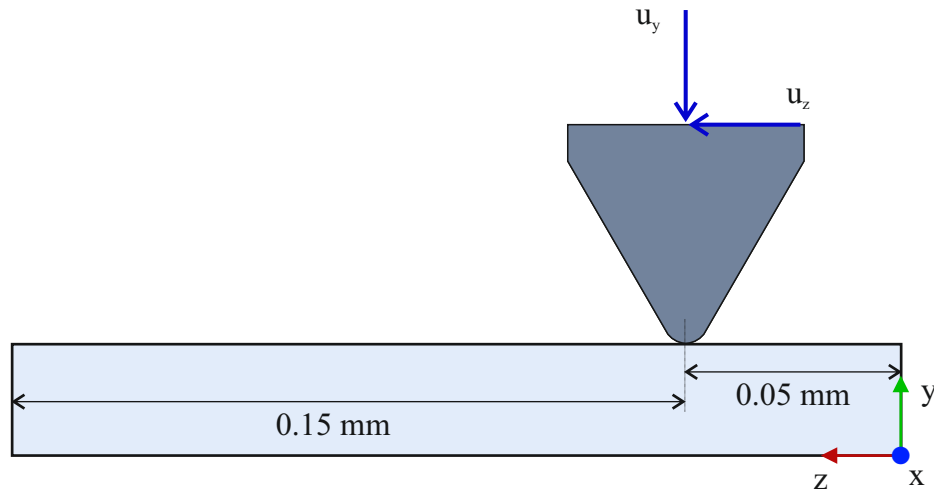


Figure 8.1: Schematic representation of the scratch test in the initial undeformed configuration

- second, in the scratching step, a horizontal displacement is applied to slide the indenter in the z -direction at a constant indentation depth the same as in the previous step.

During the process, the contact area and the reaction forces are recorded. For minimizing the number of elements and thereby the computational time, the symmetry condition regarding the x -axis applies to the geometry.

A standard surface-to-surface contact discretization with the finite sliding tracking approach applies to the model, which allows for arbitrary separation, sliding, and rotation of the contacting surfaces. In this algorithm, each slave (specimen) node is checked for penetration through the master (abrasive particle) surface. The connectivity of the currently active contact constraints changes upon the relative motion of the contacting surfaces. When the contact is established, then incremental searching is used to track the position of the slave nodes on the master surface.

In a contact problem, special boundary constraints are imposed in addition to the regular boundary conditions. As mentioned in Subsection 8.1.1, for classical contact problems the non-penetration (impermeability) condition and the law of surface friction are considered. In the normal direction, the formulation of the non-penetration condition is applied as a purely geometrical constraint to prevent the penetration of one body into another. In the tangential direction, the Coulomb friction law has used to simulate the friction between the rigid indenter and the specimen using the penalty approach. The penalty stiffness is considered as the minimum of the master and the slave surface stiffness. In the contact algorithm used in this investigation, the scaling factor for the penalty stiffness is kept at the default value of 1, and the Coulomb friction coefficient is set to $\mu = 0.1$.

The boundary conditions are summarized as follows:

1. Due to the symmetry, the displacement along the x -axis is zero on the symmetry plane.
2. Coulomb friction law is applied at the contact surface between the indenter and specimen surface: when the friction stress reaches μt_N (t_N is the normal contact traction), contact surfaces slip on each other. Hence, during scratch, the local friction stress is

equal to μt_N .

3. The other surfaces of the specimen are fixed: displacements $u_x = u_y = u_z = 0$

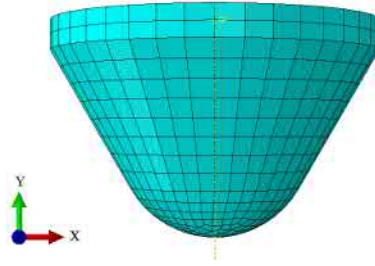


Figure 8.2: The mesh of the spherical tip used in the numerical simulations, $R=50 \mu\text{m}$.

The tip is made of quartz (SiO_2), which is much harder than the steel of the specimen. It practically does not wear during the scratching movement. Thus it is assumed to be almost rigid. For the tip, a reference point is assigned in the center of its base. The possible boundary conditions and displacements are applied to this reference point. For decreasing the computation time, the mesh of the spherical geometry should be coarse. The apex of the tip is an exception, which is the main contacting master surface. The element size around the apex is approximately $5 \mu\text{m}$. The initial model for the tip used in the numerical simulations with its discretization has depicted in Figure 8.2.

Table 8.1: Mechanical properties of the tested materials

Material	Quartz(SiO_2)	Steel (St-52)
Young's modulus (GPa)	73	210
Poisson's ratio	0.17	0.33
Density (Kg/m^3)	2200	7800
Hardness (GPa)	9.8	2

The surface to be scratched has a dimension of $200 \times 100 \times 15 \mu\text{m}$ and is made of standard steel DIN St-52 as it is used commonly in machine components. Table 8.1 listed the mechanical properties of quartz and the steel used in the model. Figure 8.3 shows the specimen with its element distribution. The 8-node linear brick elements (C3D8) are used for the discretization of the specimen. A too fine mesh or a uniform fine mesh will drastically increase the computational time, especially in the three-dimensional models. However, a coarse mesh is not sufficient to capture all changes. We use the following scheme to reduce the number of elements and consequently speed up the simulations and at the same time obtain sufficiently accurate results. The specimen is divided into three zones. In the effective zone, right under the indenter tip, where the contact takes place, the finest mesh is used. In the regions far from the contacting area, a coarse mesh is applied, as the contacting stresses are almost zero there and have no influence on the results. The intermediate zone is so defined to apply a smooth transition between the fine and the coarse mesh.

The coupled damage-plasticity material model developed in Chapter 6 is assigned to the specimen. It results in different wear regimes in the form of plastic deformation and material removal. The plastic part is modeled by extending the linearly elastic component of the stress-strain curve with a linear hardening behavior beyond the yield point, see Figure 8.4, adapted from Ribeiro et al. (2016) for steel St-52. To account for damage, the ERVE damage model is used. It leads to volume loss of the surface and consequently to the wear of the

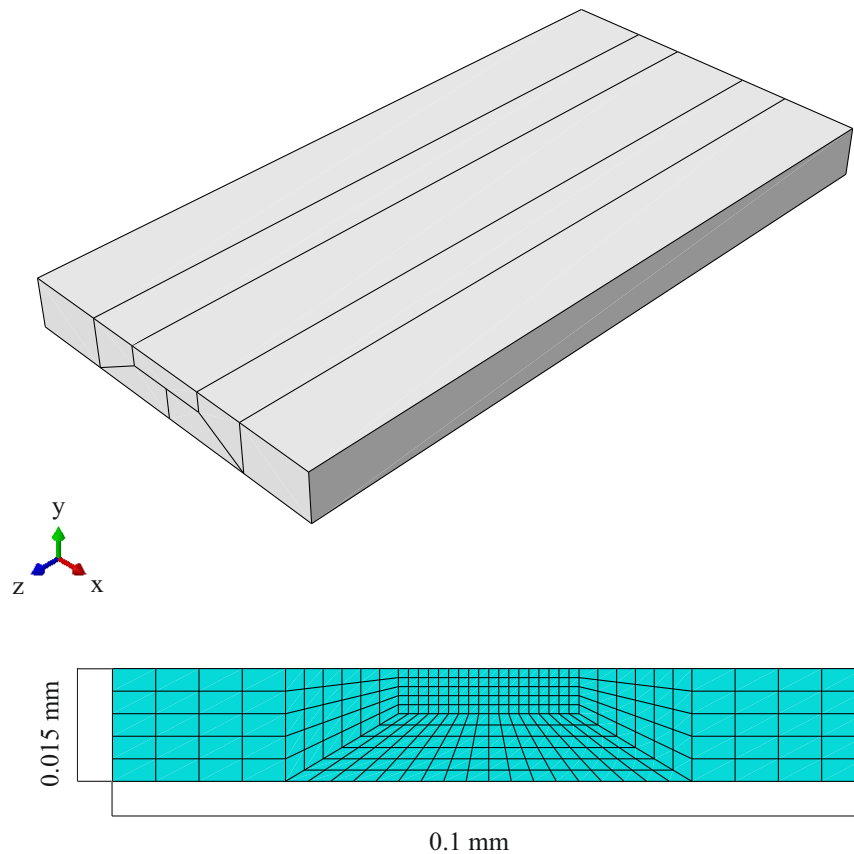


Figure 8.3: (top) The specimen used in the numerical simulations, (bottom) with a cross-section to show the element distribution and mesh size

specimen. The material input properties for the damaged part regarding the ERVE material model are listed in Table 8.2.

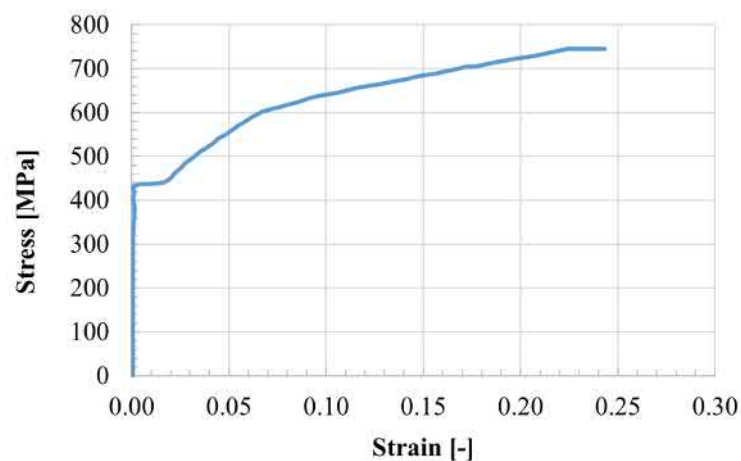


Figure 8.4: True stress-true strain relationship for St-52 steel alloy, adopted from Ribeiro et al. (2016)

The single asperity test is performed for an indentation depth of 0.002 mm. A total sliding distance of 0.1 mm was facilitated by the tangential movement of the tip. The result is a groove with a cross-section depicted in Figure 8.5.

Figure 8.6 depicts the Von Mises stress distribution on the contact surface (top view).

Table 8.2: Material parameters used in the single scratch test in conjunction with the ERVE damage model

E [MPa]	ν [-]	r_d [MPa]	n [-]	Δt [s]	α [1/s]
210000	0.33	0.1	20	1	0.05

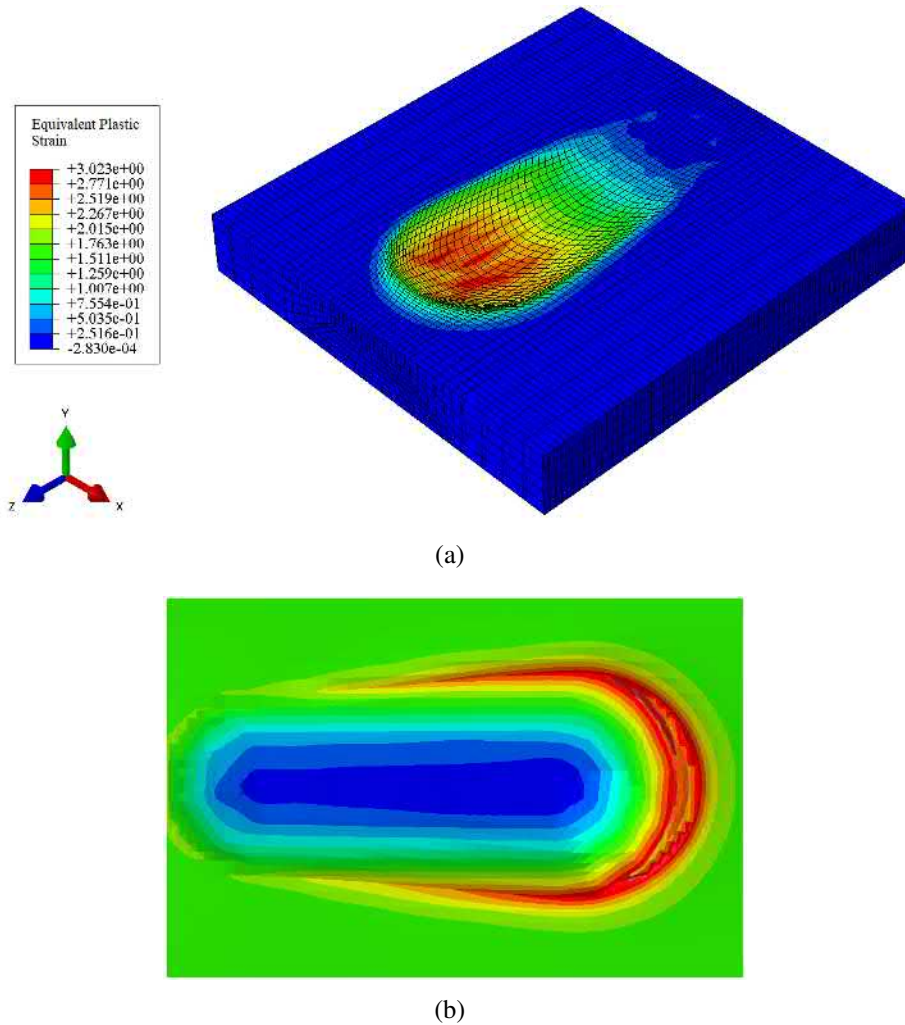


Figure 8.5: A groove resulting from a single scratch test for $d = 0.002$ mm and $R = 50$ μm (a) distribution of equivalent plastic strain in 3D view and (b) result of a microscopic height profile measurement (blue is low and red is high)

They are recorded during the growth of the indentation depth. The distribution of the effective stress during the compression of the indenter is axisymmetric. The width of the non-zero effective stress and the indentation depth are becoming dimensionless using the thickness of specimen h . As is shown in Figure 8.6, with the growth of the indentation depth, the plastic zones and the contact area also increase. The stress reduces from the center of contact to the borders monotonously, except for the small region where the material extruded up, namely the shoulder area in red color.

Based on the literature such as Hokkirigawa and Kato (1988) and Woldman et al. (2017), three primary abrasive mechanisms may occur in the contact between a scratching tip and a deformable surface: plowing, wedging, and cutting. During the system operation, a tran-

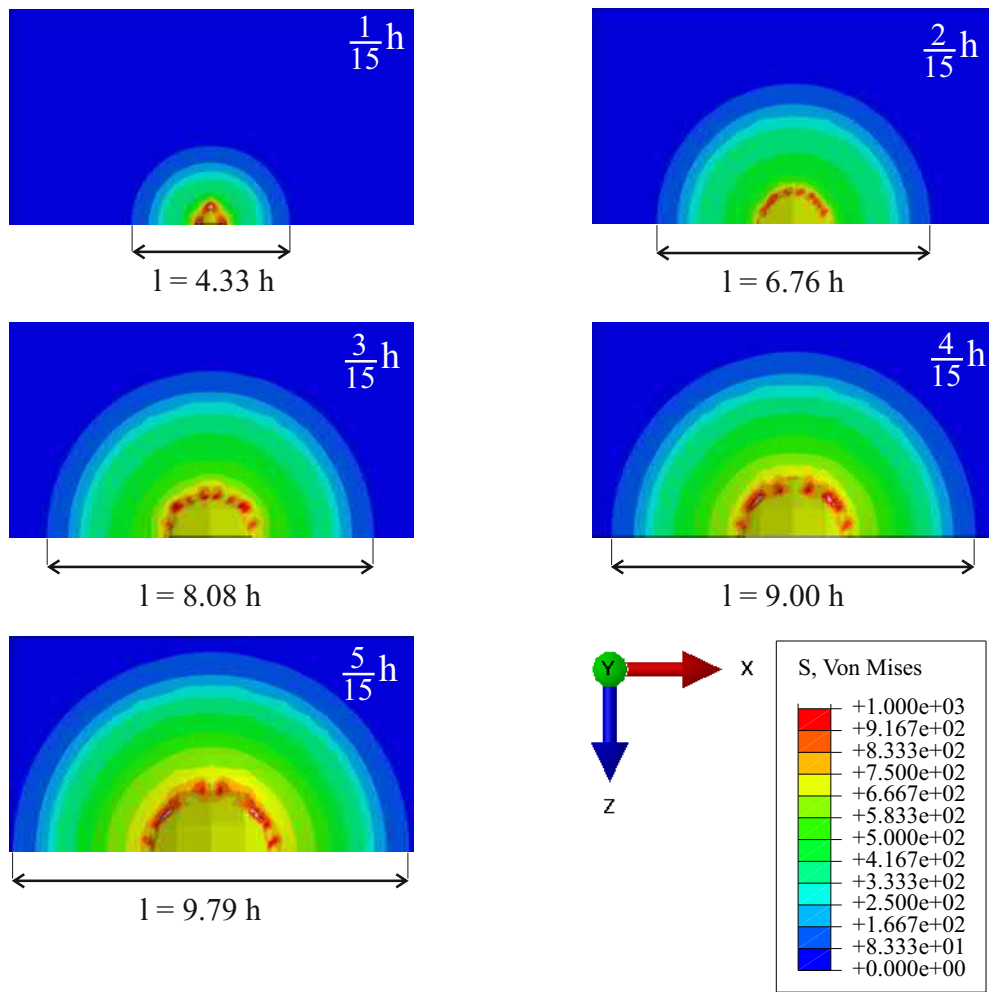


Figure 8.6: Distribution of Von Mises stress with an increasing indentation depth

sition from one mode to another may happen and can act simultaneously. At low load and therefore low indentation depth, a shallow groove is formed. In this situation, the material is pushed downwards and to the shoulders, and thus no material removal is recorded.

In the wedge forming, the wedge type of wear debris is formed as a consequence of a non-steady-state mechanism, where the scratched material forms a bow in front of the tip. The bow will grow up till it finally breaks off and the wear occurs. In the cutting mode, almost all materials of the groove are removed from the surface in the form of the long, curled ribbon-like particles. This is the most severe abrasive wear stage, which typically happens under extreme conditions, like very high loads, large indentation depth, or sharp abrasive particles.

The shape of an abrasive particle, the difference between the hardness of the abrasive particle and the specimen material, the load, and the shear strength at the contact interface determine the state of the abrasive wear. Figure 8.7 shows a schematic cross-section of a typical wear scar, where A_g is the groove area, A_s the area of the shoulders, w the width of the groove, and d the indentation depth.

Referring to Woldman et al. (2017), the degree of wear f_{ab} relates the area of the groove

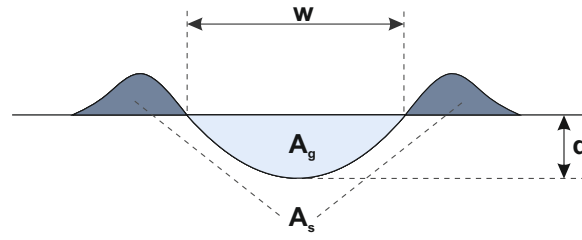


Figure 8.7: Schematic illustration of the cross-section of a wear scar

to the area of the plowed material using the following equation:

$$f_{ab} = \frac{A_g - A_s}{A_g} \quad (8.5)$$

Assuming purely plastic deformation with the consistency of volume and no material removal, a value of 0 corresponds to ideal micro-plowing with all material being pushed to the sides, whereas a value of 1 corresponds to ideal micro-cutting with all material being chipped out.

Hokkirigawa and Kato (1988) derived an equation for the degree of penetration D_p , which is equal to the ratio of indentation depth and the half-width of the groove. It is defined as

$$D_p = \frac{2d}{w} \quad (8.6)$$

It is a dimensionless parameter for characterizing the relative indentation depth. Note that the degree of wear increases with increasing the degree of penetration, i.e., a higher value of D_p indicates the cutting wear, and a lower value is linked to the plowing mechanism.

8.2.2 Study of Important Parameters

There are many effective parameters for defining the dominant wear regime and the abrasive behavior in a single scratch test. To facilitate the analysis, some parameters are kept constant and more influencing parameters are investigated. Whether only plastic deformation takes place on the contact surface or material removal is also probable, will be mostly determined by the indentation depth and the abrasive particle size, as will be discussed in detail in the following.

Influence of Indentation Depth

In this part, a series of tests with varying indentation depth is established. They prove that for a fixed indenter radius, the indentation depth determines the dominant wear mechanism. The scratch simulations are done using a tip with a constant radius of $50 \mu\text{m}$ and varying indentation depth from $1 \mu\text{m}$ to $5 \mu\text{m}$.

During the deformation, the contact pressure is equal to the hardness of the deformable material, i.e., the steel specimen, therefore, the size of the contact area can be expressed as the ratio of the normal contact force and the hardness. Figure 8.8 shows the distribution

of the normal contact force for different indentation depths. For a constant tip radius, by increasing the indentation depth, the total contact area and the normal contact force will increase. For all cases, the contact force will increase almost linearly till the maximum indentation is achieved, then at the beginning of the sliding, the force will experience a drop and is followed by a curve with a very slow slope and some fluctuations.

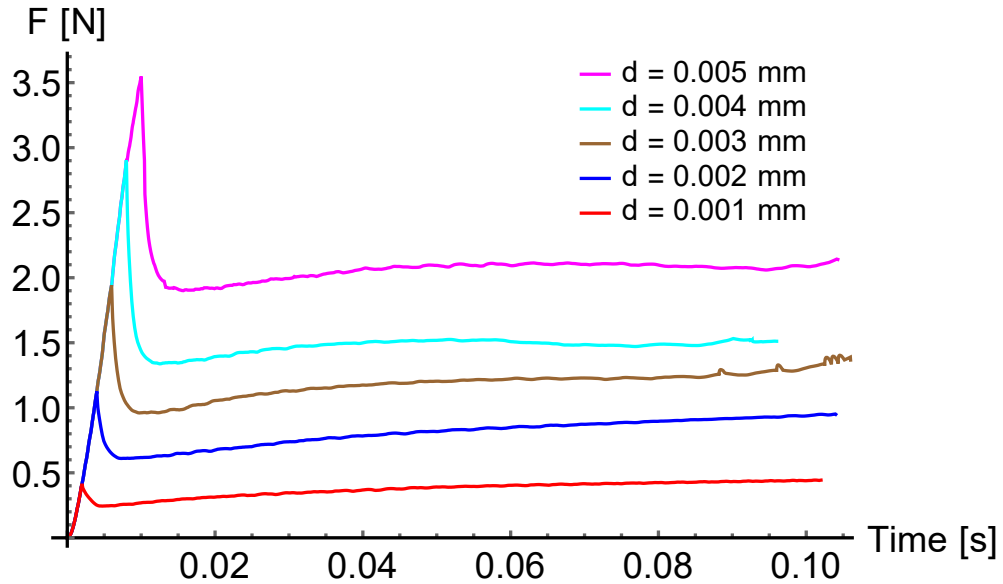


Figure 8.8: Distribution of normal contact force for different indentation depths

Figure 8.9 shows the numerical result for the plowing mechanism. It indicates the predominantly plastic deformation without material removal. The simulated groove cross-section results in the penetration degree of around 0.2 for the plowing stage.

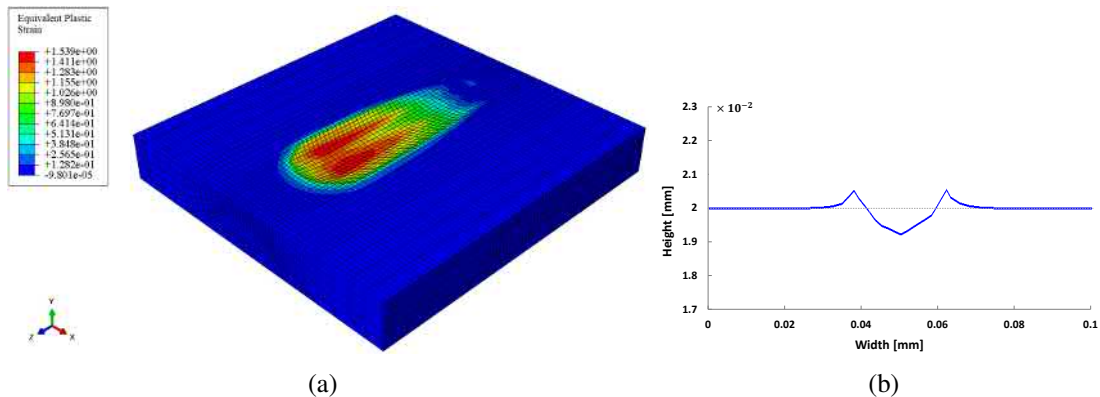


Figure 8.9: Numerical results for plowing (a) distribution of equivalent plastic strain and (b) cross-section of the groove

Cutting is the critical abrasive wear mode, which occurs for the degree of wear larger than 0.7, resulting in purely material removal with almost no shoulders. A transition from plowing to cutting regime is obtained for the degree of wear between 0.2 and 0.7. It is known as the wedge formation mode, which is a non-steady-state regime. Investigating the results reveal that for a constant indenter size, increasing the indentation depth will cause the wear regime to transform from micro-plowing into micro-cutting and ends up with a larger degree of wear.

Influence of Particle Size

The next step is investigating the influence of the abrasive particle size on the wear volume. From literature, the size effect has studied for abrasive particles up to around $100\ \mu\text{m}$. Hence, the simulations are performed for three tip radii of 25, 50, and $100\ \mu\text{m}$ with the cone angle of 60° as shown in Figure 8.10. In these simulations, the indentation depth is constant and equal to $3\ \mu\text{m}$.

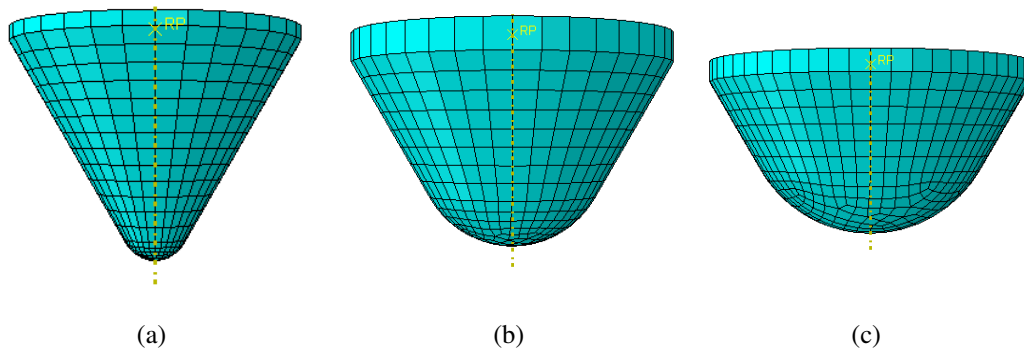


Figure 8.10: Representation of the tips used in the simulations (a) $R=25\ \mu\text{m}$ (b) $R=50\ \mu\text{m}$ and (c) $R=100\ \mu\text{m}$

Figure 8.11 shows the normal contact force distribution as a function of horizontal sliding distance. An initial indentation stage is not included in the diagram, and thus the contact forces jump from zero to the required compressive force applied on the indenter. By increasing the tip radius for a constant indentation depth, the normal contact force and the contact area will increase to assure the constant hardness for the specimen.

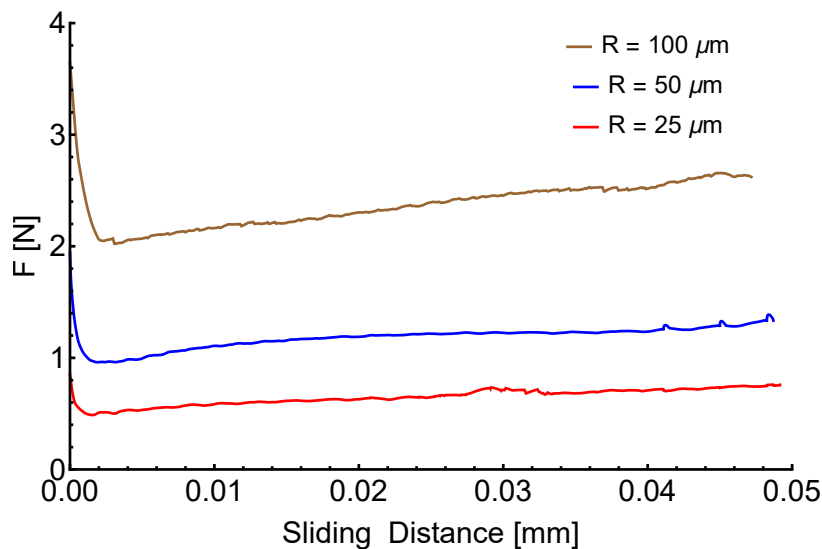


Figure 8.11: Normal contact force during scratching for the different tip radii

The simulation results are depicted in Figure 8.12. It appears that the tip with a smaller radius produces a groove with lower shoulders and consequently causes more wear. It means that for constant indentation depth, the wear volume increases with decreasing tip size. Note that this effect is observed for scratching a surface with only one particle, and it opposes the

size effect reported in the literature. In the experiments, the particle size effect is studied using a grid of particles or tips. For a grid of particles under constant pressure, the force per particle has a direct relation with its radius. Because the number of particles per unit area decreases for larger particles. It results in a larger amount of wear caused by every single particle. This effect has discussed in detail in Section 8.3, where a grid of particles is simulated using DEM.

The cross-sectional geometry of the groove caused by a tip with a radius of $100 \mu\text{m}$ reveals a completely plastic deformation with large shoulders and no material removal. Contrary, in the scratch cross-section built by the tip with a radius of $25 \mu\text{m}$, almost no shoulders are observable, and large wear volume is recorded.

8.3 Abrasive Particle Simulation

The simulation of abrasive particles is performed using the discrete element method in PFC^{3D} software. The abrasive particles used in the simulations are quartz grains, as they are one of the significant abrasive particles in the soil. Table 8.3 shows the mechanical properties of quartz grains. Before starting the simulations, the parameter identification procedure, introduced in Chapter 5, is carried out to determine the DEM contact parameters. The simulations are divided into two categories; homogeneous materials and particle mixture.

Table 8.3: Mechanical properties of quartz particles

Parameter	Value
Diameter [μm]	150-450
Density [kg/m^3]	2200
Internal friction angle [$^\circ$]	12
Elastic modulus [GPa]	73
Shear modulus [GPa]	31
Compressive strength [GPa]	1.1

8.3.1 Homogeneous Material Simulation

The setup for homogeneous material consists of a box with unit dimensions filled with particles of equal radius. They are generated randomly inside the box and then settled down by applying gravity. Due to the small size of particles, the settling step takes a very long time and is the most time-consuming step in the simulation. To have a better settlement, the box is shaken applying a small velocity to the side walls. A linear contact model is considered between the particles. The simulations indicate that the inter-particle friction coefficient does not have a significant effect on the number of contacting particles with the surface, therefore, all wall and particle contacts are supposed to be frictionless. A pressure is applied to the top surface of the particles. The number of contacting particles per unit area (N_c) is a function of the particle's diameter. The results are depicted in Figure 8.13. As is shown in the following diagrams, the particle diameter has divided by the length of the contacting

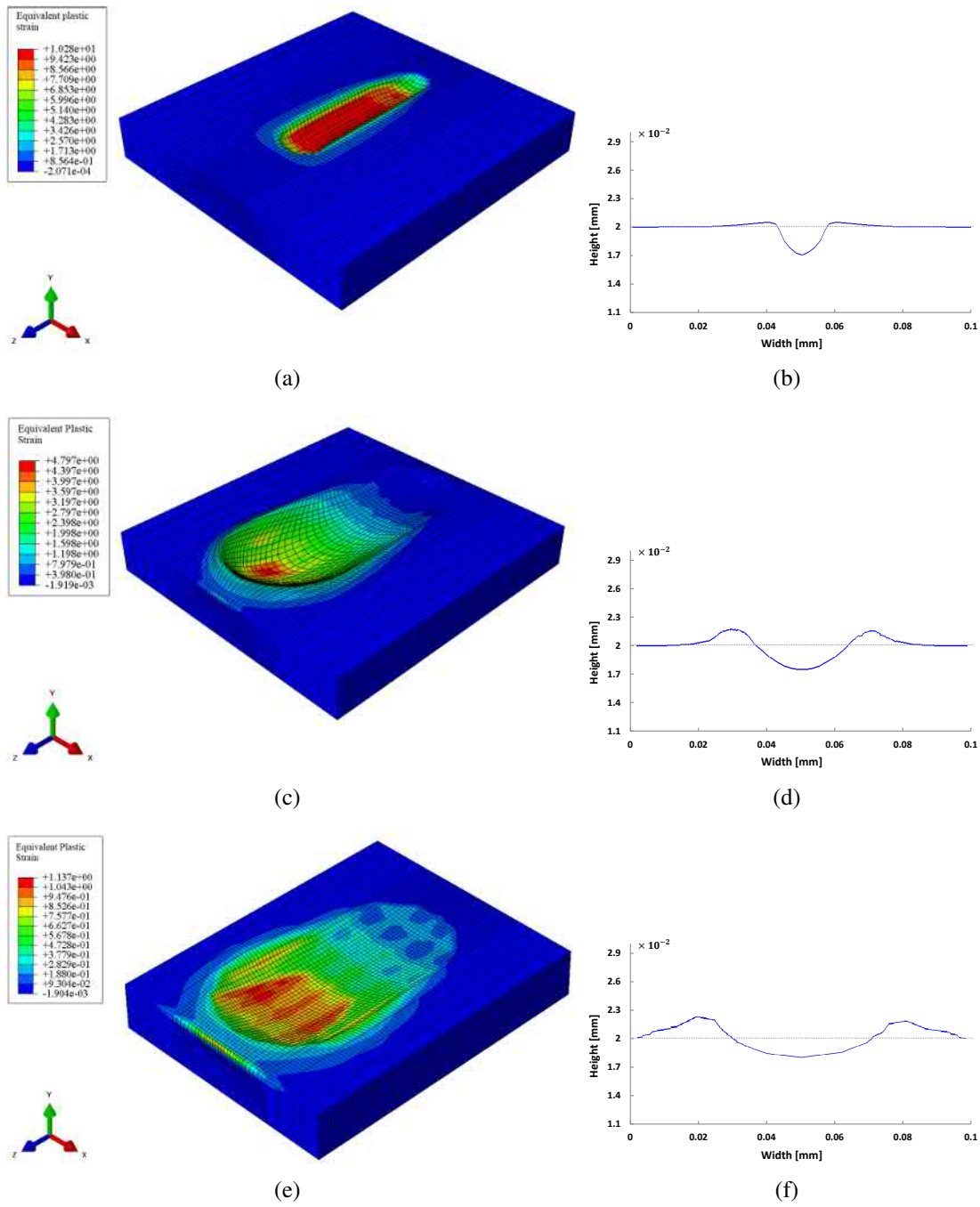


Figure 8.12: Particle size effect (left) distribution of equivalent plastic strain for (a) $R=25 \mu\text{m}$ (c) $R=50 \mu\text{m}$ and (e) $R=100 \mu\text{m}$ and (right) cross-section of the groove for (b) $R=25 \mu\text{m}$ (d) $R=50 \mu\text{m}$ and (f) $R=100 \mu\text{m}$

surface to make the horizontal axis dimensionless. Then, the number of contacting particles is calculated as

$$N_c = 0.9 D^{-2}. \quad (8.7)$$

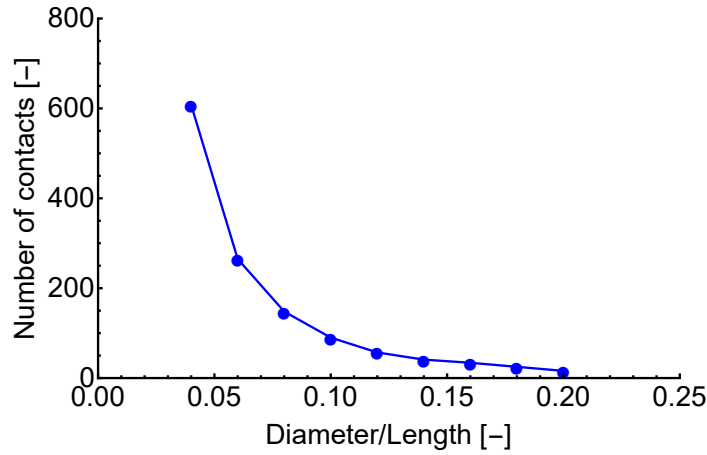


Figure 8.13: Relation between number of contacts and particle diameter for homogeneous material.

8.3.2 Mixture of Particles

In practice, the extrapolation of these predictions to the soil that consists of a large number of different particles is relevant. Therefore, a particle mixture with two different radii is considered. The setup is similar to the one used for homogeneous material simulation. In this case, two types of particles are assumed with the same mechanical properties, but different diameters. A unit dimension box is created and randomly filled with particles A and B with a defined volume ratio. If D_A and D_B are the particle diameters and θ_A and θ_B are the volume ratios of particles A and B , respectively, then

$$D_A \geq D_B \quad \rightarrow \quad r_{AB} = \frac{D_A}{D_B} \quad (8.8)$$

and

$$\theta_A + \theta_B = 1. \quad (8.9)$$

After particle generation, they settle down due to their weight. Pressure is applied to the top surface of the particles. Finally, a parametric study is performed to derive a relation for the number of contacting particles as a function of particle size and volume ratio. By varying the diameter and volume ratio, a large database is created for each particle type. Figures 8.14 and 8.15 present the results for the number of contacts by A -particles and B -particles for the special case $r_{AB} = 2$ as an example. The best curve is fitted to these data points using the MATLAB curve fitting tool. The derived equation for the number of contacts per unit area for each particle, $N_{c,i}$, is expected to be in the form of

$$N_{c,i} = a \theta_i^\alpha D_i^\beta. \quad (8.10)$$

The result of curve fitting shows that despite constant a and β , the parameter α is a function of r_{AB} and can be found in an iterative procedure. They define as

$$A\text{-particle} : \quad \alpha = 2 - \frac{1}{r_{AB}}, \quad (8.11a)$$

$$B\text{-particle} : \quad \alpha = \frac{1}{r_{AB}}. \quad (8.11b)$$

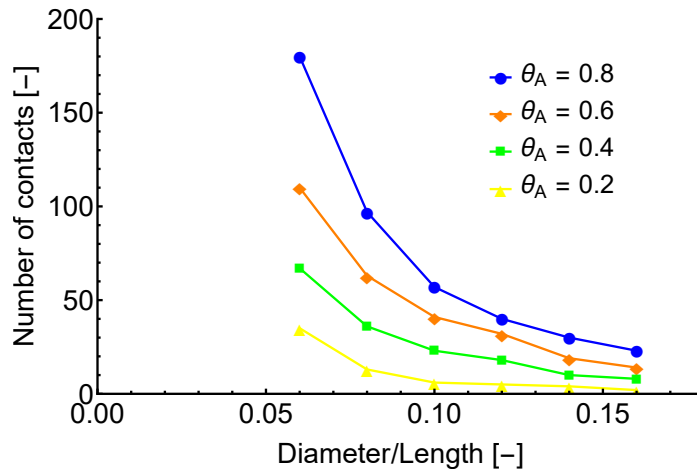


Figure 8.14: Relation between number of contacts and particle diameter for different volume ratio for A-Particles

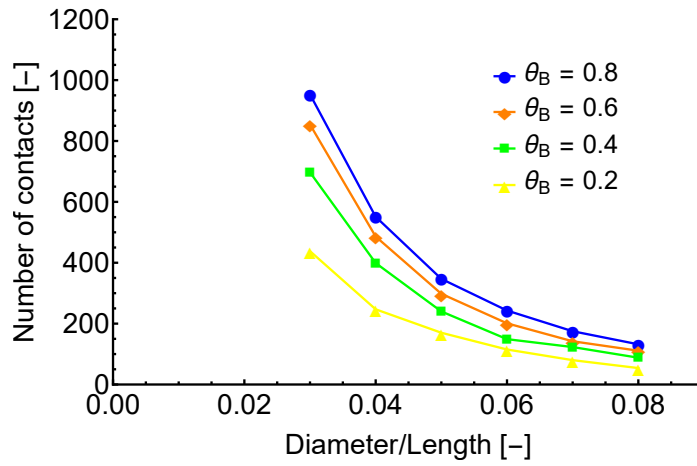


Figure 8.15: Relation between number of contacts and particle diameter for different volume ratio for B-Particles

Finally, the equations for A - and B -particles, by considering r_{AB} as a ratio of D_A to D_B for $D_A \geq D_B$, are defined as

$$N_{c,A} = 0.9 \theta_A^{(2 - \frac{1}{r_{AB}})} D_A^{-2}, \quad (8.12a)$$

$$N_{c,B} = 0.9 \theta_B^{(\frac{1}{r_{AB}})} D_B^{-2}, \quad (8.12b)$$

These equations have used in the next section to estimate the total abrasive wear rate of the particle mixture.

8.4 Estimation of Abrasive Wear Rate

The abrasiveness of individual mineral particles has modeled using single scratch simulations. The extension of these predictions to the actual abrasive ground consisting of abrasive

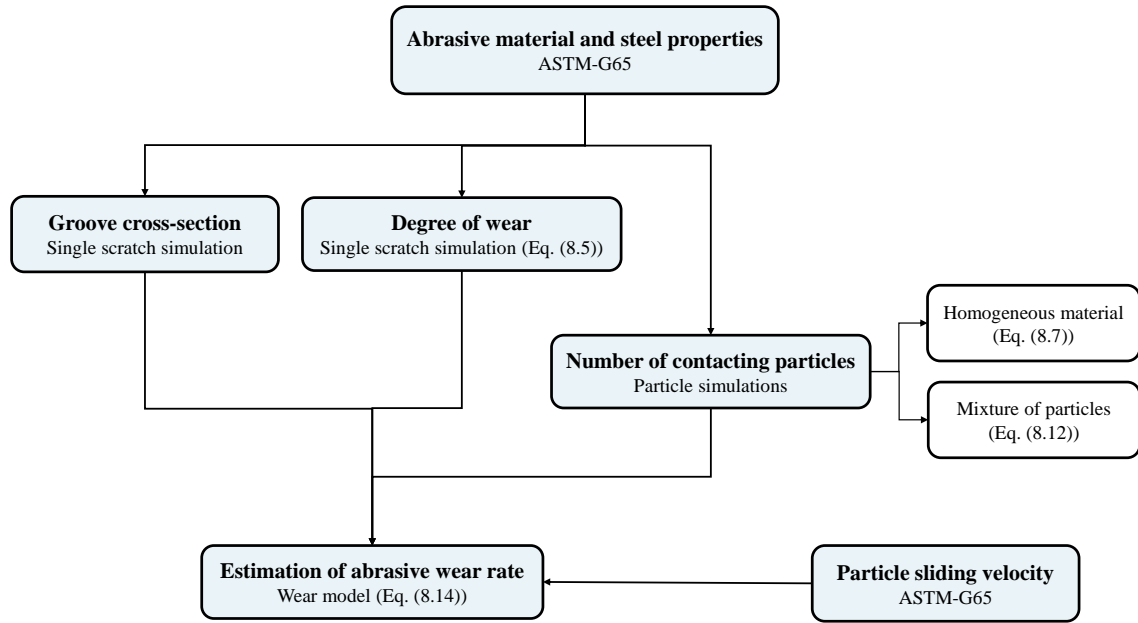


Figure 8.16: Flowchart for abrasive wear model

particles with different sizes and shapes is possible using particle simulations. The calculation procedure has illustrated as a flowchart in Figure 8.16.

The contribution of a particle to the total abrasive wear rate is defined by

$$\dot{v}_i = f_{ab} A_{g,i} v_t, \quad (8.13)$$

where v_t indicates the tangential relative velocity between the abrasive particle and the tool. It has extracted from dry sand-rubber wheel laboratory test. The average area of a groove caused by all particles of type i , $A_{g,i}$, will be obtained from simulations in Section 8.2. It is supposed to be a function of influencing parameters, i.e., mean particle size and normal contact force (or indentation depth).

The total wear rate \dot{v} of a material is the summation of the wear rate for particles in contact with the tool surface, i.e.,

$$\dot{v} = \sum_{i=1}^n N_{c,i} \dot{v}_i \quad (8.14)$$

where n is the number of different particle types and $N_{c,i}$ is the number of contacts per unit area for particles of type i . Therefore, the abrasive wear rate is determined with a new numerical procedure. The most important advantage of this approach is the large reduction in the time and costs of simulations. Because the complicated 3D simulations are replaced by simplified particle modeling and single scratch simulations.

To clarify the computational procedure of the predicted model, two specific examples, i.e., one for homogeneous material and one for particle mixture are discussed in detail. As a reference for calculations, we consider the dry sand-rubber wheel test (ASTM-G65), where the rectangular steel specimen with the dimension of 18×12.7 mm is pressed against the rubber wheel with a normal force of 130 N. The rubber wheel has a rotational velocity of

200 rpm and diameter of 228.5 mm. For this standard test, quartz grains with 150 – 450 μm size range are assumed as abrasive particles.

1. Homogeneous material

We consider a homogeneous material consists of particles with all equal diameters of $D = 100 \mu\text{m}$. The number of particles per unit area is calculated from Equation (8.7) and is equal to 9×10^7 . This quantity of particles should be scaled in the small contacting area between the steel specimen and the rubber wheel. The single scratch using a particle with a diameter of $100 \mu\text{m}$ is simulated and the cross-section of the created groove has depicted in Figure 8.17. The groove area is equal to $88.4 \mu\text{m}^2$ and referring to Equation (8.5) the degree of wear f_{ab} is 0.37, which shows a combination of plowing and wedging micromechanisms. The tangential velocity v_t of the particle is calculated from the rotational velocity of the rubber wheel (200 rpm) and its diameter (228.5 mm). Now, the total wear rate calculated from Equation (8.14) is $8.07 \times 10^{-7} \text{ m}^3/\text{s}$ for homogeneous material.

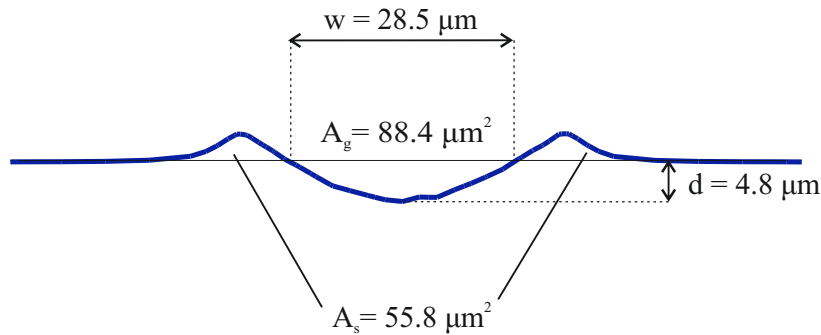


Figure 8.17: Cross-section area of a groove caused by particle with $D = 100 \mu\text{m}$

2. Mixture of particles

For the example with particle mixture, we consider a sample consists of particles with a diameter of $D_A = 200 \mu\text{m}$ and $D_B = 100 \mu\text{m}$ and the volume ratio of $\theta_A = 0.7$ and $\theta_B = 0.3$, respectively. The numbers of contacting particles per unit area are calculated from Equation (8.12) and are equal to $N_A = 1.32 \times 10^7$ and $N_B = 4.93 \times 10^7$, which should be scaled in the contacting area between the steel specimen and the rubber wheel. Similar to the previous example, the single scratch simulation is performed using a particle with a diameter of $200 \mu\text{m}$, and the cross-section of the created groove is depicted in Figure 8.18. The resulted groove has an area of $60 \mu\text{m}^2$ and the degree of wear is $f_{ab} = 0.12$, which is related to the pure plastic behavior. Finally, the total wear rate for this mixture of particles calculated from Equation (8.14) is $4.68 \times 10^{-7} \text{ m}^3/\text{s}$.

For a particle mixture with different diameters, the total wear rate decreases by increasing the number of bigger (rounder) particles. It means that a mixture with a higher amount of large grains will result in less wear rate. A related point to consider is that both single scratch tests are performed under the same contact force, i.e., $f_N = 2 \text{ N}$, which results in more plastic deformation for large particles, and more material removal for small particles. Moreover, according to the literature, the material loss measured from an experimental test is lower than our predicted values. This could have two reasons: First, the predicted values represent the groove area during the simulations, while the experimental values are based on the groove after removal of the indenter. As in the laboratory tests, the elastic part of deformations will disappear after the load removal, this part of indentation depth is not

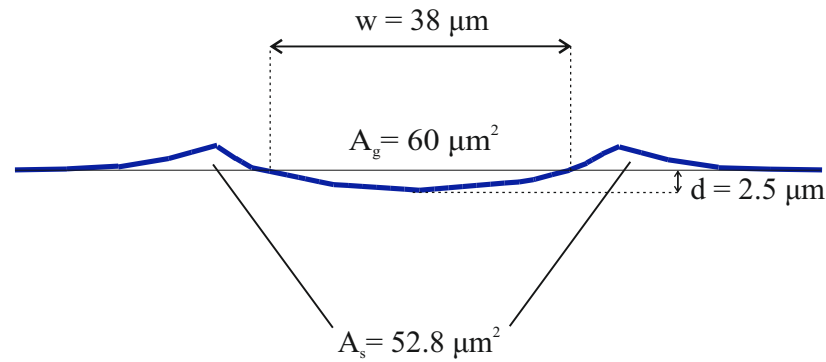


Figure 8.18: Cross-section area of a groove caused by particle with $D = 200 \mu\text{m}$

Table 8.4: Results of the wear rate calculations for homogeneous and mixture materials

Material	Wear rate [$\times 10^{-7} \text{ m}^3/\text{s}$]
Homogeneous with $D=100 \mu\text{m}$	8.07
90 % $D=100 \mu\text{m}$ + 10 % $D=200 \mu\text{m}$	7.67
70 % $D=100 \mu\text{m}$ + 30 % $D=200 \mu\text{m}$	6.83
50 % $D=100 \mu\text{m}$ + 50 % $D=200 \mu\text{m}$	5.87
30 % $D=100 \mu\text{m}$ + 70 % $D=200 \mu\text{m}$	4.68
10 % $D=100 \mu\text{m}$ + 90 % $D=200 \mu\text{m}$	2.93
Homogeneous with $D=200 \mu\text{m}$	0.44

considered in the groove geometry. Second, the cross-section of the groove at different scratch positions along the sliding length is not uniform, as it could also be observed in the height profile shown in Figure 8.5. Besides, some volume of the scratched material forms a bow in front of the indenter and is not considered in the estimation of the wear rate. For the predicted model, we consider ideally a section in the middle of the scratch length.

The performed study highlights the influencing parameters for the abrasive behavior and the wear rate. They divide into three categories: abrasive medium characteristic, machinery component properties, and the contact algorithm.

Regarding abrasive medium, the abrasivity of rocks deduce from the mineralogical composition, especially the contribution of hard minerals such as quartz. Due to Archard (1953), the important mechanical and geometrical properties of particles are size, shape, and hardness. Based on the literature, larger particles generate a higher contact force, remove the material surface faster, and create a harder texture. However, our observations in the single scratch test oppose the size effect from the literature. We have found that smaller particles, with sharper tips, cause more wear in the form of material removal compared to the plastic deformation caused by larger particles. The reason is that, under a constant load, a smaller particle penetrates deeper into the material and creates a larger groove area. Our results for the scratch simulation are in perfect agreement with the experimental results of the single asperity scratch test performed by Woldman et al. (2013).

In general, there is a linear relation between material removal rate and particle hardness. Harder particles act as rigid indenters compared to the softer particles and increase the surface roughness. However, for the occurrence of a significant abrasion, the ratio between the hardness of the particles and the surface is important. According to Zum Gahr (1987), for

hardness differences higher than around 1.2 the abrasive wear rate remains constant despite a further increase in the hardness difference. In the tunneling applications, the most abrasive particles are quartz, which according to Table 8.1 is almost five times harder than steel surfaces such as construction steel. Therefore, it will be considered that the possible variation in the hardness of sand particles has no influence on the resulting abrasive rate.

The contact algorithm implemented for simulation of the interaction between the indenter and the steel specimen could capture the wear mechanisms to a certain extent, especially for plowing. Nevertheless, besides all mentioned influencing parameters, the actual wear type could be quantified by the friction coefficient. The presence of larger friction forces between contacting bodies will result in severe wear mechanisms, such as cutting. This effect is not included in this study and could be a possible direction for future work.

9 Conclusions and Outlook

9.1 Conclusions

In this study, a wear model is presented for estimating the total abrasive wear rate of the particle mixture. It achieved using the two numerical methods, DEM and FEM. Performing a parameter identification procedure, the mixture of particles modeled with the numerical method DEM. Furthermore, having developed a coupled regularized damage-plasticity material model, the single scratch test is modeled in FEM code Abaqus. That gives rise to the relations for estimating the abrasive wear rate.

In the context of parameter identification, a simple relationship is established between the elastic parameters and the yield strength of the material on the one hand and the microscopic contact parameters for DEM simulations on the other hand. For this purpose, microscopic energies are defined at the level of the contact points and then related to the total specimen free energy. Because a system always tries to minimize energy, an analytical approach based on the minimization of free energy is introduced. It leads to anisotropic linear-elastic material law from which the elastic modulus and the Poisson's ratio are determined directly as a function of the contact stiffness. The developed relations are valid for both granular materials and bonded materials. Besides, for bonded materials, there is a similar relationship between the yield strengths according to Rankine and Tresca and the strength of the bonds in the normal or tangential direction. These relations have been validated by performing a 3D compression test in PFC^{3D}. Furthermore, the Mohr circles are drawn for two specific materials based on a set of confined compression tests.

Two coupled damage-plasticity material models have been developed. The first material model, labeled as Model I, is equipped with a regularization framework via gradient enhancement of the free energy function. The enhancement is performed using an efficient evaluation of the Laplace operator combined with strategies from meshless methods. The second material model is labeled as Model II. It uses a variational regularization approach based on the relaxation of the (condensed) free energy in a time-incremental setting. This procedure is called emulated representative volume element (ERVE). The implementation algorithms and material tangent matrix have been presented for both models.

Several numerical examples show the behavior of the material models on the global level as well as the distribution of internal parameters. The following three boundary value problems have been considered: the plate with a circular hole, the double-notch specimen, and the sharp-notch specimen. Simulations performed for a localized as well as regularized damage by varying the regularization parameter. Both material models provide perfectly mesh-independent finite element results including force-displacement curves and distributions of damage and accumulative plastic strain. Model I represents a smooth transition between the damaged and undamaged zones and experiences a very steep drop in the force-displacement curve. Whereas, a sharp transition zone has been observed in Model II for both

localized and regularized cases. Nevertheless, although the stiffness reduction for Model II occurs slower, anyhow its force-displacement curve approach zero forces with increasing displacement. The most remarkable advantage of Model II is its straightforward implementation at the material point level. Contrarily, since the formulation of Model I operates at the element level and due to the complicated routines for the Laplace operator, it has a difficult implementation procedure. That is the reason for choosing Model II for the simulation of the single scratch test.

The developed material model is implemented as a user subroutine in Abaqus and used for simulating the single scratch test. The contact algorithm has been established for the interaction between the rigid indenter and the surface of a steel specimen. The characteristic groove shape created by sliding the indenter on the surface is quantified by the degree of wear parameter, which has a relation with the different abrasive wear mechanisms. The influence of the abrasive particle size, as well as the indentation depth, are investigated. The smaller particle with a sharper tip creates scars with almost no shoulder and is related to the cutting micromechanism. While the larger particle with a rounder tip deforms the surface almost plastically, pushing materials to the groove shoulder. Moreover, homogeneous materials as well as particle mixtures are modeled with DEM to determine the number of contacting particles of each type with the surface. Finally, the results of the two mentioned steps are combined to derive a numerical wear model for estimating the total abrasive wear rate of the particle mixture.

9.2 Outlook

Although we have achieved quite good results for the behavior and shape of the groove and wear mechanisms, the contact simulations can improve further. First, a comparative study should perform with the experimental data of the single scratch laboratory test to examine the accuracy of our scratch simulations. One possible direction of future work is to execute a parametric study with a wider range of indenter size and indentation depth and consequently extend the relations obtained for estimating abrasive wear.

Furthermore, regarding the findings described in Chapter 8, the model has some restrictions for capturing severe wear mechanisms. To gain a better insight into abrasive wear mechanisms, some extensions should apply in future works. The effects of friction coefficient in contact algorithms have to be investigated thoroughly to improve the model capability in the simulation of wedging and cutting micromechanisms.

Finally, another possible objective for further work is to make use of the developed wear algorithm for optimizing the topology of the cutting tools in mechanized tunneling applications. In association with this perspective, a topology optimization approach has already been developed in the Institute of Mechanics of Material at the Ruhr-Universität Bochum, which is based on the modeling of materials using thermodynamic extremal principles, see work of Jantos et al. (2019). The process developed in this way will then apply to specific tool designs in practice.

References

- Allix, O. (2013). The bounded rate concept: A framework to deal with objective failure predictions in dynamic within a local constitutive model. *International Journal of Damage Mechanics* 22(6), 808–828.
- Arbeitsblatt, G. (2002). 7: Tribologie–verschleiß, reibung, definitionen, begriffe, prüfung. *Gesellschaft für Tribologie eV (GfT)*.
- Archard, J. (1953). Contact and rubbing of flat surfaces. *Journal of applied physics* 24(8), 981–988.
- Asaf, Z., D. Rubinstein, and I. Shmulevich (2007). Determination of discrete element model parameters required for soil tillage. *Soil and Tillage Research* 92(1), 227–242.
- ASTM, A. (2013). Standard terminology relating to wear and erosion. *G40*.
- Bagi, K. (1996). Stress and strain in granular assemblies. *Mechanics of materials* 22(3), 165–177.
- Bagi, K. (2006). Analysis of microstructural strain tensors for granular assemblies. *International Journal of Solids and Structures* 43(10), 3166–3184.
- Bailey, C. (2002). The unifying laws of classical mechanics. *Foundations of Physics* 32(1), 159–176.
- Ball, J. M. (1977). Constitutive inequalities and existence theorems in nonlinear elastostatics. In *Nonlinear analysis and mechanics: Heriot-Watt symposium*, Volume 1, pp. 187–241. Pitman London.
- Bargmann, S. and P. Steinmann (2005). Finite element approaches to non-classical heat conduction in solids. *Comput. Model. Eng. Sci* 9(2), 133–150.
- Bazant, Z. P., T. B. Belytschko, T.-P. Chang, et al. (1984). Continuum theory for strain-softening. *Journal of Engineering Mechanics* 110(12), 1666–1692.
- Bazant, Z. P. and M. Jirásek (2002). Nonlocal integral formulations of plasticity and damage: survey of progress. *Journal of engineering mechanics* 128(11), 1119–1149.
- Bazant, Z. P. and G. Pijaudier-Cabot (1988). Nonlocal continuum damage, localization instability and convergence.
- Bedford, A. (1985). *Hamilton's principle in continuum mechanics*, Volume 139. Pitman advanced publishing program Boston, MA.
- Belheine, N., J.-P. Plassiard, F.-V. Donzé, F. Darve, and A. Seridi (2009). Numerical simulation of drained triaxial test using 3d discrete element modeling. *Computers and Geotechnics* 36(1), 320–331.
- Belytschko, T., W. K. Liu, B. Moran, and K. Elkhodary (2013). *Nonlinear finite elements for continua and structures*. John Wiley & sons.
- Biot, M. A. (1962). Mechanics of deformation and acoustic propagation in porous media. *Journal of applied physics* 33(4), 1482–1498.
- Bonet, J. and R. D. Wood (1997). *Nonlinear continuum mechanics for finite element analysis*. Cambridge university press.
- Bowden, F. P., F. P. Bowden, and D. Tabor (2001). *The friction and lubrication of solids*, Volume 1. Oxford university press.
- Brepols, T., S. Wulfinghoff, and S. Reese (2017). Gradient-extended two-surface damage-plasticity: micromorphic formulation and numerical aspects. *International*

- Journal of Plasticity* 97, 64–106.
- Cambou, B., M. Chaze, and F. Dedecker (2000). Change of scale in granular materials. *European Journal of Mechanics-A/Solids* 19(6), 999–1014.
- Carstensen, C., K. Hackl, and A. Mielke (2002a). Non-convex potentials and microstructures in finite-strain plasticity. In *Proceedings of the Royal Society of London A: Mathematical, Physical and Engineering Sciences*, Volume 458, pp. 299–317. The Royal Society.
- Carstensen, C., K. Hackl, and A. Mielke (2002b). Nonconvex potentials and microstructures in finite-strain plasticity. *Royal Soc. London, Proc. Ser. A* 458, 299–317.
- Chaboche, J.-L. (1981). Continuous damage mechanics—a tool to describe phenomena before crack initiation. *Nuclear Engineering and Design* 64(2), 233–247.
- Chaboche, J. L., F. Feyel, and Y. Monerie (2001). Interface debonding models: a viscous regularization with a limited rate dependency. *International journal of solids and structures* 38(18), 3127–3160.
- Chadwick, P. (2012). *Continuum mechanics: concise theory and problems*. Courier Corporation.
- Cleary, P. W., G. Metcalfe, and K. Liffman (1998). How well do discrete element granular flow models capture the essentials of mixing processes? *Applied Mathematical Modelling* 22(12), 995–1008.
- Coetzee, C. and D. Els (2009). Calibration of discrete element parameters and the modelling of silo discharge and bucket filling. *Computers and electronics in agriculture* 65(2), 198–212.
- Comi, C. (2001). A non-local model with tension and compression damage mechanisms. *European Journal of Mechanics-A/Solids* 20(1), 1–22.
- Cundall, P. A. and R. D. Hart (1992). Numerical modelling of discontinua. *Engineering computations* 9(2), 101–113.
- Cundall, P. A. and O. D. Strack (1979). A discrete numerical model for granular assemblies. *geotechnique* 29(1), 47–65.
- Czichos, H., D. Klaffke, E. Santner, and M. Woydt (1995). Advances in tribology: the materials point of view. *Wear* 190(2), 155–161.
- Dacorogna, B. (1982). Quasiconvexity and relaxation of nonconvex problems in the calculus of variations. *Journal of functional analysis* 46(1), 102–118.
- de Borst, R., J. Pamin, and M. G. Geers (1999). On coupled gradient-dependent plasticity and damage theories with a view to localization analysis. *European Journal of Mechanics-A/Solids* 18(6), 939–962.
- de Souza Neto, E. A., D. Peric, and D. R. Owen (2011). *Computational methods for plasticity: theory and applications*. John Wiley & Sons.
- Demtröder, W. (2017). *Mechanics and Thermodynamics*. Springer.
- Derjaguin, B. V., V. M. Muller, and Y. P. Toporov (1975). Effect of contact deformations on the adhesion of particles. *Journal of Colloid and interface science* 53(2), 314–326.
- Dimitrijevic, B. and K. Hackl (2008). A method for gradient enhancement of continuum damage models. *Technische Mechanik* 28(1), 43–52.
- Dimitrijevic, B. and K. Hackl (2011). A regularization framework for damage–plasticity models via gradient enhancement of the free energy. *International Journal for Numerical Methods in Biomedical Engineering* 27(8), 1199–1210.
- Doghri, I. (1995). Numerical implementation and analysis of a class of metal plasticity models coupled with ductile damage. *International Journal for Numerical Methods in Engineering* 38(20), 3403–3431.
- Donzé, F. V., V. Richefeu, and S.-A. Magnier (2009). Advances in discrete element method applied to soil, rock and concrete mechanics. *State of the art of geotechni-*

- cal engineering. Electronic Journal of Geotechnical Engineering 44.*
- Drucker, D. C. and W. Prager (1952). Soil mechanics and plastic analysis or limit design. *Quarterly of applied mathematics 10*(2), 157–165.
- Düllmann, J., F. Hollmann, M. Thewes, and M. Alber (2013). Analysis of soil-machine-interactions (part 1): Processing of tbm-machine-data and extraction of excavation-specific data. In *3rd International Conference on Computational Methods in Tunneling and Subsurface Engineering, Ruhr University Bochum*, pp. 17–19.
- Eringen, A. C. (1981). On nonlocal plasticity. *International Journal of Engineering Science 19*(12), 1461–1474.
- Eringen, A. C. and D. Edelen (1972). On nonlocal elasticity. *International journal of engineering science 10*(3), 233–248.
- Faria, R., J. Oliver, and M. Cervera (1998). A strain-based plastic viscous-damage model for massive concrete structures. *International journal of solids and structures 35*(14), 1533–1558.
- Fish, J. and T. Belytschko (2007). *A first course in finite elements*. Wiley.
- Francfort, G. and A. Mielke (2006). Existence results for a class of rate-independent material models with nonconvex elastic energies. *Journal für die reine und angewandte Mathematik 2006*(595), 55–91.
- Frenzel, C., H. Käsling, and K. Thuro (2008). Factors influencing disc cutter wear, geomechanik und tunnelbau, heft: 1-9.
- Friedrich, K., Z. Lu, and R. Scherer (1991). Wear and friction of composite materials. *Composite Materials—ICAM 91*, 67–85.
- Gharahbagh, E. A., J. Rostami, and A. Palomino (2011). New soil abrasion testing method for soft ground tunneling applications. *Tunnelling and Underground Space Technology 26*(5), 604–613.
- Gurson, A. L. (1977). Continuum theory of ductile rupture by void nucleation and growth: Part i-yield criteria and flow rules for porous ductile media.
- Gurtin, M. E., E. Fried, and L. Anand (2010). *The mechanics and thermodynamics of continua*. Cambridge University Press.
- Hackl, K. (1997). Generalized standard media and variational principles in classical and finite strain elastoplasticity. *J. Mech. Phys. Solids 45*, 667–688.
- Hackl, K. and F. D. Fischer (2008). On the relation between the principle of maximum dissipation and inelastic evolution given by dissipation potentials. *Proceedings of the Royal Society A: Mathematical, Physical and Engineering Sciences 464*(2089), 117–132.
- Halphen, B. and Q. S. Nguyen (1975). Sur les matériaux standard généralisés.
- Hamilton, W. R. (1834). Xv. on a general method in dynamics; by which the study of the motions of all free systems of attracting or repelling points is reduced to the search and differentiation of one central relation, or characteristic function. *Philosophical transactions of the Royal Society of London 124*, 247–308.
- Hamilton, W. R. (1835). Vii. second essay on a general method in dynamics. *Philosophical Transactions of the Royal Society of London 125*, 95–144.
- Hansen, N. and H. Schreyer (1994). A thermodynamically consistent framework for theories of elastoplasticity coupled with damage. *International Journal of Solids and Structures 31*(3), 359–389.
- Harsha, A. and U. Tewari (2003). Two-body and three-body abrasive wear behaviour of polyaryletherketone composites. *Polymer testing 22*(4), 403–418.
- Haupt, P. (2013). *Continuum mechanics and theory of materials*. Springer Science & Business Media.
- Herrenknecht, A. (2021). www.herrenknecht.com.

- Hertz, H. (1882). On the contact of elastic solids. *Z. Reine Angew. Mathematik* 92, 156–171.
- Hill, R. (1998). *The mathematical theory of plasticity*, Volume 11. Oxford university press.
- Hokkirigawa, K. and K. Kato (1988). An experimental and theoretical investigation of ploughing, cutting and wedge formation during abrasive wear. *Tribology international* 21(1), 51–57.
- Holzapfel, G. (2000). 20 0 0. nonlinear solid mechanics: A continuum approach for engineering.
- Hoormazdi, G. and K. Hackl (2018). On the identification of the contact parameters of the discrete element method for complex particle ensembles. *PAMM* 18(1), e201800112.
- Itasca, C. (1999). Pfc 3d-user manual. *Itasca Consulting Group, Minneapolis*.
- Jantos, D. R., K. Hackl, and P. Junker (2019). An accurate and fast regularization approach to thermodynamic topology optimization. *International Journal for Numerical Methods in Engineering* 117(9), 991–1017.
- Jirásek, M. (2002). Objective modeling of strain localization. *Revue française de génie civil* 6(6), 1119–1132.
- Jirásek, M. and Z. P. Bazant (2001). *Inelastic analysis of structures*. John Wiley & Sons.
- Jirásek, M. and S. Rolshoven (2003). Comparison of integral-type nonlocal plasticity models for strain-softening materials. *International Journal of Engineering Science* 41(13-14), 1553–1602.
- Johnson, K. L., K. Kendall, and a. Roberts (1971). Surface energy and the contact of elastic solids. *Proceedings of the royal society of London. A. mathematical and physical sciences* 324(1558), 301–313.
- Ju, J. (1989). On energy-based coupled elastoplastic damage theories: constitutive modeling and computational aspects. *International Journal of Solids and structures* 25(7), 803–833.
- Junker, P. and K. Hackl (2016). A discontinuous phase field approach to variational growth-based topology optimization. *Structural and Multidisciplinary Optimization* 54(1), 81–94.
- Junker, P. and P. Hempel (2017). Numerical study of the plasticity-induced stabilization effect on martensitic transformations in shape memory alloys. *Shape Memory and Superelasticity* 3(4), 422–430.
- Junker, P., S. Schwarz, D. R. Jantos, and K. Hackl (2019). A fast and robust numerical treatment of a gradient-enhanced model for brittle damage. *International Journal for Multiscale Computational Engineering* 17(2).
- Kachanov, L. M. (1958). Time of the rupture process under creep conditions, *izy akad. Nank SSR Otd Tech Nauk* 8, 26–31.
- Käsling, H. and K. Thuro (2010). Determining abrasivity of rock and soil in the laboratory. In *11th IAEG Congress, Auckland, New Zealand*, Volume 235, pp. 1973–1980.
- Köppl, F. (2014). *Abbauwerkzeugverschleiß und empirische Verschleißprognose beim Vortrieb mit Hydroschild TVM in Lockergesteinen*. Ph. D. thesis, Technische Universität München.
- Kröner, E. (1967). Elasticity theory of materials with long range cohesive forces. *International Journal of Solids and Structures* 3(5), 731–742.
- Kruyt, N. and L. Rothenburg (1996). Microinechanical definition of the strain tensor for granular materials. *Appi. Mech* 118, 706–711.
- Kuhn, M. R. (1997). Deformation measures for granular materials. In *Mechanics of Deformation and Flow of Particulate Materials*, pp. 91–104. ASCE.
- Küpferle, J., A. Röttger, and W. Theisen (2017a). Excavation tool concepts for tbms–

- understanding the material-dependent response to abrasive wear. *Tunnelling and Underground Space Technology* 68, 22–31.
- Küpferle, J., A. Röttger, and W. Theisen (2017b). Fatigue and surface spalling of cemented carbides under cyclic impact loading—evaluation of the mechanical properties with respect to microstructural processes. *Wear* 390, 33–40.
- Laursen, T. and J. Simo (1993). Algorithmic symmetrization of coulomb frictional problems using augmented lagrangians. *Computer methods in applied mechanics and engineering* 108(1-2), 133–146.
- Laursen, T. A. (2013). *Computational contact and impact mechanics: fundamentals of modeling interfacial phenomena in nonlinear finite element analysis*. Springer Science & Business Media.
- Lemaitre, J. (1971). Evaluation of dissipation and damage in metals. In *Proc. ICM Kyoto*, Volume 1.
- Liao, C.-L., T.-P. Chang, D.-H. Young, and C. S. Chang (1997). Stress-strain relationship for granular materials based on the hypothesis of best fit. *International Journal of Solids and Structures* 34(31–32), 4087 – 4100.
- Lubarda, V. (1994). An analysis of large-strain damage elastoplasticity. *International journal of solids and structures* 31(21), 2951–2964.
- Lubliner, J. (2008). *Plasticity theory*. Courier Corporation.
- Maier, G. (1969). Some theorems for plastic strain rates and plastic strains (minimum theorems for plastic strain rates and plastic strains governed by holonomic elastoplastic theory utilizing quadratic functions). *Journal de Mécanique* 8, 5–19.
- Makowski, J., H. Stumpf, and K. Hackl (2006). The fundamental role of nonlocal and local balance laws of material forces in finite elastoplasticity and damage mechanics. *International Journal of Solids and Structures* 43(13), 3940–3959.
- Martin, J. and A. R. Ponter (1966). A note on a work inequality in linear viscoelasticity. *Quarterly of Applied Mathematics* 24(2), 161–165.
- Maugin, G. A. (1992). *The thermomechanics of plasticity and fracture*, Volume 7. Cambridge University Press.
- Mazars, J. and G. Pijaudier-Cabot (1989). Continuum damage theory-application to concrete. *Journal of Engineering Mechanics* 115(2), 345–365.
- Menzel, A., M. Ekh, K. Runesson, and P. Steinmann (2005). A framework for multiplicative elastoplasticity with kinematic hardening coupled to anisotropic damage. *International Journal of Plasticity* 21(3), 397–434.
- Miehe, C., F. Welschinger, and M. Hofacker (2010). Thermodynamically consistent phase-field models of fracture: Variational principles and multi-field fe implementations. *International journal for numerical methods in engineering* 83(10), 1273–1311.
- Mielke, A. (2003). Energetic formulation of multiplicative elasto-plasticity using dissipation distances. *Continuum Mechanics and Thermodynamics* 15(4), 351–382.
- Mises, R. v. (1913). Mechanik der festen körper im plastisch-deformablen zustand. *Nachrichten von der Gesellschaft der Wissenschaften zu Göttingen, Mathematisch-Physikalische Klasse* 1913, 582–592.
- Mohr, O. (1900). Welche umstände bedingen die elastizitätsgrenze und den bruch eines materials. *Zeitschrift des Vereins Deutscher Ingenieure* 46(1524-1530), 1572–1577.
- Mühlhaus, H.-B. and E. Alfantis (1991). A variational principle for gradient plasticity. *International Journal of Solids and Structures* 28(7), 845–857.
- Nedjar, B. (2001). Elastoplastic-damage modelling including the gradient of damage: formulation and computational aspects. *International Journal of Solids and Structures* 38(30-31), 5421–5451.

- Needleman, A. (1988). Material rate dependence and mesh sensitivity in localization problems. *Computer methods in applied mechanics and engineering* 67(1), 69–85.
- Nguyen, G. D., A. M. Korsunsky, and J. P.-H. Belnoue (2015). A nonlocal coupled damage-plasticity model for the analysis of ductile failure. *International Journal of Plasticity* 64, 56–75.
- Niazi, M. S., H. Wisselink, and V. T. Meinders (2012). Viscoplastic regularization of local damage models: a latent solution. In *Key engineering materials*, Volume 504, pp. 845–850. Trans Tech Publ.
- Obermüller, G. (1989). *Ein Beitrag zur Strukturoptimierung unter stochastischen Lasten*. Institut für Mechanik, Ruhr-Universität Bochum.
- Ogden, R. and E. Sternberg (1985). Nonlinear elastic deformations.
- Orowan, E. (1934). Die mechanischen festigkeitseigenschaften und die realstruktur der kristalle. *Zeitschrift für Kristallographie-Crystalline Materials* 89(1-6), 327–343.
- Ortiz, M. and E. Repetto (1999). Nonconvex energy minimization and dislocation structures in ductile single crystals. *Journal of the Mechanics and Physics of Solids* 47(2), 397–462.
- Peerlings, R., M. Geers, R. De Borst, and W. Brekelmans (2001). A critical comparison of nonlocal and gradient-enhanced softening continua. *International Journal of Solids and Structures* 38(44-45), 7723–7746.
- Pijaudier-Cabot, G. and Z. P. Bažant (1987). Nonlocal damage theory. *Journal of engineering mechanics* 113(10), 1512–1533.
- Pijaudier-Cabot, G., Z. P. Bažant, and M. Tabbara (1988). Comparison of various models for strain-softening. *Engineering computations*.
- Popov, V. L. (2010). *Contact mechanics and friction*. Springer.
- Prager, W. (1956). A new methods of analyzing stresses and strains in work hardening plastic solids. *J. Appl. Mech.(ASME)* 23, 493–496.
- Rabinowicz, E. and R. Tanner (1966). Friction and wear of materials.
- Rabotnov, Y. N. (1969). Creep rupture. In *Applied mechanics*, pp. 342–349. Springer.
- Rad, P. F. (1975). Bluntness and wear of rolling disk cutters. In *International Journal of Rock Mechanics and Mining Sciences & Geomechanics Abstracts*, Volume 12, pp. 93–99. Elsevier.
- Rankine, W. J. M. (1872). *A manual of applied mechanics*. Charles Griffin and Company.
- Refaat, M. and S. Meguid (1997). Updated lagrangian formulation of contact problems using variational inequalities. *International journal for numerical methods in engineering* 40(16), 2975–2993.
- Ribeiro, J., A. Santiago, and C. Rigueiro (2016). Damage model calibration and application for s355 steel. *Procedia Structural Integrity* 2, 656–663.
- Röttger, A. (2019). Wear mechanisms of hard phase containing materials. *PAMM* 19(1), e201900440.
- Röttger, A., J. Küpferle, S. Brust, A. Mohr, and W. Theisen (2015). Abrasion in tunneling and mining. In *International Conference on Stone and Concrete Machining (ICSCM)*, Volume 3, pp. 246–261.
- Schütte, H. (2001). *Ein finites Modell für spröde Schädigung basierend auf der Ausbreitung von Mikrorissen*. Inst. für Mechanik.
- Schwarz, S. (2019). Efficient approaches for regularized damage models.
- Schwarz, S., K. Hackl, and P. Junker (2019). An efficient treatment of the laplacian in a gradient-enhanced damage model. *PAMM* 19(1), e201900125.
- Schwarz, S., P. Junker, and K. Hackl (2020). Variational regularization of damage models based on the emulated rve. *Continuum Mechanics and Thermodynamics*, 1–27.
- Silhavy, M. (1997). *The Mechanics and Thermodynamics of Continuous Media*. Springer

- Science & Business Media.
- Silmo, J. (1987). Strain-and stress-based continuum damage models.
- Simo, J. C. and T. J. Hughes (2006). *Computational inelasticity*, Volume 7. Springer Science & Business Media.
- Simo, J. C. and T. Laursen (1992). An augmented lagrangian treatment of contact problems involving friction. *Computers & Structures* 42(1), 97–116.
- Sluys, L. and R. De Borst (1992). Wave propagation and localization in a rate-dependent cracked medium-model formulation and one-dimensional examples. *International Journal of Solids and Structures* 29(23), 2945–2958.
- Soyarslan, C. (2009). Modelling damage for elastoplasticity.
- Stacey, R. (1994). New finite-difference methods for free surfaces with a stability analysis. *Bulletin of the Seismological Society of America* 84(1), 171–184.
- Straßberger, M. (1997). *Aktive Schallreduktion durch digitale Zustandsregelung der Strukturschwingungen mit Hilfe piezo-keramischer Aktoren*. Ph. D. thesis, Inst. für Mechanik.
- Svedberg, T. and K. Runesson (1998). Thermodynamically consistent nonlocal and gradient formulations of plasticity. In *Nonlocal aspects in solid mechanics (Mulhouse, 20-22 April 1998)*, pp. 32–37.
- Svedberg, T. and K. Runesson (2000). An adaptive finite element algorithm for gradient theory of plasticity with coupling to damage. *International journal of solids and structures* 37(48-50), 7481–7499.
- Tanaka, H., A. Oida, M. Daikoku, K. Inooku, O. Sumikawa, Y. Nagasaki, and M. Miyazaki (2007). Dem simulation of soil loosening process caused by a vibrating subsoiler. *Agricultural Engineering International: CIGR Journal*.
- Taylor, G. I. (1934). The mechanism of plastic deformation of crystals. part i. theoretical. *Proceedings of the Royal Society of London. Series A, Containing Papers of a Mathematical and Physical Character* 145(855), 362–387.
- Theisen, W. (1997). *Bearbeiten verschleißbeständiger Legierungen aus werkstofftechnischer Sicht*. VDI Verlag.
- Tresca, H. E. (1869). *M 'e memory on the é flow of solid bodies*, Volume 18. Imp 'e riale.
- Truesdell, C. and W. Noll (2004). The non-linear field theories of mechanics. In *The non-linear field theories of mechanics*, pp. 1–579. Springer.
- Tunnel-Online (2013). The next revolution in epb cutters - new cutter designs make an impression in mixed ground. *Issue 04/2013*.
- Voyiadjis, G. Z. and P. I. Kattan (1992). A plasticity-damage theory for large deformation of solids-i. theoretical formulation. *International Journal of Engineering Science* 30(9), 1089–1108.
- Westerhoff, B. (1995). *Eine Untersuchung zum geschwindigkeitsabhängigen Verhalten von Stahl*. na.
- Woldman, M., E. Van Der Heide, T. Tinga, and M. A. Masen (2013). The influence of abrasive body dimensions on single asperity wear. *Wear* 301(1-2), 76–81.
- Woldman, M., E. Van Der Heide, T. Tinga, and M. A. Masen (2017). A finite element approach to modeling abrasive wear modes. *Tribology transactions* 60(4), 711–718.
- Wriggers, P. and G. Zavarise (2004). Computational contact mechanics. *Encyclopedia of computational mechanics*.
- Zavarise, G., P. Wriggers, and B. Schrefler (1995). On augmented lagrangian algorithms for thermomechanical contact problems with friction. *International Journal for Numerical Methods in Engineering* 38(17), 2929–2949.
- Zhu, Y. and S. Cescotto (1995). A fully coupled elasto-visco-plastic damage theory for

- anisotropic materials. *International Journal of Solids and Structures* 32(11), 1607–1641.
- Zienkiewicz, O. C., R. L. Taylor, and J. Z. Zhu (2005). *The finite element method: its basis and fundamentals*. Elsevier.
- Zum Gahr, K.-H. (1987). *Microstructure and wear of materials*, Volume 10. Elsevier.

Curriculum Vitae

Personal Data

Name	Golnaz Hoormazdi
Date of Birth	01. July. 1987
Place of Birth	Shiraz, Iran

Employment

08/2016 - present	Research assistant, Institute of Mechanics of Materials, Ruhr-Universität Bochum, NRW, Germany
03/2015 - 02/2016	Student assistant, Institute of Continuum Mechanics, Ruhr-Universität Bochum, NRW, Germany
10/2011 - 02/2013	Computational engineer, Vara design idea, Shiraz, Iran

University Education

08/2016 - present	Doctoral student, Institute of Mechanics of Materials, Ruhr-Universität Bochum, NRW, Germany
03/2014 - 07/2016	Master of Science, Computational Engineering, Ruhr-Universität Bochum, NRW, Germany
09/2009 - 08/2011	Master of Science, Civil Engineering, Structural Mechanics Shiraz university, Shiraz, Iran
09/2005 - 08/2009	Bachelor of Science, Civil Engineering, Persian Gulf university, Bushehr, Iran

School Education

09/2001 - 06/2005	High school, Shiraz, Iran
09/1998 - 06/2001	Secondary school, Shiraz, Iran
09/1993 - 06/1998	Primary school, Shiraz, Iran

**Mitteilungen aus dem Institut für Mechanik
RUHR-UNIVERSITÄT BOCHUM
Nr. 187**

ISBN 978-3-935892-65-0